Ministério da Ciência e Tecnologia
Observatório Nacional

GRADIENTES DE METALICIDADE NO DISCO GALÁCTICO: ABUNDÂNCIAS DE ESTRELAS OB

Simone Daflon dos Santos

Tese de doutorado
Orientadora: Drª Katia Cunha
Rio de Janeiro - Janeiro de 2002

A Tese foi apresentada às 14 horas do dia 21 de Fevereiro de 2002, no auditório do Observatório Nacional, sendo a banca examinadora composta por:

Dr^a Katia Cunha (orientadora, presidente) (ON)

Dr^a Beatriz Barbuy (IAG/USP)

Dr. Walter Maciel (IAG/USP)

Dr. Luiz Paulo Vaz (UFMG)

Dr^a Miriani Pastoriza (UFRGS)

Dr. Dalton Lopes (suplente) (ON)

Dr. José Renan de Medeiros (suplente) (UFRN)

Estrelas
Para mim
Para mim
Estrelas
São para mim
Estrelas para mim
Estrelas
Estrelas
Para quê?
Para quê?
Para quê?
Estrelas para mim
Só para mim
Para mim
Para mim
Para mim
E a treva entre as estrelas
Só para mim.

Sérgio Britto & Arnaldo Antunes

Agradecimentos

- Agradeço à Dra Kátia Cunha por ter proposto e orientado este projeto de pesquisa, pelo incentivo e pelo exemplo de conduta profissional.

- Agradeço à CAPES pelo financiamento deste projeto, ao DAAD pelo estágio na Universidade de Munique e à Comissão de Pós-graduação do Observatório Nacional, que financiou as missões observacionais ao McDonald Observatory, nos Estados Unidos, e ao European Southern Observatory (ESO), no Chile.

- Este trabalho contou com a valiosa contribuição do Dr. Verne Smith nas observações realizadas no McDonald e dos Drs. Natalie S. Batalha, Cláudio Bastos, Celso Batalha, Lício da Silva nas observações realizadas no ESO. A todos, o meu muito obrigada.

- Muito obrigada a Keith Butler, Sylvia Becker e Norbert Przybilla pela colaboração nos cálculos fora do ETL e pela acolhida no Departamento de Astronomia da Universidade de Munique, Alemanha.

- Agradeço também a João Luiz Kohl e Aluísio, pela manutenção da estrutura computacional da Coordenação de Astronomia e Astrofísica e da Pós-Graduação, e ao apoio da secretaria da PG e da biblioteca.

- A todos os amigos da Pós-graduação do Observatório Nacional, conquistados durante os anos da minha formação. A todos os amigos, em geral, que preenchem e iluminam a minha vida. Difícil enumerar todos os amigos sem correr o risco de esquecer alguém... Eu considero isso um bom sinal e agradeço a todos pela convivência alegre e edificante.

- Agradeço, finalmente, à minha família e meu marido Paulo, que dividiram comigo os bons momentos e sempre estiveram presentes nos momentos, digamos, um pouco mais complicados.

Resumo

Abundâncias de carbono, nitrogênio, oxigênio, magnésio, alumínio, silício e enxofre foram determinadas para uma amostra de 70 estrelas O9-B2 da seqüência principal, pertencentes a associações OB, aglomerados abertos e regiões H II do disco Galáctico. A análise das abundâncias seguiu uma metodologia única, aplicada a todas as estrelas da amostra, a fim de produzir um conjunto homogêneo de dados de abundâncias, que permita tanto a análise local do padrão de abundâncias quanto a análise da distribuição das abundâncias em função da distância ao centro Galáctico. O método empregado baseia-se na síntese de perfis espectrais fora do Equilíbrio Termodinâmico Local. A combinação da síntese espectral com um tratamento mais realista das populações dos níveis atômicos oferece duas grandes vantagens: além de abundâncias absolutas mais corretas, também torna-se possível analisar quimicamente estrelas com altas velocidades rotacionais projetadas, típicas das estrelas B. No contexto local, a associação de Cep OB2 foi analisada detalhadamente, considerando a maior base de dados de abundâncias disponível para esta associação até o momento. A distribuição de abundâncias obtida sugere que esta associação é quimicamente homogênea e não apresenta variações significativas de abundâncias em função das idades e posições dos dois subgrupos estelares distintos que a compõem e que foram também identificados neste trabalho. A distribuição das abundâncias também foi analisada em termos de gradientes radiais de abundâncias no disco Galáctico, cobrindo uma região entre 4.4 e 12.9 kpc do centro da Galáxia, considerando $R_\odot$=7.6 kpc. Os gradientes obtidos variam entre $-0.031\,\mathrm{dex\,kpc^{-1}}$, o gradiente obtido para o oxigênio, e $-0.049\,\mathrm{dex\,kpc^{-1}}$, para o silício. O gradiente de oxigênio encontrado é menos inclinado do que aqueles obtidos nos estudos mais recentes de gradientes radiais de abundâncias utilizando-se estrelas B.

Abstract

Abundances of carbon, nitrogen, oxygen, magnesium, aluminum, silicon and sulfur are derived for a sample of 70 O9-B2 main sequence stars, members of OB associations, open clusters and H II regions of the Galactic disk. A unique methodology was applied throughout the sample to proceed the chemical analysis, in order to produce a homogeneous set of abundance data. With such a database it is possible to analyze local patterns of the chemical composition (for example, inside OB associations) as well as the distribution of the abundances in the Galactic disk. The methodology adopted in this study is based on the fitting of theoretical line profiles to the observed spectra without the simplifications introduced by the Local Thermodinamical Equilibrium. The adoption of more realistic calculations of the atomic level populations yields absolute abundances that are more correct. At the same time, the fitting of synthetic profiles permits the chemical analysis of stars with high projected rotational velocities, which is very frequent among B star. A detailed analysis of the Cep OB2 association, based on the most complete set of abundances up to now for this association, suggests that Cep OB2 is chemically homogenous, with no significative abundance variations as a function of age or relative position, considering the two stellar subgroups present in this association. In a general context, the distribuition of the chemical abundances are analyzed in terms of radial gradients in the Galactic disk, within $4.4 - 12.9$ kpc from the center of the Galaxy, with the Sun at $R_{\odot}$=7.6 kpc. The derived gradients are between $-0.031\,\mathrm{dex\,kpc^{-1}}$, as for oxygen, and $-0.049\,\mathrm{dex\,kpc^{-1}}$, as for silicon. The oxygen gradient is flatter that those presented by the most recent studies about the radial gradients of stellar abundances.

Índice

Lista de Tabelas

Lista de Figuras

Capítulo 1

Introdução

As estrelas OB são as estrelas mais jovens e massivas (com $M>10M_{\odot}$) da Galáxia. Elas encontram-se geralmente agrupadas em associações OB, distribuídas preferencialmente ao longo do disco Galáctico [1]. Durante a vida da Galáxia, várias gerações de estrelas massivas nascem e evoluem, terminando suas vidas explodindo como supernovas de tipo II (SN II). Estas estrelas contribuem quase que instantaneamente (quando comparado com escalas de tempo galácticas) para o enriquecimento do meio interestelar, através da ejeção de metais produzidos durante a sua evolução. A formação e a evolução subseqüente das estrelas massivas têm, portanto, impacto direto na evolução química do meio interestelar que as envolve. Em escalas menores, a evolução das estrelas OB de idades diferentes, membros de uma associação OB, pode definir um padrão interno de abundâncias na associação. No contexto Galáctico, a análise da composição química de estrelas OB dispostas ao longo do raio Galactocêntrico pode apontar variações da distribuição das abundâncias químicas no disco da Galáxia.

1.1 Padrões de Abundâncias em Associações OB

As associações OB, além das estrelas massivas que as caracterizam, contêm também, em muitos casos, estrelas de baixa massa e nuvens moleculares, a partir das quais se formarão as

---

[1] Nesta tese, convencionamos escrever os adjetivos “Galáctico” e “Galactocêntrico” com letra maiúscula sempre que se referirem à nossa Galáxia.

novas estrelas. Além das explosões de supernovas, vários outros processos contribuem para o enriquecimento do meio, ao mesmo tempo que a formação de novas estrelas remove do meio os elementos ejetados pelas gerações anteriores. Dentro de uma associação, vários desses processos de produção e destruição dos elementos químicos estão presentes em menor escala do que no contexto Galáctico, permitindo a análise da evolução química local. Algumas associações OB apresentam grupos estelares de idades distintas, caracterizando um processo seqüencial de formação estelar, ou seja, podemos observar mais de uma geração estelar dentro do tempo de vida de uma mesma associação jovem. Geralmente, os subgrupos mais velhos são mais dipersos e livres de matéria interestelar. Os subgrupos mais jovens, por outro lado, estão normalmente associados a nuvens de gás e poeira e as estrelas encontram-se mais concentradas. Neste cenário, foi levantada a possibilidade de que as explosões de SN II resultantes da evolução das estrelas mais velhas pudessem contaminar o meio interestelar com os elementos ejetados durante a explosão; evidências desse processo ficariam registradas nas abundâncias das novas gerações estelares, formadas a partir do gás enriquecido. Cunha & Lambert (1992, 1994) estudaram 18 estrelas pertencentes a 4 grupos estelares distintos presentes na associação de Ori OB1. Eles encontraram indícios de variação nas abundâncias de oxigênio e silício entre as estrelas estudadas, correlacionada com a posição e idade das estrelas na associação, sugerindo que processos de auto-enriquecimento teriam ocorrido em Órion. Tal variação nas abundâncias químicas poderia ser observada também entre os grupos estelares de outras associações OB? Para responder a essa pergunta, é necessário testar a hipótese de auto-enriquecimento em outras associações OB do disco Galáctico.

1.2 Distribuição de Abundâncias na Galáxia

As estrelas OB são objetos bastante apropriados para traçar a composição química do disco Galáctico uma vez que *(i)* são objetos jovens (com idades da ordem de 10^7 anos) e, portanto, as suas abundâncias devem ser similares às abundâncias do gás a partir do qual essas estrelas se formaram; *(ii)* por serem jovens, provavelmente essas estrelas ainda estão próximas dos seus locais de formação e *(iii)* as estrelas OB estão localizadas preferencialmente no disco da Galáxia, distribuídas pelos braços espirais e regiões de formação estelar. A distribuição das abundâncias químicas no disco Galáctico, assim como, por exemplo, a distribuição da taxa de formação estelar, a relação idade-metalicidade e a composição química do Sol constituem importantes vínculos observacionais aos modelos de formação e evolução química da Galáxia.

Os resultados observacionais, entretanto, quando tomados isoladamente, podem ser reproduzidos por muitos dos modelos de evolução química propostos atualmente. Em conjunto, estes representam uma restrição muito mais forte. Assim sendo, é necessário que se tenha um conjunto de dados observacionais de alta qualidade para restringir as condições iniciais dos modelos de evolução química e guiar a construção de modelos cada vez mais completos e realistas. Os modelos de evolução química e alguns resultados observacionais obtidos especificamente para os gradientes radiais de abundâncias serão descritos resumidamente a seguir. As previsões dos modelos para a distribuição de abundâncias no disco Galáctico são comparadas com os resultados observacionais, a fim de mostrar a necessidade de se estabelecer vínculos robustos aos modelos.

1.2.1 Modelos de Evolução Química da Galáxia

Os primeiros modelos de evolução química da Galáxia eram baseados em um sistema fechado e homogêneo, constituído inicialmente de gás puro e com função de massa inicial constante. A dificuldade de se reproduzir os resultados observacionais (como por exemplo, a distribuição de metalicidade das anãs-G) exigiu considerações mais sofisticadas, tais como função de massa inicial variável, acréscimo de matéria no disco Galáctico (*infall*) e fluxos radiais de gás.

Os modelos mais atuais consideram os processos de formação da Galáxia, formação e evolução estelar, síntese de elementos químicos durante a evolução estelar, reciclagem do gás em diferentes gerações estelares e a troca de material com o meio extragaláctico. As previsões dos modelos devem representar as propriedades químicas atuais da vizinhança solar e do disco Galáctico e precisam sempre estar guiadas pelas observações. Entre os vínculos observacionais locais estão as abundâncias solares que, em princípio, representam a composição química do meio interestelar a partir do qual o Sol se formou; a evolução das razões de abundância, que representa a escala de tempo de enriquecimento do gás; as taxas relativas de supernovas tipo I e II observadas na vizinhança solar; a distribuição de metalicidade das anãs G; o número relativo de estrelas do halo e do disco na vizinhança solar e a fração relativa de gás e estrelas no disco Galáctico. Em um contexto mais geral, em termos do disco Galáctico, os modelos de evolução química devem procurar reproduzir a taxa de formação estelar, a densidade de gás e estrelas ao longo do disco Galáctico e os gradientes radiais de abundância, sendo estes observados não só na Via Láctea como também em galáxias externas.

1.2.2 O Gradiente de Metalicidade na Galáxia

Gradientes de metalicidade são comumente observados em galáxias elípticas e espirais (Vila-Costas & Edmunds 1992; Henry & Worthey 1999). Os gradientes variam de acordo com a classe morfológica de modo que as galáxias elípticas apresentam gradientes mais planos (da ordem de $-0.02\,\mathrm{dex\,kpc^{-1}}$) enquanto que nas galáxias espirais a variação da metalicidade em função da distância galactocêntrica é da ordem de $-0.07\,\mathrm{dex\,kpc^{-1}}$. Os gradientes das espirais barradas são, em geral, menores do que os gradientes das espirais normais e, além disso, apresentam uma dependência em relação ao tamanho da barra (Martin & Roy 1994).

Na nossa Galáxia, os gradientes de abundâncias no disco podem ser determinados a partir da análise do gás ionizado, das fotosferas estelares e da metalicidade de aglomerados abertos. Em geral, os resultados obtidos por diferentes métodos concordam quanto à existência de gradientes radiais, porém questões importantes em relação à magnitude e à forma dos gradientes ainda permanecem em aberto. Alguns resultados de análises de gradientes no disco Galáctico estão resumidos a seguir.

Regiões H II

Em um dos primeiros estudos realizados sobre gradientes de abundâncias no disco Galáctico, Shaver *et al.* (1983) analisaram o padrão de abundâncias do disco através das abundâncias de regiões H II, cobrindo um intervalo em distância Galactocêntrica de 4 a 14 kpc. Este estudo foi realizado utilizando uma combinação de dados em rádio (para a determinação dos parâmetros físicos) e no óptico (para a determinação de abundâncias através da intensidade relativa de linhas). As distâncias (cinemáticas) das regiões H II foram calculadas a partir de velocidades radiais observadas, considerando $\mathrm{R}_\odot = 10\mathrm{kpc}$. Os gradientes obtidos por Shaver *et al.* são iguais a $-0.07\pm0.015\ \mathrm{dex\,kpc^{-1}}$ para o oxigênio e $-0.09\pm0.015\ \mathrm{dex\,kpc^{-1}}$ para o nitrogênio. Posteriormente, as distâncias cinemáticas das regiões H II da amostra de Shaver foram recalculadas por Henry & Worthey (1999), considerando as mesmas velocidades radiais publicadas, porém adotando $R_\odot = 8.5$kpc; nessa escala, o gradiente de abundâncias de oxigênio foi modificado para -0.05 ± 0.01 dex kpc^{-1}.

Regiões H II situadas na parte mais interna do disco Galáctico, $0 < R_g < 11.4$kpc, foram analisadas por Afflerbach *et al.* (1997). Os gradientes obtidos para N, O e S apresentam a mesma magnitude (~ -0.07 dex kpc^{-1}); a distribuição das abundâncias obtidas foi melhor representada por uma função linear em todo o disco sugerindo que não há variação do gradiente na direção do centro da Galáxia. A parte externa do disco Galáctico foi especialmente estudada por Vílchez & Esteban (1996). Eles determinaram abundâncias de N, O e S para regiões H II localizadas entre 12 e 18 kpc a partir do centro Galáctico. Seus resultados sugerem que o gradiente de oxigênio é menos inclinado na direção do anti-centro Galáctico, da ordem de -0.036 ± 0.02 dex kpc^{-1}. Os gradientes de nitrogênio e enxofre seguem a mesma tendência e parecem ser mais planos na parte externa do disco.

Mais recentemente, Deharveng *et al.* (2000) reacenderam a discussão sobre a magnitude do gradiente radial de oxigênio quando apresentaram um gradiente igual a -0.039 ± 0.005 dex kpc^{-1}, para regiões H II entre 5 e 15 kpc do centro da Galáxia. Eles também compararam as suas determinações de abundâncias com resultados da literatura, utilizando para isso razões de linhas publicadas por diferentes autores. Em relação a Shaver *et al.* (1983), por exemplo, eles recalcularam abundâncias de oxigênio para 15 regiões H II e obtiveram abundâncias menores que aquelas listadas por Shaver, especialmente para as regiões H II situadas na parte interna do disco. De acordo com Deharveng *et al.*, a superestimativa das abundâncias de oxigênio na parte interna do disco (conseqüência da subestimativa das respectivas temperaturas) resultaram no gradiente de oxigênio mais inclinado apresentado por Shaver. Na Tabela 1.1 estão listados alguns exemplos de gradientes de nitrogênio, oxigênio e enxofre determinados a partir de abundâncias nebulares, incluindo as abundâncias de regiões H II.

Nebulosas Planetárias

Outra importante fonte de dados de composição química da Galáxia são as nebulosas planetárias (NP), ejetadas de estrelas com massas intermediárias ($0.8M_\odot < M < 8M_\odot$). As nebulosas planetárias são classificadas de acordo com critérios dinâmicos e evolutivos, de modo que as nebulosas do tipo I (NP I) são as mais jovens, formadas a partir de estrelas com massas

Tabela 1.1: Gradientes de Abundâncias Nebulares ($\mathrm{dex\,kpc^{-1}}$)

Autores	N	O	S
Regiões H II			
Shaver *et al.* (1983)	-0.09 ± 0.015	-0.07 ± 0.015	-0.01 ± 0.02
Afflerbach *et al.* (1997)	-0.072 ± 0.006	-0.064 ± 0.009	-0.063 ± 0.006
Deharveng *et al.* (2000)	–	-0.039 ± 0.005	–
Nebulosas Planetárias			
Maciel & Chiappini (1994)	-0.07	–	–
Maciel & Köppen (1994)	–	-0.069 ± 0.006	-0.067 ± 0.006
Maciel & Quireza (1999)	–	-0.058 ± 0.007	-0.077 ± 0.011
Martins & Viegas (2000)	-0.084 ± 0.034	-0.054 ± 0.014	-0.064 ± 0.035

entre 2.4 e 8 $M_\odot$ e estão distribuídas no disco fino; as nebulosas do tipo III estão associadas ao disco espesso enquanto que as nebulosas do tipo IV pertencem à população do halo. As nebulosas do tipo II (NP II) são ejetadas por estrelas com massas entre 1.2 e 2.4 $M_\odot$ e estão livres de contaminação pela nucleossíntese estelar (exceto para He, C e N). Dentre as nebulosas planetárias, as NP II são que melhor representam a composição química do meio interestelar na região e na época em que foram formadas. Uma análise dos gradientes de abundâncias obtidos separadamente para cada tipo de nebulosa planetária foi realizada por Maciel & Köppen (1994) na verificação de variações temporais dos gradientes. Eles reuniram dados de abundância de O, Ne, S e Ar publicados na literatura para nebulosas planetárias de tipos I, II e III e obtiveram gradientes de abundâncias de O e S para as NP II da ordem de $-0.07\,\mathrm{dex\,kpc^{-1}}$. Além disso, as diferenças entre os gradientes obtidos das nebulosas de tipos I, II e III foram interpretadas como uma evolução temporal dos gradientes, sugerindo que os gradientes se tornam mais acentuados com o tempo, embora os autores tenham examinado outras hipóteses. Maciel & Quireza (1999) redeterminaram os gradientes de O, Ne, S e Ar para a amostra de NP II de Maciel & Köppen, com algumas atualizações, e considerando $\mathrm{R}_\odot = 7.6\mathrm{kpc}$. Os gradientes obtidos basicamente confirmam os resultados de Maciel & Köppen, considerando as incertezas envolvidas na análise.

Martins & Viegas (2000) analisaram o efeito de erros sistemáticos na determinação dos parâmetros físicos de nebulosas planetárias sobre as abundâncias químicas e, consequentemente, sobre os gradientes. Para isso, elas recalcularam as temperaturas, densidades eletrônicas e abundâncias de N, O, Ne e Ar de 43 NP II a partir de razões de linhas publicadas na literatura. O gradiente de oxigênio obtido a partir dessa amostra é de $-0.054\pm0.014\,\mathrm{dex\,kpc^{-1}}$. Elas mostraram ainda que flutuações de temperatura, nem sempre consideradas nas análises de abundâncias em NP, tendem a produzir gradientes mais inclinados. Os gradientes de abundâncias obtidos das análises de nebulosas planetárias descritas aqui estão listados na Tabela 1.1

Abundâncias Estelares

A análise da composição química estelar também permite a determinação de padrões de abundâncias na Galáxia. O primeiro estudo da distribuição de abundâncias de estrelas OB foi conduzido por Gehren *et al.* (1985), baseado na análise de abundâncias de nitrogênio e oxigênio de 11 estrelas OB, utilizando a aproximação do Equilíbrio Termodinâmico Local (ETL). Os objetos analisados estão distribuídos no intervalo $8.5 < R_g < 17$ Kpc, considerando $R_\odot$=10 kpc. Os seus resultados sugeriam que o gradiente de abundâncias, se de fato existesse, não era significativo, em desacordo com os resultados obtidos pela análise da composição química do gás. Fitzsimmons *et al.* (1990) estudaram 20 estrelas OB da seqüência principal pertencentes a 4 aglomerados estelares jovens. Eles determinaram as abundâncias em ETL de N, O, Mg, Al e Si e também encontraram variações radiais nulas ou quase nulas nas abundâncias de N e O, para distâncias Galactocêntricas R_g entre 5.5 e 10.3 Kpc, considerando $R_\odot$=8.5 kpc. Num estudo posterior, Fitzsimmons *et al.* (1992) reuniram larguras equivalentes de linhas de N II e O II para estrelas de 11 aglomerados abertos e associações OB do disco, com $6< R_g <13$ Kpc. Eles determinaram abundâncias em não-ETL de O e N com base na grade de larguras equivalentes teóricas calculadas fora do ETL por Becker & Butler (1988b,c), baseados em modelos atmosféricos inadequados de Gold (1984). Esse modelos incluem um número insuficiente de linhas metálicas na descrição da função distribuição de opacidades, modificando a estrutura de temperatura da atmosfera estelar e, consequentemente, comprometendo as abundâncias absolutas obtidas. Os gradientes obtidos dessa análise também são próximos de zero. Kaufer *et al.* (1994) determinaram as abundâncias em ETL de C, N, O, Mg, Al, Si e S para 16 estrelas OB com $7< R_g <16$ Kpc.

As abundâncias de nitrogênio e oxigênio obtidas foram combinadas com abundâncias de 55 estrelas publicadas na literatura; para esta amostra ampliada, eles obtiveram gradientes de abundâncias de N e O próximos de zero. Kilian-Montenbruck *et al.* (1994) determinaram abundâncias em não-ETL de C, N, O, Mg, Al e Si (novamente, com base nos modelos de Gold, 1984), além de abundâncias em ETL de Ne, S e Fe para estrelas OB de 3 aglomerados abertos na vizinhança solar. Os resultados obtidos, juntamente com abundâncias de outras estrelas OB obtidas pelos autores anteriormente, indicam que os gradientes de abundância de N e O são quase nulos na região $5 < R_g < 10$Kpc.

Smartt & Rolleston (1997) apresentaram pela primeira vez um gradiente de abundâncias de oxigênio igual a $-0.07 \pm 0.01\,\mathrm{dex\,kpc^{-1}}$ a partir da análise fora do ETL da composição química de estrelas OB do disco. Eles atribuem os gradientes quase nulos obtidos pelas análises estelares desenvolvidas até então a dois fatores: *(i)* as amostras eram pequenas e restritas espacialmente a uma região interna a $\mathrm{R_g} \sim 10$kpc; *(ii)* algumas estimativas de distâncias estavam erradas. Por outro lado, as abundâncias de oxigênio de Smartt & Rolleston (1997) foram calculadas interpolando-se na grade de larguras equivalentes teóricas calculadas fora do ETL por Becker & Butler (1988b). Essa grade, por sua vez, foi calculada com base nos modelos atmosféricos ETL de Gold (1984), de modo que os resultados de Smartt & Rolleston (1997) não representam corretamente as abundâncias de oxigênio.

A amostra de Kaufer *et al.* (1994) foi complementada e reanalisada por Gummersbach *et al.* (1998), contando com 16 estrelas distribuídas entre 5.6 e 13.5 kpc. Eles apresentaram abundâncias de C, N, O, Mg, Al e Si calculadas através do ajuste de perfis teóricos não-ETL a perfis observados. A análise consistente e homogênea de Gummersbach *et al.* indica uma variação na distribuição de abundâncias estelares ao longo do disco Galáctico. Os gradientes obtidos por Gummersbach *et al.* estão listados na Tabela 1.2. O oxigênio, especificamente, apresenta um gradiente de $-0.067 \pm 0.024\ \mathrm{dex\,kpc^{-1}}$, fortemente dependente de uma estrela, Sh2 217-3, que está localizada a $\mathrm{R_g} = 13.5$kpc. Do ajuste obtido com 15 estrelas da amostra, ou seja, descartando Sh2 217-3, obtemos um gradiente menos acentuado para o oxigênio, igual a $-0.035 \pm 0.024\ \mathrm{dex\,kpc^{-1}}$.

Rolleston *et al.* (2000) reuniram parâmetros atmosféricos ($\mathrm{T_{eff}}$, $\log g$ e velocidade de microturbulência) e larguras equivalentes publicadas na literatura e determinaram abundâncias em ETL para estrelas OB do disco, cobrindo a região compreendida entre 6 e 17.6 kpc. Em se tratando de uma compilação, a sua amostra total poderia ser dividida em diferentes sub-amostras, de acordo com o método de determinação dos parâmetros atmosféricos e do conjunto de linhas metálicas utilizadas. Na avaliação dos autores, porém, as diferentes características das análises originais (de onde foram obtidas os parâmetros atmosféricos e as larguras equivalentes) não introduzem tendências críticas no estudo desenvolvido. Rolleston *et al.* também testaram a relevância da utilização de cálculos fora do ETL para o oxigênio e magnésio; a partir dos resultados obtidos para esse dois elementos, eles concluiram que a utilização de cálculos fora do ETL não são determinantes na obtenção do gradiente em si, apesar das abundâncias absolutas para cada estrela possivelmente estarem erradas. Entretanto, comparações entre abundâncias químicas de estrelas OB determinadas em ETL e fora do ETL (Daflon *et al.* 2001a, Daflon *et al.* 2001b) mostram que as correções nas abundâncias, introduzidas por cálculos em não-ETL, podem ser bastante significativas e certamente são indispensáveis para um estudo onde se pretende acessar características tão finas como os perfis de abundâncias no disco Galáctico. Os gradientes obtidos por Rolleston *et al.* (2000) também encontram-se listados na Tabela 1.2.

Tabela 1.2: Gradientes de Abundâncias Estelares (dex kpc^{-1})

	SR1997 [a]	G1998 [b]	R2000 [c]	S2001 [d]
C	–	-0.035 ± 0.014	-0.07 ± 0.02	-0.07 ± 0.02
N	–	-0.078 ± 0.023	-0.09 ± 0.01	–
O	-0.07 ± 0.01	-0.067 ± 0.024	-0.067 ± 0.008	–
Mg	–	-0.082 ± 0.026	-0.07 ± 0.01	-0.09 ± 0.02
Al	–	-0.045 ± 0.023	-0.05 ± 0.015	-0.05 ± 0.01
Si	–	-0.107 ± 0.028	-0.06 ± 0.01	-0.07 ± 0.01

[a] Smartt & Rolleston 1997, [b] Gummersbach *et al.* 1998, [c] Rolleston *et al.* 2000, [d] Smartt *et al.* 2001

A análise de estrelas situadas na parte interna do disco Galáctico é prejudicada pela forte extinção presente nessa região, de modo que as amostras estelares geralmente cobrem distâncias a partir de 5 kpc do centro da Galáxia. Smartt *et al.* (2001) empreenderam uma busca por estrelas na direção do centro da Galáxia e analisaram 4 estrelas com distâncias Galactocêntricas entre 2.5 e 4.7 kpc. As abundâncias químicas foram determinadas a partir de ajuste de perfis teóricos calculados em ETL. Os resultados obtidos para as quatro estrelas analisadas mostram altas abundâncias para todos os elementos estudados (C, N, Mg, Al, Si e S), exceto oxigênio, que apresenta um padrão de abundâncias típico da vizinhança solar. De modo geral, as abundâncias obtidas para as quatro estrelas são compatíveis com os gradientes de C, N, Mg, Al e Si obtidos por Rolleston *et al.* (2000), quando extrapolados para regiões internas a $\mathrm{R_g}$=5 kpc; no caso do oxigênio, um ajuste satisfatório para todo o disco não pôde ser obtido com uma função linear, sugerindo que o gradiente de oxigênio é menos acentuado na direção do centro da Galáxia.

Além das estrelas OB, as cefeidas também têm sido utilizadas como traçadoras da composição química no disco Galáctico. Andrievsky *et al.* (2002a) determinaram distribuições de abundâncias para uma amostra de cefeidas localizadas na região de 6 a 11 kpc do centro da Galáxia (para $R_\odot$=7.9 kpc). Os gradientes obtidos estão entre -0.02 e -0.04 dex kpc^{-1}; em particular, o gradiente de oxigênio é igual a -0.022 dex kpc^{-1} e o de ferro é -0.029 dex kpc^{-1}. A amostra de cefeidas foi estendida na direção do centro da Galáxia por Andrievsky *et al.* (2002b), com a inclusão de 5 estrelas entre 4 e 6 kpc do centro Galáctico. De modo geral, a distribuição de abundâncias obtida dentro do intervalo R_g=4-11 kpc é menos inclinada na região da vizinhança solar e torna-se mais inclinada na região interna do disco ($R_g < 6.6$kpc). Caputo *et al.* (2001) determinaram, simultaneamente, a metalicidade, o avermelhamento e distâncias para uma amostra de cefeidas, a partir de dados fotométricos. A distribuição de metalicidade obtida para a região de 6 a 19 kpc do centro Galáctico pode ser descrita por um gradiente único igual a -0.05 ± 0.01 dex kpc^{-1}, mas o ajuste de dois gradientes de metalicidade, com uma descontinuidade em R_g=10 kpc, é igualmente possível.

Gradientes de ferro também podem ser obtidos a partir da análise da metalicidade de aglomerados abertos, inferida através de seus índices fotométricos, como em Janes (1979) e Cameron (1985). Janes (1979) obteve um gradiente de [Fe/H] igual a -0.05 dex kpc^{-1} no intervalo compreendido entre 8 e 14 kpc do centro da Galáxia. Os seus resultados, porém, favorecem a hipótese de que o gradiente seja próximo de zero na parte interna do disco Galáctico e mais pronunciado para $R_g > 11$kpc. A mesma tendência foi sugerida na análise de Cameron (1985): a distribuição de abundâncias de 38 aglomerados entre 7 e 11 kpc parece ser mais inclinada na parte externa do disco Galáctico ($d[Fe/H]/dR = -0.15$ dex kpc^{-1} para $R_g > 8.5$kpc) do que na parte interna do disco (-0.06 dex kpc^{-1}). Friel (1995) reuniu dados de metalicidade, determinados a partir de espectros de baixa-média resolução, para 74 aglomerados localizados entre 7.4 e 18.7 kpc do centro Galáctico. O gradiente de [Fe/H] obtido é igual a -0.091 ± 0.014 dex kpc^{-1}.

Das informações sobre o estudo observacional da distribuição de abundâncias aqui apresentadas, percebe-se que ainda existem controvérsias a respeito da magnitude e da forma dos gradientes radiais de abundâncias, principalmente no que diz respeito às abundâncias estelares. Somente através da análise de uma base de dados homogênea e com significância estatística, baseada em considerações mais realistas e sofisticadas, será possível discutir as variações sutis de abundâncias no disco Galáctico.

1.2.3 As Previsões dos Modelos

Uma variedade de modelos de evolução química da Galáxia, com diferentes abordagens, está disponível atualmente na literatura. Os modelos podem incluir, entre outros, fluxos radiais, diferentes funções de massa inicial (variáveis ou constantes) ou ventos galácticos. Os modelos de evolução química podem também considerar processos hidrodinâmicos na formação da Galáxia - modelos quimiodinâmicos. Estes seriam os mais realistas e completos. Neste momento, entretanto, vamos nos restringir aos modelos clássicos que tratam a evolução química e dinâmica separadamente. Com relação aos gradientes de abundâncias no disco Galáctico, os modelos clássicos conseguem, de modo geral, produzir gradientes de diferentes magnitudes, dependendo das condições iniciais adotadas, mas ainda divergem quanto à variação temporal e espacial dos gradientes.

O modelo de evolução química da Galáxia de Chiappini *et al.* (2001) considera dois episódios distintos na formação da Galáxia: o primeiro, formando rapidamente o halo e o bojo, e o segundo formando o disco em uma escala de tempo que varia em função do raio da Galáxia. O tempo de formação do halo é um dos parâmetros que modificam a magnitude e a forma dos gradientes previstos, de modo que é igualmente possível reproduzir o gradientes de oxigênio de Shaver *et al.* (1983) assim como o de Deharveng *et al.* (2000). Quanto à evolução temporal dos gradientes, os resultados sugerem que os gradientes tendem a aumentar com o tempo, especialmente nas regiões internas do disco.

Alibés *et al.* (2001) consideraram uma taxa de formação estelar ('star formation rate', SFR) variável ao longo do raio Galáctico na construção dos seus modelos, além de incluir o acréscimo de gás extragaláctico na formação do disco Galáctico, considerando dois tipos de composição química para o material acretado: primordial ou enriquecido. A queda de material enriquecido produz gradientes menores do que aqueles produzidos pela queda de material com abundâncias primordiais, devido basicamente às abundâncias da parte externa do disco, onde a formação estelar é menos eficiente. Para o material acretado enriquecido, eles obtiveram gradiente de oxigênio igual a $-0.047\,\mathrm{dex\,kpc^{-1}}$ no intervalo de 4 a 16 kpc em distância Galactocênctrica. Dividindo o disco Galáctico em duas regiões entre $4-10$ e $10-16$ kpc, os gradientes obtidos são -0.040 e $-0.062\,\mathrm{dex\,kpc^{-1}}$ na região interna e externa, respectivamente. Diferente dos modelos de Chiappini *et al.* (2001), os modelos de Alibés *et al.* produzem gradientes que se tornam menos acentuados com o tempo, com uma evolução rápida nos primeiros 5×10^9 anos, seguida de uma lenta evolução até os valores atuais.

Os modelos de Hou *et al.* (2000) também adotam uma SFR variável radialmente e acréscimo de material extragaláctico, porém suprimiram a contribuição da metalicidade produzida pelas estrelas de massas intermediárias a fim de testar o seu peso na definição do padrão de abundâncias observado na Galáxia. Eles obtiveram que gradientes de abundâncias da ordem de $-0.07\,\mathrm{dex\,kpc^{-1}}$ podem ser explicados em termos da contribuição de estrelas massivas apenas. De acordo com os seus modelos, os gradientes tendem a diminuir com o tempo, tornando-se menos acentuados.

1.3 A Proposta deste Trabalho

Este projeto visa construir uma base de dados de abundâncias químicas de estrelas OB homogênea e auto-consistente, que permita estudar a distribuição de abundâncias estelares tanto em um contexto local (dentro da associação OB), quanto na escala do disco da Galáxia. A construção de tal base de dados deve ser feita, necessariamente, a partir do ajuste de perfis espectrais calculados fora do ETL a espectros estelares de alta resolução. Uma metodologia homogênea deve ser adotada para toda a amostra a fim de minimizar possíveis erros sistemáticos, o que poderia mascarar possíveis relações entre abundâncias das estrelas e a sua posição relativa no sistema em questão, quer seja uma associação OB, quer seja o disco Galáctico. No contexto local, o nosso objetivo é estudar a distribuição de abundâncias químicas na associação de Cep OB2 e testar a hipótese de auto-enriquecimento nesta associação, a partir de parâmetros atmosféricos e abundâncias químicas determinados homogeneamente para o maior número possível de estrelas nesta associação. Em uma abordagem mais ampla, pretendemos analisar as abundâncias químicas de uma amostra de estrelas OB representativa do disco Galáctico a fim de verificar possíveis variações da composição química ao longo do raio Galáctico.

Nossa amostra foi definida de modo a ser bastante homogênea e consiste de estrelas da seqüência principal com tipos espectrais entre O9 e B3 que, em princípio, devem representar a composição química primordial do gás que as formou, uma vez que não apresentam ainda contaminação nucleossintética nas suas atmosferas. A análise química das estrelas OB é favorecida por pelo menos dois aspectos: *(i)* as linhas metálicas presentes em seus espectros permitem estudar, além do nitrogênio, oxigênio e enxofre, comumente analisados no gás, alguns elementos importantes para a evolução química da Galáxia, como o carbono, magnésio, alumínio e silício; *(ii)* os seus espectros apresentam várias regiões de contínuo livres de linhas, o que facilita a normalização dos espectros. Por outro lado, no regime de temperaturas típicas dessas estrelas (entre 20000 e 32000K), as limitações da aproximação ETL na teoria de formação de linhas tornam-se consideráveis. A grande vantagem da utilização da aproximação ETL até então, menor tempo de processamento, enfraqueceu-se com os novos computadores e a utilização de algoritimos otimizadores. Aliado a esse fato, os modelos atômicos utilizados nos cálculos não-ETL são cada vez mais completos, possibilitando cálculos mais corretos das populações dos níveis de energia. Dessa forma, a inclusão dos efeitos não-ETL na teoria de formação de linhas torna-se uma ferramenta essencial para a análise correta e fisicamente mais realista das abundâncias químicas em estrelas quentes. Essa será a abordagem adotada nesse trabalho.

Nos capítulos que se seguem, são apresentados resultados de parâmetros atmosféricos e abundâncias químicas calculadas fora do ETL para estrelas OB pertencentes a associações OB, aglomerados abertos e regiões H II do disco Galáctico. A distribuição das abundâncias químicas como função das posições das estrelas no disco é discutida em seguida, assim como as implicações desses resultados nos modelos de evolução química da Galáxia. A análise de abundâncias químicas foi baseada em espectros de alta resolução obtidos em dois observatórios: a amostra do hemisfério Norte foi observada no Mc Donald Observatory, da Universidade do Texas, Austin, enquanto que a amostra do hemisfério Sul foi observada no European Southern Observatory, Chile (dentro do tempo concedido ao Observatório Nacional por ocasião do convênio ESO/ON). Pelo o menos um espectro foi obtido para cada estrela, sendo que, para muitas delas, mais de um espectro foram obtidos na mesma noite ou em noites diferentes. Os dados foram processados e analisados nas estações de trabalho da Coordenação de Astronomia e Astrofísica do Observatório Nacional, onde estão implementados os programas de redução de dados (IRAF, 'Image Reduction and Analysis Facility'), determinação dos parâmetros estelares, cálculo dos modelos atmosféricos e cálculo dos perfis espectrais teóricos (em ETL e fora do ETL).

A apresentação e discussão dos resultados deste trabalho de tese será feita da seguinte forma: os textos dos capítulos 3, 4 e 5 correspondem aos textos integrais de artigos publicados no Astrophysical Journal; os capítulos 6 e 7 estão apresentados na forma de *pre-prints* a serem submetidos para publicação ao Astrophysical Journal. Um breve resumo, em português, do conteúdo de cada um desses artigos (*pre-prints*) é apresentado no início de cada capítulo. O capítulo 2 apresenta uma visão geral do cálculo fora do ETL das populações dos níveis adotado neste trabalho, juntamente com uma descrição dos modelos e dados atômicos utilizados. O capítulo 3 é dedicado à associação de Cep OB2; parte dos resultados discutidos nesse capítulo (parâmetros estelares e abundâncias de alguns elementos em ETL) estão descritos na dissertação de Mestrado (Daflon, 1997). No capítulo 4, são analisadas estrelas pertencentes a cinco associações OB do disco Galáctico. A análise da composição química, até então restrita a estrelas com baixas velocidades rotacionais projetadas, é extendida para estrelas com altos $v \sin i$ no capítulo 5. Estrelas OB distribuídas ao longo do disco Galáctico, cobrindo um intervalo mais representativo em distâncias Galactocêntricas, são analisadas no capítulo 6. O capítulo 7 é dedicado à analise da distribuição das abundâncias estelares em termos das suas posições relativas no disco Galáctico, definindo um gradiente radial de abundâncias químicas. Uma visão geral dos principais resultados deste estudo é delineada no capítulo 8.

Capítulo 2

Os Cálculos Fora do Equilíbrio Termodinâmico Local

2.1 Introdução

Descrever uma atmosfera estelar significa descrever, através da equação de transporte, todos os processos que acontecem com a radiação emitida no centro da estrela à medida que o feixe de radiação atravessa (e interage com) a atmosfera estelar. O que se observa, então, é diferente do que foi produzido inicialmente, uma vez que o feixe inicial foi modificado por vários processos radiativos e colisionais que acontenceram no meio do caminho. Dessa forma, a análise das informações observacionais de uma estrela depende do estudo do seu campo de radiação, caracterizado, primariamente, pela temperatura. Dependendo do fenômeno estudado para a sua determinação, a temperatura pode ser definida como temperatura cinética das partículas, temperatura de excitação e temperatura de ionização. Os valores dessas três temperaturas podem ser diferentes entre si mas, supondo que o material esteja isolado, os processos interativos das partículas com o campo radiativo e das partículas entre si podem levar a uma situação de equilíbrio em que todas as definições de temperatura tenham o mesmo valor. A matéria, nesse caso, é dita em equilíbrio termodinâmico (ET) e o campo de radiação pode ser descrito por um único valor de temperatura.

Essa simplificação seria aplicável às atmosferas estelares? O campo de radiação nas atmosferas estelares não é isotrópico, uma vez que a estrela emite radiação. Desse modo, o

ET não pode ser aplicado às atmosferas estelares. Mas, pode-se supor, por exemplo, que, em pequenas porções da atmosfera estelar, o ET seja válido. Se o livre caminho médio dos fótons e partículas é menor do que as distâncias para as quais verificam-se variações na temperatura, o ET é válido localmente, definindo o equilíbrio termodinâmico local (ETL).

Nas condições físicas dos interiores estelares, o ETL é uma boa aproximação: as condições de densidade e pressão do gás colaboram para que a taxa de processos colisionais seja maior do que a taxa de processos radiativos, assegurando, localmente, uma situação de equilíbrio. Nessas condições, a descrição dos números de ocupação dos estados de energia é bastante facilitada uma vez que: a intensidade do campo de radiação pode ser representada pela função de Planck; os campos de radiação e de velocidades das partículas são descritos por uma única temperatura; a equação de Saha-Boltzmann descreve a distribuição dos íons sobre os estágios de ionização e dos átomos e íons sobre os estados de excitação, enquanto que a a distribuição das velocidades das partículas é descrita pela equação de Maxwell-Boltzmann; as probabilidades de transição entre dois níveis energéticos são iguais para os processos diretos e os seus inversos (equilíbrio detalhado).

Nas camadas mais superficiais (as camadas observáveis) das atmosferas estelares, entretanto, na presença de gradientes de temperaturas e de um campo de radiação não-isotrópico, os processos radiativos afastam-se do equilíbrio detalhado. Além disso, dadas as condições de densidade e pressão do meio, as taxas de colisões são menores do que nas camadas mais internas e os processos radiativos tornam-se mais importantes. Nessas condições, os verdadeiros números de ocupação dos estados passam a ser especificados pelas equações de equilíbrio estatístico, que devem considerar todos os processos, radiativos e colisionais, diretos e inversos, que levam as partículas de um estado i para um estado j.

2.2 O Cálculo Fora do ETL

Em condições fora do ETL (ou não-ETL), o estado de excitação e ionização do gás é fortemente influenciado pelo campo de radiação que, por sua vez, é determinado pelo estado do gás via equação de transporte. Dessa forma, as equações de transporte radiativo e de equilíbrio estatístico estão acopladas e é necessário que a solução de ambas as equações seja completamente auto-consistente e simultânea. A solução das equações representa, ponto a ponto na atmosfera, a distribuição do campo de radiação como função da freqüência, da temperatura e da densidade do material e da distribuição dos átomos e íons sobre todos os estados ligados, definindo as populações dos níveis. Então, para cada ponto da atmosfera calculado, há um vetor solução associado. O número de elementos de cada vetor é função do número de freqüências considerado (k) mais número de estados descritos (l) mais parâmetros termodinâmicos do material (temperatura T, densidade N, densidade eletrônica n_e). Para se determinar cada um desses vetores, é necessário escrever $k+l+3$ equações não-lineares, que devem ser resolvidas iterativamente. Para se ter uma idéia do número de equações envolvidas no cálculo das populações de uma espécie, os modelos atômicos utilizados neste estudo contém tipicamente 80-100 níveis energéticos (com exceção do alumínio, representado por um modelo atômico mais simples) e o número de freqüências considerado varia de 2200 a 3200 pontos.

Uma descrição completa do cálculo fora do ETL pode ser encontrada em Mihalas (1978). Em termos gerais, a equação de transporte radiativo pode ser escrita como

$$\mu \frac{dI_\nu}{d\tau_\nu} = I_\nu - S_\nu, \tag{2.1}$$

onde μ é o cosseno direcional, I_ν é a intensidade do campo e S_ν é a função fonte, em cada freqüência ν. A solução formal da equação 2.1 pode ser expressa em termos da intensidade média do campo J_ν como

$$J_\nu = \Lambda[S_\nu], \tag{2.2}$$

onde o operador Λ é definido como

$$\Lambda[f(t)] = \frac{1}{2}\int_0^\infty f(t) E_1 |t-\tau| dt. \tag{2.3}$$

A modificação do feixe de radiação pode ser expressa em termos dos coeficientes de absorção κ_ν e de emissão j_ν que retiram ou somam energia ao feixe. Os processos que removem energia do feixe podem ser através de absorção verdadeira ou de espalhamento do fóton da direção original, enquanto que os processos de emissão e espalhamento de um fóton para uma região específica contribuem para aumentar a energia do feixe. A função fonte, em termos dos coeficientes de absorção verdadeira κ_ν^A e absorção por espalhamento κ_ν^S é dada por

$$S_\nu = \frac{\kappa_\nu^S}{\kappa_\nu^A + \kappa_\nu^S} J_\nu + \frac{\kappa_\nu^A}{\kappa_\nu^A + \kappa_\nu^S} B_\nu, \tag{2.4}$$

onde B_ν é a função de Planck. Os coeficientes j_ν e κ_ν estão relacionados com as constantes atômicas dos níveis e transições através dos coeficientes de Einstein A_{ji}, B_{ji} e B_{ij}, que expressam as probabilidades de emissão espontânea, de emissão estimulada e de absorção, respectivamente. A contribuição da emissão espontânea para o coeficiente de emissão é

$$j_\nu = N_j A_{ji} h\nu, \tag{2.5}$$

onde N_i e N_j são as populações dos níveis i e j e $h\nu$ é a energia do nível mais baixo. O coeficiente de absorção pode ser expresso em termos da energia absorvida do feixe

$$\kappa_\nu \rho I_\nu = N_i B_{ij} I_\nu h\nu - N_j B_{ji} I_\nu h\nu. \tag{2.6}$$

Em uma situação de equilíbrio, $N_j A_{ji} + N_j B_{ji} I_\nu = N_i B_{ij} I_\nu$. Os coeficientes de Einstein estão relacionados entre si através das energias e pesos estatísticos (g_i e g_j) dos níveis

$$\frac{B_{ji}}{B_{ij}} = \frac{g_i}{g_j} \tag{2.7}$$

e

$$\frac{A_{ji}}{B_{ji}} = \frac{2h\nu^3}{c^2}. \tag{2.8}$$

A função fonte, em termos das equações 2.5 a 2.8, pode ser re-escrita como

$$S_\nu = \frac{2h\nu^3}{c^2} \frac{1}{(N_i/N_j)(g_j/g_i) - 1} \tag{2.9}$$

explicitando a dependência da função fonte sobre as populações dos níveis energéticos que, por sua vez, são determinadas pela interação do material com o campo de radiação. A interdependência das variáveis físicas – freqüências, ângulos e transições – cria um acoplamento entre as equações de transporte e de equilíbrio estatístico que deve ser tratado, matematicamente, através de métodos iterativos.

No processo iterativo entre as populações dos níveis atômicos e o campo radiativo, cada iteração corresponde ao movimento dos fótons em uma unidade de livre caminho médio. A convergência desse processo depende do livre caminho médio $\bar{l}$ dos fótons: para $\bar{l}$ mais curtos, é necessário um número maior de iterações para que uma pequena distância seja percorrida, o que 'atrasa' a convergência e significa um alto custo em termos de tempo computacional.

2.2.1 Descrição dos Programas

Pela necessidade de se diminuir o tempo computacional, foram elaboradas diferentes técnicas de aceleração de convergência (Hubeny, 1992). A aceleração consiste, basicamente, em determinar soluções aproximadas da equação de transporte, obtidas com operadores mais simples (ou 'aproximados'), e corrigí-las iterativamente, a fim de se obter o resultado exato do problema de transporte radiativo. As várias técnicas propostas diferenciam-se quanto à definição do operador aproximado; em conjunto, essas técnicas são conhecidas genericamente como Iteração Lambda Aproximada ('Approximate Lambda Iteration', ALI). O operador lambda aproximado Λ^* é definido de modo que

$$\Lambda = \Lambda^* + (\Lambda - \Lambda^*) \tag{2.10}$$

onde $(\Lambda - \Lambda^*)$ é o termo de correção. A equação 2.2, então, pode ser re-escrita como

$$J_\nu^i = \Lambda^*[S_\nu^i] + (\Lambda - \Lambda^*)[S_\nu^{i-1}]. \tag{2.11}$$

Quando este processo converge, ou seja, quando $S_\nu^i = S_\nu^{i-1}$, a solução exata da equação de transporte, definida pelo operador Λ, é obtida.

Neste trabalho, as soluções das equações de equilíbrio estatístico combinadas com as equações de transporte, representadas pelas populações dos níveis, são obtidas com a versão mais recente do programa DETAIL (Butler, 1994). As informações iniciais necessárias são modelos atmosféricos, modelos atômicos para as espécies de interesse e os processos radiativos e colisionais que ocorrem entre os níveis de energia, representados pelas seções de choque e pela força de oscilador. Como resultado, são obtidos os números de ocupação dos estados dos átomos e íons nas atmosferas estelares. Esta versão do programa DETAIL é baseada no algoritmo de Werner & Husfeld (1985) para o cálculo de formação de linhas fora do ETL. Este algoritmo adota o operador Λ^* de Scharmer (1981) e pode ser apresentado resumidamente da seguinte maneira:

- calculam-se as escalas de profundidade óptica e funções fonte para todas as freqüências a partir de estimativas iniciais dos números de ocupação, que podem ser obtidas de cálculos em ETL.

- calcula-se o termo de correção $\Delta J_\nu = (\Lambda - \Lambda^*) S_\nu = \Lambda S_\nu - \Lambda^* S_\nu$ para todas as freqüências a partir da diferença entre uma solução 'formal' da equação 2.1 e uma solução aproximada, obtida com o operador Λ^*.

- Resolvem-se simultaneamente as equações aproximadas de equilíbrio estatístico e de transporte para cada profundidade. Este procedimento é repetido até que se atinja a convergência, ou seja, até que as mudanças nos números de ocupação e funções fonte sejam pequenas.

Os perfis de linha são calculados com o programa SURFACE (Butler, 1984), dividindo as populações dos termos de acordo com o peso estatístico dos sub-níveis j. Cada componente do multipleto é, então, calculada para o comprimento de onda observado, considerando que o perfil da linha é um perfil de Voigt. Neste cálculo são incluídas constantes de alargamento radiativo e colisional. Além disso, os efeitos da microturbulência também são incluídos no alargamento do perfil como um termo adicional do alargamento Doppler.

2.3 Modelos Atômicos: Níveis de Energia e Transições

O cálculo das linhas fora do ETL exige a construção de modelos atômicos bastante completos quanto à descrição dos níveis de energia do estágio de ionização principal, além dos níveis de energia mais baixa dos estágios adjacentes, com populações relevantes no regime de parâmetros atmosféricos em questão. Como o campo de radiação, modificado por uma das transições possíveis, poderá afetar qualquer outra transição do átomo, formando uma cadeia de interações, *a completeza dos modelos atômicos adotados é essencial para garantir o equilíbrio de ionização e o cálculo correto das populações dos níveis.* Cada nível atômico é descrito pelo seu peso estatístico e potencial de excitação. As transições que levam ao povoamento e despovoamento de cada nível são descritas por suas forças de oscilador ou seções de choque. Nem todas as transições descritas, porém irão influenciar diretamente os níveis energéticos de interesse no tratamento de um conjunto de linhas espectrais, de modo que o conjunto de transições pode ser dividido em dois: para aqueles níveis diretamente relacionados com as linhas de interesse é necessário um tratamento mais rigoroso e auto-consistente, enquanto que os demais níveis podem ser tratados com menor rigor, sem que as populações finais sejam afetadas. As transições do primeiro grupo devem ser explicitamente calculadas fora do ETL, através da linearização das equações a elas associadas. Para as transições do segundo grupo, o cálculo em ETL das populações, através das equações de Saha-Boltzmann, é uma boa aproximação. Uma breve descrição dos modelos atômicos adotados e das transições consideradas é apresentada a seguir.

Carbono

No modelo do C II (Eber & Butler, 1988), todos os níveis de energia até n=6, com termos convergindo para o nível fundamental do C III ($2s^2\ ^1s$), e até n'=4, para termos convergindo para o nível $2s2p^3P^o$, são incluídos explicitamente nas equações de equilíbrio estatístico. Os termos referentes a n=7, n=8 e n'=5, n'=6 são mantidos fixos em ETL. O nível fundamental (NF) e os dois primeiros estados excitados do C III, além do NF do C IV, são calculados explicitamente fora do ETL. O C I não é significativo nas temperaturas típicas das estrelas OB e, portanto, não está incluído no modelo atômico.

Todas as transições ligado-ligado (bb) são consideradas; dentre elas, 73 transições são linearizadas: aquelas com $1000\text{Å} < \lambda < 9000\text{Å}$; aquelas com $f > 10^{-2}$; transições relacionadas com o nível 3d ou 4f do C II; NF do C II e do C III. Os níveis e transições (fixas em ETL e calculadas explicitamente) considerados na construção do modelo de C II estão representados na Figura 2.1.

No modelo do carbono duas vezes ionizado (Eber, 1987), são incluídos todos os níveis de energia até n=6 e n'=4, totalizando 5 níveis do C II + 68 níveis do C III + o nível fundamental do C IV, explicitamente calculados, além de 21 níveis de C II e 22 do C III fixos em ETL.

Todas as transições radiativas bb são consideradas, sendo que todas as transições entre níveis NETL e com $f > 10^{-2}$, em um total de 89 transições, são linearizadas.

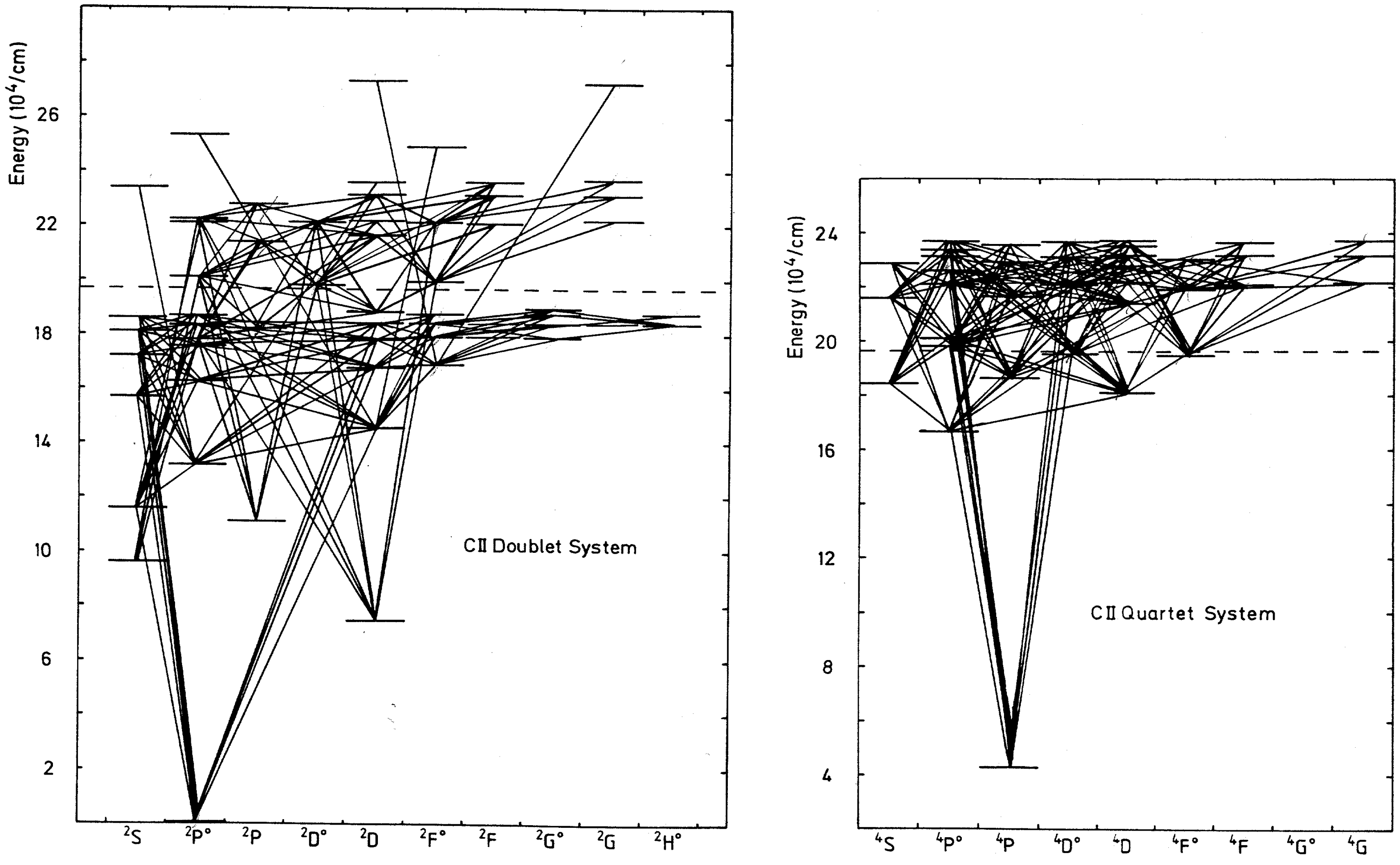

Figura 2.1: Diagramas de Grotrian para os sistemas de dubletos (painel esquerdo) e quartetos (painel direito), considerados na construção do modelo atômico do carbono (de Eber & Butler, 1988). As energias dos níveis, em unidades de $10^4\mathrm{cm}^{-1}$, estão representadas no eixo das ordenadas enquanto que os termos considerados estão identificados pela sua notação espectroscópica no eixo das abscissas. As linhas tracejadas representam o limite de ionização.

Nitrogênio

Todos os níveis até n=4, que produzem as linhas na região 4000–5000Å, são considerados na construção do modelo atômico do nitrogênio (Becker & Butler, 1988). Os níveis até n=10 também são incluídos, mas são mantidos fixos em relação ao NF do próximo estágio de ionização. No total, são considerados 3 níveis de N I, 50 níveis de N II calculados explicitamente + 23 níveis de N II em ETL, 5 níveis de N III e o NF do N IV.

Todas as transições radiativas permitidas entre os níveis NETL são incluídas. Além disso, algumas transições que envolvem níveis ETL, com $f > 10^{-4}$, também são consideradas. No total, 215 transições são consideradas, sendo 48 delas linearizadas. Os sistemas de singleto e tripleto são tratados simultaneamente. Os processos de fotoionização são tratados para todos os níveis NETL. Os níveis e transições considerados na construção do modelo de N II estão representados na Figura 2.2.

Oxigênio

A região centrada em $4000 < \lambda < 5000$Å contém mais de 100 linhas de O II, sendo que as transições nesse intervalo de comprimento de onda envolvem principalmente os níveis n=3 e n=4. Desse modo, no modelo atômico do oxigênio (Becker & Butler, 1989) as populações NETL são calculadas para todos os níveis até n=4; além disso todos os níveis até n=10 também são incluídos, porém, fixos em ETL. O modelo atômico é composto por 3 níveis de O I, 52 níveis NETL de O II + 27 níveis ETL de O II, 3 níveis de O III e o NF do O IV.

Todas as transições bb permitidas entre os níveis NETL do O II foram incluídas, além das transições que envolvem os níveis fixos. Apenas as transições com $f < 10^{-4}$ não foram incluídas. No total, foram consideradas 234 transições; destas, 73 foram linearizadas. Os sistemas dubleto e quarteto foram tratados simultaneamente. Os processos de fotoionização foram tratados para todos os níveis NETL. Os diagramas de Grotrian para o oxigênio estão representados nas Figuras 2.3 e 2.4.

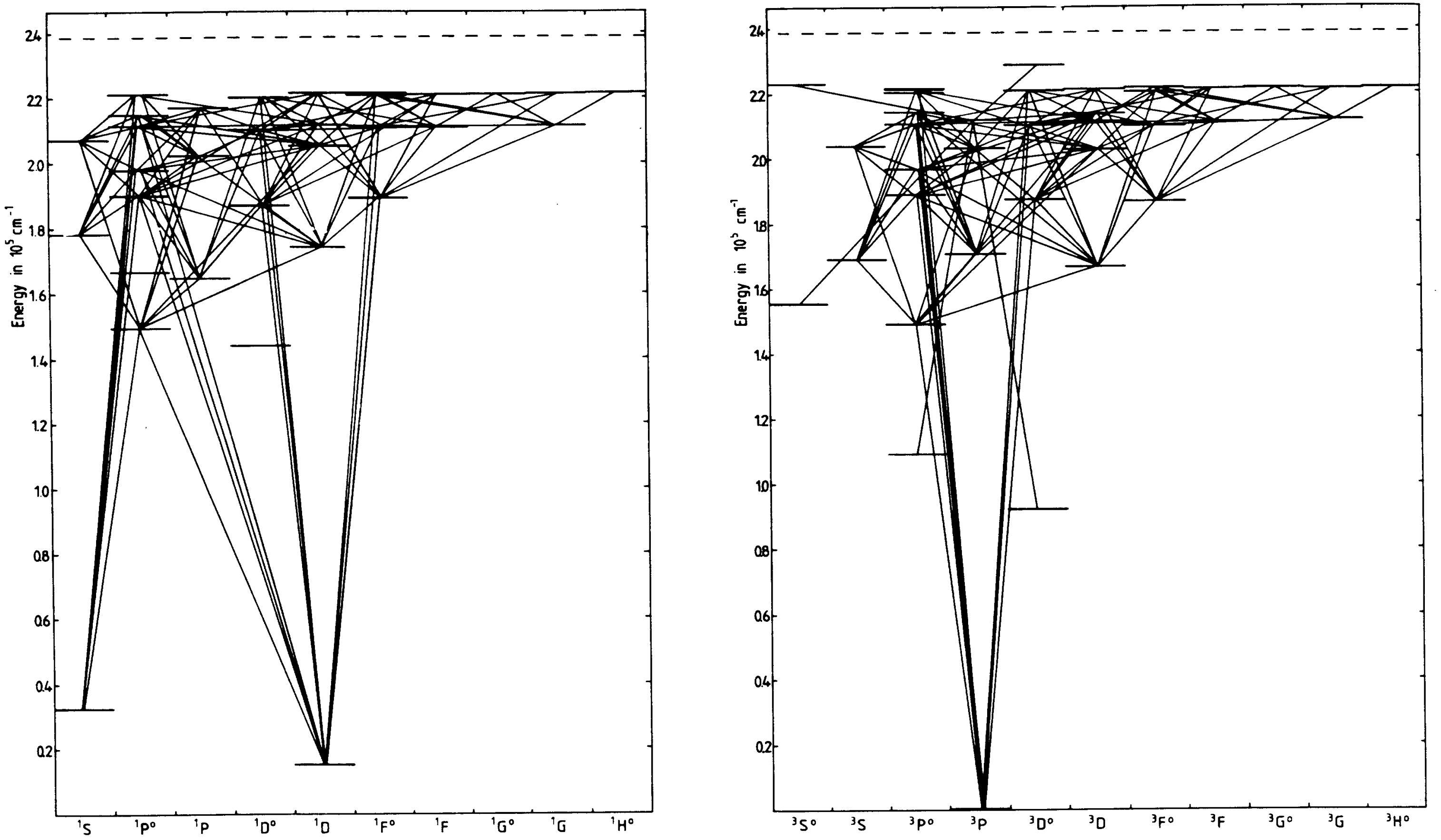

Figura 2.2: Diagramas de Grotrian para os sistemas de singletos (painel esquerdo) e tripletos (painel direito) considerados no modelo atômico do nitrogênio (de Becker & Butler, 1989). As energias dos níveis, em unidades de 10^5cm^{-1}, estão representadas no eixo das ordenadas enquanto que os termos considerados estão identificados pela sua notação espectroscópica no eixo das abscissas. As linhas tracejadas representam o limite de ionização.

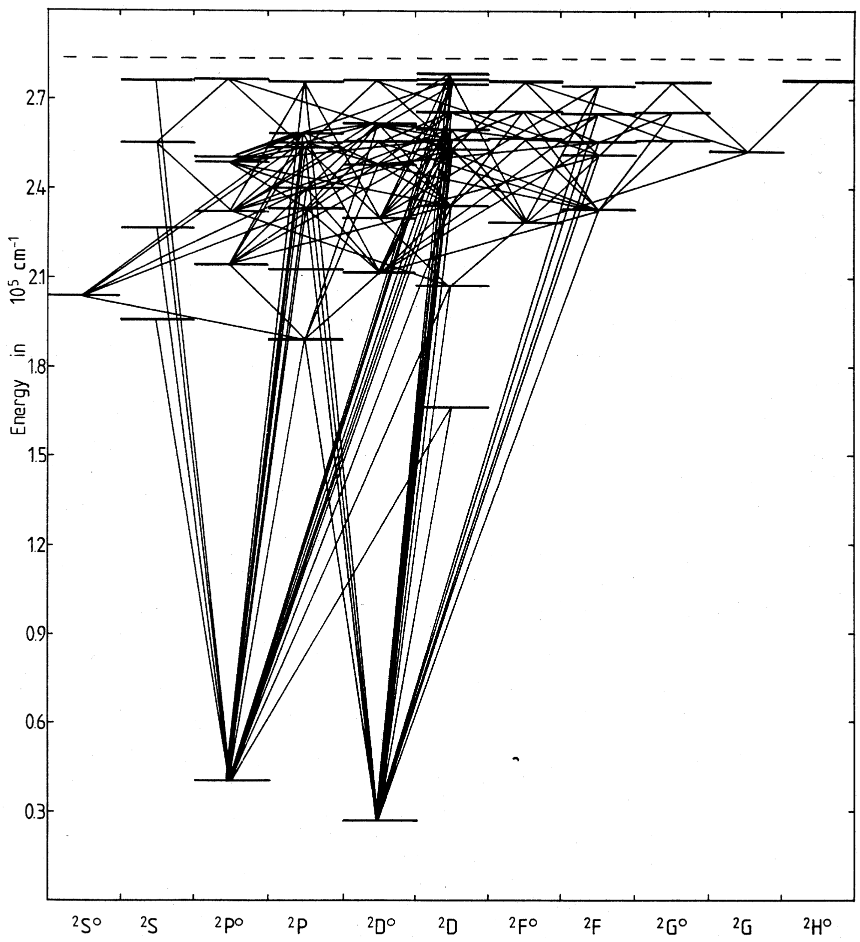

Figura 2.3: Diagrama de Grotrian para o sistema de dubletos do O II (de Becker & Butler, 1988). As energias dos níveis, em unidades de 10^5cm^{-1}, estão representadas no eixo das ordenadas enquanto que os termos considerados estão identificados pela sua notação espectroscópica no eixo das abscissas. A linha tracejada representa o limite de ionização.

Magnésio

Para o Mg I, todos os níveis até n=9 são incluídos explicitamente, além de considerar também os níveis até n=12 em ETL (Przybilla *et al.*, 2001). Todos os níveis do Mg II até n=10 (para $l \leq 4$) são incluídos em NETL, enquanto que os níveis l complementares são considerados em ETL. No total, o modelo atômico é constituído por 71 níveis do Mg I, 28 do Mg II e o NF do Mg III. Todas as transições radiativas permitidas entre os níveis NETL são incluídas,

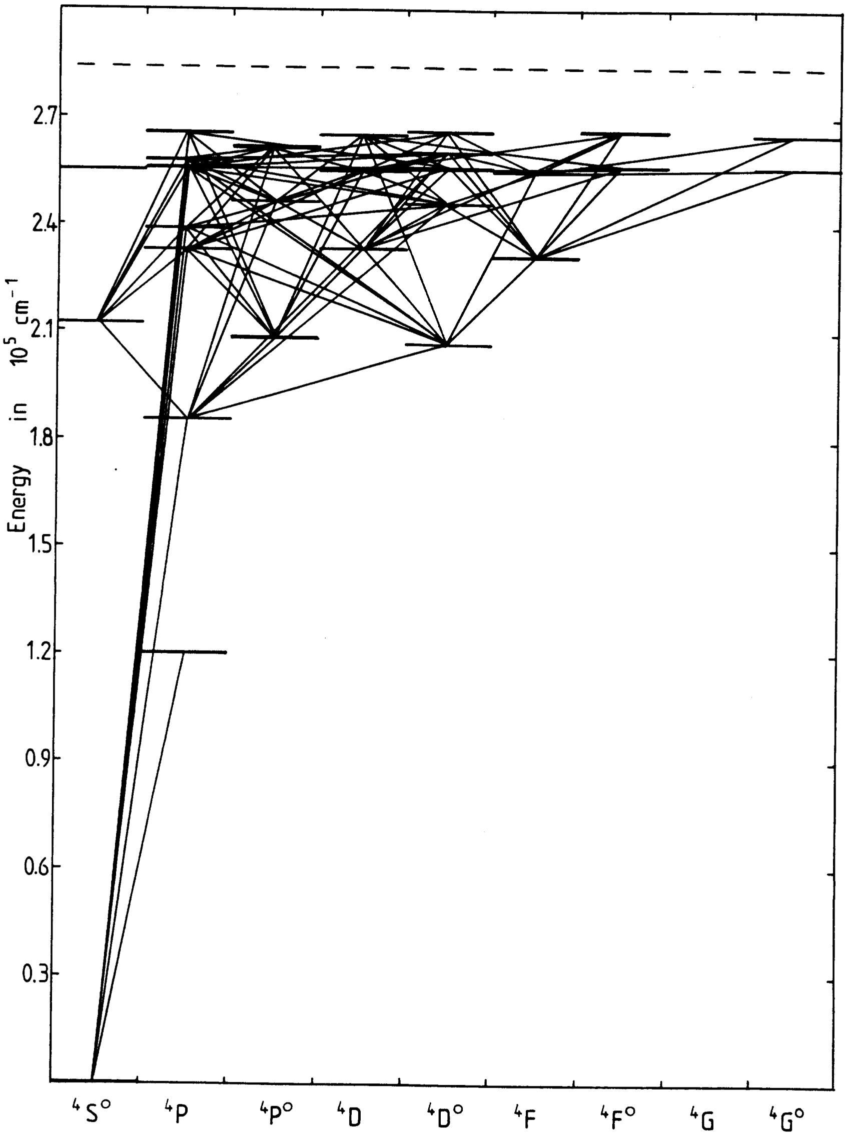

Figura 2.4: Diagrama de Grotrian para o sistema de quartetos do O II (de Becker & Butler, 1988). As energias dos níveis, em unidades de 10^5cm^{-1}, estão representadas no eixo das ordenadas enquanto que os termos considerados estão identificados pela sua notação espectroscópica no eixo das abscissas. A linha tracejada representa o limite de ionização.

assim como todas as fotoionizações a partir de níveis NETL, totalizando 71 transições. Os singletos e tripletos são tratados simultaneamente para Mg I/Mg II. Os modelos de Mg I e Mg II estão representados nas Figuras 2.5 e 2.6, respectivamente.

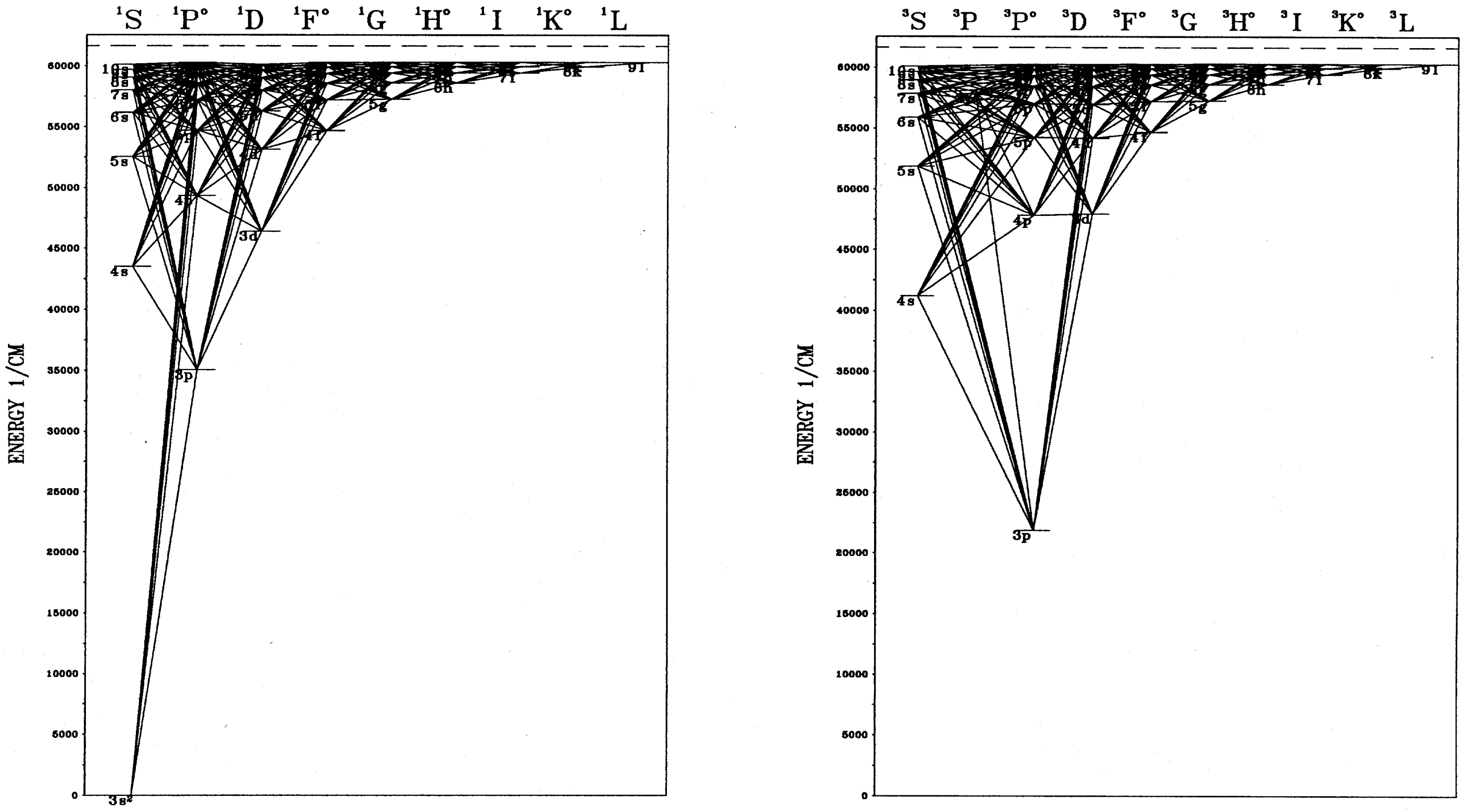

Figura 2.5: Diagramas de Grotrian para os sistemas de singletos (painel esquerdo) e tripletos (painel direito) do Mg I (de Przybilla *et al.*, 2001). As energias dos níveis, em unidades de cm^{-1}, estão representadas no eixo das ordenadas enquanto que os termos considerados estão identificados pela sua notação espectroscópica no eixo das abscissas. As linhas tracejadas representam o limite de ionização.

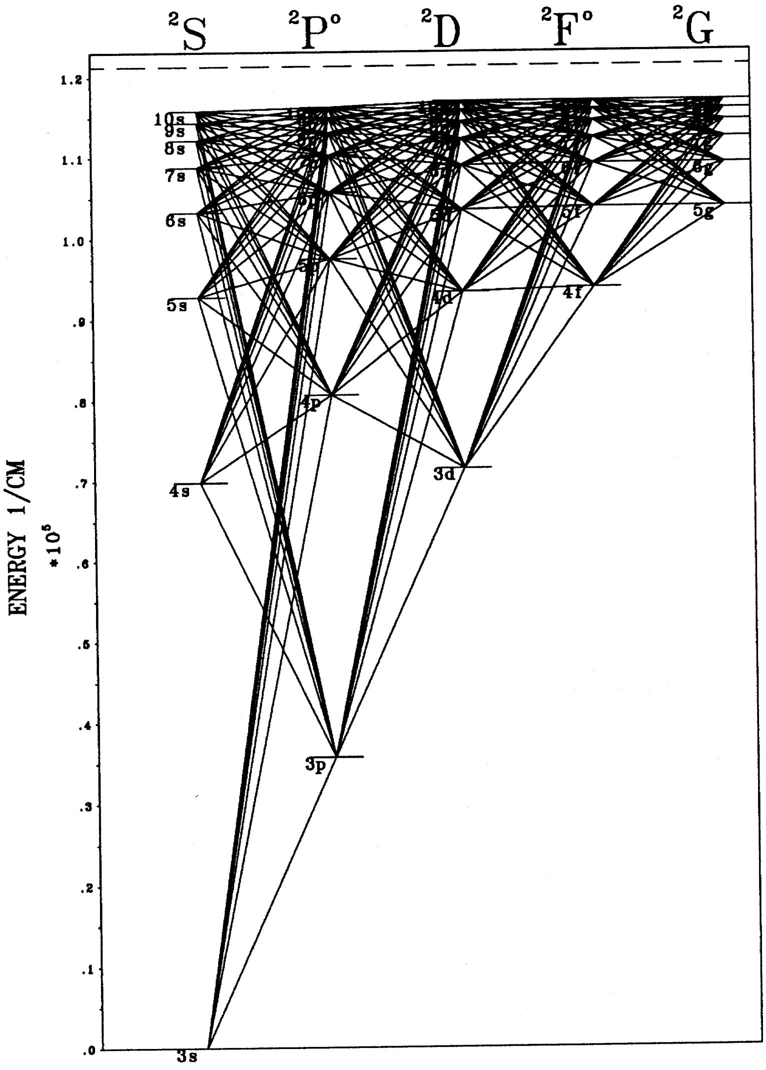

Figura 2.6: Diagrama de Grotrian para o Mg II (de Przybilla *et al.*, 2001). As energias dos níveis, em unidades de cm^{-1}, estão representadas no eixo das ordenadas enquanto que os termos considerados estão identificados pela sua notação espectroscópica no eixo das abscissas. As linhas tracejadas representam o limite de ionização.

Alumínio

O modelo atômico do alumínio (Dufton *et al.*, 1986) é composto por 12 níveis de Al III mais o NF do Al IV. Nos intervalos de temperaturas efetivas e gravidades superficiais típicos das estrelas OB, tanto Al II quanto Al V não apresentam populações significativas.

Vinte e duas transições bb permitidas são calculadas explicitamente, sendo 11 delas linearizadas. As demais são mantidas fixas em ETL. Os processos de fotoionização a partir do NF e dos quatro níveis mais baixos do Al III são incluídos. A Figura 2.7 apresenta o diagrama de Grotrian para o alumínio, com os níveis e transições considerados na construção do modelo atômico.

Silício

O modelo atômico do silício (Becker & Butler, 1990) considera, explicitamente, 12 níveis do Si II + 28 níveis do Si III + 18 níveis do Si IV e o NF do Si V. Outros termos até n=10 também são incluídos, fixos em ETL.

Todas as transições bb permitidas com $f > 10^{-4}$ (126 transições) são consideradas, sendo que todas as transições com $f \geq 10^{-2}$, em um total de 73 transições, são linearizadas. Os níveis e transições considerados na construção do modelo de Si III estão representados na Figura 2.8.

Enxofre

S II e S III são tratados simultaneamente no modelo atômico do enxofre (Vrancken *et al.*, 1996) para garantir que o equilíbrio de ionização seja correto. Todos os níveis do S II para n=3,4,5 e 6 são inlcuídos explicitamente, em um total de 81 níveis. Para o S III, 21 níveis são considerados, todos em NETL. Os 3 níveis mais baixos do S I, assim como os níveis mais baixos do S IV e o NF do S V também são incluídos no modelo atômico. Para modelos atmosféricos com temperaturas mais baixas, o S V é omitido e o S IV é representado apenas por seu NF. Além destes, todos os níveis até n=10, fixos em ETL, são incluídos para todos os íons.

Todas as transições radiativas bb permitidas com $f > 10^{-4}$ são consideradas, tanto para o S II quanto para o S III. Os processos de fotoionização a partir de todos os níveis NETL, também são consideradas. Os níveis e transições considerados na construção dos modelos de S II e S III estão representados nas Figuras 2.9 e 2.10, respectivamente.

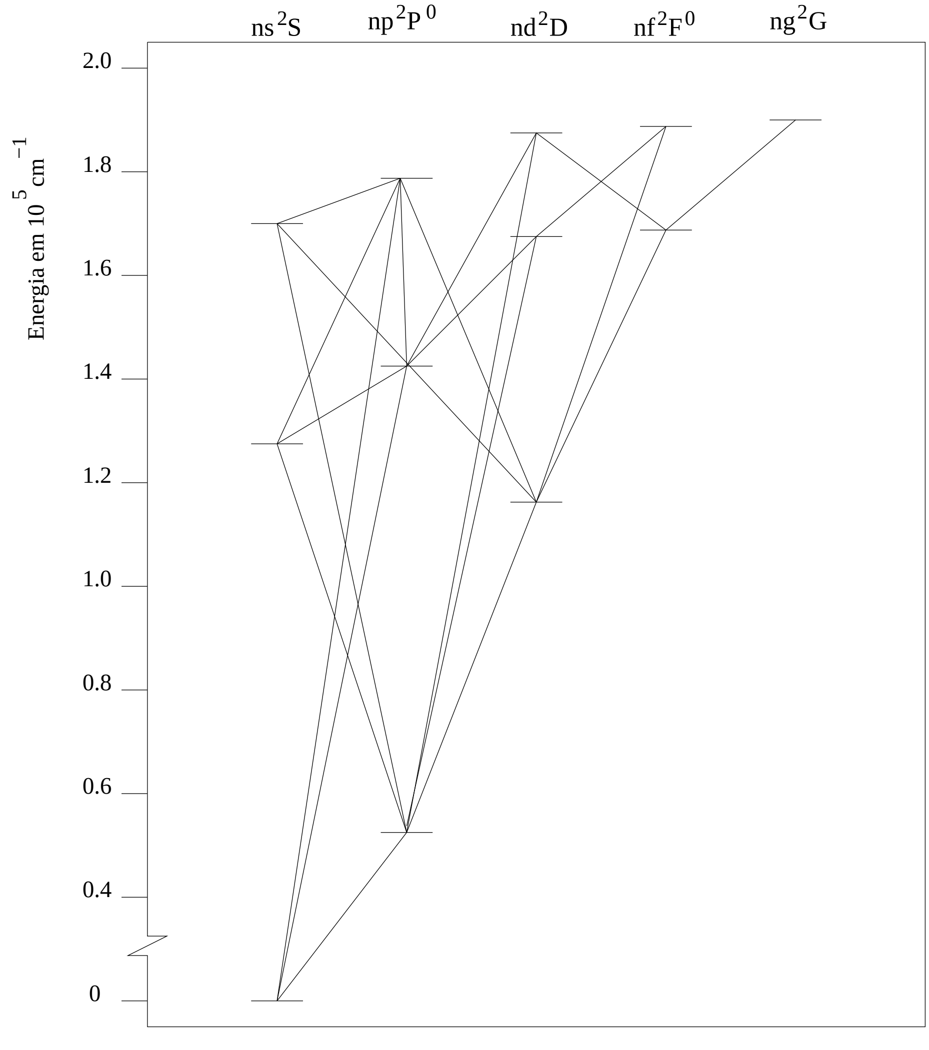

Figura 2.7: Diagrama de Grotrian para o sistema de dubletos do Al III. As energias dos níveis, em unidades de 10^5cm^{-1}, estão representadas no eixo das ordenadas enquanto que os termos considerados estão identificados pela sua notação espectroscópica no eixo das abscissas.

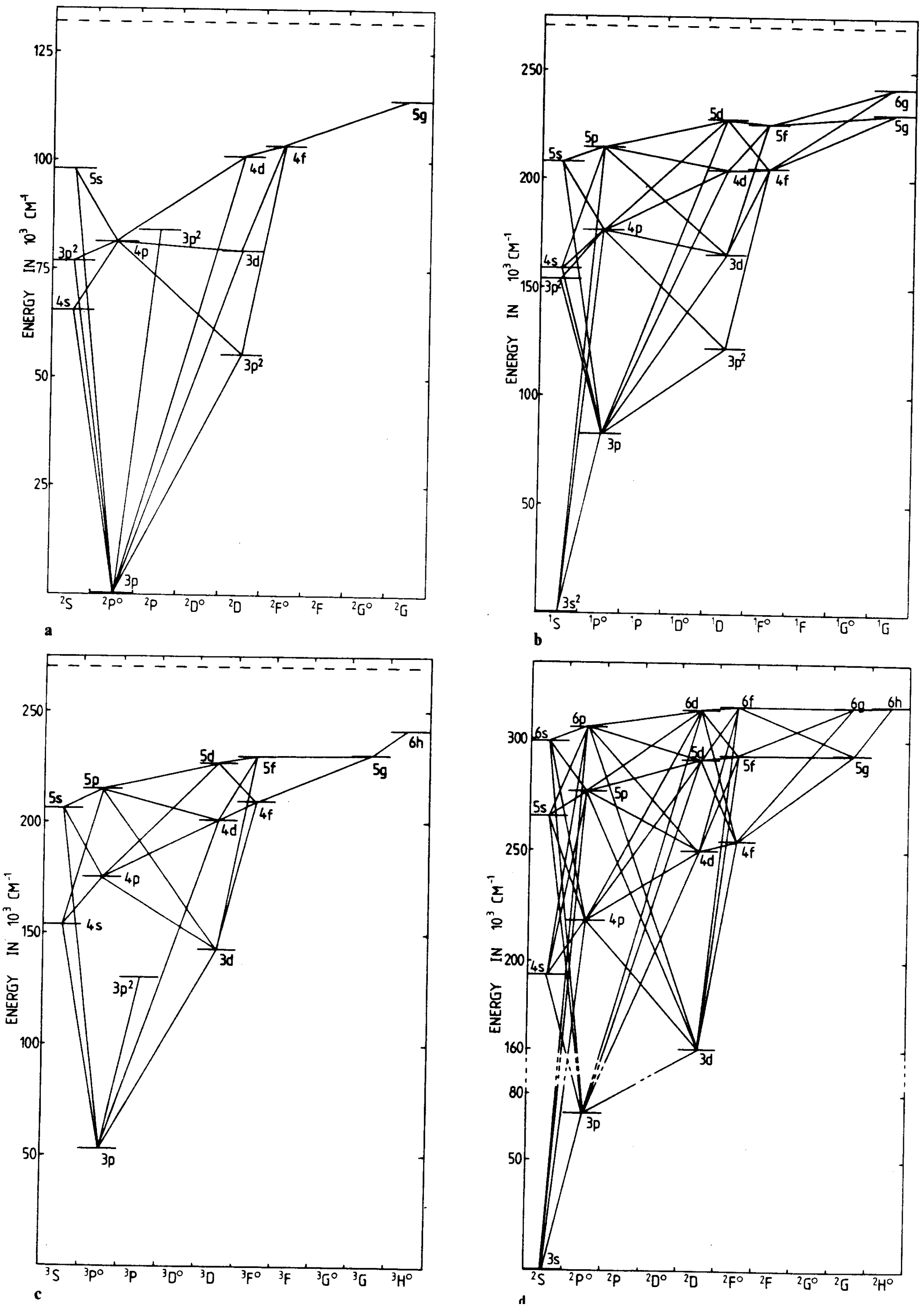

Figura 2.8: Diagramas de Grotrian para os sistemas de dubleto do Si II (painel a), singletos e tripletos do Si III (painéis b e c) e dubletos do Si IV (painel d) (de Becker & Butler, 1990). As energias dos níveis, em unidades de 10^3cm^{-1}, estão representadas no eixo das ordenadas enquanto que os termos considerados estão identificados pela sua notação espectroscópica no eixo das abscissas. As linhas tracejadas representam o limite de ionização.

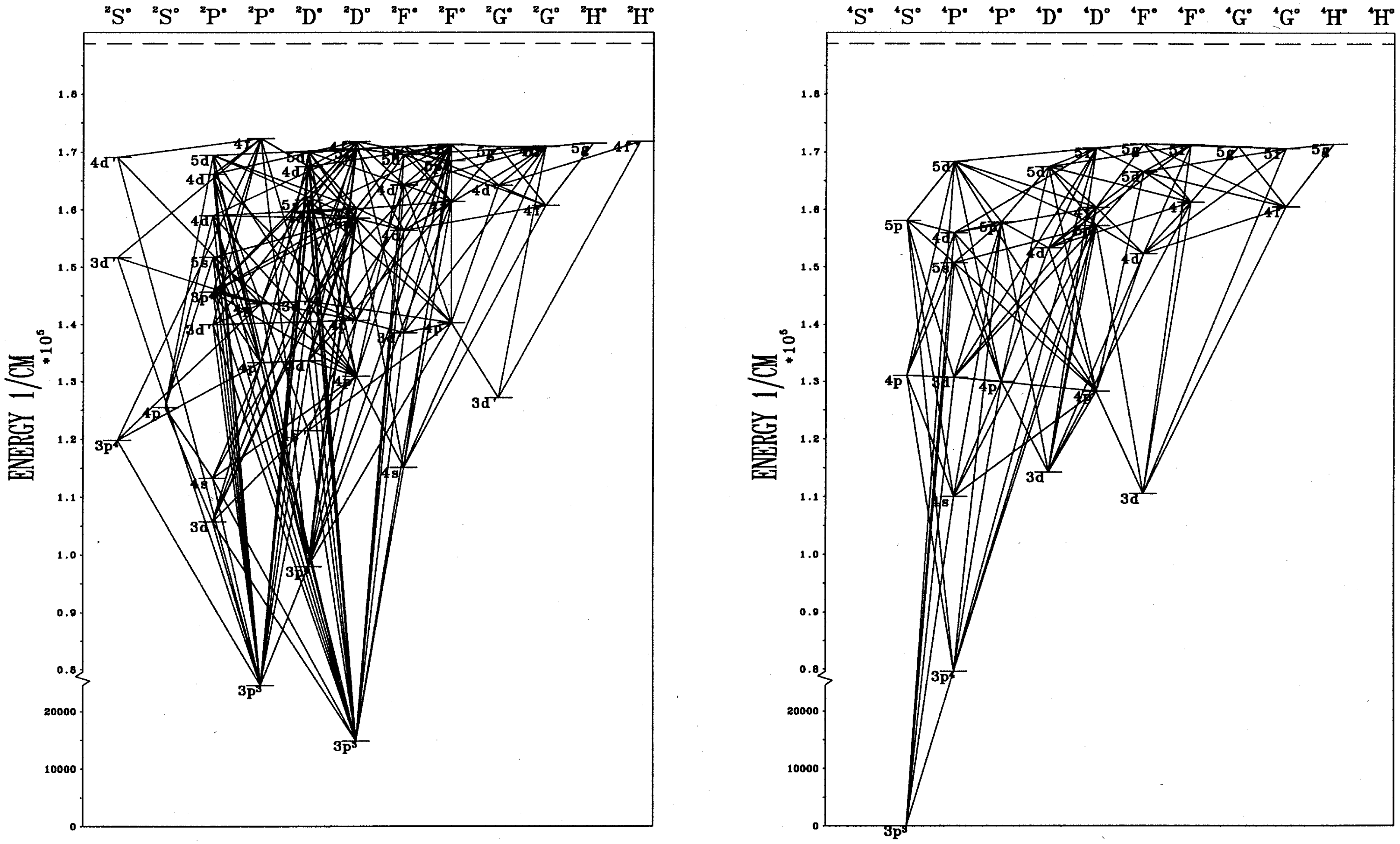

Figura 2.9: Diagramas de Grotrian para os sistemas de dubletos (painel esquerdo) e quartetos (painel direito) do S II (de Vrancken *et al.*, 1996). As energias dos níveis, em unidades de cm^{-1}, estão representadas no eixo das ordenadas enquanto que os termos considerados estão identificados pela sua notação espectroscópica no eixo das abscissas. As linhas tracejadas representam o limite de ionização.

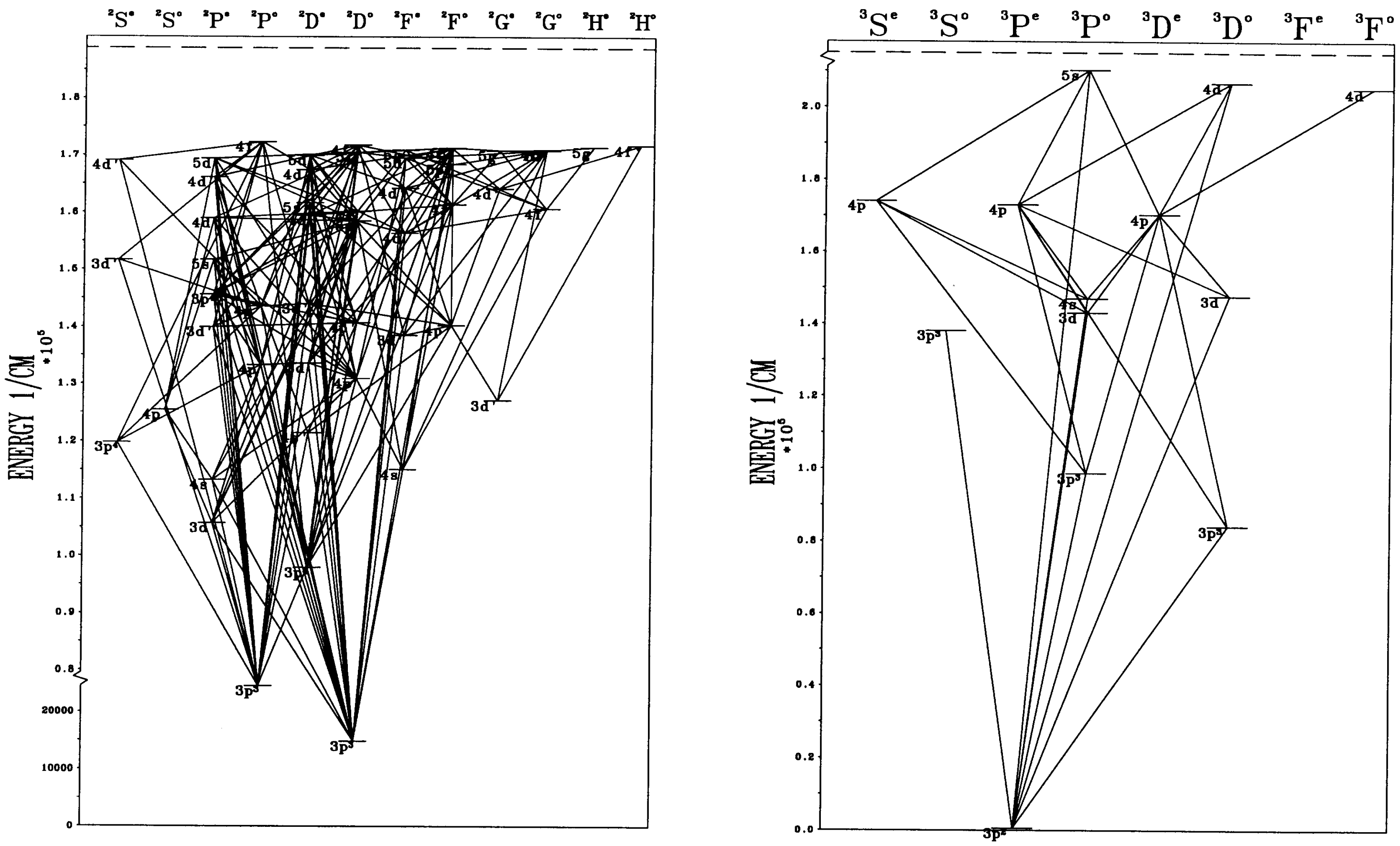

Figura 2.10: Diagramas de Grotrian para os sistemas de singletos (painel esquerdo) e tripletos (painel direito) do S III (de Vrancken *et al.*, 1996). As energias dos níveis, em unidades de cm^{-1}, estão representadas no eixo das ordenadas enquanto que os termos considerados estão identificados pela sua notação espectroscópica no eixo das abscissas. As linhas tracejadas representam o limite de ionização.

2.4 Dados Atômicos

As probabilidades de transição para os processos de excitação radiativa são dadas pela força de oscilador de cada transição, enquanto que, para as transições ligado-livre (bf), as probabilidades de transição são expressas em termos da seção de choque de fotoionização. As transições colisionais (bb e bf) também são representadas por seções de choque. Seções de choque colisionais determinadas experimentalmente estão disponíveis na literatura para algumas poucas transições de C III, N I/N III, O III, Mg I/Mg II, Al III e Si III. De modo geral, porém, as seções de choque colisionais são determinadas a partir de fórmulas semi-empíricas, considerando parâmetros atômicos de transições radiativas.

Transições Radiativas

Os valores da força de oscilador para as transições radiativas bb são do 'Opacity Project' (OP – Cunto & Mendonza, 1992), exceto para o alumínio. Para este elemento, os valores da força de oscilador adotados foram calculados por McEachran & Cohen (1983). Os valores de gf para as transições que produzem as linhas selecionadas para a análise de abundâncias estão listadas nas Tabelas 3.2, 4.5 e 5.2. Com relação às transições ligado-livre, as seções de choque de fotoionização a partir do nível fundamental do carbono, nitrogênio e oxigênio foram calculadas segundo a fórmula de Henry (1970),

$$a_\lambda = \sigma \left(B \left(\frac{\lambda}{\lambda_o} \right)^s + (1 - B) \left(\frac{\lambda}{\lambda_o} \right)^{s+1} \right) \tag{2.12}$$

que expressa as seções de choque a_λ como função do comprimento de onda correspondente à transição e dos parâmetros de ajuste σ, B e s, que são tabelados para cada espécie atômica. Para o silício e alumínio e os demais níveis de CNO, as seções de choque a_ν são dadas pela fórmula de Burgess & Seaton (1960)

$$a_\nu = \frac{4\pi \alpha a_o^2}{3} (I + \kappa^2) \frac{S}{\omega} \tag{2.13}$$

onde I é a energia de ionização , ω é o peso estatístico do nível fundamental, α é a constante de estrutura fina, κ é a energia cinética do elétron e a_o é o raio de Bohr. O valor de S é definido em termos de integrais das funções de onda tabeladas. Para o magnésio e enxofre, as seções de choque são do OP.

Transições Colisionais

As transições induzidas por colisões são importantes para se determinar corretamente as populações dos níveis atômicos, mas, como os processos radiativos dominam sobre os processos colisionais no regime de temperaturas das estrelas OB, a utilização de aproximações para se calcular as seções de choque das transições colisionais são justificadas. As seções de choque das excitações colisionais permitidas Q_{ij} são, em geral, calculadas com a fórmula de van Regemorter (1962)

$$Q_{ij} = \frac{8\pi}{\sqrt{3}} \frac{1}{\kappa_i^2} \frac{I_H}{E_j - E_i} f \overline{g} \pi a_o^2 \tag{2.14}$$

onde $E_{i,j}$ são as energias dos níveis i e j, f é a força de oscilador e $\overline{g}$ é o fator de Gaunt efetivo deduzido observacionalmente. As seções de choque das excitações colisionais proibidas Q_f são calculadas segundo Allen (1973)

$$Q_f = \pi \Omega a_o^2 / g_1 \varepsilon \tag{2.15}$$

onde g_1 é o peso estatístico do nível mais baixo, ε é a energia do elétron incidente antes da colisão e Ω é a probabilidade de colisão, cujo valor adotado no cálculo das seções de choque das excitações colisionais é igual a 1. As seções de choque das ionizações colisionais Q_c são tratadas segundo a aproximação de Seaton (1962)

$$Q_c = 4n \left(\frac{I_H}{I}\right)^2 \left(\frac{I}{W}\right) \left(1 - \frac{I}{W}\right) \pi a_o^2 \tag{2.16}$$

onde I é o potencial de ionização, I_H é o potencial de ionização do hidrogênio, n é o número de elétrons do átomo e W é a energia cinética eletrônica.

Através dos programas e parâmetros atômicos aqui descritos, é possível adotar uma abordagem mais realista, fora do ETL, na teoria de formação de linhas, a partir da qual obteremos abundâncias de carbono, nitrogênio, oxigênio, magnésio, alumínio, silício e enxofre para uma amostra de estrelas OB distribuídas ao longo do disco Galáctico, conforme será apresentado nos capítulos seguintes.

Capítulo 3

Abundâncias Químicas de Estrelas B da Associação de Cep OB2 [1]

Resumo: Neste capítulo apresento abundâncias em ETL e não-ETL de C, N, O e Si, além de abundâncias em ETL de Fe, para uma amostra de oito estrelas B da seqüência principal pertencentes à associação de Cep OB2. As temperaturas efetivas adotadas nesta análise foram obtidas a partir do índice livre de avermelhamento Q, segundo $T_{\rm eff} = (43280\pm17073) + (98718\pm45096)\ Q + (98236\pm 29462)\ Q^2$, e estão ancoradas em uma escala de $T_{\rm eff}$'s determinadas iterativamente a partir de calibrações fotométricas para os índices Strömgren combinadas com o ajuste de perfis da linha $H\gamma$. A associação de Cep OB2 apresenta dois sub-grupos de idades diferentes, com 7 e 3 $\times10^6$ anos, e é um objeto interessante para se testar a hipótese de auto-enriquecimento químico devido à explosão de supernovas do tipo II. Essa hipótese foi testada por Cunha & Lambert (1994) para a associação de Ori OB1 e os resultados obtidos sugerem que processos de auto-enriquecimento podem ter ocorrido em Órion. Cep OB2, todavia, apresenta uma composição química bastante homogênea: as abundâncias dos elementos estudados não mostram variações significativas e as dispersões de abundâncias observadas podem ser explicadas em termos das incertezas envolvidas na análise. Os nossos resultados indicam que Cep OB2 é relativamente pobre em metais ([Fe/H]$= -0.3$). Os demais elementos estudados também apresentam abundâncias sub-solares. Considerando, porém, as novas (e mais baixas) abundâncias de oxigênio no Sol, obtém-se [O/H]~ -0.1.

---

[1] **Daflon, S., Cunha, K. & Becker, S. R. (1999) The Astrophysical Journal, 522, 950-959 (Paper I)**

3.1 Introduction

The Milky Way has numerous OB associations which define its spiral arms and contain some of the youngest and most massive stars in the Galaxy. The stars belonging to these associations are not gravitationally bound and disperse into the Galactic field within about 10-20 million years. Moreover, some OB associations are believed to contain distinct stellar groups which represent different epochs of star formation occurring within the lifetime of the association. The Orion association is an example where progressive star formation seems to have happened resulting in 4 stellar subgroups of different ages. The abundance patterns observed in Orion suggest that chemical self-enrichment has taken place during the life of the association and altered the oxygen abundance of some of the stellar members of its youngest subgroups (Cunha & Lambert 1994; Cunha, Smith & Lambert 1998): this enrichment presumably occurred via supernovae contamination because oxygen is the primary product ejected into the interstellar medium from the most massive core-collapse supernovae (SNII). Is the chemical enrichment a property of most OB associations or is it only a characteristic of the larger associations with several distinct stellar subgroups? In this paper we begin a chemical analysis of an OB association which does not appear to show the same degree of progressive star formation as Orion. Cep OB2 is such an association.

Cep OB2 is a medium size association ($96^o < l < 107^o$, $2^o < b < 8^o$) located about 615 pc away from the Sun (de Zeeuw *et al.* 1999) and 60 pc above the Galactic plane. Two open clusters are identified in this association: Trumpler 37 (Tr 37), which is embedded in the H II region IC 1396 and excited mainly by the O6V star HD 206267A, and NGC 7160 . Simonson & van Someren Greve (1976) suggested the division of Cep OB2 into two subgroups of different ages: Cep OB2a and Cep OB2b with estimated ages of 7 and 3 $\times 10^6$ years, respectively. The younger of these subgroups (Cep OB2b) is associated with the open cluster Tr 37, while the older subgroup (Cep OB2a) extends over a larger area which contains the open cluster NGC7160, as well as a large number of massive evolved stars, at least one runaway star, λ Cep (estimated to have been ejected $\sim 10^6$ years ago), and filamentary wisps which were probably left over from an extinct H II region. These characteristics together suggest that, in the past, there was an active site of star formation in the Cep OB2 association and it is possible that the most massive stars produced then evolved into supergiants and supernovae. In addition, the ages derived for the two open clusters in Cep OB2 seem to support the existence of an age spread in this association. Battinelli & Capuzzo-Dolcetta (1991) studied 100 open clusters in the solar neighborhood and estimated an age of 10^6 years for Tr 37 and 10^7 years for NGC 7160. An age estimate for Cep OB2 comes from de Zeeuw & Brand (1985), who do not especifically divide Cep OB2 into two subgroups (unlike other associations in their study) but derive kinematic and nuclear ages for the entire association in the range of 8 - 12 $\times 10^6$ years. More recently, however, based on Hipparcos data de Zeeuw *et al.* (1999) conclude that most of the massive members around NGC 7160 are evolved stars supporting the claim that NGC 7160 is older than Tr 37 where no evolved stars are found. The above studies would thus suggest that star formation occurred within Cep OB2 over a period of at least a few million years, possibly occurring in two separated events.

Abundance patterns in stellar members of Cep OB2 can be used to probe for chemical inhomogeneities as was done previously for Orion. Comparing the degree of chemical inhomogeneity of the gas that formed the young stars in different OB associations thus provides important constraints to the chemical evolution and to the understanding of the star formation process in these relatively small systems. However, due to the rapid rotation of most of these hot stars, a limited number of OB stellar members of associations have had their abundances analyzed. Cep OB2 is one of the associations of the Galactic plane in which metal abundances have not yet been investigated, and, in this paper, we present LTE and non-LTE abundances of carbon, nitrogen, oxygen, silicon and LTE abundances of iron for a sample of 8 slowly rotating OB stars in this association. Results derived for Cep OB2 can then be compared to the results obtained for the Orion association, which is an example of a larger OB association, where progressive star formation is more pronounced. Section 2 describes the observations. In Section 3, we present the effective temperatures and surface gravities of the stars and show the abundance results and uncertainties. In Section 4, the abundance results are discussed.

3.2 Observations

The study of chemical abundances from an equivalent width analysis in early type stars is restricted to those stars which rotate slowly enough so that severe blending does not affect the spectral lines. For this program, we observed 40 main-sequence stars with spectral types between O9 and B3 from the list of Garmany & Stencel (1992), however, here we will analyse just those eight stars in our sample which have small projected rotational velocities (Vsini $\leq$ 70 kms^{-1}): either because they rotate slowly or because they are seen pole on. Our final sample of stars is presented in Table 3.1: it contains five stars in the region of the open cluster Tr 37 (HD 205794, HD 206183, HD 206267D, HD 207538 and HD 239724), and three stars (HD 206327, HD 239742 and HD 239743) in the general region of the older subgroup in Cep OB2. We also list five other stars (marked with an asterisk in Table 3.1) from our larger observed Cep OB2 sample, which rotate too rapidly, but that were added to this study in order to provide additional points to anchor the T$_{eff}$ calibration (discussed in Section 3.3.2).

Table 3.1: Sample Stars

Star	ST	V	Q	T_{eff} (K)	$\log g$
HD205794	B0.5V	8.43	-0.795	26890	4.21
HD205948 *	B2V	8.65	-0.747	24350	4.25
HD206183	O9.5V	7.40	-0.891	33310	4.52
HD206267D	B0V	8.02	-0.781	26100	4.21
HD206327	B2V	9.19	-0.689	21900	3.99
HD207538	O9V	7.31	-0.876	32190	4.32
HD207951 *	B2V	8.18	-0.651	20650	3.88
HD208266 *	B1V	8.12	-0.757	24840	3.98
HD209339 *	B0V	6.66	-0.863	31250	4.28
HD239724	B1V	9.14	-0.756	24790	3.83
HD239729 *	B0V	8.34	-0.821	28450	4.22
HD239742	B2V	9.41	-0.704	22470	4.07
HD239743	B2V	9.01	-0.680	21580	3.99

High-resolution spectra for the program stars were obtained with the McDonald Observatory's 2.1m telescope plus the Sandiford Cassegrain echelle spectrometer and a CCD detector (McCarthy *et al.*, 1993). The spectra were observed at a nominal 2-pixel resolution of R=60,000 at two grating tilts which covered the spectral ranges between 4225 - 4625Å and 4855 - 5285Å. We also obtained lower-resolution spectra (R=12,000) in the region of the Hγ profile with the 2.7m telescope plus a Coudé spectrometer and a CCD detector; these were used in order to derive the stellar parameters. All the observed spectra were reduced in a standard way using the IRAF data package. The data reduction procedure consisted of bias subtraction, division by an internal quartz lamp, extraction of one-dimensional spectra and wavelength calibration. The reduction of the echelle spectra also included the important step of subtraction of the scattered light in the CCD. The typical S/N achieved was generally greater than 200, as estimated from flat regions in the spectra. In Figure 3.1 we show a sample spectrum for one of our target stars in the region around 4640Å. The spectral lines in this region are identified in the figure.

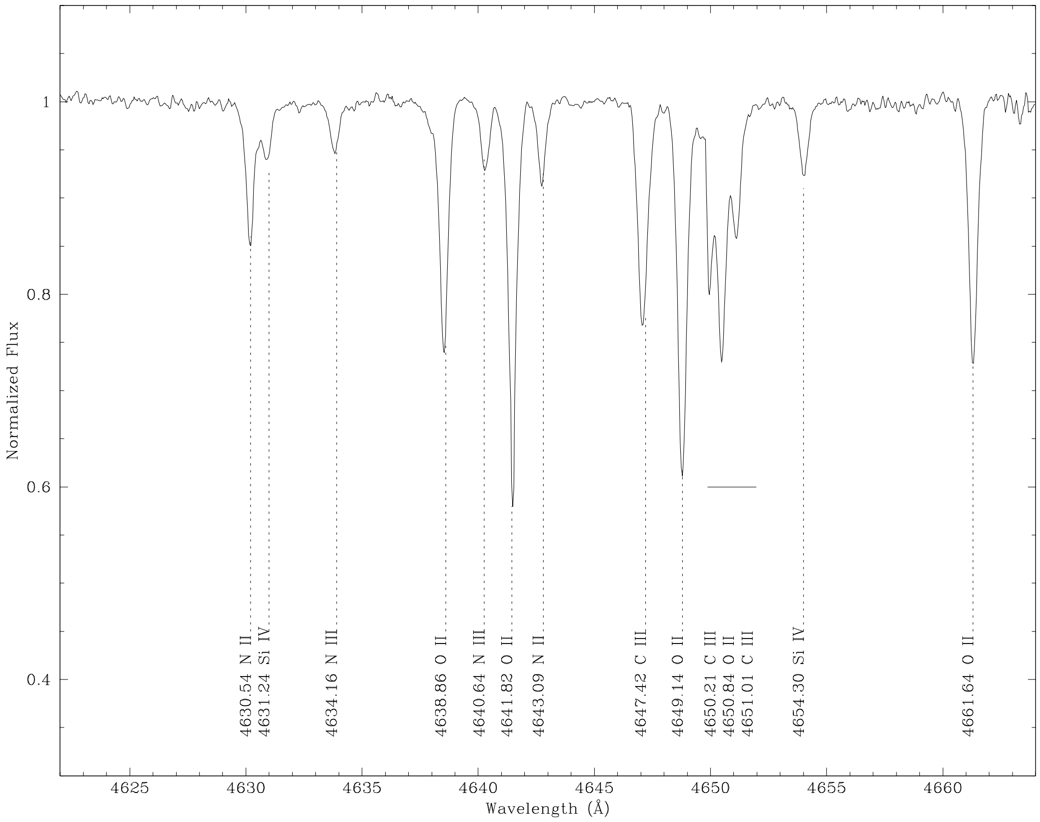

Figure 3.1: One sample echelle order for the star HD205794 in the region 4622 - 4664Å.

3.3 Analysis

The first step in this study was to select a sample of unblended spectral lines of carbon, nitrogen, oxygen, silicon and iron suitable for an equivalent-width abundance analysis. In this section, we discuss the line selection and atomic data, as well as the determination of the stellar parameters (T_{eff} and $\log g$) for the sample stars.

3.3.1 Line Selection and Atomic Data

The lines in the observed spectra were identified on the basis of linelists compiled by Aller & Jugaku (1958) and Kilian, Montenbruck & Nissen (1991). Our selected sample of unblended features contained 3 C II lines arising from the same multiplet, 8 N II lines (from 5 different multiplets), 16 of O II from several different multiplets, 5 transitions of Fe III and 3 transitions of Si III also from the same multiplet (see Table 3.2). The N II line at λ 4237.00Å refers to the mean wavelenght weighted by the *gf*-value of the two blended N II lines at 4236.93Å and 4237.05Å. An important ingredient in an abundance analysis is the value of the oscillator strengths adopted for the studied transitions. Here we used the values from the Opacity Project (TOPbase - Cunto & Mendoza 1992) which are accurate to within 10% (Seaton *et al.* 1992) and we computed the individual transition gf-values from the TOPbase multiplet gf-values, assuming that their relative line strengths are the values appropriate for LS-coupling.

The spectra of B stars, contrary to stars of later spectral types, are easily analyzed because their stellar continua are well-defined due to many spectral regions being relatively line-free: line equivalent widths are readily measurable in the spectra of these stars. Our measurements were done using a Gaussian fit and/or a straight numerical integration with the IRAF data package. The measured equivalent widths (in mÅ) are shown in Table 3.3.

Table 3.2: Selected Transitions and Atomic Data.

Ion	λ(Å)	Transition	χ(eV)	log(gf)
C II	5143.49	$3s'\,^4P - 3p'\,^4P$	20.70	-0.21
	5145.16		20.71	0.19
	5151.08		20.71	-0.18
N II	4237.00^a	$3d\,^3D^o - 4f\,^3F$	23.24	0.84
	4241.78		23.24	0.72
	4607.15	$3s\,^3P - 3p\,^3P$	18.46	-0.48
	4630.53		18.48	0.09
	4643.08		18.48	-0.39
	5005.15	$3p\,^3D - 3d\,^3F^o$	20.66	0.59
	5007.33	$3p\,^3S - 3p\,^3P^o$	20.94	0.17
	5010.62	$3s\,^3P - 3p\,^3S$	18.47	-0.61
O II	4349.43	$3s\,^4P - 3p\,^4P^o$	23.00	0.06
	4414.88	$3s\,^2P - 3p\,^2D^o$	23.44	0.22
	4416.97		23.42	-0.04
	4452.37		23.44	-0.73
	4466.60	$3d\,^2P - 4f\,^2D^o$	28.94	0.24
	4591.01	$3s'\,^2D - 3p'\,^2F^o$	25.66	0.32
	4609.37	$3d\,^2D - 4f\,^2F^o$	29.07	0.71
	4638.86	$3s\,^4P - 3p\,^4D^o$	22.97	-0.35
	4641.82		22.98	0.05
	4649.14		23.00	0.33
	4661.64		22.98	-0.25
	4890.85	$3p\,^4S^o - 3d\,^4P$	26.30	-0.35
	4906.82		26.30	-0.05
	4941.10	$3p\,^2P^o - 3d\,^2D$	26.55	0.07
	4943.00		26.56	0.33
	5190.56	$3p\,^2P^o - 3d\,^2P$	26.55	-0.46
Si III	4552.62	$4s\,^3S - 4p\,^3P$	19.02	0.28
	4567.84		19.02	0.06
	4574.76		19.02	-0.42
Fe III	4310.35	$4f\,^7F - 5g\,^7G$	25.74	1.19
	5156.11	$4s\,^5D - 4p\,^5P$	8.64	-2.25
	5243.31	$4d\,^7D - 5p\,^7P$	18.27	0.41
	5276.48		18.26	0.01
	5282.30		18.26	0.12

[a] Blend of N II at 4236.93 and 4237.05 Å.

Table 3.3: Equivalent Width Measurements

Ion	λ(Å)	HD205794	HD206183	HD206267D	HD206327	HD207538	HD239724	HD239742	HD239743
C II	5143.49	17	-	*	32	-	22	27	31
	5145.16	28	-	*	49	-	33	50	60
	5151.08	17	-	*	36	-	19	25	33
N II	4237.00	41	13	18	35	36	41	35	38
	4241.78	47	24	34	41	49	50	32	-
	4607.15	28	11	-	-	18	46	36	30
	4630.53	-	-	-	56	-	137	59	63
	4643.08	34	-	-	32	-	-	33	40
	5005.15	64	-	*	48	46	91	50	47
	5007.33	27	7	*	19	16	39	27	23
	5010.62	29	6	*	23	-	34	21	24
O II	4349.43	150	87	114	52	107	186	58	-
	4414.88	153	70	127	76	105	193	73	85
	4416.97	129	68	103	66	90	125	60	92
	4452.37	67	25	48	31	-	69	25	-
	4466.60	47	17	-	15	-	-	11	-
	4591.01	121	50	91	44	105	142	49	47
	4609.37	66	-	-	-	-	-	31	-
	4638.86	120	58	88	56	-	140	49	61
	4641.82	160	-	90	64	-	-	-	85

∗ source was not observed; − absent or blended line.

Table 3.3: Equivalent Width Measurements

Ion	λ(Å)	HD205794	HD206183	HD206267D	HD206327	HD207538	HD239724	HD239742	HD239743
	4649.14	181	112	-	-	-	-	89	90
	4661.64	129	68	-	-	94	145	53	-
	4890.85	35	9	*	9	-	20	12	18
	4906.82	54	27	*	16	37	53	19	17
	4941.10	54	13	*	16	20	43	18	16
	4943.00	-	38	*	26	44	45	30	42
	5190.56	24	10	*	-	39	-	8	-
Si III	4552.62	184	93	125	111	147	312	110	109
	4567.84	156	83	110	97	132	253	83	100
	4574.76	105	44	80	59	72	160	65	90
Fe III	4310.35	-	-	-	15	-	16	14	-
	5156.11	22	-	*	33	-	57	29	35
	5243.31	26	-	*	24	-	31	18:	28
	5276.48	20	-	*	10	-	29	11:	23
	5282.30	12	-	*	18	-	30	9:	20

∗ source was not observed; − absent or blended line.

3.3.2 Stellar Parameters

Our approach for deriving the effective temperatures (T_{eff}) and surface gravities ($\log g$) for the sample stars was based on a calibration of the reddening-free Q-parameter with the effective temperature (tied to the temperature scale of Cunha & Lambert 1992), and on the comparison between the observed and theoretical Hγ profiles.

The method adopted by Cunha & Lambert (1992), which relies on calibrations of the Strömgren indices c_1 and β coupled with the fits to the pressure broadened line wings of Hγ profiles, represents an accurate way to derive stellar parameters for OB stars. Basically, Cunha & Lambert (1992) considered a first estimate of T_{eff} as the average temperature calculated from the Strömgren calibrations of Lester, Gray & Kurucz (1986) and Balona (1984), adjusted upwards respectively by 4.2 and 5.2%. This average T_{eff} was then used to construct a grid of Hγ profiles (from Kurucz's 1979 models) and to obtain the $\log g$ which represented the best fit to the observed Hγ line wings. With this new estimate of $\log g$, a new T_{eff} was derived which was then used to construct a new grid of H_γ line-profiles so that a new $\log g$ could be determined. This procedure was repeated until a consistent T_{eff}, to within 50K, was obtained. (Here we will refer to the T_{eff}'s derived by this iterative method as T_{iter}). We note that the small number of sample stars (only 3) for which we could find Strömgren measurements in the literature prevents us from adopting the method described above to derive stellar parameters for the Cep OB2 stars.

Alternatively, effective temperatures for OB stars can also be estimated from calibrations of the photometric indices of U-B or B-V with T_{eff}. Measurements of the broadband magnitudes U, B and V are much more numerous in the literature than Strömgren measurements. But, in order to obtain the intrinsic B-V, for example, one needs to know the reddening in the direction of the stars, which is significant and variable (E(B-V)=0.40 - 1.00) towards the Cep OB2 association. In particular, a comparison of the values of E(B-V) in the direction of the sample stars, from different sources in the literature (e.g. Simonson 1968, Deutchman *et al.* 1976, Garrison & Kormendy 1976, Garmany & Stencel 1992), revealed an uncertainty of the order of 0.03 mags in some lines-of-sight to our targets. Such an uncertainty in E(B-V) translates into a very large difference in the value of T_{eff} ($\sim$ 3000K) when considering a calibration of $(B\text{-}V)_o$ and T_{eff}. A better alternative is to use the Q-parameter, which is defined to be nearly independent of the reddening, in the determination of the effective temperatures for our target stars. The Q-parameter was defined by Johnson (1958) in the UBV system as Q= (U-B) - X (B-V), where X = E(U-B) / E(B-V). Defined in this way, Q becomes a function of the intrinsic $(U\text{-}B)_o$ and $(B\text{-}V)_o$ colors, which are themselves a function of T_{eff}. Johnson (1958) determined empirically a value of Q = 0.72 ± 0.03 for main-sequence B stars. More recently, Cardelli *et al.* (1989) have presented a detailed analysis of ultraviolet, visual and infrared interstellar extinction curves and, based upon their best fit to various lines-of-sight, they derive values of X = 0.69 - 0.71, depending on the value of R_v (typically ranging from 2.6 to 3.3). Here, we use the value from Johnson (1958) of X = 0.72, as this number was derived specifically from main-sequence B stars and is not discrepant from values in Cardelli *et al.* (1989).

In order to obtain a calibration between Q and T_{eff}, we adopted the effective temperature scale for the stars in the Orion association (T_{iter}; Cunha & Lambert 1992), with the addition of those 3 sample Cep OB2 stars with available Strömgren photometry. The stellar parameters for all stars used to define the Q calibration were thus derived in the same consistent way. (From the sample of 18 stars studied in Cunha & Lambert 1992, we did not include the stars HD 37020 and HD 37042, which show slight variability of the UBV colors). It is an advantage to use the Orion stars in defining the calibration, as they span a range in T_{eff} which overlaps with our sample stars and which is larger than the range encompassed by the 3 stars from Cep OB2. In addition, the abundances of the Cep OB2 stars will be compared to the Orion stars and it is useful to tie all temperatures to the same T_{eff}-scale. The calibration of the Q-parameter with effective temperature for the sample of Orion and Cep OB2 stars is shown in Figure 3.2. The polynomial used to fit the points is given by the following relation:

$$T_{eff} = 43280.162 + 98718.195Q + 98236.823Q^2.$$

The fit between Q and T_{eff} is quite good, with a scatter of ± 650K between the accepted calibrator effective temperatures and the fitted curve. The second-degree polynomial provides a better fit than a linear relation, and marginally better than a third-degree polynomial, so we adopt the second-degree fit to provide a relationship between Q and T_{eff}.

Once the effective temperatures for the studied stars were derived by the Q-calibration, their $\log g$'s were then obtained from a χ^2 minimization of the differences between the observed and model Hγ line wings. (The latter were taken from Kurucz's 1979 grid for consis-

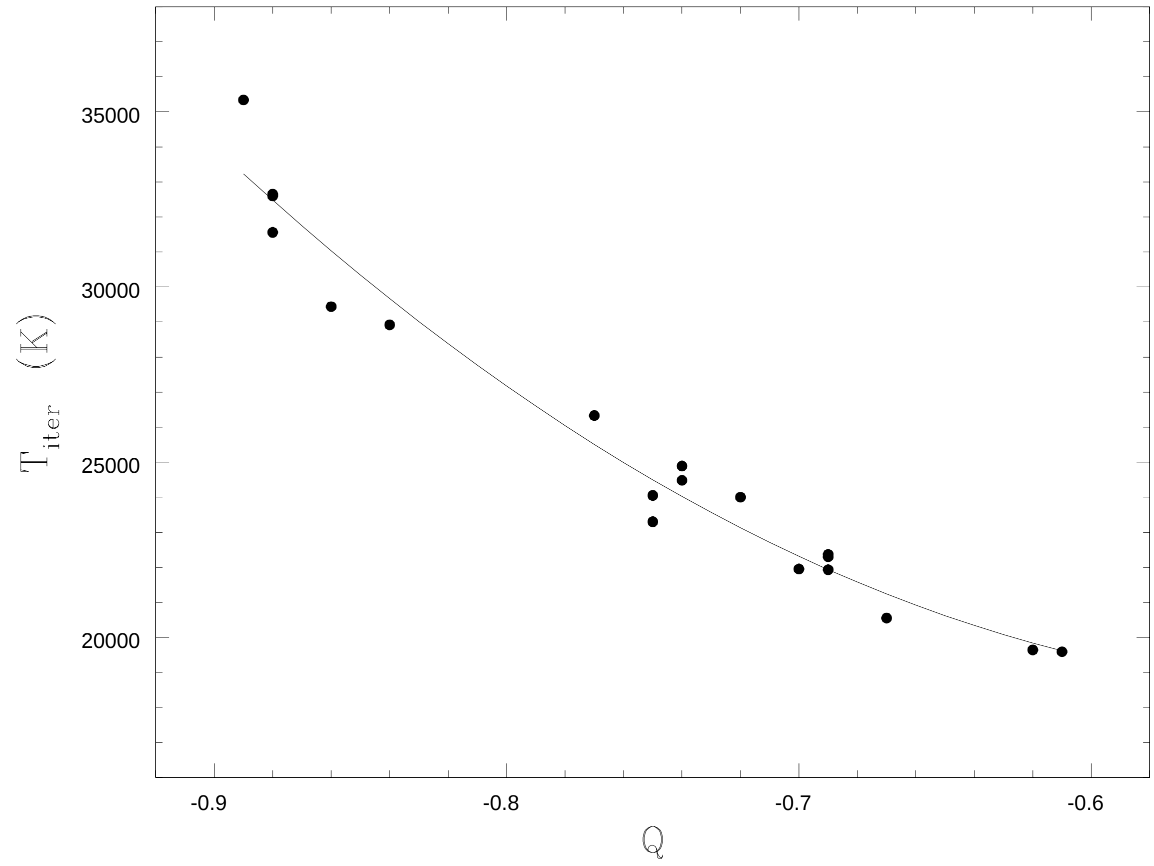

Figure 3.2: Calibration of Q-parameter with effective temperature for the sample of Orion and Cep OB2 stars. The fit to the points shown in the figure is given by $T_{eff} = 43280.162 + 98718.195Q + 98236.823Q^2$.

tency with the previous work in Orion. However, these are not significantly different from the more modern grid computed by ATLAS9). The central regions (~3Å) of the Hγ profiles were not considered in the fits, since non-LTE effects are stronger in the line cores. Moreover, the line cores are formed in the outer regions of the atmosphere where the model atmospheres are less reliable. Also, for the same reason, the line center contains little density information. In Figure 3.3 we illustrate the best fit theoretical profile (dashed line) and the observed spectrum (solid line) in the region of Hγ for the star HD 205794. The derived effective temperatures and surface gravities for the studied stars are presented in Table 3.1.

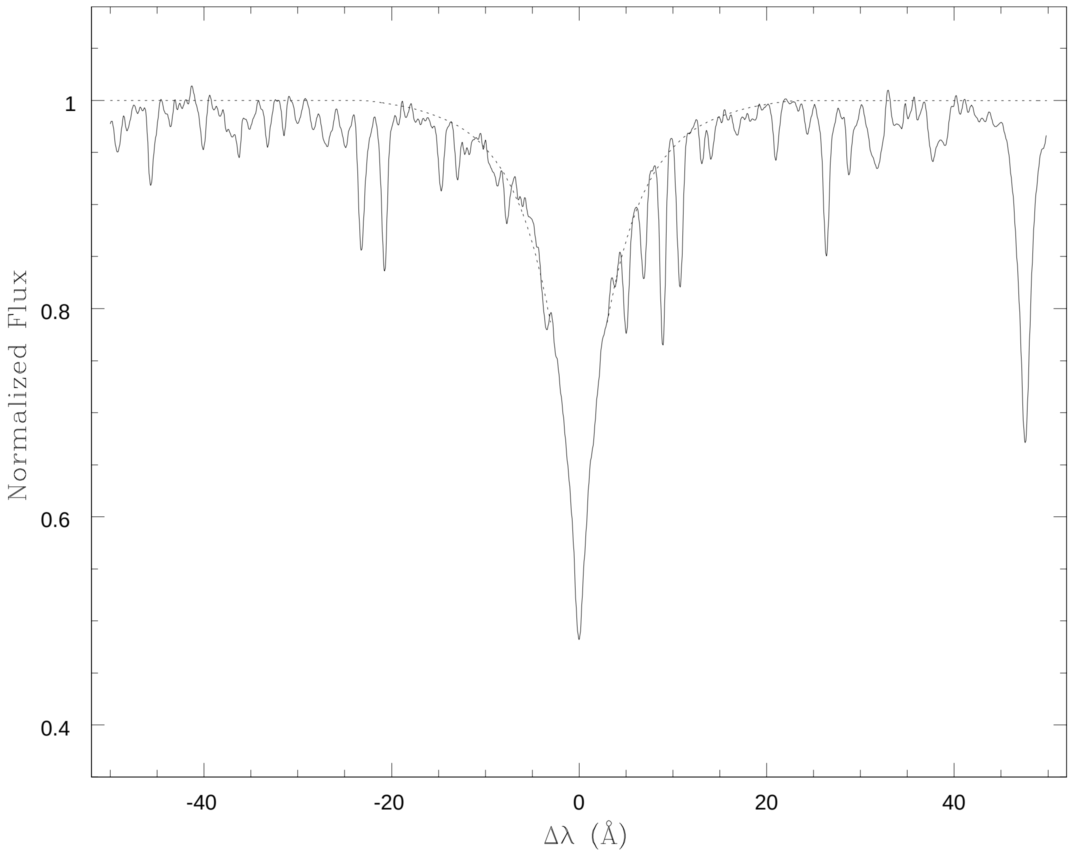

Figure 3.3: A comparison between observed (solid line) and synthetic (dashed line) Hγ profiles for HD 205794. The synthetic spectrum was calculated for T$_{eff}$=26890K and $\log g$=4.21.

3.3.3 Uncertainties in T_{eff} and $\log g$

Our derived effective temperatures are subject to errors in the photometric measurements which were used to calculate the Q-parameter. We estimate that the uncertainties in the adopted UBV indices and Q-parameters are of the order of 0.01 mag. Such an uncertainty will impart an error of roughly 1.3%, for T_{eff} 's around 20000K, and 2.4%, for T_{eff}'s around 30000K. However, this level of uncertainty is certainly less than the systematic errors related to the T$_{eff}$-scale. In order to estimate the magnitude of the systematic uncertainties, we compared our T$_{eff}$'s with other determinations in the literature, but it should be kept in mind that these other determinations also suffer from systematic errors and are not derived from fundamental relations.

For all stars in our sample, we have found at least one independent determination of T_{eff} from studies in the literature. A comparison of our derived temperatures with other temperature determinations is presented in Figure 3.4: the study which contains the largest number of stars in common with us is Garmany & Stencel (1992). Their temperature scale relied on de-redenned (B-V) colors and used the calibration of (B-V)$_o$ versus T_{eff} from Flower (1977). The comparison of the results is quite good; a linear least squares fit between Garmany & Stencel and this study finds differences of -1.4 % at T_{eff}=20000K, +2.1 % at T_{eff}=25000K and +4.4 % at T_{eff}=30000K. In particular, the largest differences are found for two stars: HD 239743 (for which we derive T_{eff}=21580K and Garmany & Stencel derive a lower T$_{eff}$=18620K) and HD 207538 (Garmany & Stencel estimate T$_{eff}$=36310K, while we estimate a lower T$_{eff}$=32190K). For this last star, however, other determinations in the literature indicate lower values of T$_{eff}$ which are in better agreement with our estimate. Morisson (1975) estimates two different values: T_{eff}=31500K (from a comparison with synthetic colors from the non-LTE models of Mihalas 1972) and T_{eff}=33000K (from the temperature scale of Conti 1973). Morossi & Crivellari (1980) also compute an effective temperature for this star which is lower than the one estimated by Garmany & Stencel: T_{eff}=32000K; their T$_{eff}$ was obtained from theoretical fits to observed profiles of hydrogen and helium lines.

The effective temperatures from the UBV calibration in Gulati *et al.* (1989) for the 3 stars we have in common (HD 207538, HD 207951 and HD 209339; represented by open circles in Figure 3.4) show a significant spread relative to our results, as well as to the results from Garmany & Stencel (1992). However, the differences in the derived T_{eff}'s for these 3 stars come mainly from differences in the adopted values of E(B-V). In particular, if we assume the SAME (B-V)$_o$ as in Garmany & Stencel (1992), and re-compute the effective temperatures for these 3 stars by means of the calibration in Gulati *et al.* (1989), we obtain T_{eff}'s which are in much better agreement. Judging from the discussion above of the results from our adopted T$_{eff}$-scale in comparison with other effective temperatures from the literature (although the latter are not derived from fundamental relations), we estimate that an uncertainty of 4% is reasonable to represent the total uncertainties in our derived

T_{eff}'s.

The method employed in this study for deriving the surface gravities relied on the broadened wings of the Hγ profiles. Apart from systematic errors, the major source of uncertainty in our estimated $\log g$'s comes from the placement of the continuum. We estimate that the measurement errors in our determinations are of the order of ± 0.1 dex. For one star in our sample, HD 207538, we can directly compare our determination of $\log g$ (= 4.32) with the result from Morossi & Crivellari (1980): $\log g = 3.92 \pm 0.5$ (obtained from the comparison between the theoretical and observed profiles of the wings of H and He lines) and from Morrison (1975): $\log g = 3.8$ (for $T_{eff} = 31500$ K) and 4.0 (for $T_{eff} = 33000$ K). Therefore, our estimated gravity for this star coincides with their result, within the estimated errors of the determinations.

3.3.4 LTE Abundances

LTE abundances were derived using the program WIDTH6 (Kurucz, priv. comm.) and LTE model atmospheres computed with the ATLAS9 code (Kurucz, 1992) for a depth-independent microturbulent velocity of 2 kms^{-1} and solar composition. These models assume the validity of LTE, but, most importantly, they include complete line blanketing from millions of lines. Presently, in the absence of non-LTE model atmospheres which are fully blanketed (calculation of such models require a very large computational effort), a choice must be made between fully-blanketed LTE model atmospheres and partially blanketed model atmospheres and non-LTE line formation. In this study we will adopt the fully-blanketed LTE models from Kurucz as these probably are as good a representation as possible of the atmospheres of main-sequence OB stars.

The computed mean LTE abundances of C, N, O, Si and Fe (on a scale where log ϵ(H) is 12) are presented in Table 3.4 together with the standard deviation of the mean, the respective number of lines considered, and the microturbulence velocities (ξ) adopted for the studied stars. These microturbulences were obtained from the canonical requirement that the abundance be independent of the measured equivalent widths; we used the O II lines to define the slope. The ξ's obtained for the sample stars range from 8 to 12 km s^{-1} and we estimate the uncertainties in these microturbulences to be ~1.5 kms^{-1}. Figure 3.5 contains different panels displaying the trends of the derived LTE abundances with the

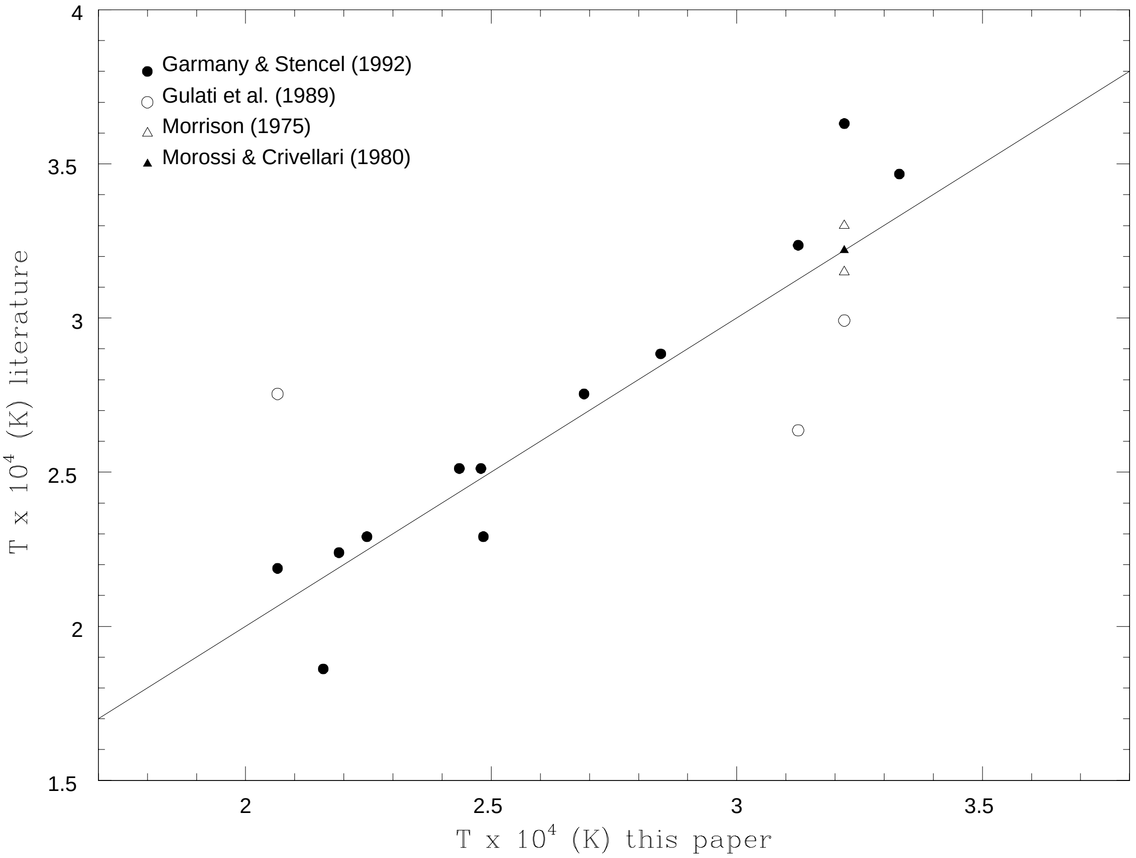

Figure 3.4: Effective temperatures derived from the Q-calibration compared with other temperatures published in the literature for Cep OB2 stars. The solid line represents perfect agreement.

effective temperatures for all elements studied. The dashed line in each panel indicates the solar elemental abundance from Grevesse, Noels & Sauval (1996). Inspection of this figure indicates that the abundances in Cep OB2 are generally below solar, showing a reasonably small scatter for most elements studied; with no major trends of abundance with T_{eff}. This is the case, especially, for oxygen, in which the abundance is very flat with T_{eff}. For carbon and iron we find a small variation of the abundances with effective temperature in the relatively small range spanned in T_{eff}: a least squares fit of the points indicates that the carbon and iron abundances are decreased by ~0.2 dex as the temperature runs from 21000 to 27000K. Note that in the case of Fe, the small trend appears mostly because of the derived Fe abundance for the coolest star in our sample, which is somewhat higher than the average abundance for the other stars. For nitrogen and silicon, we find trends of opposite sign: the abundances seem to increase with T$_{eff}$, especially when the two hottest stars in our sample are considered. The trend is more pronounced for Si: the Si abundance increases by ∼0.5 dex when the effective temperature runs from 21000 to 33000K, while the nitrogen abundance is increased by ∼0.2 dex for nitrogen.

The observed trends of LTE abundances with effective temperature are the result of systematic uncertainties in the analysis. They can be partially removed by adjustments of the T$_{eff}$-scale, within its estimated uncertainties: if we increase the effective temperatures by roughly 4% (which is our estimated uncertainty for our T$_{eff}$-scale) for T$_{eff}$ >25000K, the silicon abundances will be roughly 0.35 dex smaller, while the nitrogen abundances will be decreased by about 0.2 dex; for T$_{eff}$ <25000K, the correction for silicon and nitrogen will be positive and around 0.1 dex. For carbon and iron, if the same adjustment to the T$_{eff}$-scale of 4% is adopted, the observed trend can also be partially removed. Non-LTE effects are also partially responsible for the observed abundance trends with T$_{eff}$ and the behavior of non-LTE abundances with effective temperature will be investigated in the next section.

Table 3.4: LTE Abundances.

Star	ξ(km s^{-1})	$\log\epsilon(C)$	n	$\log\epsilon(N)$	n	$\log\epsilon(O)$	n	$\log\epsilon(Si)$	n	$\log\epsilon(Fe)$	n
HD205794	10	8.04±0.08	3	7.63±0.09	7	8.64±0.08	13	7.23±0.02	3	7.13±0.09	4
HD206183	10	-	-	7.70±0.21	5	8.47±0.12	11	7.46±0.10	3	-	-
HD206267D	8	-	-	7.52±0.01	2	8.58±0.09	6	6.97±0.12	3	-	-
HD206327	10	8.21±0.10	3	7.53±0.12	7	8.41±0.11	11	6.97±0.06	3	7.20±0.10	5
HD207538	10	-	-	7.95±0.16	5	8.63±0.16	6	7.70±0.05	3	-	-
HD239724	12	8.04±0.10	3	7.65±0.10	6	8.73±0.15	7	7.76±0.20	3	7.14±0.22	4
HD239742	8	8.13±0.04	3	7.57±0.07	8	8.45±0.06	12	7.00±0.04	3	7.09±0.14	5
HD239743	10	8.27±0.01	3	7.59±0.06	5	8.63±0.16	10	7.17±0.21	3	7.43±0.11	4

3.3.5 Non-LTE Abundances

Departures from LTE can affect the strengths of the photospheric lines at the temperatures and gravities of the studied stars. Several studies have investigated the magnitude of non-

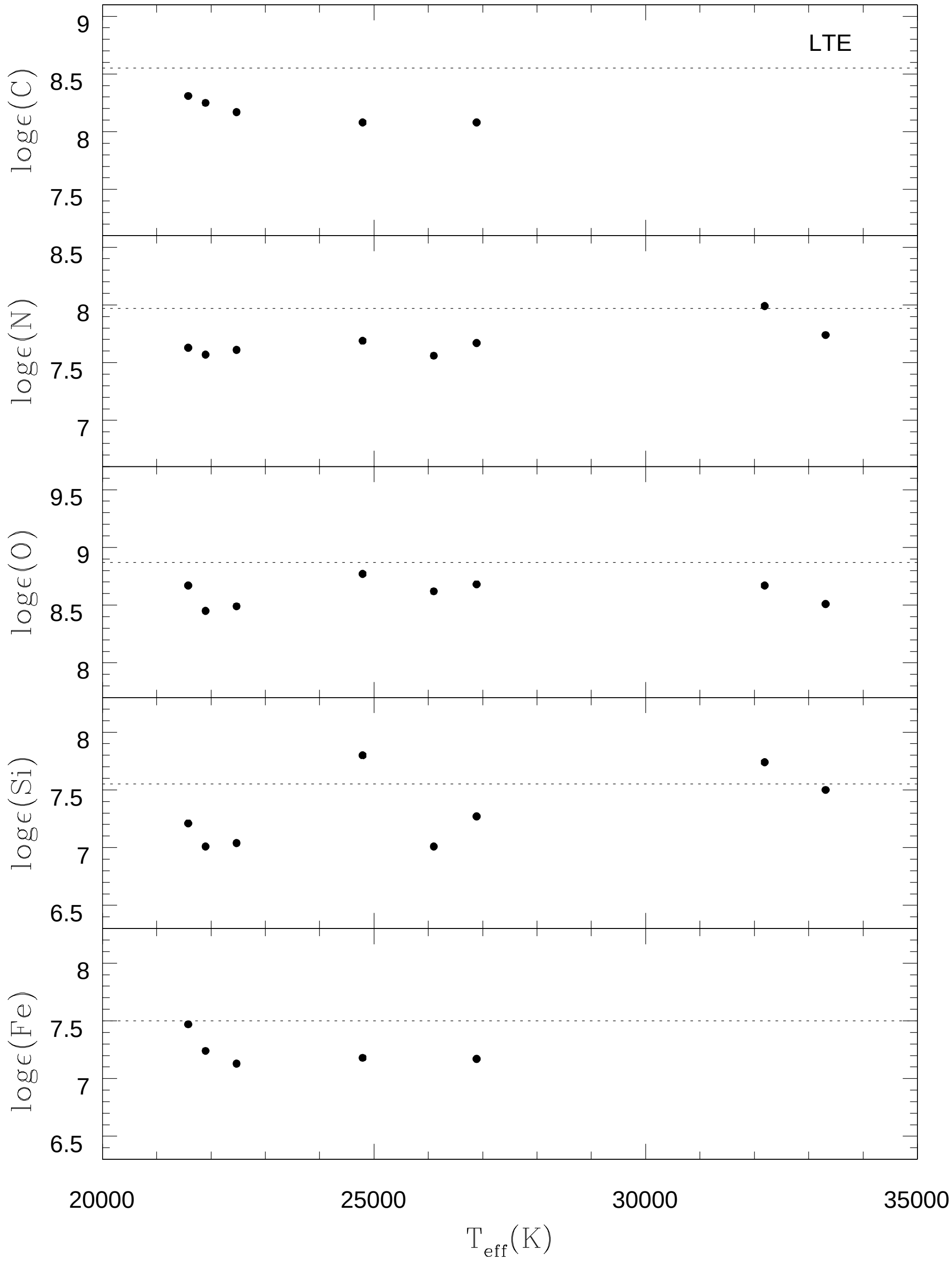

Figure 3.5: LTE C, N, O, Si and Fe abundances as a function of T_{eff}. The dashed line represents the solar abundances derived by Grevesse, Noels & Sauval (1996).

LTE corrections of C II (Eber & Butler 1988), N II (Becker & Butler 1989), O II (Becker & Butler 1988a,b,c) and Si III (Becker & Butler 1990) for temperatures and gravities corresponding to our target stars. However, these non-LTE corrections cannot be directly applied to the LTE abundances derived here because they are based on a different family of model atmospheres (Gold, 1984) which are not fully blanketed. Instead, new calculations were performed based on the model atmospheres used in this current analysis. The model atoms are those described in the original papers mentioned above. A newer version of the line formation suite of programs DETAIL and SURFACE has been used (Butler, priv. comm.). The new versions use the ALI (accelerated lambda iteration, Werner & Husfeld 1985, Werner 1988) scheme for the solution of the coupled integro-differential equations. While this new version reproduces the previously published results it has proved to be more stable. It also allows more elaborate calculations to be performed which require a significantly larger number of frequency points such as the inclusion of millions of lines as background opacities to adequately describe the UV radiation field. While tests have shown that such a treatment is important for silicon in O stars, in our case the temperatures are sufficiently low that the results were not affected by the inclusion of the additional opacities.

Thus, the grids are calculated in the same way as the published grids. The abundance range is centered on the LTE result and a range of microturbulent velocities has been covered. The O II lines were used to derive the microtubulent velocities for the program stars in a similar manner as used for the LTE analysis discussed previously. A comparison of the microturbulent velocities derived from the LTE analysis (Table 3.4) with the ones derived from non-LTE (Table 3.5) shows that the non-LTE values are, in general, smaller than the LTE ones. Since the microturbulence is a factor introduced in the analysis in order to force an agreement between the strong and weak lines, the somewhat smaller values for this parameter indicates that the non-LTE line formation theory is an improved representation for these stars. The trends of elemental abundances with effective temperature are also improved, or unchanged, in the case of the adoption of non-LTE: inspection of Figure 3.6 (here again the dashed line in each panel depicts the solar abundance) shows that the abundance trends with T_{eff} found especially for nitrogen and marginally for silicon are smaller than for LTE. Carbon and oxygen, on the other hand, remain approximately unchanged. However, the trends are not completely removed in any case. Additionally, the magnitude of the non-LTE

Table 3.5: Non-LTE Abundances.

Star	ξ(km s^{-1})	$\log\epsilon(C)$	$\log\epsilon(N)$	$\log\epsilon(O)$	$\log\epsilon(Si)$
HD205794	8	8.09±0.08	7.57±0.09	8.63±0.08	7.09±0.11
HD206183	5	-	7.62±0.15	8.50±0.12	7.61±0.07
HD206267D	5	-	7.49±0.08	8.66±0.15	6.90±0.21
HD206327	8	8.23±0.14	7.58±0.16	8.50±0.12	6.92±0.12
HD207538	10	-	7.82±0.12	8.55±0.09	7.49±0.10
HD239724	12	8.08±0.11	7.62±0.08	8.74±0.12	7.51±0.05
HD239742	5	8.15±0.01	7.59±0.10	8.57±0.05	7.00±0.16
HD239743	8	8.30±0.02	7.65±0.07	8.75±0.21	7.17±0.32

corrections are rather small; a comparison of the non-LTE abundances in Table 3.5 with the LTE results (shown in Table 3.4) indicates that the non-LTE corrections are generally of the order of 0.1 dex or smaller and the dependance of the abundances with T$_{eff}$ typically exceeds this number.

3.3.6 Abundance Uncertainties

Uncertainties in the stellar parameters, equivalent width measurements, gf-values and microturbulent velocities contribute to the abundance scatter we observe from line to line. However, if the selected lines of a particular species are all from the same multiplet, and from a similar excitation potential, the errors in the stellar parameters will roughly affect all the lines in a similar way and will not contribute significantly to the scatter of the individual line abundances. The standard deviations of the mean abundances are presented in Tables 3.4 and 3.5: note that these are typically smaller than ~0.1 dex, with only a few of them being larger or of the order of 0.2 dex. In order to investigate the magnitude of the total uncertainties in this anlysis, we re-computed the abundances for all stars in our sample by means of slightly different model atmospheres, according to the estimated uncertainties in T$_{eff}$, $\log g$ and ξ. (When one of these parameters was changed, the others were kept constant). In Table 3.6 we present the resulting changes in the LTE abundances of C, N, O, Si and Fe when the parameters are changed according to our estimate of the errors of 4%

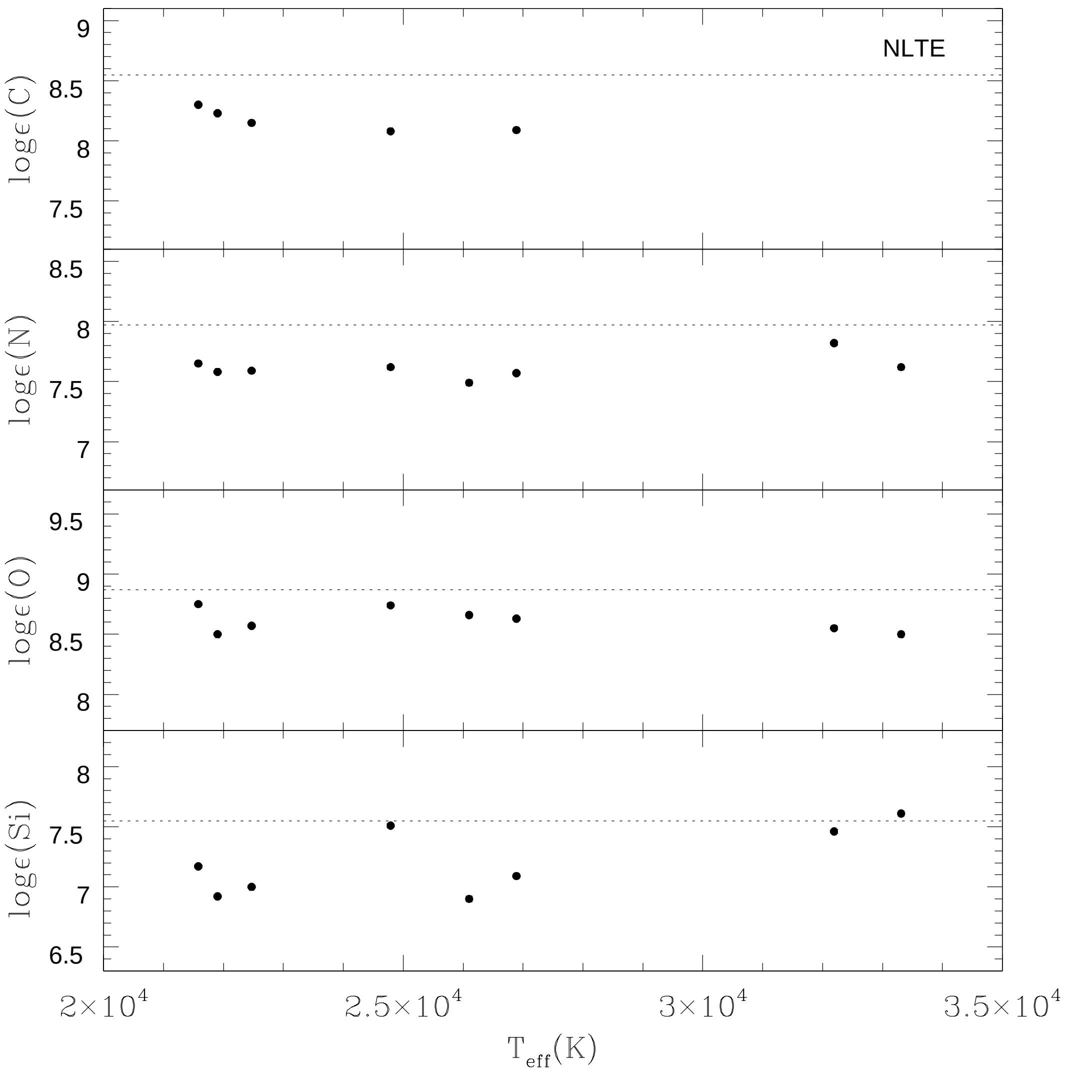

Figure 3.6: Non-LTE abundances derived for C, N, O and Si as function of effective temperature. The dashed line represents the solar abundances derived by Grevesse, Noels & Sauval (1996).

for T_{eff}, 0.1 dex for $\log g$, 1.5 kms^{-1} for the microturbulence. The last line for each element in this table lists the total errors (δ_t), which were calculated assuming that all these errors discussed previously are independent. The total errors are, in general, smaller than ~0.15 dex for all elements, except silicon. These relatively larger errors for silicon are essentially dominated by the uncertainties in T$_{eff}$ and microturbulences (the sample Si III lines are strong ones).

3.4 Discussion

In this spectroscopic study of the Cep OB2 association we found that the average LTE Fe abundance for our studied sample of B stars is roughly 0.3 dex below solar (log ϵ(Fe)= 7.24±0.14) and the average non-LTE abundances of C, N, O, and Si are all subsolar by about the same amount: logϵ(C)=8.17±0.09, logϵ(N)=7.62±0.10, logϵ(O)=8.61±0.10, logϵ(Si)=7.21±0.28. These results thus place the Cep OB2 association as being slightly metal poor relative to the Sun, a fact that is in general agreement with abundance results from studies of other Galactic B stars (e.g. Gies & Lambert 1992). A direct comparison of the B-star abundances with the gas content of the H II region associated with the cluster Trumpler 37 (IC 1396) is presently not possible as IC 1396 has not been analyzed spectroscopically in order to derive its chemical composition. However, nebular abundance studies generally conclude that carbon, nitrogen and oxygen are lower than the solar value (Mathis 1995): this condition of under-abundance relative to the Sun seems therefore to be a common property of B stars and H II regions. (It should be noted that for the H II regions the abundances depend upon the temperature structure of the nebulae.) The observation that these relatively young populations have metal abundances lower than the Sun (which is ~ 4.5 billion years old) has been a puzzling result since this would be contrary to simple chemical evolution models which predict that the overall metallicity increases with time.

Table 3.6: Abundance Uncertainties.

Specie	Correction	HD205794	HD206183	HD206267D	HD206327	HD207538	HD239724	HD239742	HD239743
C II	$\delta(T_{eff})$	+0.07	-	-	-0.01	-	+0.07	+0.01	-0.03
	$\delta(\log g)$	-0.01	-	-	+0.01	-	-0.02	+0.04	-0.01
	$\delta(\xi)$	-0.01	-	-	-0.01	-	-0.01	-0.02	-0.01
	δ_t	+0.09	-	-	+0.06	-	+0.09	+0.05	+0.07
N II	$\delta(T_{eff})$	+0.06	+0.22	+0.05	-0.08	+0.20	+0.05	-0.07	-0.09
	$\delta(\log g)$	0.00	-0.04	-0.01	+0.06	-0.03	-0.01	+0.01	+0.02
	$\delta(\xi)$	-0.02	0.00	-0.02	-0.04	-0.01	-0.02	-0.01	-0.02
	δ_t	+0.09	+0.23	+0.08	+0.12	+0.23	+0.08	+0.09	+0.11
O II	$\delta(T_{eff})$	-0.03	+0.10	-0.07	-0.15	+0.13	-0.08	-0.15	-0.17
	$\delta(\log g)$	+0.02	-0.02	+0.05	+0.09	-0.03	+0.03	+0.08	+0.07
	$\delta(\xi)$	-0.06	-0.01	-0.06	-0.07	-0.04	-0.06	-0.04	-0.06
	δ_t	+0.11	+0.13	+0.12	+0.20	+0.15	+0.14	+0.18	+0.20
Si III	$\delta(T_{eff})$	+0.06	+0.36	+0.02	-0.12	+0.35	-0.01	-0.12	-0.14
	$\delta(\log g)$	+0.01	-0.06	+0.02	+0.08	-0.06	+0.02	+0.07	+0.05
	$\delta(\xi)$	-0.09	-0.03	-0.08	-0.13	-0.07	-0.11	-0.07	-0.10
	δ_t	+0.16	+0.38	+0.14	+0.23	+0.38	+0.19	+0.20	+0.20
Fe III	$\delta(T_{eff})$	+0.09	-	-	-0.08	-	+0.11	-0.07	-0.10
	$\delta(\log g)$	+0.01	-	-	+0.05	-	+0.02	+0.07	+0.05
	$\delta(\xi)$	-0.01	-	-	-0.01	-	-0.01	-0.01	-0.01
	δ_t	+0.08	-	-	+0.11	-	+0.12	+0.09	+0.13

From our discussion of the abundance uncertainties in Section 3.6, it became apparent that the total abundance spread arising from the estimated errors in the analysis was typically smaller than 0.15 dex except for silicon which has a much larger uncertainty: up to 0.38 dex. Although the small number of stars studied in Cep OB2 prevents us from performing further statistical analyses, it can be stated here that the C, N, O, Si and Fe abundances in the studied B stars can be represented by a single abundance value with the observed distribution described by a Gaussian distribution defined by the analysis errors. Since it is a reasonable hypothesis to assume that these main-sequence stars have not undergone substantial internal mixing to modify their original composition, the observed abundances indicate that the gas that formed these B stars in Cep OB2 was probably chemically homogeneous. In summary, from our studied sample of stars we find no evidence of self-enrichment in Cep OB2, in contrast to what was found from a previous study of 18 B stars in Ori OB1 (Cunha & Lambert 1994). There, a Monte Carlo simulation of the abundance spread arising from the estimated errors indicated that the oxygen abundance distribution in particular, was likely to reflect an intrinsic abundance spread.

The associations of Ori OB1 and Cep OB2 have distinct histories: the large Orion association has 4 subgroups of different ages with the age of its oldest subgroup being 12 million years, while its youngest subgroup is perhaps less than one million year old (Blaauw 1964). Cep OB2 may be younger (its oldest subgroup is 7-10 million years old; Simonson & van Someren Greve 1976 and Battinelli & Capuzzo-Dolcetta 1991) and star formation in this association seems to have been more concentrated in time, with its star formation happening in two distinct events probably separated by a few million years. The abundance pattern observed for oxygen in Ori OB1 suggests that the process of self-enrichment may occur on time scales of a few million years, but the degree and extent of the self-enrichment depends upon the density of the containing cloud which has to be large enough in order to entrain the processed material ejected by SNII (see discussion in Cunha & Lambert 1992). In Orion, some (but not all) of the youngest B stars seem to be more enriched in oxygen than the stars in the oldest subgroups. Furthermore, this signature of self-enrichment found for the B stars was confirmed from a study of the much cooler FG-star members of the association, where a large spread in the derived oxygen abundances was also observed and identified as the signature of SNII (Cunha, Smith & Lambert 1998). A simple comparison of the average oxygen abundances from B stars in the two associations shows that Cep OB2 is slightly oxygen poor when compared to Orion; in our sample we did not observe any B stars with roughly solar or above solar oxygen abundances as found for some stars in the youngest subgroups of Orion. In fact, the highest oxygen abundance observed here is roughly 0.15 dex below solar and mostly the oxygen abundance distribution is in the range between 8.50 - 8.65. The simplest chemical evolution model which predicts that the younger association (being Cep OB2) would have higher metallicity is inconsequential. Although both associations have a population of star subgroup members with similar ages, the Orion association has experienced a relatively longer star formation process, which might account for the observed signature of self-enrichment. In addition, however, other variables certainly play an important role, as the number of massive stars (and associated stellar winds), the number of stars that explode as SNII, as well as the density of the interstellar medium where such explosions occur. Our discussion of the results above reinforces the idea that the age-metallicity relation has to take into account the different chemical histories of each star forming region. This process of self-enrichment could account for part of the abundance spread observed at a given metallicity.

Another related issue in the context of Galactic chemical evolution, is the existence, or lack thereof, of an abundance gradient in the young disk population (H II regions and B stars) which is still under debate. For the Galactic B stars, in particular, several spectroscopic studies find no abundance gradient (or a very small one) with Galactocentric distance (e. g. Fitzsimmons *et al.* 1990, 1992, Kilian-Montenbruck *et al.* 1994, Kaufer *et al.* 1994). However, the more recent and self-consistent study by Gummersbach *et al.* (1998) finds gradients of metal abundances with distance to the Galactic center. In their Figure 2.11 they present the trends of C, N, O and Si for a sample of 16 main-sequence B stars with Galactocentric distances between 5 and 14 kpc. (We note that their study does not include any star in Cep OB2). Our Cep OB2 abundance results, as represented by the average abundance of the sample stars, puts Cep OB2 right at the observed trend for all elements analyzed. For oxygen, for example, their abundance results suggest the existence of a steep gradient: $\Delta[O/H]/\Delta R_{GC}$= -0.07 ± 0.02 dex/kpc. Cep OB2 is roughly at 8.7 kpc from the Galactic center and, in terms of oxygen content, sits right at the average abundance for its Galactocentric distance. The Sun (R_{GC}=8.5 kpc), on the contrary, has an oxygen abundance which is among the highest for its Galactocentric distance. One possibility is that this could indicate that the Sun formed out of material which has been self-enriched, perhaps in an environment not unlike that found in the Orion association.

3.5 Concluding Remarks

We have presented LTE and non-LTE abundances of C, N, O, Si and Fe in 8 main-sequence B stars from Cep OB2. We found that the observed abundance dispersions are compatible with our estimates of expected errors in this analysis: the derived abundances show no significant variations with position or age across the association when compared to the expected errors. This result, although based on a small number of studied stars, could suggest that the chemical composition in the Cep OB2 association is homogeneous, without signatures of self-enrichment. Cep OB2 is under-abundant compared to the Sun by roughly 0.3 dex, however, the stars in Cep OB2 have abundances which fit well the abundance gradient found in the Galaxy by Gummersbach *et al.* (1998).

Capítulo 4

Abundâncias Químicas de Estrelas B em Cinco Associações OB do Disco Galáctico [1]

Resumo: Este capítulo é dedicado à análise de abundâncias químicas de 15 estrelas B com baixas velocidades rotacionais projetadas pertencentes a cinco associações: Cyg OB3, Cyg OB7, Lac OB1, Vul OB1 e Cep OB3. Essas associações encontram-se no disco Galáctico em uma região limitada a ∼3 kpc de distância ao Sol. São apresentadas as abundâncias em ETL de magnésio, alumínio, enxofre e ferro, além de abundâncias em não-ETL de carbono, nitrogênio, oxigênio e silício. Dentre os elementos estudados, as abundâncias em não-ETL de carbono, nitrogênio, oxigênio e silício, assim como as abundâncias em ETL de alumínio e ferro são, em geral, sub-solares em $\sim$ 0.2-0.4 dex. As abundâncias em ETL de magnésio e enxofre estão mais próximas dos valores solares nas cinco associações. As associações estudadas aqui estão concentradas em uma região do disco próxima do círculo solar e não cobrem um intervalo significativo em distâncias Galactocêntricas; as abundâncias obtidas, entretanto, concordam com o padrão de abundâncias esperado por estudos da distribuição de abundâncias químicas em função do raio Galactocêntrico.

---

[1] **Daflon, S., Cunha, K., Becker, S. R. & Smith, V. V. (2001) The Astrophysical Journal, 552, 309-320 (Paper II)**

4.1 Introduction

Measuring the chemical abundances in B stars provides key information on two fronts pertaining to Galactic chemical evolution. On the first front, these stars are useful in defining the overall chemical makeup of the Galaxy over somewhat large distance scales. Being rather luminous (a typical B2V star has $M_V \sim$ -2), B stars are observable, down to some specific limiting magnitude, over much larger distances and volumes than solar-type stars. Working to V=12 at high spectroscopic resolution (possible now with 2m-class telescopes), the above-mentioned B2V star could be studied out to distances of 6 kpc from the Sun (neglecting reddening). In this regard, these higher-mass main-sequence stars are excellent probes of the current chemical abundances in the Galaxy over a sizable volume. They probe the current abundances because main-sequence B-stars are necessarily young objects (a B2V star with M $\sim$8–10$M_{\odot}$ will have a main-sequence lifetime of $\sim$ 2–4 $\times 10^7$ yr), with ages much less than a Galactic rotation time, and their abundances should reflect, in general, the abundances in the interstellar gas from which they formed.

Examining Galactic chemistry on global scales defines general chemical evolution and star formation in the Milky Way over space and time, and may even shed light on galactic type. Often, global abundance trends in spiral galaxies are characterized as “abundance gradients”: as noted in the review by Smartt (2000), non-barred spirals exhibit a pattern of decreasing heavy-element abundances (e.g. oxygen) with increasing galactocentric distances. Recently, Smartt & Rolleston (1997) and Gummersbach *et al.* (1998) have used samples of B stars to probe the abundance gradients within the Milky Way disk.

In addition to their usefulness in probing large-scale chemical patterns in the Galaxy, B stars may be involved in more local aspects of chemical evolution. Most B stars are formed in OB associations, which are complexes of gas, dust, molecular clouds, and stars. Some OB associations contain distinct stellar groups, which represent different epochs of star formation occurring over the lifetimes of the associations (typically $\sim 10^7$ yr – Blaauw 1991). The timescales of star formation and association lifetime are such that the most massive stars formed in an OB association may have time to evolve to core-collapse supernovae of type II (SN II), exploding within an association. Such massive SN II are expected to produce large amounts of freshly synthesized heavy elements, especially oxygen (a $25M_{\odot}$ star produces $3M_{\odot}$ of ^{16}O, with a $20M_{\odot}$ star producing $2M_{\odot}$, Woosley & Weaver 1995). If these enriched SN II ejecta can significantly contaminate interstellar gas within the association from which new generations of stars are being formed, measurable changes in the O abundance might occur amongst different stellar groups in an association. This idea was first put forth by Reeves (1972, 1978), elaborated somewhat by Olive & Schramm (1982), and observationally studied in the Orion association by Cunha & Lambert (1992, 1994). Thus, there is the possibility that some OB associations may undergo chemical self-enrichment, leading to a spread in abundances, probably principally oxygen, within an association at a single Galactocentric distance.

This paper is the second in a study of a number of OB associations (Daflon, Cunha, & Becker's (1999) paper on Cep OB2 was the first), with the purpose being to both lay the foundations for an eventual determination of the Galactic abundance gradient, using a number of elements, as well as to probe certain individual associations for chemical uniformity, or lack thereof. We present chemical abundances for fifteen stars belonging to five OB associations along the Galactic disk: 3 stars in Cyg OB3, 2 in Cyg OB7, 3 in Cep OB3, 5 in Lac OB1, and 2 in Vul OB1. Some characteristics of the studied associations are presented in Table 4.1. The paper is organized as follows: Section 2 has a discussion of the observational data, while stellar effective temperatures and gravities are derived in Section 3. The chemical analyses are described in Section 4, and results are discussed in Section 5.

4.2 Observations

The observations were carried out at the University of Texas' McDonald Observatory. High-resolution spectra (R=60,000) were obtained with the 2.1m Otto Struve telescope coupled to the Sandiford cassegrain echelle spectrometer and a CCD detector. Spectra were taken in two spectral regions covering wavelengths between 4225-4625 and 4855-5285 Å, respectively. Lower-resolution spectra (R=12,000) were also obtained in the region of $H\gamma$ with the 2.7m Harlan J. Smith telescope plus a coudé spectrometer and CCD detector. $H\gamma$ line-profiles were used to derive surface gravities, as will be described in Section 3.

A total of 27 main-sequence stars belonging to the five OB associations listed in Table 4.1 were observed. These target stars were selected from the list of Garmany & Stencel (1992). Candidate stars for an equivalent-width abundance analysis were then selected based

Table 4.1: Individual Associations

Association	Coordinates	$d_\odot$(kpc)	Age (Myr)	Ref.
VulOB1	$59^o < l < 61^o$ $-1.^o2 < b < -1.^o5$	3.5	5	SJ81
Cyg OB3	$71^o < l < 74^o$ $-1.^o2 < b < +3.^o4$	2.29	8.3	BS85
Cyg OB7	$84.^o0 < l < 96.^0$ $-4.^o9 < b < +9.0$	0.83	13	BS85
Lac OB1	$92^o < l < 107^o$ $-7^o < b < -20^o$	0.368	16-25*	Z99, B91
Cep OB3	$109.^o4 < l < 112.^o9$ $2.^o3 < b < 5.^o2$	0.73	4-8*	B64

* Two subgroups. References - SJ81: Sagar & Joshi (1981), BS85: Bochkarev & Sitnik (1985), Z99: de Zeeuw *et al.* (1999), B64: Blaauw (1964), B91: Blaauw (1991)

upon the criterion of a low projected rotational velocity ($v \sin i$) for which features could be identified in the spectra: high values of $v \sin i$ ($\geq 70 kms^{-1}$) broaden and blend the spectral features to such an extent, that well-defined equivalent widths cannot be measured. Based on this restriction, the final sample examined here for chemical analysis was limited to 15 stars, while the atmospheric parameters T_{eff} and $\log g$ were derived for all the stars. The reduction of spectra was done in a standard way (bias subtraction, division by flat-field, subtraction of scattered light, extraction and wavelength calibration) using IRAF routines. A sample spectrum in the region 4560-4620 Å for the program star HD 197512 is shown in Figure 4.1. In Table 4.2 we present the spectral types, V magnitudes and Q parameters for the studied stars. The UBV photometry used to derive the Q-parameters listed in the table has been taken from Garmany & Stencel (1992), Crampton (1971), Harris III (1955), Zelwanowa & Schoeneich (1971) and Golay (1958).

Table 4.2: Sample Stars

Association	Star	MK	V	Q
Vul OB1	BD+24° 3880	B0.5V	10.89	-0.851
	HD 344783	B0IV	9.75	-0.860
Cyg OB3	BD+35° 3956	B0.5V	8.85	-0.757
	HD 191566	B0V	7.33	-0.802
	HD 227460	B1I V	9.51	-0.798
	HD 227586	B0.5V	8.90	-0.811
	HD 227696	B0.5V	8.29	-0.831
	HD 227757	O9.5V	9.20	-0.880
	HD 227877	B2V	9.04	-0.723
	HD 228199	B0.5V	9.25	-0.843
Cyg OB7	HD 197512	B1V	8.55	-0.730
	HD 199579	O6V	5.96	-0.886
	HD 201666	B2V	7.66	-0.623
	HD 202163	B2V	8.62	-0.531
	HD 202253	B1.5IV	7.75	-0.711
	HD 202347	B1.5V	7.50	-0.724
	HD 203064	O7.5III	5.01	-0.928
Lac OB1	HD 214167	B1V	5.73	-0.792
	HD 214680	O9V	4.87	-0.896
	HD 216916	B2IV	5.58	-0.729
	HD 217227	B2V	7.16	-0.567
	HD 217811	B2V	6.38	-0.580
	HD 218674	B3IV	6.73	-0.563
Cep OB3	BD+62° 2125	B1.5V	8.95	-0.728
	BD+62° 2127	B2IV	10.16	-0.708
	HD 217657	B0.5V	8.14	-0.813
	HD 218342	B0IV	7.43	-0.845

4.3 Stellar Parameters

The derivation of the primary stellar parameters, effective temperature and surface gravity, followed the same procedure as described in Daflon, Cunha & Becker (1999 - hereafter, Paper

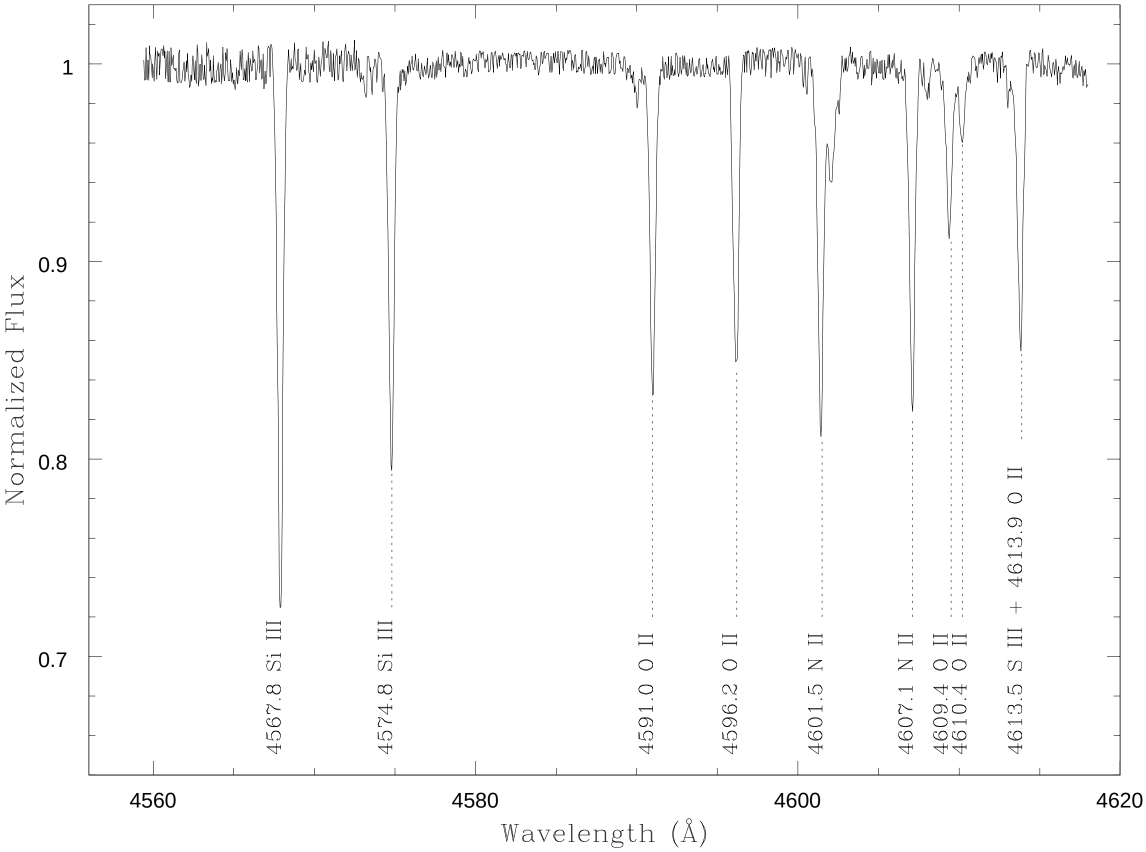

Figure 4.1: Sample echelle order in the region 4560-4620Å for the star HD 197512.

I). The T$_{eff}$'s were derived from a calibration obtained in Paper I. This calibration was based upon the reddening-free Q-parameter and T_{eff}'s derived iteratively from a combination of the Strömgren photometric indices (c_1, b-y and β), with fits to the wings of $H\gamma$ line-profiles (the latter is referred to as T_{iter}, see Paper I for a discussion). In general, the iterative technique is deemed a superior method, however, it requires Strömgren photometry for target stars. Many stars in the OB associations do not have available Strömgren photometry, but do have Johnson UBV; this drove the need, in Paper I, to derive a calibration between the iterative T$_{eff}$-scale, and a scale based on the reddening-free Q index (derived from UBV).

Surface gravities for the program stars were obtained by fitting the line-wings of model $H\gamma$ profiles to the observed ones. Once a T_{eff} was defined for a star, we interpolated in the grid of theoretical LTE $H\gamma$ profiles calculated by Kurucz (1979) and minimized the differences between observed and model profiles to choose the best fit, ignoring the line-center region of $\sim 3\text{Å}$, which is strongly influenced by non-LTE effects. The adopted effective temperatures $[T(Q)]$ and surface gravities for the sample of 27 stars are listed in Table 4.3.

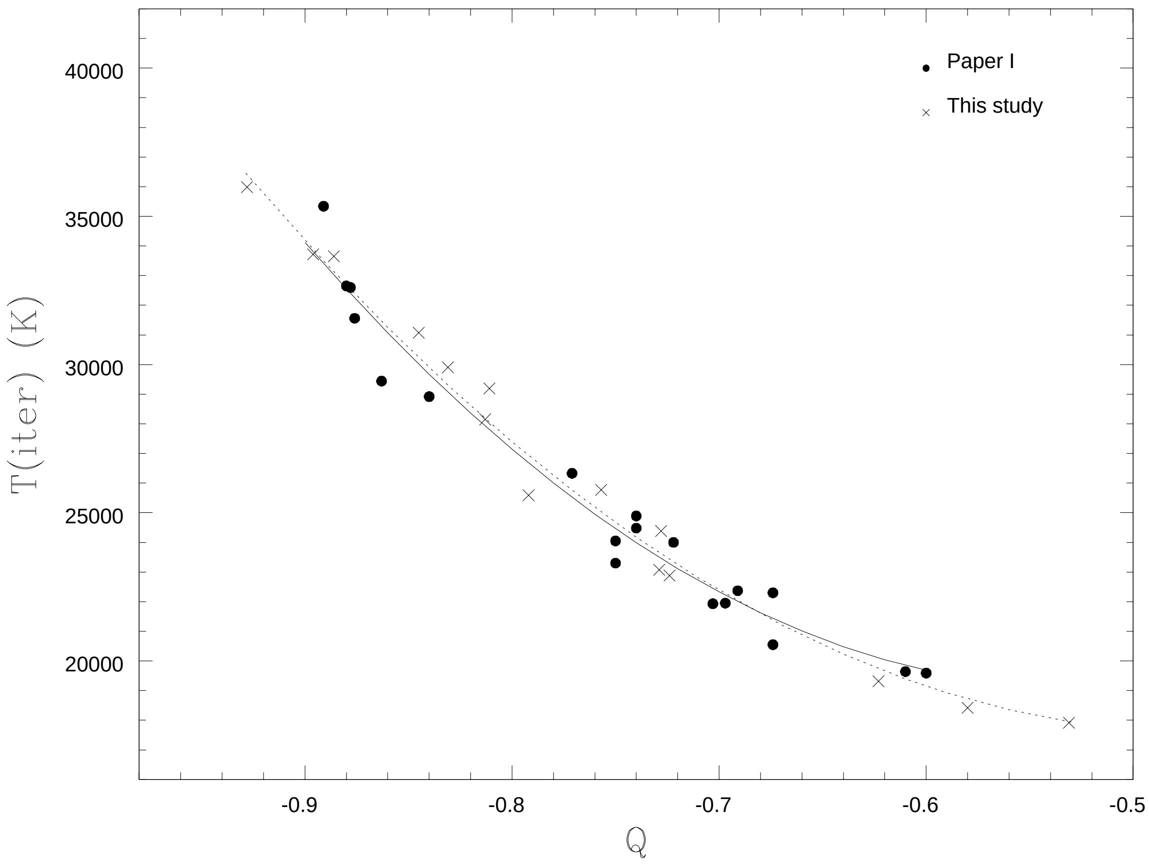

Figure 4.2: The adopted $Q \times T_{eff}$ relation (—) derived in Paper I for Orion and Cep OB2 stars (solid circles). With the addition of 15 stars of the present sample (×) to the sample analyzed in Paper I, a new $Q \times T_{eff}$ calibration can be obtained (....). The two different $Q \times T_{eff}$ relations are in agreement to about 2%. The relation from Paper I was used to derive the effective temperatures here, in order to assure consistency of the temperature scale.

For a subsample of 15 stars, Strömgren photometry was available in the literature and effective temperatures could also, in these cases, be derived by means of the iterative method. In Table 4.4 we list the stars' Strömgren indices c_1, b-y and β (Hauck & Mermilliod 1998;

Table 4.3: Adopted Stellar Parameters

Association	Star	T_{eff} (K)	$\log g$
Vul OB1	BD+24° 3880	30410	4.57
	HD 344783	31010	4.26
Cyg OB3	BD+35° 3956	24840	4.25
	HD 191566	27290	3.98
	HD 227460	27060	4.34
	HD 227586	27830	4.15
	HD 227696	29100	4.45
	HD 227757	32480	4.22
	HD 227877	23260	4.50
	HD 228199	29870	4.47
Cyg OB7	HD 197512	23570	4.02
	HD 199579	32930	4.12
	HD 201666	19900	4.23
	HD 202163	18560	4.30
	HD 202253	22750	3.95
	HD 202347	23280	4.13
	HD 203064	36300	3.62
Lac OB1	HD 214167	26720	5.00
	HD 214680	33690	4.27
	HD 216916	23520	4.00
	HD 217227	19000	4.20
	HD 217811	19070	3.92
	HD 218674	18840	3.75
Cep OB3	BD+62° 2125	23480	4.05
	BD+62° 2127	22630	3.96
	HD 217657	27950	4.38
	HD 218342	30020	4.20

Hauck & Mermilliod 1980), their color excess E(B-V) (Garmany & Stencel 1992), as well as the iterated effective temperatures and gravities. By adding the present sample of stars

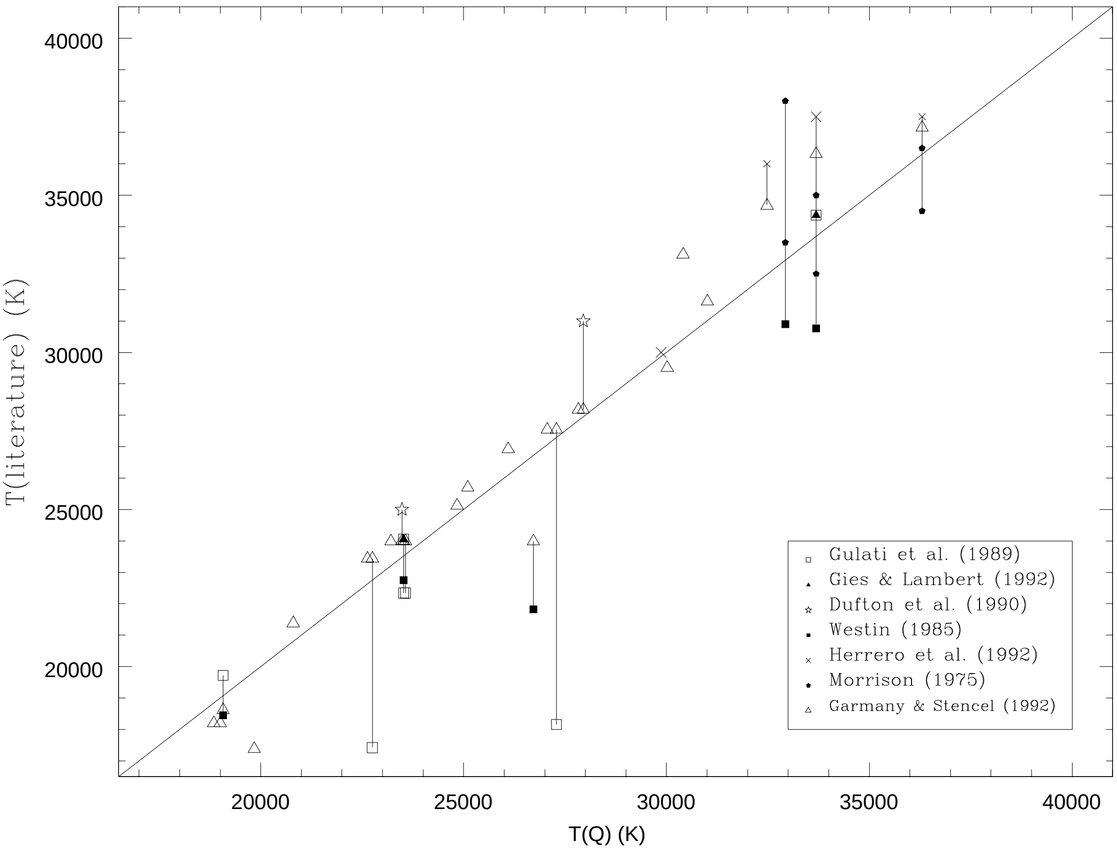

Figure 4.3: Effective temperatures derived from the Q-parameter compared with temperatures from the literature for the studied stars. The different symbols represent different studies in the literature and are identified in the figure. The diagonal line represents perfect agreement. Vertical lines connect different values of T_{eff} for the same star.

to the sample analyzed previously in Paper I, a new $Q \times T_{eff}$ calibration was obtained. As a consistency check, this new relation can be compared to the calibration derived in Paper I in order to see if there are any significant differences. This comparison is shown in Figure 4.2: the solid line represents the calibration adopted in this study and the dotted line depicts the relation derived for the combined sample (Paper I + present sample). Note that the two fits are quite similar; the two different $Q \times T_{eff}$ relations are in agreement to within a few hundred degrees (about 1-2%). We elect to use the relation from Paper I to derive the effective temperatures here, in order to assure consistency of the temperature scale with the study of OB stars in the Cep OB2 association. The small differences in the derived temperature scales, which result from the use of the two different samples of stars to calibrate Q X T$_{eff}$, would have no significant impact on the derived abundances.

Table 4.4: T_{eff} and $\log g$ from Iterative Method.

Association	Star	c_1	$b-y$	β	E(B-V)	T_{eff} (K)	$\log g$
Cyg OB3	BD+35° 3956	0.069	0.218	2.606	0.46	25770	4.26
	HD 227586	0.004	0.210	2.602	0.49	29190	4.35
	HD 227696	-0.004	0.212	2.590	0.49	29900	4.53
Cyg OB7	HD 199579	-0.081	0.106	2.581	0.36	33650	4.24
	HD 201666	0.250	0.044	2.653	0.21	19320	3.96
	HD 202163	0.311	0.018	2.722	0.15	17910	4.03
	HD 202347	0.106	-0.013	2.629	0.19	22880	4.05
	HD 203064	-0.109	0.053	2.559	0.30	35990	4.37
Lac OB1	HD 214167	0.024	-0.045	2.609	0.12	25590	4.65
	HD 214680	-0.110	-0.067	2.588	0.11	33720	4.42
	HD 216916	0.091	-0.047	2.630	0.12	23070	4.00
	HD 217811	0.288	0.039	2.661	0.21	18420	3.76
Cep OB3	BD+62° 2125	0.166	0.532	2.635	0.91	24380	4.19
	HD 217657	0.063	0.410	2.612	0.78	28150	4.40
	HD 218342	0.008	0.368	2.595	0.71	31070	4.44

4.3.1 Uncertainties in the Stellar Parameters

As discussed in Paper I, the uncertainties in the derived T_{eff}'s are influenced by the errors in the UBV photometry and the resultant Q parameter. The typical uncertainty in the adopted photometric indices is ~0.01 mag and this imparts an error in T_{eff} varying from 1% to 2.5% in the T_{eff} interval spanned by the program stars. The intrinsic scatter in fitting the Q-parameter to the effective temperature derived iteratively is $\overline{T_{iter} - T(Q)} = +121 \pm 754$K; indicating that there is effectively no zero-point offset and that $T(Q)$, from UBV photometry, can be fitted to T_{iter} within, typically, ~750 K. This intrinsic scatter within the $T_{iter} - T(Q)$

scales – 4% at T_{eff}=20,000 K and 2.5% at T_{eff}=30,000 K – seems to be a fair estimate of the uncertainties in assigning effective temperatures to the studied OB stars.

As a further step in obtaining estimates of the uncertainties in the adopted effective temperatures, we compare our results for $T_{\rm eff}$'s with values from the literature for stars in common: this is shown in Figure 4.3. There is a large overlap with the study of Garmany & Stencel (1992), who used a photometric calibration of the intrinsic color (B-V)$_o$ to derive effective temperatures for 25 stars in common with us. The mean difference between $T(Q)$ and Garmany & Stencel's effective temperatures is -369±1327 K (discarding HD 199579, for which Garmany & Stencel list T=42660K and we obtain T=32930K). Another study that derives a photometric calibration of the intrinsic color (B-V)$_o$ is Gulati *et al.* (1989). For the 7 stars in common with us there is a difference of +2200±3690K. The largest discrepancies are found for HD 191566 and HD 202253. We note, however, that a smoother spectral type – $T_{\rm eff}$ is derived with our temperatures. Westin (1985) also derived effective temperatures for some of the stars belonging to our sample. He used a photometric calibration for the index c_o from Davis & Shobbrook (1977) and his listed temperatures are systematically lower than ours by roughly 3% at 20,000 K and 8% at 30,000 K.

Two stars in the Cep OB3 association have been studied by Dufton *et al.* (1990). They determined effective temperatures from photometric calibrations of Strömgren indices (T(Strömgren)) and/or from silicon (Si II/Si III/Si IV) ionization equilibrium (T(Si)) and adopted the mean value of both temperatures as the effective temperature, when both were available. They listed T(Strömgren)=23500K and T(Si)=26000K for star BD+62^o 2125, while the adopted (mean) temperature is 25000K. We obtained T_{iter}=23480K and T(Q)=24380K for this star so we have excellent agreement. For the star HD 217657, they present only a silicon temperature of 31000K, higher than ours (T_{iter}=27950K and T(Q)=28150K). However, 3 stars in their sample have both T(Strömgren) and T(Si), and for two of them, T(Si) is 10-15% higher than T(Strömgren), which suggests that the temperature of 31000K for HD 217657 could also be overestimated relative to their T(Strömgren): lowering T(Si) for this star by 12% would yield $T_{\rm eff}$=27280K, in good agreement with our T_{iter} or T(Q).

For 3 stars in our sample, stellar parameters have been determined by Morrison (1975) using two distinct methods: comparison with synthetic colors from the non-LTE models of

Mihalas (1972) and the spectroscopic temperature scale of Conti (1973). Her spectroscopic temperatures are always higher than the photometric ones by roughly 10%. The temperatures derived by Morrison (1975) are plotted in Figure 4.3 as solid pentagons and show, in general, good agreement with our values. On the other hand, Herrero *et al.* (1992) determined stellar parameters by fitting theoretical non-LTE profiles of hydrogen and helium lines and find T_{eff}'s higher by ∼10% for the two stars in common with Morrison (HD 214680 and HD 203064). Our adopted T_{eff}'s for these stars are between the results for these studies. We also note the expected good agreement of our T_{eff}'s for stars HD 214680 and HD 216916, belonging to Lac OB1, and the temperatures derived by Gies & Lambert (1992) using the iterative method, which consists of a photometric calibration plus fitting the $H\gamma$ profiles, as described above. These two points are represented by filled triangles in Figure 4.3. Overall, except for a few cases, the agreement between the various temperature determinations is good.

Surface gravities were determined by fitting theoretical wing profiles of $H\gamma$ lines to the observed ones. The uncertainties in gravity determination come mainly from effective temperatures and normalization of spectra in the region of ±20 Å centered on the $H\gamma$ line. We estimate an error of ±0.1 dex in the gravity determination, which is the difference in $\log g$ for which one can distinguish between two different theoretical profiles. Morrison (1975) listed two values of gravity for the stars HD 214680 ($\log g$=3.5 and 3.7) and HD 203064 ($\log g$=3.5 and 4.0), where we derive values of 4.27 and 3.62, respectively. The gravities derived by Gies & Lambert are consistent with our values within 0.1 dex. This agreement, within the uncertainties, is also observed for the gravities derived by Howarth & Prinja (1989) and Dufton *et al.* (1990).

4.4 Abundance Analysis

4.4.1 Line Selection and Atomic Data

The selected line sample consists of unblended lines of carbon, nitrogen, oxygen, magnesium, aluminum, silicon, sulfur and iron, for which an abundance analysis based on equivalent-width measurements can be done. The list of lines is basically that adopted in Paper I and consists of 3 C II lines, 8 N II lines, 15 lines of O II, 3 lines of Si III and 5 Fe III lines.

Oscillator strengths for the selected multiplets have been taken from the Opacity Project (TOPbase; Cunto & Mendonza 1992). The list of lines and the corresponding atomic data - transitions, excitation potentials and log(gf) - are presented in Table 2 of Paper I. In this paper we have added one line of Mg II, 3 lines of Al III and 2 S III lines, which are listed in Table 4.5. The equivalent widths of the selected lines have been measured with tasks in the IRAF data package using gaussian fitting and/or numerical integration. By doing a number of independent equivalent-width measurements, we obtain an error of ~10% for weak lines and ~5% for intermediate to relatively strong lines in the equivalent widths. Table 4.6 lists the equivalent widths for the sample stars.

Table 4.5: Atomic Data

Ion	λ(Å)	Transition	χ(ev)	log(gf)
Mg II	4481.21 [a]	$3d^2D - 4f^2F$	8.86	0.82
Al III	4479.93 [b]	$4f^2F^o - 5g^2G$	20.78	1.11
	4512.56	$4p^2P^o - 4d^2D$	17.81	0.40
	4529.19		17.81	0.66
S III	4361.53	$4s^3P^o$ - $4p^3D$	18.24	-0.75
	4364.75	$3d^3D^o$ - $4p^3D$	18.32	-0.85

[a] blend of $\lambda\lambda$4481.13 Å and 4481.33 Å of Mg II.

[b] blend of $\lambda\lambda$4479.88 Å and 4479.97 Å of Al III.

4.4.2 LTE Abundances

LTE abundances of C, N, O, Si, Fe, Mg, Al and S were derived using LTE model atmospheres and the WIDTH9 code (Kurucz 1992). The atmospheric models were constructed for the adopted effective temperatures and gravities (Table 4.3), assuming solar composition and a depth-independent microturbulent velocity of 2 kms^{-1}, by interpolation in a grid of atmosphere models calculated by Kurucz (1992) with the ATLAS9 code. LTE abundances of the sample of O II lines were calculated for a range of microturbulent velocities (varying from 2 to 12 kms^{-1}) to find an appropriate microturbulence that produced abundances independent of equivalent widths. The derived LTE abundances (on a scale where log ϵ(H) =

Table 4.6: Measured Equivalent widths

Ion	λ(Å)	HD227460	HD227586	HD227757	HD214167	HD214680	HD216916	HD217227	HD217811
C II	5143.5	27	13	-	-	-	34	15	19
	5145.2	42	22	-	-	-	53	28	34
	5151.1	-	-	-	-	-	-	-	-
N II	4236.9	54	18	-	29	7	45	18	16
	4241.8	56	38	-	27	12	47	12	15
	4607.1	58	17	b	26	-	43	15	18
	4630.5	91:	b	b	53:	-	79	29	32
	4643.1	54	29	b	36	-	48	18	20
	5005.1	81	66	-	-	-	65	27:	35
	5007.3	47	28	-	-	-	33	-	-
	5010.6	53	-	-	-	-	36	29:	14
O II	4414.9	175	129	85	68	44	100	36	38
	4416.9	153	105	58	54	17:	83	33	29
	4452.4	70	59	25	22	-	35	10:	13
	4466.6	49	-	22	16	-	-	-	-
	4591.0	130	103	70	47	30:	82	18	16
	4609.4	67	b	b	21	b	47	8	13
	4638.9	105	106	97:	46	55:	69	22	24
	4641.8	151	135	117:	65	77:	93	29	29
	4649.1	170	170:	b	84	b	119	43	40
	4661.6	131	105	-	43	44	73	24	21
	4890.8	36	-	-	-	-	22	-	-
	4906.8	64	65	-	-	23	30	-	-
	4941.1	66	55	28:	-	-	27	-	-
	4943.0	90	66	51:	-	-	34	-	-
	5190.6	-	-	-	-	-	-	-	-
Mg II	4481.2	134	85	94	146	81	139	204	190
Al III	4479.9	37	-	17	35	13	52	20	20
	4512.6	48	20	-	36	6:	43	23	24
	4529.2	53	38	-	50	b	83	35	39
Si III	4552.6	189	174	107	108	80	145	79	75
	4567.8	158	131	84	82	62	125	56	54
	4574.7	138	108	42	56	21:	91	31	32
S III	4361.5	61	26	-	14:	-	22	8:	8:
	4364.7	b	b	-	11:	-	12	-	-
Fe III	4310.3	25	b	-	-	-	23	13	9
	5156.1	-	-	-	-	-	-	-	-
	5243.3	32	-	-	-	-	38	-	13
	5276.5	24	-	-	-	-	27	-	-
	5282.3	31	-	-	-	-	27	-	-

- absent; b blended; : uncertain.

Table 4.6: Measured Equivalent widths (*continued*)

Ion	λ(Å)	HD197512	HD202253	BD+62° 2125	HD217657	HD218342	BD+24° 3880	HD344783
C II	5143.5	24	-	-	-	-	-	-
	5145.2	30	-	-	-	-	-	-
	5151.1	-	-	-	-	-	-	-
N II	4236.9	69	55	-	-	-	53	-
	4241.8	64	50	-	-	-	59	20
	4607.1	71	57	37	10:	b	51	b
	4630.5	114	b	74	-	-	86	b
	4643.1	77	b	35	27	b	51	b
	5005.1	92	-	48	21	12:	81	-
	5007.3	54	-	38	-	-	-	-
	5010.6	67	-	31	-	-	-	-
O II	4414.9	97	103	130	135	172	157	93
	4416.9	89	89	118	97	139	133	84
	4452.4	40	45	47	42	44	70	23
	4466.6	29	b	b	33	-	46:	-
	4591.0	64	85	76	87	100	113	90:
	4609.4	39:	b	56	48	b	53	b
	4638.9	69	b	82	93	110	101	50:
	4641.8	96	b	104	123	b	b	b
	4649.1	120	b	118	151	b	174	b
	4661.6	86	85	95	91	115	107	96
	4890.8	-	-	-	-	-	-	-
	4906.8	25	-	32	26	62	67:	-
	4941.1	33	-	36	55	51	-	-
	4943.0	39	-	51	62	70	-	50
	5190.6	-	-	-	-	-	-	-
Mg II	4481.2	133	-	111	84	108:	125	82
Al III	4479.9	35	48	b	16	b	31	18
	4512.6	41	-	-	20	-	29	19
	4529.2	56	24	51	38:	27	54	-
Si III	4552.6	137	139	137	147	190	187	122
	4567.8	113	133	128	132	144	163	116
	4574.7	91	92	95	86	84	109	65
S III	4361.5	21	-	-	26	-	40	24:
	4364.7	15	-	-	-	-	41	-
Fe III	4310.3	24	-	-	27	-	21:	-
	5156.1	-	-	-	-	-	-	-
	5243.3	44	-	-	-	-	-	-
	5276.5	20	-	-	-	-	-	-
	5282.3	21	-	30	-	-	-	-

- absent; b blended; : uncertain.

12), adopted microturbulences and number of lines considered in the calculation of the mean abundances are listed in Table 4.7.

In Figures 4.4 and 4.5 we present the LTE abundances as a function of effective temperature. The dotted line depicts the solar abundance for each element, as listed by Grevesse, Noels & Sauval (1996). Inspection of these figures shows that the LTE elemental abundances for the OB stars in our sample are generally subsolar, except for sulfur and magnesium, and do not show significant trends with temperature. The largest trend with temperature is observed for silicon, where there is a slight increase in the silicon abundance of 0.15 dex as the effective temperature increases from 20000K to 30000K.

4.4.3 Non-LTE Abundances

Non-LTE synthetic profiles have been calculated from the same grid of LTE model atmospheres, plus model atoms from Eber & Butler (1988 – C II), Becker & Butler (1989 – N II), Becker & Butler (1988a, 1988b – O II) and Becker & Butler (1988c, 1990 – Si III). The solutions of the equations of statistical equilibrium and transfer are obtained with the program DETAIL assuming LS-coupling; the line profiles are computed with Voigt profile functions using the program SURFACE. The equivalent widths for the synthetic profiles have been measured using the same procedure as for the observed lines. The O II lines were used to derive the microturbulent velocities for the program stars in a similar manner as done for the LTE analysis, i.e., we chose the microturbulence that produced an oxygen abundance independent of the equivalent width.

The non-LTE abundances derived for the program stars are presented in Table 4.8. The same line sample was used to derive mean LTE and non-LTE abundances. Our derived Non-LTE microturbulent velocities vary between 5 and 11 kms^{-1} and the mean value is 7.7±1.7 kms^{-1}. This is slightly less than our mean LTE microturbulence (8.9±1.7 kms^{-1}). Our results are in line with Gies & Lambert (1992), who derived $<\xi_{\rm LTE}>= 6.2 \pm 2.7 kms^{-1}$ and $<\xi_{\rm Non-LTE}>= 5.0 \pm 3.3 kms^{-1}$ for their studied sample of field main sequence B stars. The non-LTE microturbulences obtained by Gummersbach *et al.* (1998) are also in rough agreement with our derived values, when the uncertainties are considered. Their values range from 1 to 13 kms^{-1} with a mean value of 5.6 ± 4.1 kms^{-1}. Our adopted uncertainty for the microturbulent velocity is ±1.5 kms^{-1}, which is approximately the interval of ξ-values that

Table 4.7: LTE Abundances

Star	ξ(km s^{-1})	$\log\epsilon(C)[n]$	$\log\epsilon(N)[n]$	$\log\epsilon(O)[n]$	$\log\epsilon(Si)[n]$
BD+24° 3880	9.0	-	8.07±0.09 [5]	8.76±0.04 [7]	7.70±0.03 [3]
HD 344783	8.0	-	7.66* [1]	8.52±0.11 [6]	7.59±0.06 [3]
HD 227460	10.0	8.28±0.08 [2]	7.86±0.10 [7]	8.76±0.08 [12]	7.41±0.14 [3]
HD 227586	10.0	8.01±0.07 [2]	7.64±0.08 [5]	8.52±0.08 [9]	7.24±0.11 [3]
HD 227757	9.0	-	-	8.54±0.07 [7]	7.54±0.05 [3]
HD 197512	8.0	8.02±0.14 [2]	8.01±0.07 [7]	8.57±0.08 [11]	7.21±0.10 [3]
HD 202253	8.0	-	7.89±0.07 [3]	8.82±0.10 [5]	7.38±0.07 [3]
HD 214167	7.0	-	7.60±0.09 [5]	8.49±0.07 [9]	7.14±0.05 [3]
HD 214680	11.0	-	7.55* [1]	8.64±0.10 [4]	7.53±0.04 [3]
HD 216916	8.0	8.27±0.07 [2]	7.72±0.08 [8]	8.57±0.10 [11]	7.30±0.04 [3]
HD 217227	7.0	8.26±0.03 [2]	7.78±0.09 [5]	8.82±0.07 [9]	7.47±0.07 [3]
HD 217811	6.0	8.26±0.03 [2]	7.72±0.13 [7]	8.62±0.09 [8]	7.30±0.06 [3]
BD+62° 2125	12.0	-	7.63±0.08 [5]	8.63±0.09 [11]	7.05±0.14 [3]
HD 217657	10.0	-	7.62* [1]	8.51±0.10 [11]	7.23±0.07 [3]
HD 218342	11.0	-	-	8.66±0.09 [9]	7.41±0.05 [3]

* Uncertain

presents consistent abundances for strong and weak oxygen lines.

The non-LTE abundances versus T$_{\rm eff}$ are shown in Figure 4.6. Overall, the non-LTE abundances for C, N, O, and Si are not changed significantly with respect to LTE: the magnitude of the non-LTE corrections (LTE - non-LTE abundances) are typically $\leq$0.2 dex. The "non-LTE corrections" themselves, in the form of (LTE - non-LTE), are illustrated in Figure 4.7 plotted versus the effective temperatures. Included in Figure 4.7 are the non-LTE corrections for the sample of Cep OB2 stars from Paper I (filled triangles) which were obtained with the same set of spectral lines, model atoms, and atmospheres as in the present paper.

Table 4.7: LTE Abundances *(continued)*

Star	ξ(km s^{-1})	$\log \epsilon(Mg)[n]$	$\log \epsilon(Al)[n]$	$\log \epsilon(S)[n]$	$\log \epsilon(Fe)[n]$
BD+24° 3880	9.0	7.87 [1]	6.30±0.04 [1]	7.45±0.06 [2]	7.36* [1]
HD 344783	8.0	7.74 [1]	6.27±0.09 [1]	7.32 [1]	-
HD 227460	10.0	7.71 [1]	6.20±0.09 [3]	7.56 [1]	7.33±0.12 [4]
HD 227586	10.0	7.37 [1]	6.00±0.15 [3]	7.01 [1]	-
HD 227757	9.0	7.83 [1]	6.25 [1]	-	-
HD 197512	8.0	7.55 [1]	6.05±0.02 [3]	7.08±0.03 [2]	7.34±0.09 [4]
HD 202253	8.0	-	6.15 [1]	-	-
HD 214167	7.0	7.70 [1]	6.14±0.02 [3]	7.17±0.01 [2]	-
HD 214680	11.0	7.86 [1]	6.15±0.07 [2]	-	-
HD 216916	8.0	7.57 [1]	6.25±0.10 [3]	7.05±0.11 [2]	7.39±0.10 [4]
HD 217227	7.0	7.78 [1]	6.32±0.02 [3]	7.58 [1]	-
HD 217811	6.0	7.86 [1]	6.22±0.05 [3]	7.36 [1]	7.35±0.01 [2]
BD+62° 2125	12.0	7.14 [1]	5.92 [1]	-	-
HD 217657	10.0	7.41 [1]	5.92±0.10 [3]	7.07 [1]	7.33* [1]
HD 218342	11.0	7.69 [1]	6.10 [1]	-	-

* Uncertain

4.4.4 Abundance Uncertainties

Abundance determinations are subject to uncertainties in stellar parameters, equivalent-width measurements, gf-values and microturbulent velocities. Each of these sources of uncertainty contributes to the dispersions around the mean abundances listed in Table 4.7 and 4.8, where we present LTE and non-LTE abundances, respectively. Most of the line-to-line dispersion for LTE abundances are smaller than 0.1 dex, with maximum scatter of 0.15 dex. Non-LTE abundances show roughly the same scatter, except for the silicon abundances, for which we find four stars with standard deviations of about 0.2 dex. Silicon abundances are strongly influenced by the microturbulent velocity because the Si III lines used in this study have fairly large equivalent widths. The dependence on microturbulence is more pronounced when the LTE approximation is adopted, but it does not vanish for non-LTE calculations. Therefore the derived silicon abundances have a higher uncertainty, when compared to other elements, and depend more strongly on the choice of microturbulence.

In Table 6 of Paper I we present the total errors (δ_t) expected in our abundance analysis for carbon, nitrogen, oxygen, silicon and iron. The total errors are, in general, smaller than ~0.15 dex for all elements, except silicon. In this paper we investigate the sensitivity of the derived abundances of Mg, Al and S by recomputing the LTE abundances for four stars with representative effective temperatures, considering errors of 4% for T_{eff}, 0.1 dex for $\log g$ and 1.5 kms^{-1} for the microturbulence. The resulting changes in the LTE abundances of Mg, Al and S for each parameter, and the total errors derived, are presented in Table 4.9. The total errors for Al and S are typically smaller than 0.2 dex, but for Mg they can be of the order of 0.3 dex for the coolest stars in the sample.

4.5 Discussion

The final non-LTE abundances of carbon, nitrogen, oxygen, and silicon are typically sub-solar and quite uniform: average values for all stars are [C/H]=-0.31±0.17, [N/H]=-0.28±0.18, [O/H]=-0.27±0.18, and [Si/H]=-0.30±0.19. These modest underabundances of many elements in solar-neighborhood B-stars, relative to the Sun, are well-known (e.g., Gies & Lambert 1992), and have been observed also in the Cep OB2 association (Paper I). The LTE results for Fe and Al are also sub-solar by roughly 0.15 and 0.30 dex, respectively. However, our LTE magnesium and sulfur results are scattered around solar values. Because the magnesium abundances are derived from one rather strong Mg II line, for which the non-LTE effects on line formation need to be investigated, the systematically larger Mg abundances found are not considered significant at the present stage.

The sulfur abundances, on the other hand, are harder to ignore. Non-LTE calculations for S II and S III have been done by Vrancken, Butler & Becker (1996), using model atmospheres of Kurucz (1992). They show that S III lines are little influenced by non-LTE effects for the temperatures found in B stars, which suggests that LTE results from the S III lines should yield good estimates for the sulfur abundance. It remains to be seen if the somewhat high (~solar) abundances of sulfur, when compared to the other elements, arise from uncertainties involved in the abundance analysis, or are a real and significant result that needs to be explained.

Table 4.8: Non-LTE Abundances

Star	ξ(km s^{-1})	$\log \epsilon(C)[n]$	$\log \epsilon(N)[n]$	$\log \epsilon(O)[n]$	$\log \epsilon(Si)[n]$
BD+24° 3880	8.0	-	8.01±0.08	8.64±0.06	7.50±0.10
HD 344783	9.0	-	7.54*	8.29±0.06	7.39±0.09
HD 227460	8.0	8.32±0.07	7.82±0.12	8.70±0.09	7.30±0.20
HD 227586	8.0	7.99±0.07	7.55±0.10	8.49±0.09	7.14±0.17
HD 227757	8.0	-	-	8.42±0.12	7.50±0.03
HD 197512	6.0	8.05±0.14	8.01±0.09	8.61±0.10	7.07±0.17
HD 202253	6.0	-	7.95±0.05	8.92±0.06	7.24±0.14
HD 214167	6.0	-	7.59±0.09	8.50±0.08	7.01±0.09
HD 214680	11.0	-	7.55*	8.58±0.12	7.53±0.03
HD 216916	6.0	8.38±0.04	7.70±0.12	8.65±0.08	7.19±0.13
HD 217227	7.0	8.34±0.01	7.82±0.08	8.92±0.08	7.38±0.04
HD 217811	5.0	8.35±0.01	7.73±0.09	8.72±0.11	7.21±0.04
BD+62° 2125	10.0	-	7.60±0.11	8.67±0.08	6.94±0.19
HD 217657	8.0	-	7.52*	8.40±0.09	7.04±0.12
HD 218342	9.0	-	-	8.54±0.11	7.29±0.07

* Uncertain

In the present study we have analyzed only a small number of targets in each OB association and did not find any individual stellar abundance result that was very discrepant from the mean abundance value for each association. Note that in some cases, there was only one star studied for a given element in some associations. Therefore, we simply adopt the mean abundances as representative of each association and are not in a position to discuss questions related to chemical inhomogeneities and self-enrichment. Table 4.10 lists the mean abundance results for each association together with the standard deviations. Solar abundances from Grevesse Noels & Sauval (1996) are also presented for comparison. The combination of LTE and non-LTE abundances are summarized graphically in Figure 4.8, where the average association abundances, as [X/H], are plotted versus atomic number. The dashed horizontal lines represent solar abundances ([X/H]=0.0), while the solid horizontal lines show the average C, N, O, Al, Si, and Fe abundances for each association. The general

Table 4.9: Abundance Uncertainties.

Ion	correction	HD 217811	HD 216916	HD 227460	BD+24° 3880
Al III	$\delta(T_{eff})$	-0.13	0.00	+0.08	+0.13
	$\delta(\log g)$	+0.03	+0.02	-0.01	-0.01
	$\delta(\xi)$	-0.05	-0.04	-0.06	-0.01
	δ_t	0.15	0.05	0.10	0.13
S III	$\delta(T_{eff})$	-0.17	-0.12	-0.08	-0.13
	$\delta(\log g)$	+0.05	+0.03	+0.03	0.00
	$\delta(\xi)$	-0.04	-0.01	-0.03	-0.01
	δ_t	0.19	0.12	0.09	0.13
Mg II	$\delta(T_{eff})$	+0.10	+0.15	+0.08	+0.12
	$\delta(\log g)$	-0.03	+0.01	-0.03	-0.01
	$\delta(\xi)$	-0.25	-0.11	-0.08	-0.07
	δ_t	0.28	0.19	0.12	0.14

subsolar abundances found for each association stand out, as well as the general agreement in the amount of the underabundance for each element, except for Mg and S.

Table 4.10: Mean Abundances

Element	Vul OB1	Cyg OB3	Cyg OB7	Lac OB1	Cep OB3	Sun
C	-	8.15±0.23	8.05**	8.36±0.02	-	8.55
N	7.77±0.33	7.68±0.19	7.98±0.04	7.68±0.11	7.56±0.06	7.97
O	8.46±0.25	8.54±0.14	8.76±0.22	8.67±0.16	8.54±0.13	8.87
Mg*	7.80±0.09	7.63±0.24	7.55**	7.75±0.12	7.41±0.27	7.58
Al*	6.28±0.02	6.15±0.13	6.10±0.07	6.22±0.07	5.98±0.10	6.47
Si	7.44±0.08	7.22±0.11	7.15±0.12	7.26±0.20	7.09±0.18	7.55
S*	7.38±0.09	7.28±0.39	7.08**	7.29±0.23	7.07**	7.33
Fe*	7.36**	7.33**	7.34**	7.37±0.03	7.33**	7.50

∗ LTE abundances; ∗∗ only one star.

Comparisons to other recent studies of B stars, which investigate Galactic abundances on large scales, can be made to see if the associations studied here fit onto derived Galactic abundance gradients. Gummersbach *et al.* (1998) studied 16 B stars and derived radial gradients with slopes equal to -0.03, -0.08, -0.07, -0.08, -0.04, and -0.11 dex/kpc, for carbon, nitrogen, oxygen, magnesium, aluminum and silicon, respectively. Smartt & Rolleston (1997) derived a radial gradient of -0.07 dex/kpc for oxygen. The five OB associations investigated in this study are distributed in a relatively small region around the Sun, from 7.4 to 8.8 kpc from the center of the Galaxy (adopting the Galactocentric distance for the Sun as 8.5 kpc) and span too small a range in distance to establish an independent radial gradient. In Figure 4.9 we plot the abundances taken from Gummersbach (C, N, O, Mg, Al and Si - represented by ×) and Smartt & Rolleston (only oxygen - represented by squares) as a function of Galactocentric distance. Inspection of this figure indicates that the chemical abundances derived for the associations studied in this paper are consistent with the abundances expected, as predicted by the various abundance gradients, given the respective distances of the OB associations from the Galactic Center.

Overall, the results obtained by the various recent analyses of the B stars are consistent, with each element appearing to exhibit a total scatter of roughly ~0.5 dex at the solar Galactocentric distance (or at any distance, but we have now added more data near the Sun). Some of this scatter must be due to the analysis, with perhaps some intrinsic abundance scatter in the real gradients. If the various studies impart an analysis scatter of, say, ~0.3 dex, it would still leave room for ~0.4 dex scatter in the current abundances at the solar Galactocentric distance. It is also worth noting that in all elements studied, except for Mg and S, the Sun is near the high end of the abundance scatter at R_g= 8.5 kpc.

4.6 Conclusion

We present LTE abundances of Mg, Al, S and Fe and non-LTE abundances of C, N, O and Si for a sample of 15 slowly rotating B-stars belonging to OB associations of the Galactic disk, namely Cyg OB3, Cyg OB7, Lac OB1, Vul OB1 and Cep OB3. We verified that the derived abundances for the sample stars are consistent with the predicted abundances for their respective positions in the Galactic disk, according to abundance gradients established from previous studies.

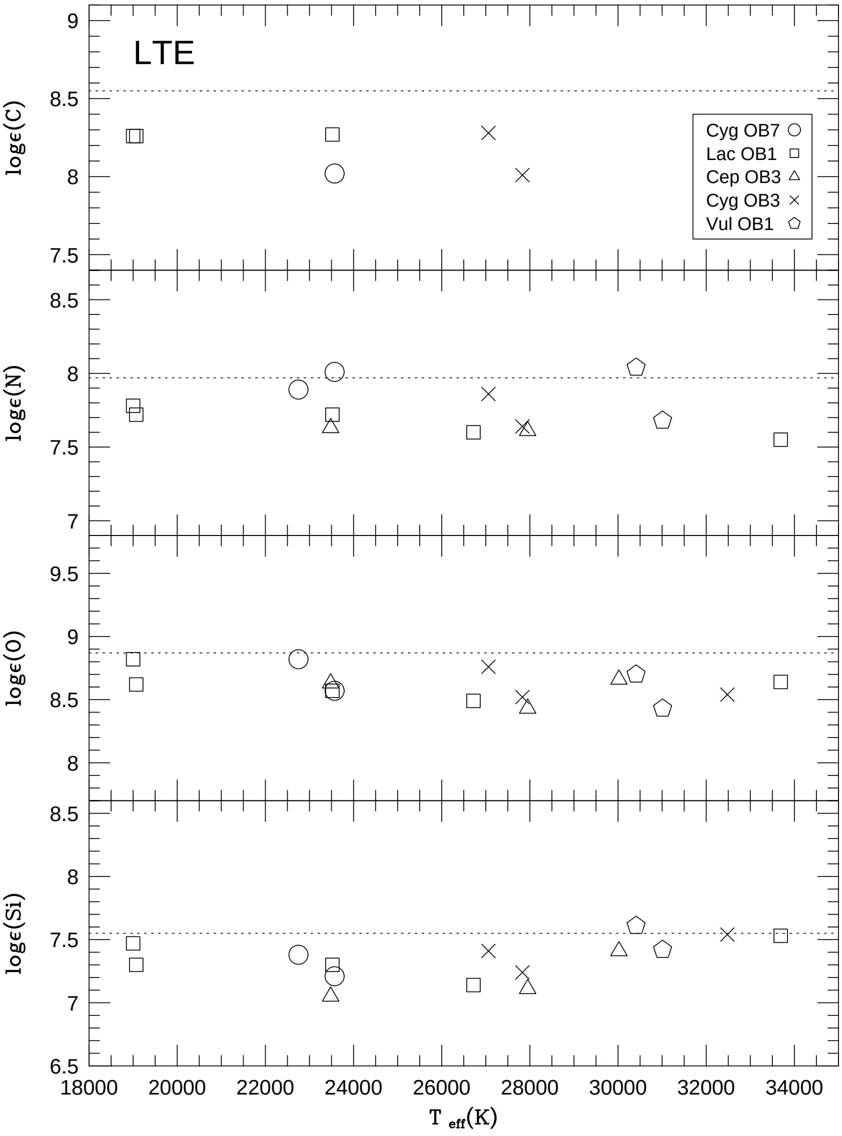

Figure 4.4: LTE C, N, O and Si abundances as a function of T_{eff}. The dashed lines represent the solar abundances from Grevesse, Noels, & Sauval (1996). LTE elemental abundances for the OB stars are generally subsolar and do not show significant trends with temperature: the largest trend with temperature is observed for silicon. Different symbols are used to represent the stars belonging to each OB association.

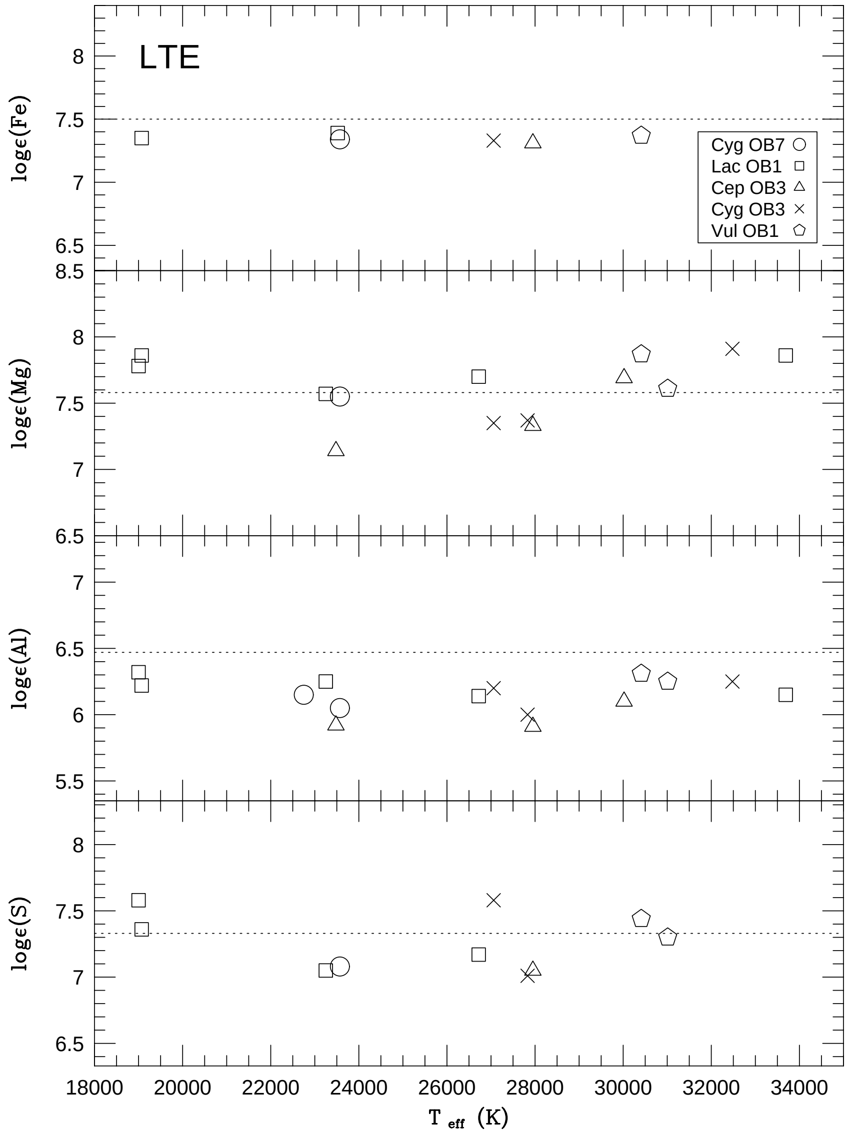

Figure 4.5: LTE Fe, Mg, Al and S abundances as a function of T_{eff}. The dashed lines represent the solar abundances from Grevesse, Noels & Sauval (1996). LTE abundance of iron and aluminum are, in general, subsolar, while sulfur and magnesium show some spread around the solar value. Different symbols are used to represent the stars belonging to each OB association.

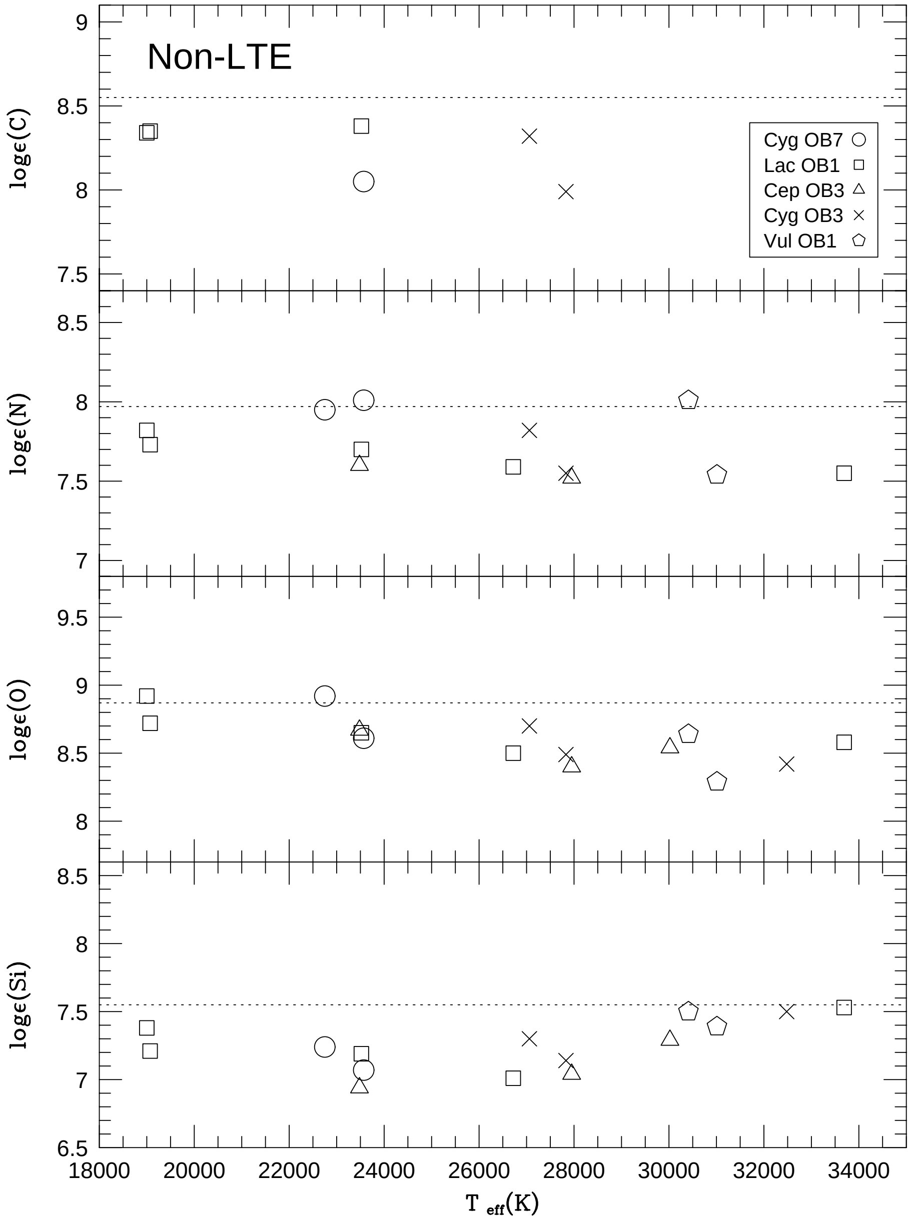

Figure 4.6: Non-LTE C, N, O and Si abundances as a function of T_{eff}. The dashed lines represent the solar abundances from Grevesse, Noels & Sauval (1996). The trends of non-LTE abundances with T_{eff} do not present significant changes with respect to LTE. Different symbols are used to represent the stars belonging to each OB association.

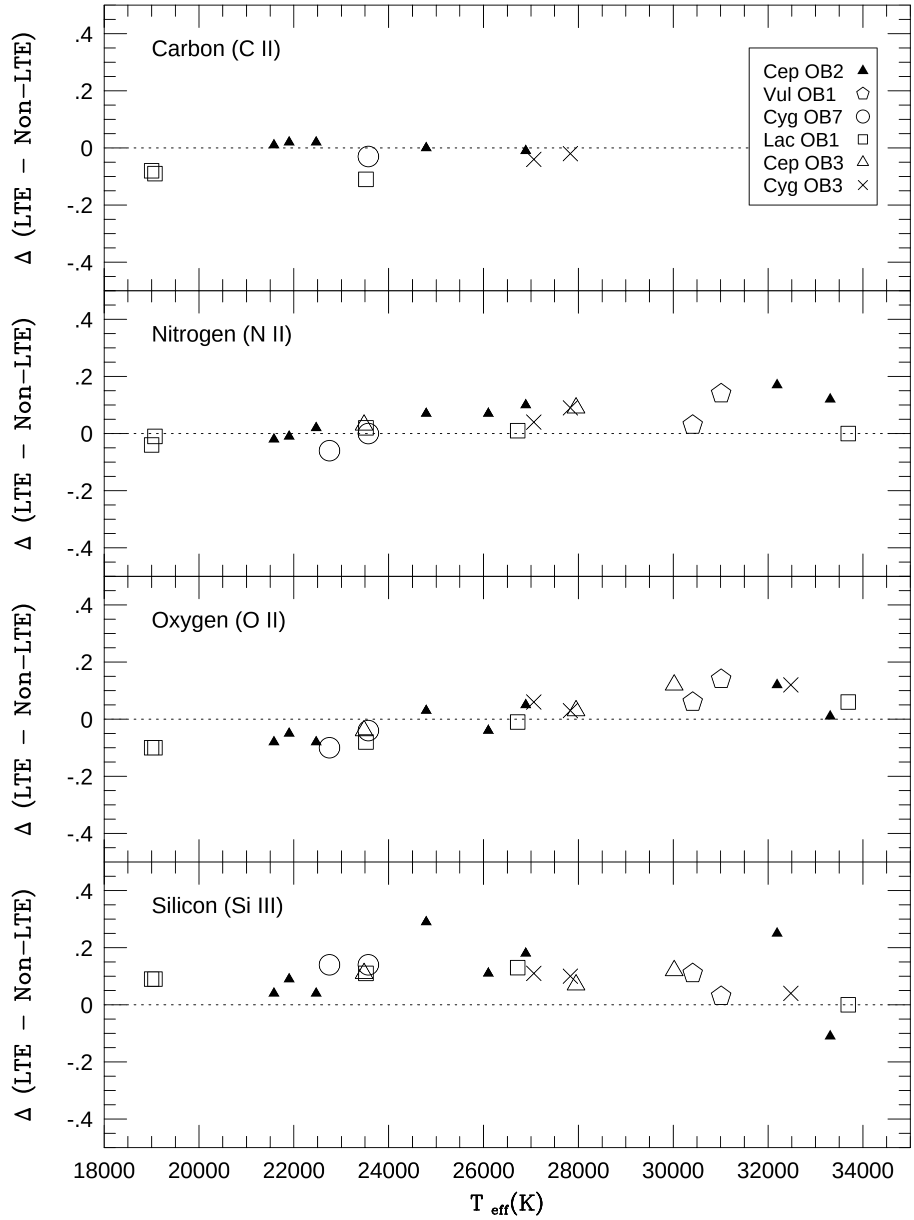

Figure 4.7: LTE - non-LTE differences for the studied stars (open symbols) as a function of T_{eff}, including results from Paper I (solid triangles. The non-LTE corrections generally show a small positive correlation with T_{eff}, especially for nitrogen and oxygen. The results for silicon show non-LTE corrections of about +0.15 dex. Carbon presents corrections from 0 to -0.15dex and nitrogen, ±0.07dex. The correction for oxygen varies from -0.1 dex at $T_{eff} \sim$ 20000K to +0.15 dex at $T_{eff} \sim$ 30000K.

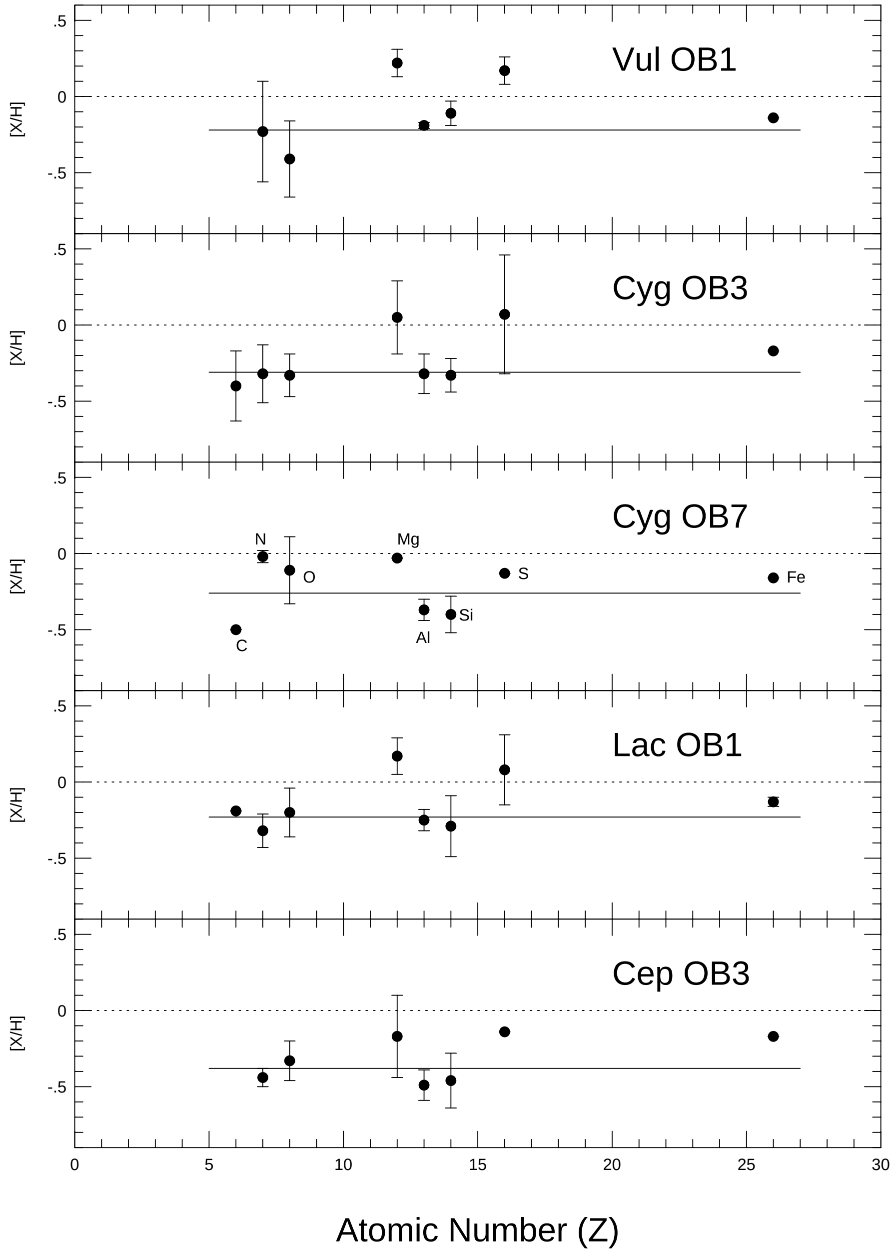

Figure 4.8: Summary of mean association abundances, in [X/H] notation, versus atomic number. Plotted values are non-LTE abundances for C, N, O, and Si, and LTE abundances for Mg, Al, S, and Fe. The dashed horizontal lines in each panel show the solar abundance, i.e. [X/H]=0.0, while the solid horizontal lines represent the association means for C, N, O, Al, Si, and Fe. The general subsolar association abundances are emphasized in the plot, as well as the fact that no drastically non-solar abundance ratios are apparent. Note that the Mg and S abundances are consistently larger than those of the other elements: the significance, or lack thereof, of these differences are discussed in the text.

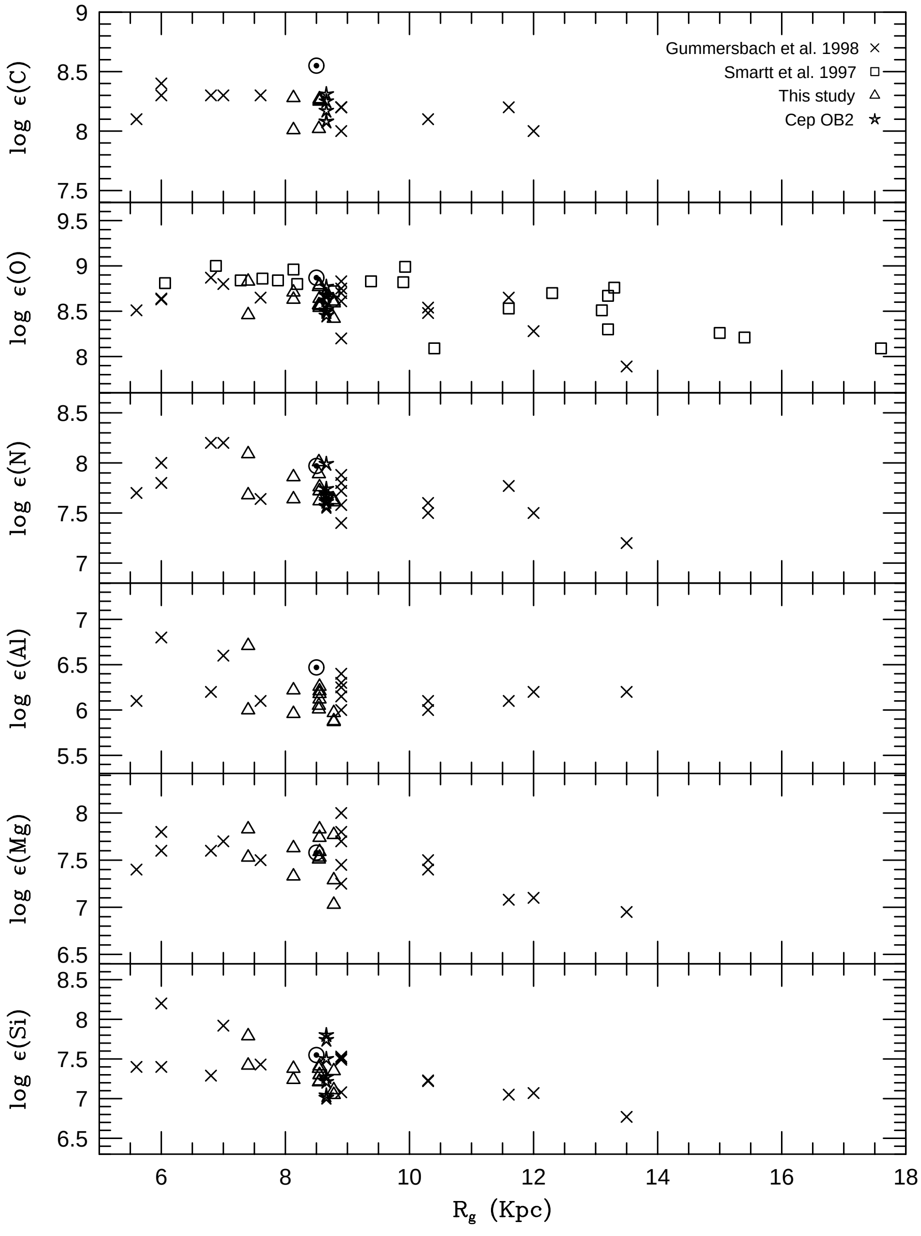

Figure 4.9: A comparison between derived abundances for OB associations with abundances derived for B stars in open clusters and OB associations of the Galactic disk listed in the literature (× – Gummersbach *et al.* 1998, □ – Smartt & Rolleston 1997). The adopted distances from the Sun are listed in Table 4.1.

Capítulo 5

Abundâncias Químicas de Estrelas B com Altas Velocidades Rotacionais Projetadas [1]

Resumo: Abundâncias de C, N, O, Al, Mg, Si e S foram obtidas para uma amostra de 12 estrelas B com altas velocidades rotacionais projetadas ($v \sin i$ > 60kms^{-1}), pertencentes às associações de Cep OB2, Cyg OB3 e Cyg OB7. As abundâncias foram obtidas através da síntese espectral, usando cálculos em ETL e não-ETL. As abundâncias médias são ligeiramente sub-solares em 0.1−0.3 dex. No caso do oxigênio, mesmo considerando os recentes - e mais baixos - valores de abundâncias solares, as abundâncias das estrelas B são menores que as solares. As abundâncias obtidas para 9 estrelas de Cep OB2 dessa amostra podem ser combinadas com resultados anteriores obtidos para estrelas dessa associação com baixo $v \sin i$, produzindo o mais completo estudo de abundâncias químicas de Cep OB2 até o momento. Dois sub-grupos com idades distintas são identificados em Cep OB2, com uma distribuição de abundâncias bastante uniforme. Duas estrelas do sub-grupo mais velho, com estágios evolutivos mais avançados, apresentam uma alta razão N/O, além de estarem entre as estrelas com maiores massas e maiores $v \sin i$ da associação. Estas características estão de acordo com as modificações nas abundâncias superficiais induzidas pela rotação, previstas por modelos de estrelas massivas com altos $v \sin i$.

---

[1] **Daflon, S., Cunha, K., Butler, K. & Smith, V. V. (2001) The Astrophysical Journal, 563, 325-333 (Paper III)**

5.1 Introduction

The determination of the chemical abundance distributions in stars often requires the identification and isolation of a suitable set of absorption lines whose individual line strengths, or equivalent widths, are well-defined and can be measured. These equivalent widths become the primary datasets upon which the abundance analyses of the stars are based. For early-type stars that have small values of $v \sin i$, defining a set of spectral lines whose equivalent widths can be measured accurately is usually a straightforward task, because their spectra are relatively free of blending lines. As rotational velocity increases and spectral line-widths broaden, however, a point is reached beyond which it becomes impossible to find adequate sets of unblended spectral lines on which to anchor a detailed abundance analysis. The distribution of projected rotational velocity, $v \sin i$, as a function of spectral type increases from F-G stars, where $v \sin i$ almost vanishes, to OB stars that typically rotate rapidly. Wolff *et al.* (1982) studied the distribution of rotational velocities in early-type stars and observed that, among hot stars, early B-type stars show the lowest rotational velocities; $< v \sin i >= 110 \mathrm{kms}^{-1}$. However, even at the low end, these values of $v \sin i$ are high enough to blend the absorption lines to such an extent that prevents line identification and individual equivalent-width measurements. In this case, spectrum synthesis can be used to model the blended line profiles and extract elemental abundances.

Our previous studies of chemical abundances in OB stars - Daflon, Cunha & Becker (1999) and Daflon *et al.* (2001), hereafter Papers I and II, respectively - analyzed only those observed targets with sharp lines ($v \sin i < 60 \mathrm{kms}^{-1}$) as the method adopted to derive elemental abundances was based on equivalent-width measurements. Due to this restriction, the final list of OB stars analyzed in these previous papers consisted of about 25% of the total number of observed targets for this project. However, many of the observed stars with relatively high $v \sin i$ still have conspicuous features in their spectra that can be compared with broadened synthetic line-profiles and thus provide information about their chemical compositions. This paper focuses on a subset of the observed sample OB stars having $v \sin i$ between roughly 60 and 140 kms^{-1} with the intent being to derive stellar parameters and chemical abundances. Four stars are included from Paper I (HD 205948, HD 207951, HD 209339 and HD 239729 of the Cep OB2 association) and 3 stars from Paper II (HD 227696 and HD 228199 of Cyg OB3 and HD 202347 of Cyg OB7) for which stellar parameters were already derived but an abundance analysis was not done. In addition to these 7 stars, 5 other stars belonging to the Cep OB2 association are analyzed here. The addition of this set of rapidly rotating stars to those with lower projected rotational velocities analyzed already, enlarges our sample of observations for the current study of chemical abundances of OB stars in the Galactic disk as much as possible. In particular, this completes the sample for the study of the abundance distribution and investigation of possible inhomogeneities in the chemical composition of the gas that formed the main-sequence members (with spectral types between O9 and B3 and for which an abundance analysis can be done) of the Cep OB2 association.

In addition to their usefulness as probes of the general abundance distributions found in the Galactic disk and in OB associations, rapidly rotating B-stars can have their surface abundances altered by rotationally induced mixing. In a recent study, Heger & Langer (2000) have presented surface abundance predictions for elements sensitive to mixing, such as boron, carbon, or nitrogen, in a set of stellar models of differing mass, rotational velocity, and age. The members of a typical OB association are all formed in the same place, but at slightly different times (with age differences of $\sim 10^5$–10^7 yrs), with differing masses and rotation velocities. Mass, age, and rotation are all variables that play a role in the degree of stellar mixing expected. In this paper certain elements sensitive to mixing, such as, C, N, and O, are analyzed in Cep OB2 and the results can be used to test the rotating stellar models.

5.2 Observations and Stellar Parameters

The observations and data reduction are described in Papers I and II, however, a brief summary of the instruments follows. The data consist of spectra with a resolution of R$\sim$ 60,000, high signal-to-noise (S/N $\geq$150), covering the spectral range from 4225–5285Å and obtained with the 2.1m Otto M. Struve telescope plus Cassegrain Sandiford echelle spectrometer at the McDonald Observatory of the University of Texas. Additional spectra were obtained with the 2.7m Harlan J. Smith telescope, also at McDonald Observatory, and Coudé spectrometer having R=12,000 and centered on the region of $H\gamma$ (4340Å).

In Paper I, an effective temperature scale for OB stars was derived using the reddening-free Q parameter from UBV photometry. The $T_{\rm eff}$-Q calibration, when combined with an analysis of the Hγ line-profiles, has been found to be adequate for the derivation of the fundamental stellar parameters, $T_{\rm eff}$ and log g, needed to conduct an abundance analysis for the main-sequence OB stars. The adopted stellar parameters for the studied stars are collected in Table 5.1. Most of these are from Papers I and II and in this study we add the determinations for 5 rapidly rotating stellar members of the Cep OB2 association: HD235618, HD239681, HD239710, HD239745 and HD239748. All of the additional stellar parameters presented here were derived following the same approach adopted in Paper I. (See that paper for a more detailed discussion of the method). LTE plane-parallel model atmospheres were then calculated with the ATLAS9 code (Kurucz, 1992) for solar metallicity and a constant microturbulence velocity of 2kms^{-1}. These model atmospheres were adopted for both the LTE and non-LTE abundance analyses.

Table 5.1: Atmospheric Parameters

Star	Association	$T_{\rm eff}$(K)	$\log g$
HD 202347	Cyg OB7	23280 ^{b}	4.13 ^{b}
HD 205948	Cep OB2	24350 ^{a}	4.25 ^{a}
HD 207951	Cep OB2	20650 ^{a}	3.88 ^{a}
HD 209339	Cep OB2	31250 ^{a}	4.28 ^{a}
HD 227696	Cyg OB3	29100 ^{b}	4.45 ^{b}
HD 228199	Cyg OB3	29870 ^{b}	4.45 ^{b}
HD 235618	Cep OB2	27180	3.75
HD 239681	Cep OB2	26830	3.70
HD 239710	Cep OB2	21900	4.50
HD 239729	Cep OB2	28450 ^{a}	4.22 ^{a}
HD 239745	Cep OB2	27340	4.45
HD 239748	Cep OB2	27480	4.42

a: Paper I; b: Paper II.

5.3 Analysis

As a matter of consistency with our previous studies, we tried as much as possible to use the same sets of transitions of C, N, O, Si, Mg and Al selected in Papers I and II. However, because of the high rotational velocity of the target stars this was not always possible. In particular, the weak lines of C II, S III and Fe III become too shallow in stars with relatively high $v \sin i$. As a result of this, sulfur and iron abundances were not derived in this study. Because of the lack of C II lines, an attempt was made to derive carbon abundances using C III lines, as we are interested in complementing the sample for carbon as much as possible. The only possibility was to use the 3 strong C III lines in the region centered on 4650Å, which were not used in our previous papers because these strong lines are very close to a set of O II transitions and are generally blended, even for stars that appear to rotate slowly. The selected spectral regions for this abundance study are gathered in Table 5.2 where, in the first column, we indicate the species that is dominant and whose abundance was adjusted in that particular region. Spectral lines used to construct linelists for the syntheses were taken from the Kurucz website (URL cfaku5.harvard.edu/) and the line gf-values were taken from the Opacity Project (OP), but also from Kurucz, when the atomic data needed was not available in the OP database.

5.3.1 LTE Abundances

LTE abundances of carbon, nitrogen, oxygen, magnesium, aluminum, and silicon were determined by fitting synthetic spectra calculated with the program LINFOR (originally developed by H. Holweger, M. Steffen, & W. Steenbock) to the observed spectral regions containing the selected individual transitions. The synthetic profiles were then broadened for $v \sin i$ and limb darkening using a linear limb darkening coefficient interpolated from the values from table 2 in Wade & Rucinski (1985). In addition, the synthetic spectra were broadened by the instrumental profile, while the macroturbulent velocity was set to zero (as suggested by Ebbets 1979 for main-sequence B-stars). As done in the abundance analyses of the sample of stars with low $v \sin i$, the O II transitions were used to derive microturbulent velocities as these lines are the most numerous in the sample and, most importantly, span a range in line-strength adequate to constrain the microturbulence. As a first step in this analysis, the

O II line profiles were calculated for various values of microturbulence. The $v \sin i$s in each case were allowed to vary and the best fit oxygen abundance for each profile was determined by means of a χ^2-minimization. Figure 5.1 illustrates the type of diagram constructed in order to estimate the microturbulent velocity: this figure displays the behavior of the O II lines for the sample star HD239745, where best fit oxygen abundances (corresponding to seven spectral regions containing O II lines) are calculated for microturbulent velocities ranging from 2 to 10 kms^{-1}i.Such a diagram is the equivalent of the usual 'abundance versus equivalent width' plot, where a solution is found when zero slope is obtained. By definition, the solution in Figure 5.1 will be the microturbulence value that yields approximately the same abundance for strong and weak lines: for this star a region of coincidence is found around a microturbulent velocity of 8.0 kms^{-1}.

Once a value for the microturbulence was established for each star, LTE synthetic spectra were calculated for all of the spectral regions listed in Table 5.2. Here again the $v \sin i$s were left as free parameters and adjusted in each spectral synthesis and an individual projected rotational velocity was derived from each fit. The derived values for $v \sin i$ for the individual fits did not, as expected, differ significantly and the average values are presented in the third column of Table 5.3. The average LTE abundances for the studied elements, their standard deviations and the number [n] of fitted lines corresponding to each species are also found in Table 5.3. We stress that the carbon results in this table are for C III, while those in Papers I and II are from C II. For one star in the sample (the Cep OB2 member HD239745), however, it was possible to compare the C II and C III abundances as, for this star, the C II lines at λ5143.50Å, 5145.17Å, and 5151.08Å were strong enough to be fitted: a carbon abundance of 8.22 provides a good fit for the 3 C II lines, as well as the C III line whose abundance is listed in Table 5.3. Such an agreement between C II and C III abundances is not always achieved. In the literature, a few studies have pointed out that the C III lines at 4650Å usually provide abundances higher than the C II lines (e.g. Smartt et al. 1996, Rolleston et al. 1993). A discrepancy is also found from inspection of the results given in Gies & Lambert (1992). In order to investigate systematic differences between C II and C III abundances, we decided to pursue an analysis of the C III lines in the stars analyzed previously in Papers I and II and for which we published C II abundances. The results of the comparison will be discussed in Section 5.4.1.

Table 5.2: Linelists

Wavelength interval	λ(Å)	Species	χ(eV)	log(gf)
4234-4244	4236.93	N II	23.24	0.39
N II	4237.05	N II	23.24	0.56
	4237.94	O II	28.83	-0.99
	4239.48	O III	33.15	-2.04
	4241.75	N II	23.24	0.22
	4241.79	N II	23.25	0.72
	4242.50	N II	23.25	-0.34
4412-4419	4413.11	O II	28.94	-0.73
O II	4414.88	O II	23.44	0.22
	4416.97	O II	23.42	-0.04
	4417.10	N II	23.42	-0.34
	4418.84	S III	18.24	-1.92
4448-4455	4448.34	O II	28.36	0.07
O II	4452.38	O II	23.44	-0.73
4476-4484	4479.88	Al III	20.78	0.90
Mg II, Al III	4479.97	Al III	20.78	1.02
	4481.13	Mg II	8.86	0.74
	4481.15	Mg II	8.86	-0.56
	4481.33	Mg II	8.86	0.59
4550-4554	4552.41	S II	15.07	-0.10
Si III	4552.62	Si III	19.02	0.28
4565-4570	4567.84	Si III	19.02	0.06
Si III	4569.06	Ne II	34.93	0.14
	4569.26	O III	46.00	0.07
4572-4576	4574.42	Ne II	34.84	-0.16
Si III	4574.76	Si III	19.02	-0.42
4589-4593	4591.01	O II	25.66	0.32
O II				
4605-4614	4607.15	N II	18.46	-0.48
N II, O II	4608.08	N II	23.48	-0.25
	4609.37	O II	29.07	0.71

Table 5.2: Linelists *(continued)*

Wavelength interval	λ(Å)	Species	χ(eV)	log(gf)
4605-4614	4610.17	O II	29.06	-0.17
N II, O II	4610.61	O III	45.94	0.02
	4613.10	O II	29.07	-0.59
4628-4632	4629.97	C II	24.79	0.50
N II	4630.54	N II	18.48	0.09
	4631.27	Si IV	36.42	0.85
	4631.27	Si IV	36.42	-0.58
	4631.27	Si IV	36.42	0.96
4637-4545	4638.28	Si III	28.07	-0.44
N II, O II	4638.86	O II	22.97	-0.35
	4640.64	N III	30.46	0.14
	4641.83	O II	22.98	0.05
	4641.85	N III	30.46	-0.81
	4643.09	N II	18.48	-0.39
4647-4651	4647.42	C III	29.54	0.06
C III, O II	4647.59	O II	29.06	-0.64
	4649.14	O II	23.00	0.33
	4650.25	C III	29.54	-0.15
	4650.85	O II	23.00	-0.35
	4651.02	C III	38.22	-0.47
	4651.47	C III	29.54	-0.63
4658-4664	4659.06	C III	38.22	-0.69
O II	4661.64	O II	22.98	-0.25
	4663.64	C III	38.22	-0.57
	4665.86	C III	38.22	0.01
4904-4908	4904.78	N III	39.40	-0.26
O II	4906.82	O II	26.30	-0.05
4939-4945	4941.10	O II	26.55	0.07
O II	4943.00	O II	26.56	0.33
5003-5012	5005.15	N II	20.67	0.61
N II	5007.33	N II	20.94	0.17
	5010.62	N II	18.47	-0.61

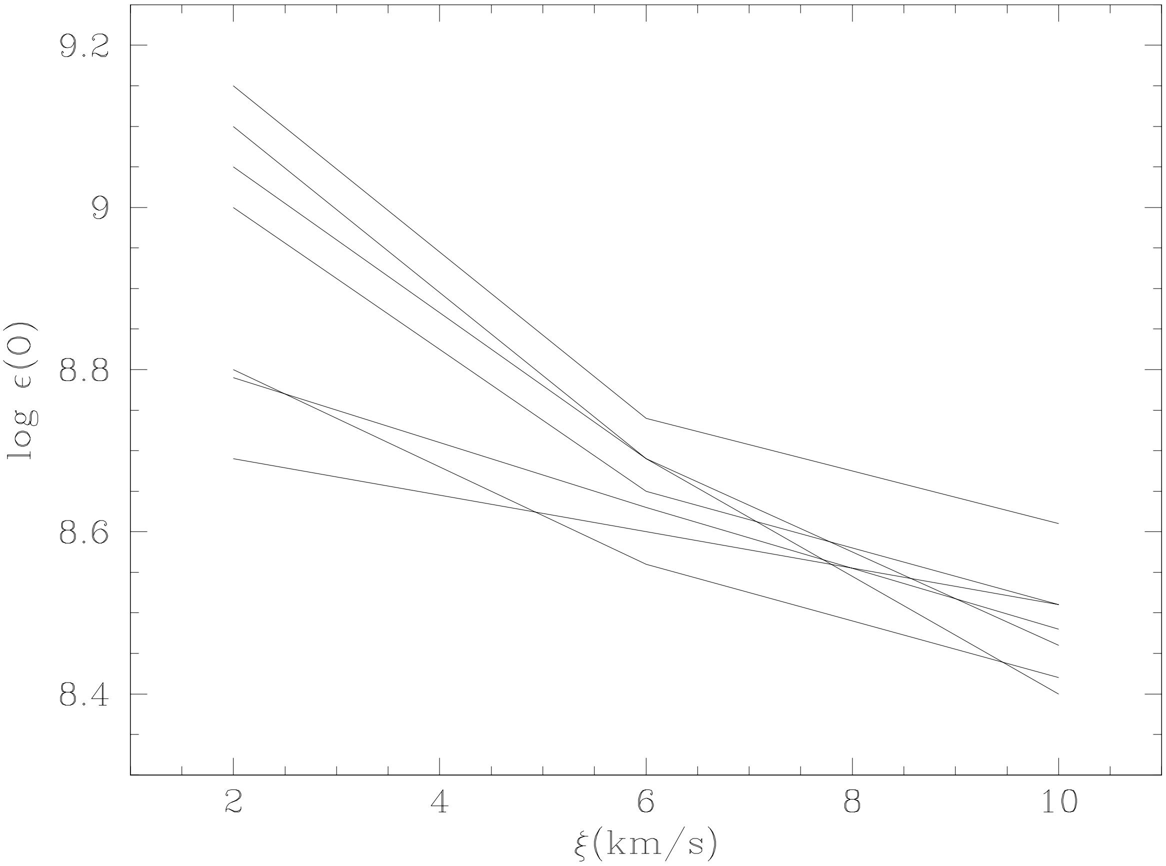

Figure 5.1: Variation of LTE oxygen abundance with the microturbulence velocity for the sample star HD 239745. The adopted solution is $\xi = 8\mathrm{kms}^{-1}$ that corresponds to $\log \epsilon(O) = 8.57 \pm 0.05$.

The LTE abundances obtained follow trends found previously, namely that the elemental abundances in OB stars are, in general, sub-solar. However, a more detailed discussion must await results that take into account non-LTE effects. Non-LTE calculations for C, N, O and Si have already been presented in Papers I and II and the effects has proven to be small for the effective temperature and surface gravity range encompassed by the sample stars. Non-LTE synthetic profiles were calculated for each observed profile, and, in this study, new non-LTE calculations were added for two additional elements: Mg and Al.

Table 5.3: LTE Abundances

Star	ξ (kms^{-1})	$v \sin i$ (kms^{-1})	$\log \epsilon$(C)	$\log \epsilon$(N)	$\log \epsilon$(O)	$\log \epsilon$(Mg)	$\log \epsilon$(Al)	$\log \epsilon$(Si)
HD 202347	7.5	121±7	-	7.67±0.10 [3]	8.62±0.11 [5]	7.15 [1]	6.30 [1]	7.28±0.04 [3]
HD 205948	7	146±12	8.27 [1]	7.53±0.09 [2]	8.47±0.10 [4]	6.98 [1]	6.20 [1]	7.13±0.13 [3]
HD 207951	6.5	84±2	8.53 [1]	7.76±0.03 [3]	8.75±0.09 [5]	-	-	7.18±0.06 [3]
HD 209339	7	101±9	-	7.47±0.13 [3]	8.55±0.14 [5]	7.32 [1]	6.10 [1]	7.63±0.13 [3]
HD 227696	12	120±5	-	7.58±0.09 [2]	8.62±0.11 [5]	-	-	7.61±0.14 [3]
HD 228199	8	105±5	8.44 [1]	7.64±0.09 [3]	8.77±0.14 [5]	7.54 [1]	6.10 [1]	7.62±0.01 [3]
HD 235618	12	101±2	8.60 [1]	7.90 [1]	8.67±0.11 [4]	7.33 [1]	6.00 [1]	7.95±0.14 [2]
HD 239681	10	140±10	8.08 [1]	7.73±0.15 [3]	8.61±0.09 [5]	7.70 [1]	6.40 [1]	7.83±0.18 [2]
HD 239710	8	63±6	8.40 [1]	7.62±0.07 [3]	8.63±0.09 [5]	7.44 [1]	5.95 [1]	7.88±0.20 [3]
HD 239729	6	100±7	-	7.44±0.11 [3]	8.49±0.20 [7]	7.19 [1]	5.90 [1]	7.07±0.02 [3]
HD 239745	8	61±3	8.22 [1]	7.58±0.07 [3]	8.57±0.05 [7]	7.20 [1]	5.80 [1]	7.16±0.12 [3]
HD 239748	6	66±3	8.25 [1]	7.68±0.09 [4]	8.63±0.09 [7]	7.35 [1]	5.97 [1]	7.31±0.06 [3]

Note: [n] indicates the number of fitted lines correspondig to each species.

5.3.2 Non-LTE abundances

Non-LTE synthetic profiles were calculated using model atoms by Eber (1987 – C III), Becker & Butler (1989 – N II), Becker & Butler (1988 – O II), Dufton *et al.* (1986 – Al III), Przybilla *et al.* (2001– Mg II) and Becker & Butler (1990 – Si III). The adopted model atoms contain most of the energy levels belonging to the main ionization stages with the addition of the lower levels of the adjacent stages with relevant populations in this temperature range. The completeness of the adopted model atoms is essential to guarantee an accurate ionization balance and the correct calculation of the level populations. The models include a number of permitted bound-bound transitions explicitly calculated, as well as transitions from levels fixed in LTE.

The level populations were computed with the program DETAIL, assuming LS-coupling to find the solution for the equations of statistical equilibrium and transfer; the line profiles were computed with Voigt profile functions using the program SURFACE. As a first step here, non-LTE synthetic profiles were fitted to the observed O II lines in order to determine the microturbulent velocity in a similar manner as done for the LTE analysis and discussed in Section 3.1. The microturbulence derived from O II lines for each star was then adopted to calculate the synthetic profiles for the species of the other studied elements.

The left panels in Figure 5.2 show synthetic spectra calculated for the region between λ4412 and 4419Å for HD239748. In this spectral region, the main contributions to the observed profiles correspond to the O II lines at λ4414Å and 4416Å. In the top left panel five synthetic profiles are shown for different oxygen abundances of $\log \epsilon(\mathrm{O}) = 8.22$, 8.37, 8.42, 8.47 and 8.62 and for $v \sin i$ of 65 km^{-1} (as indicated from the χ^2-minimization shown in the bottom right panel.) The best fit oxygen abundance is represented by the synthetic profile with a solid line. It was derived via a χ^2-minimization which is shown in the top right panel of this same figure. The bottom panel illustrates the sensitivity of the profiles to the variation of the projected rotational velocities, $v \sin i$, ranging, in this example, between 50 and 80 kms^{-1}.

Similarly to what was done in the LTE analysis, a best fit non-LTE abundance and $v \sin i$ value were obtained for each individually synthesized profile and Table 5.4 lists the average abundances and $v \sin i$ s for each target star. These are the final abundance results for C, N, O, Mg, Al and Si obtained in this study. The derived $v \sin i$ values had a small

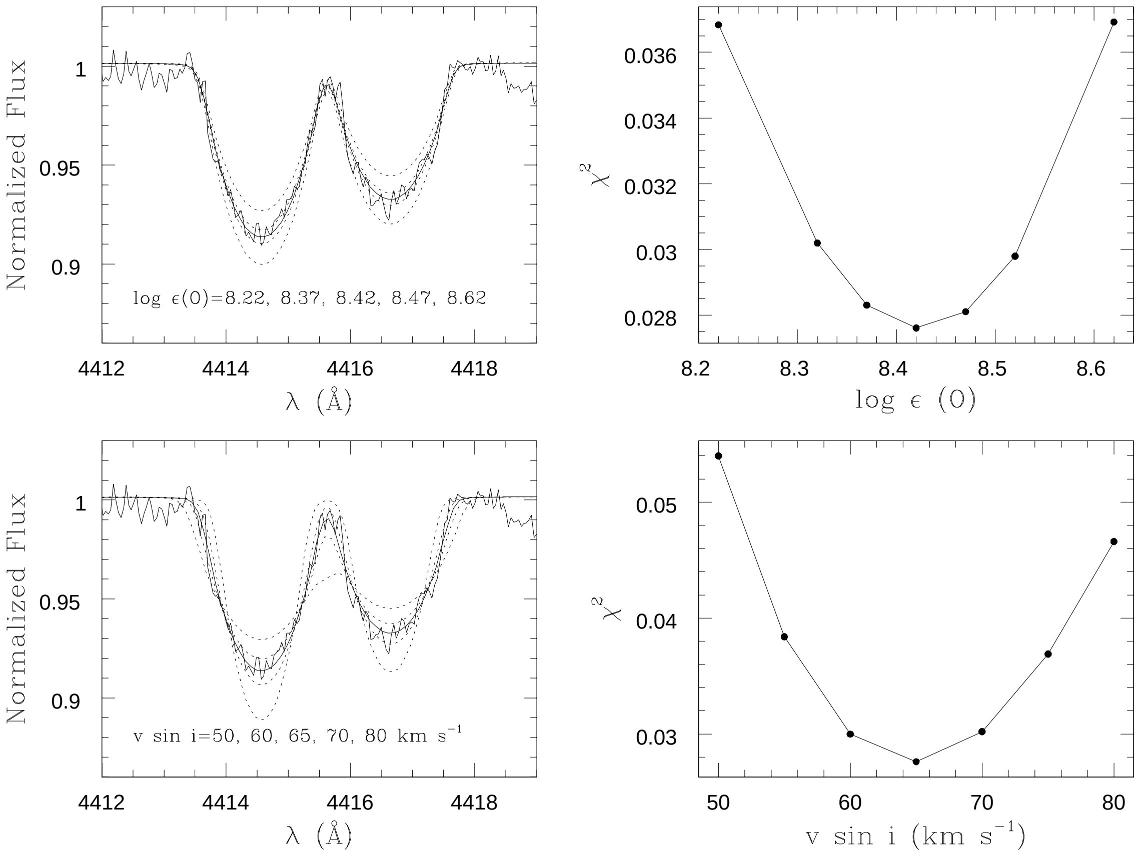

Figure 5.2: Comparison between observed and non-LTE synthetic profiles for one of the spectral regions containing O II lines. The observed spectrum is for the target star HD239748 and the synthetic profiles were calculated for different sets of parameters. *Top*: on the left panel we show synthetic profiles calculated for five values of oxygen abundances (indicated in the figure). The best fit oxygen abundance is derived for $\log\epsilon(O)$=8.42 (represented by the solid line). In the right panel we present the variation of χ^2 as a function of oxygen abundance. *Bottom*: same for different values of $v \sin i$ varying from 50 to 80 kms^{-1}.

variation from fit-to-fit with standard deviations typically smaller than 10kms^{-1}. Moreover, these $v \sin i$s are very consistent with the $v \sin i$s derived from the LTE syntheses. In order to investigate possible spurious trends due to systematic errors in the adopted $T_{\rm eff}$ scale, the non-LTE abundances obtained are plotted as a function of the effective temperatures in Figure 5.3: no major trends are found. The derived microturbulences in non-LTE are in all cases smaller than those derived in LTE, with the average being 2 km s^{-1} less. Since the microturbulence is an adhoc parameter needed in order to obtain an agreement between the abundances of strong and weak lines, it might be expected that a more realistic non-LTE treatment would reduce the need for microturbulence. This seems to be the case, but just slightly, as the derived microturbulences are still significant. However, this abundance analysis is based upon one dimensional plane-parallel model atmospheres in LTE and assume a constant microturbulent velocity. These models are still far from being able to represent the atmospheres of early-type stars perfectly and the microturbulence remains a required parameter in these calculations.

Table 5.4: Non-LTE Abundances

Star	ξ (kms^{-1})	$v \sin i$ (kms^{-1})	$\log\epsilon$(C)	$\log\epsilon$(N)	$\log\epsilon$(O)	$\log\epsilon$(Mg)	$\log\epsilon$(Al)	$\log\epsilon$(Si)
HD 202347	6	119±6	-	7.54±0.04	8.54±0.12	7.35	6.28	7.13±0.06
HD 205948	5	144±11	8.35	7.35±0.05	8.29±0.03	7.05	6.18	6.95±0.13
HD 207951	5	87±2	8.47	7.65±0.05	8.72±0.10	-	-	7.05±0.07
HD 209339	3.5	98±9	-	7.34±0.03	8.36±0.12	7.38	6.07	7.44±0.03
HD 227696	10	120±5	-	7.49±0.06	8.60±0.16	-	-	7.41±0.16
HD 228199	5	104±6	8.55	7.56±0.16	8.67±0.16	7.78	6.13	7.57±0.03
HD 235618	9	100±3	8.54	7.81	8.47±0.15	7.55	5.94	7.73±0.02
HD 239681	9	142±11	8.10	7.70±0.16	8.48±0.17	7.82	6.48	7.55±0.03
HD 239710	8	64±5	8.50	7.57±0.08	8.60±0.13	7.63	5.96	7.71±0.05
HD 239729	5	99±8	-	7.33±0.05	8.28±0.10	7.26	5.86	6.86±0.07
HD 239745	6	61±2	8.38	7.51±0.13	8.46±0.09	7.25	5.77	7.08±0.19
HD 239748	5	68±4	8.27	7.55±0.07	8.54±0.08	7.42	5.95	7.13±0.13

5.3.3 Uncertainties

The uncertainties in the adopted effective temperatures and surface gravities have been discussed in some detail in Paper I, with estimated errors of 4% in $T_{\rm eff}$ and of 0.1 dex in $\log g$. The uncertainty in the microturbulent velocity is assigned to be about ±1.5kms^{-1}. The final abundances are the non-LTE results and it is the non-LTE calculations that were used

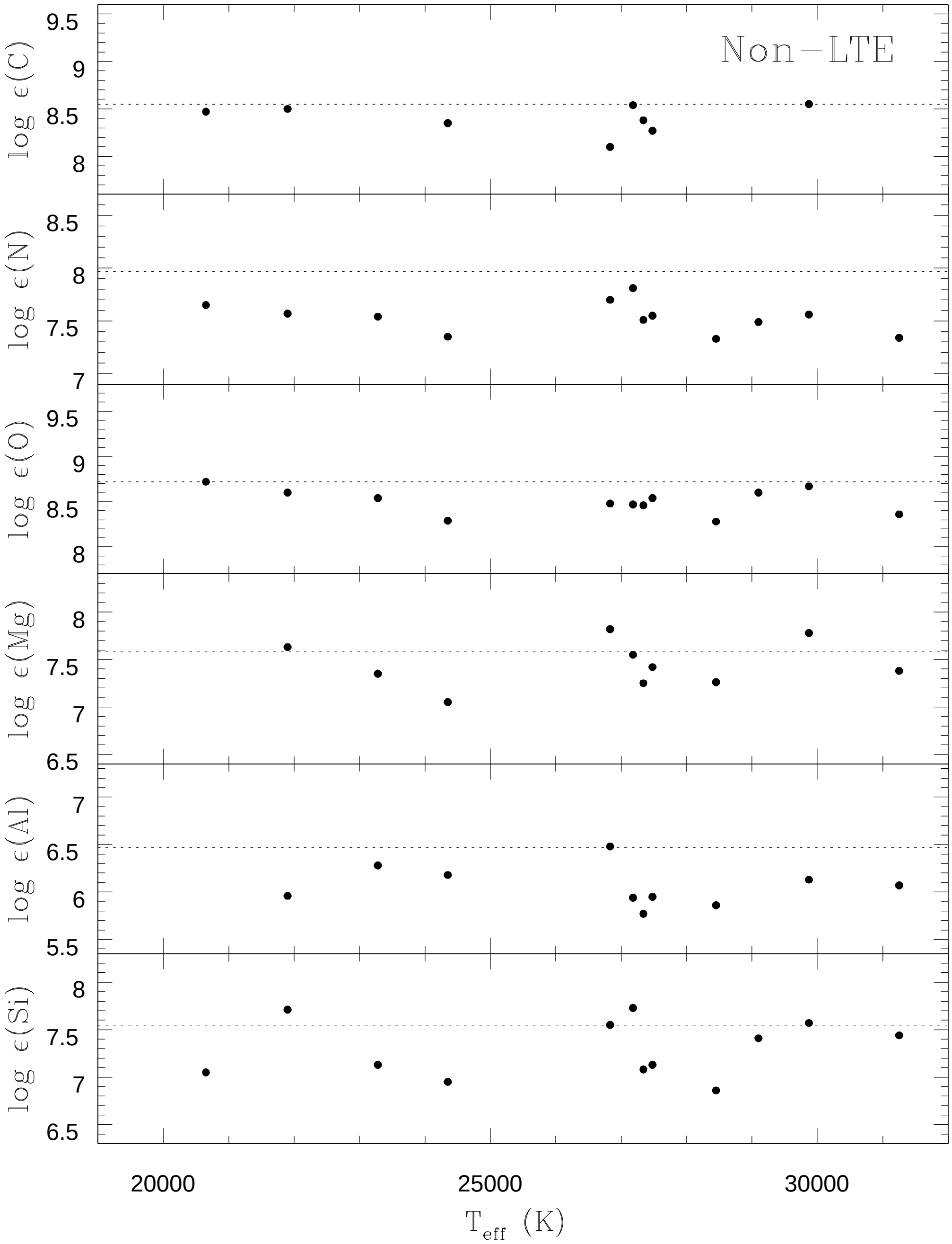

Figure 5.3: Non-LTE abundances as a function of adopted effective temperatures. The derived abundances show almost no trend with effective temperature and are, in general, sub-solar. There are some stars that have solar, and in some cases, above solar abundances of C, O, Mg, Al, and Si. The reference solar abundances (dotted lines) are from Grevesse, Noels & Sauval (1996) for all elements except for oxygen for which we adopt an average abundance value between the recent studies by Allende Prieto et al. (2001) and Holweger (2001).

to investigate the final abundance uncertainties. Non-LTE synthetic profiles were calculated for new model atmospheres generated by adding the uncertainties to the adopted parameters for two stars in the sample. The elemental abundances derived from profile fitting are also subject to uncertainties in the continuum location as well as the choice of the projected rotational velocity. Based on the the variation of χ^2 as a function of $v \sin i$, as shown on the bottom panel of Figure 5.3, an error of 7% is adopted due to $v \sin i$ and 5% due to continuum location. We note that variations in the linear limb darkening coefficient have negligible effects on both the derived values of $v \sin i$ and abundances. The resulting abundance uncertainties, as well as the total expected error (δ_t), are listed in Table 5.5. The total errors are $\sim 0.10 - 0.25$ dex, except for C III, which has a slightly larger error of ~0.3 dex that is dominated by the uncertainty in the effective temperature. The abundances of silicon and magnesium, based on strong lines, are very sensitive to the choice of the microturbulent velocity.

Previous abundances presented in Papers I and II were derived from equivalent width measurements. In order to investigate any systematic differences between abundances based on syntheses compared to those based on equivalent widths, all stars analyzed in both Papers I and II were re-analyzed using the synthesis techniques presented here. No significant offsets in the abundances were found, with differences typically less than 0.05 dex: both equivalent width and synthesis based abundances can be compared directly.

5.4 Discussion

5.4.1 The General Abundance Trends

It is usual to compare stellar abundance results with the abundances derived from the solar photosphere and meteorites. The Sun has been a reference point for obvious reasons. In this respect, several abundance studies of OB stars in the Galactic disk have noted the subsolar abundance values obtained for these early-type stars. With regard to this comparison, the non-LTE abundance results here indicate the same general pattern. For nitrogen and oxygen the derived target abundances are, in general, below the solar value. Some comments should be made concerning the accepted solar oxygen abundance. Two recent studies derive significantly lower solar O abundances than generally accepted earlier values, with Allende

Table 5.5: Abundance Uncertainties.

Ion	correction	HD 239710	HD 239745
C III	$\delta(T_{eff})$	-0.25	-0.28
	$\delta(\log g)$	+0.07	+0.08
	$\delta(\xi)$	0.00	-0.06
	$\delta(v \sin i)$	+0.03	+0.03
	δ(continuum)	+0.02	+0.04
	δ_t	+0.26	+0.30
N II	$\delta(T_{eff})$	-0.10	+0.05
	$\delta(\log g)$	+0.03	-0.01
	$\delta(\xi)$	-0.05	-0.01
	$\delta(v \sin i)$	+0.02	+0.01
	δ(continuum)	+0.02	+0.03
	δ_t	+0.12	+0.06
O II	$\delta(T_{eff})$	-0.15	-0.05
	$\delta(\log g)$	+0.03	+0.05
	$\delta(\xi)$	-0.07	-0.10
	$\delta(v \sin i)$	+0.02	+0.01
	δ(continuum)	+0.03	+0.03
	δ_t	+0.17	+0.13
Mg II	$\delta(T_{eff})$	+0.13	+0.12
	$\delta(\log g)$	-0.07	-0.07
	$\delta(\xi)$	-0.16	-0.07
	$\delta(v \sin i)$	+0.05	+0.04
	δ(continuum)	+0.03	+0.05
	δ_t	+0.22	+0.17
Al III	$\delta(T_{eff})$	-0.01	+0.03
	$\delta(\log g)$	+0.02	+0.03
	$\delta(\xi)$	-0.04	-0.04
	$\delta(v \sin i)$	+0.01	+0.01
	δ(continuum)	+0.01	+0.02
	δ_t	+0.05	+0.06
Si III	$\delta(T_{eff})$	-0.17	+0.04
	$\delta(\log g)$	+0.04	-0.02
	$\delta(\xi)$	-0.17	-0.14
	$\delta(v \sin i)$	+0.02	+0.02
	δ(continuum)	+0.02	+0.03
	δ_t	+0.24	+0.15

Prieto, Lambert & Asplund (2001) finding log ϵ(O) = 8.69 and Holweger (2001) deriving 8.74. For the time being, we simply average these recent determinations and use log ϵ (O) =8.72 as the reference solar value. This new O abundance for the Sun also brings it closer to O abundances found in the ISM, with log ϵ (O) = 8.43 being the gas phase abundance as quoted by Sofia & Meyer (2001): gas phase ISM abundances for many elements are expected to be lower than stellar abundances for gas and stars from similar populations as some material in the ISM is in the form of grains. The lower solar abundances also result in better agreement with B stars in general, although these stars still fall below even this lower abundance. Subsolar abundances are also found for Al, with the exception of one star for which a solar Al abundance was derived. For Mg and Si, it is found that four stars are above, or at, the solar abundance level, while the other stars lie below the solar abundance line. Figure 5.4 shows the non-LTE corrections for Mg II represented by Δ(LTE - non-LTE). These are always negative and can be as large as 0.25 dex. On the other hand, the LTE results would represent a very good approximation for aluminum, where the differences between LTE and non-LTE Al III abundances scatter around zero, with absolute values smaller than 0.08 dex (Figure 5.4). The corrections for nitrogen, oxygen and silicon are positive for all studied stars and typically smaller than 0.2 dex.

For carbon the abundance results are close to the solar value but these abundances need further discussion: for the 8 stars for which it was possible to obtain C abundances (derived in all cases solely from C III), 4 of them have carbon abundances that are very close (within 0.05 dex) to the solar value. We note that the derived carbon abundances here are in general closer to the solar abundance than other results in the literature, including our own in Papers I and II. This may be a systematic effect due to the choice of different lines and, in particular, different ionization stages: here strong C III lines and in Papers I and II the weaker C II transitions. Non-LTE C III corrections with respect to LTE abundances are not very large and range between -0.16 to $+0.06$ dex. These corrections, shown in Figure 5.4, are not able to bring the C II and C III into agreement. The non-LTE corrections for C II are typically smaller than 0.1 dex. A comparison of the C III and C II abundances was possible for 8 stars from Papers I and II. The derived results indicate that the LTE C III abundances are higher. For two stars we see very large discrepancies between the C III and C II results (both in LTE and non-LTE) of the order of 0.7–0.9 dex. Clearly further work is

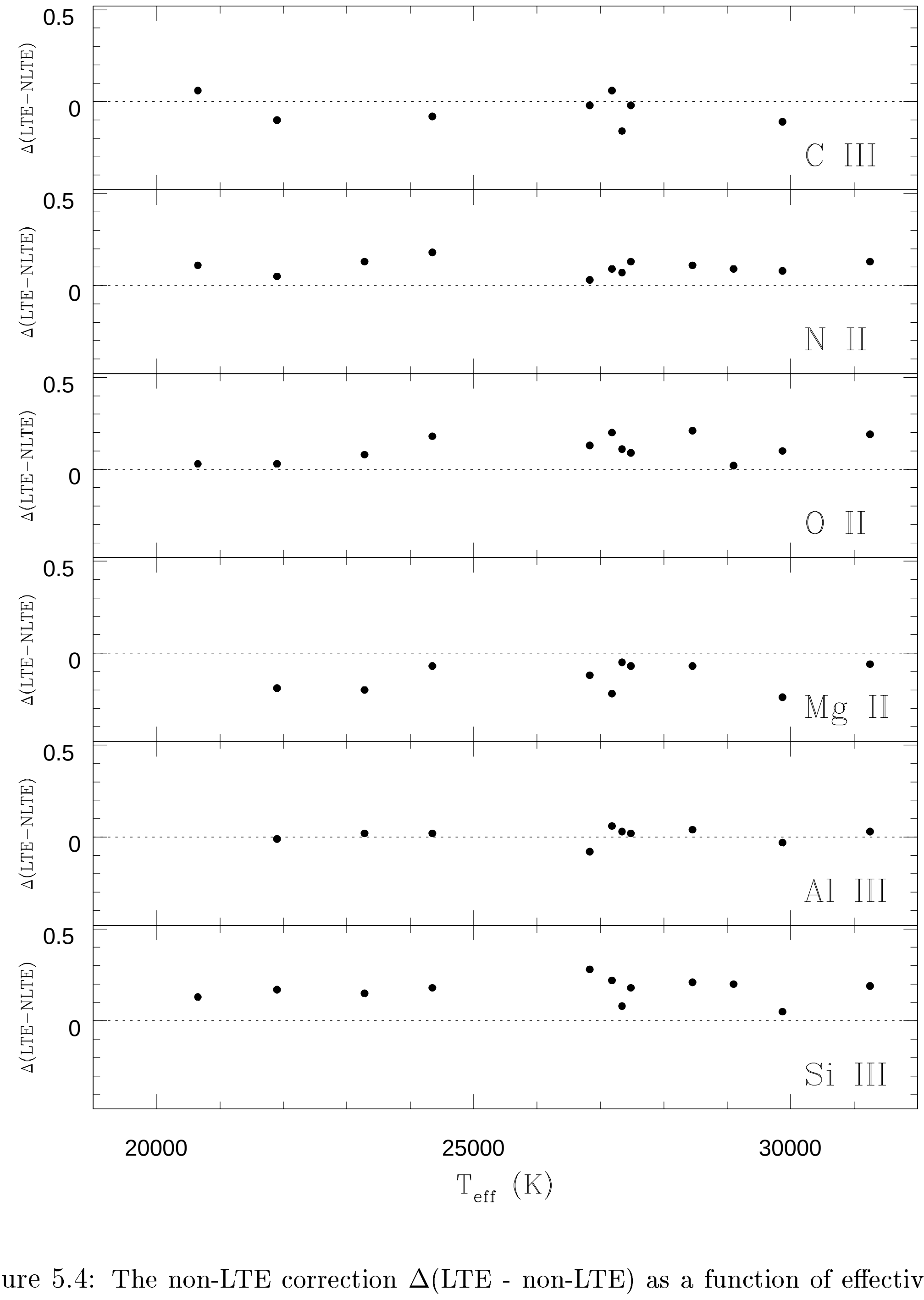

Figure 5.4: The non-LTE correction Δ(LTE - non-LTE) as a function of effective temperature.

needed to clarify the situation and this is in progress.

Taken together, the mean non-LTE abundances for this sample of B stars still point to a general pattern of sub-solar abundances. Average abundances are [C/H]= -0.15 ± 0.15, [N/H]= -0.44 ± 0.15, [O/H]= -0.22 ± 0.14, [Mg/H]= -0.13 ± 0.24, [Al/H]= -0.41 ± 0.21, and [Si/H]= -0.25 ± 0.30. The overall average abundance for all 6 elements, relative to solar, is [m/H]= -0.27 ± 0.13, or about a factor of 2 lower in metallicity than the Sun. Although subsolar, these abundances are still larger than most of the gas phase ISM abundances as summarized recently by Sofia & Meyer (2001). Two elements, N and Si, are found to be below the gas phase ISM abundances. We note, however, that even for N in the Sun this seems to be marginally the case as well, while Si has large abundance uncertainties, as noted earlier.

5.4.2 Cep OB2

Nine stars of this sample belong to the Cep OB2 association, which has already been analyzed chemically in Paper I by means of equivalent-width measurements of spectral lines in sharp lined stars. The mean non-LTE abundances for a sample of 8 low $v \sin i$ stars are $\log \epsilon$ (C)=8.17 ± 0.09, $\log \epsilon$ (N)=7.62 ± 0.10, $\log \epsilon$ (O)=8.61 ± 0.10 and $\log \epsilon$ (Si)=7.21 ± 0.28. This study may now be complemented with the present sample, for which it is found to have mean non-LTE abundances of 8.37 ± 0.15 for carbon, 7.53 ± 0.17 for nitrogen, 8.47 ± 0.14 for oxygen and 7.28 ± 0.33 for silicon. The average abundances derived from both samples agree quite well for N, O and Si, despite the somewhat higher dispersions obtained for the sample of high $v \sin i$ stars. Carbon abundances are somewhat larger in this sample than in Paper I. However, as discussed before, carbon results in this paper are based on C III, instead of C II (as in Paper I): part of this difference may thus reside in systematic effects between C II and C III. If both samples are combined, then the entire set consists of 17 stars belonging to the Cep OB2 association and this represents ~ 30 percent of all the stars formed in the Cep OB2 association with spectral types between O9 and B3. These average abundances are then, relative to solar, [C/H]= -0.26, [N/H]= -0.40, [O/H]= -0.18, and [Si/H]=-0.30: all underabundant by roughly the same amount. The mean abundances confirm the results of Cep OB2 being slightly metal poor relative to the Sun by about 0.2-0.3 dex (the average underabundance of the four elements discussed here is -0.28).

With the addition of the sample of high $v \sin i$ stars, the number of Cep OB2 stars is twice as large as the number presented in Paper I and provides tighter constraints on the chemical distribution in the association. Cep OB2 is believed to be divided into two subgroups of different ages: Cep OB2a, with an estimated age of 7×10^6 years, extending over a large area within the association, and Cep OB2b, with an estimated age of 3×10^6 years, associated with the open cluster Trumpler 37 (Tr 37). It might be assumed that those stars assigned as members of Tr 37 by Garmany & Stencel (1992) belong to the younger subgroup (HD s 205794, 206183, 206267D, 207538, 239724, 205948, 239729, and 239748), while the rest of the sample (HD s 206327, 239742, 239743, 207951, 209339, 235618, 239681, 239710 and 239745) belongs to the older subgroup, Cep OB2a.

This assumption can be tested by using the derived stellar parameters to construct a variation of an HR-diagram for Cep OB2. The surface gravity (as log g) is plotted versus log $T_{\rm eff}$ and this is shown in the top panel of Figure 5.5 for all 17 Cep OB2 members in the sample. The open symbols correspond to members assigned to Tr 37 (and would be expected to be the younger stars of Cep OB2b), while the filled symbols are the other Cep OB2 stars. Stellar model tracks from Schaller et al. (1992) are shown as solid curves for $M= 7M_\odot$, $9M_\odot$, $12M_\odot$, $15M_\odot$, and $20M_\odot$ models (with solar heavy-element abundances), while the dashed line shows the zero-age main sequence (ZAMS). It is clear from this form of an HR-diagram that the Cep OB2 members in this sample do generally segregate into two evolutionary groups, with a set of 10 stars falling very near the ZAMS, and a second, somewhat evolved group of 7 stars. The earlier assumption of assigning age status based on Tr 37 membership is a reasonable one: 7 of 8 stars identified as Tr 37 members fall on the ZAMS. Using the HR-diagram as the discriminator, 7 stars should be put into the older group (Cep OB2a: HD s 206327, 207951, 235618, 239681, 239724, 239742, and 239743), and 10 stars into the younger group (Cep OB2b: HD s 205794, 205948, 206183, 206267D, 207538, 209339, 239710, 239729, 239745, and 239748).

Abundances can be compared between the two subgroups of Cep OB2 (again using only the non-LTE abundances). Average abundances for Cep OB2a (the older subgroup) are $\log \epsilon$ (C)= 8.27±0.20, $\log \epsilon$ (N)= 7.66±0.08, $\log \epsilon$ (O)= 8.60±0.13, and $\log \epsilon$ (Si)= 7.28±0.32 (Mg and Al are not included in the subgroup comparison as non-LTE results are not available from Paper I). The corresponding average abundances for Cep OB2b are $\log \epsilon$ (C)= 8.32±0.15,

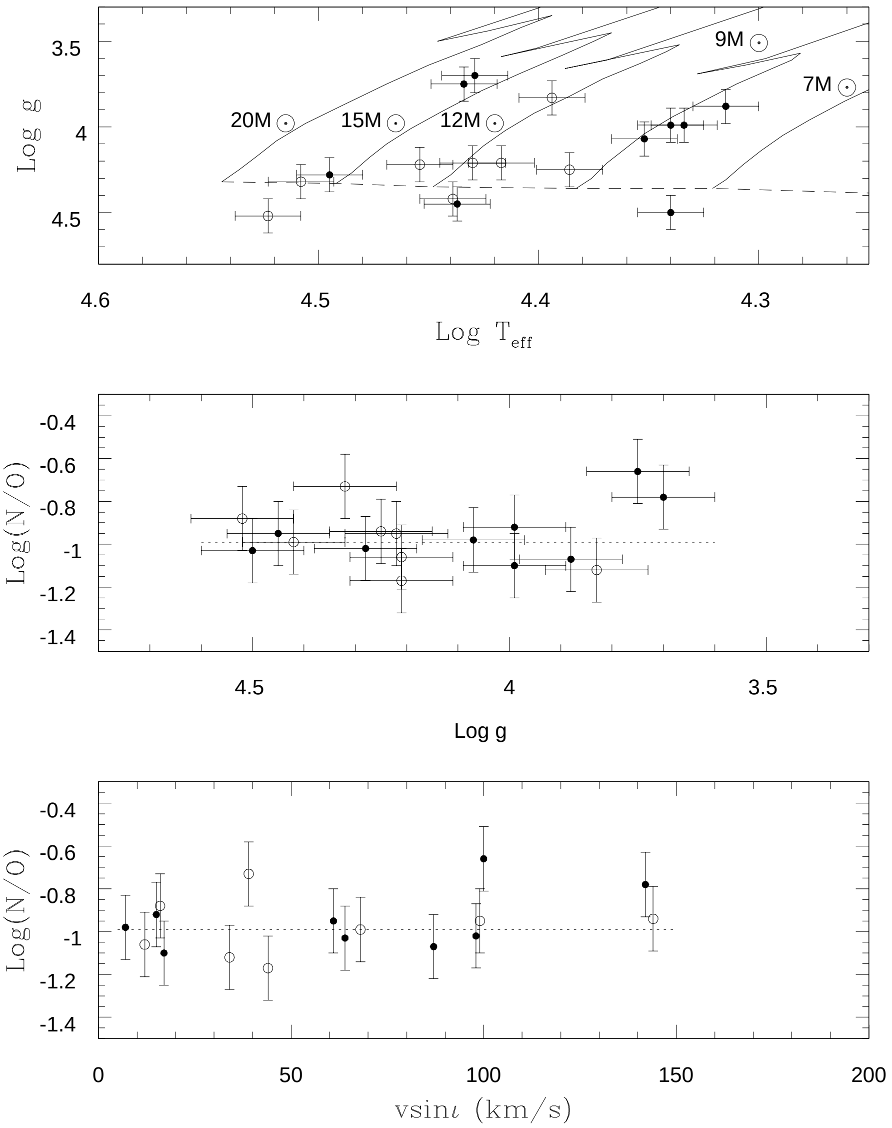

Figure 5.5: The derived stellar parameters T_{eff} and log g are plotted in the top panel to form a modified HR-diagram for Cep OB2 stars. Members of the young cluster Tr 37 are plotted as the open circles, and all other association members are plotted as filled circles. The Tr 37 members should be generally younger and this is found to be the case. Solid curves are stellar models from Schaller et al. (1992) for 7, 9, 12, 15 and $20M_\odot$ models, with the dashed line denoting the ZAMS. Two fairly well-defined, differing age subgroups are identified (based upon the Schaller et al. models, the age difference is $\sim$2–5 Myr). The middle panel shows log(N/O) abundance ratios versus surface gravity, as the surface gravity of a star will initially decrease as it evolves off of the main sequence. Note that the two highest N/O-ratio stars have the lowest surface gravities (these two are the most highly evolved of the $\sim 15M_\odot$ stars). The dotted line is the average $\log(N/O) = -0.99$ of the other Cep OB2 stars. The bottom panel plots log(N/O) versus $v \sin i$ and shows that the two N-rich evolved stars are also two of the most rapidly rotating ones: rotationally induced mixing of CN-cycle material to the surface is one viable explanation for the increased N/O ratios.

$\log\epsilon$ (N)= 7.52±0.15, $\log\epsilon$ (O)= 8.49±0.14, and $\log\epsilon$ (Si)= 7.23±0.31. The two subgroups have similar average abundances considering the abundance uncertainties, and this confirms the conclusions from Paper I that Cep OB2 is rather chemically homogeneous.

The behavior of the N/O abundance ratios are investigated more carefully in the bottom two panels of Figure 5.5, where the log(N/O) abundances are plotted versus log g (middle panel) and $v\sin i$ (bottom panel). The abundance ratio of N/O is shown, as the ratio is somewhat less sensitive to stellar parameter uncertainties, while surface gravity is used as a measure of evolutionary state (see the top panel of Figure 5.5), and projected rotational velocity is used to test for rotationally-induced mixing (Heger & Langer 2000). In general, the N/O ratios of stars in both subgroups display small scatter, with log(N/O)= −0.96±0.13, however, two N-rich stars do stand out, especially in the middle panel as having lower values of log g (and are thus more evolved). These two stars are HD235618 and HD239681 and are Cep OB2a members. In the top panel of Figure 5.5, these N-rich stars are the two most evolved stars falling nearly on the 15$M_\odot$ model track and also have two of the largest projected rotational velocities (bottom panel of Figure 5.5). It should be remembered, of course, that stars with low $v\sin i$ could also be rapid rotators viewed nearly pole-on, but stars with high $v\sin i$ values are rapid rotators, thus HD235618 and HD239681 are rotating rapidly. This suggests that rotation in fairly massive stars has led to mixing of CN-processed material to the surface. Nitrogen enhancements of nearly a factor of two are indicated. In a simple mixing scheme of only CN-processing, the sum of C plus N nuclei will be conserved; with an assumed starting abundance of $\log\epsilon$ (C)= 8.35 and $\log\epsilon$ (N)= 7.55, then an increase to $\log\epsilon$ (N)= 7.80 (as observed), would result in a carbon abundance change of only −0.08 dex: such a change in C would be lost in the noise of the C-abundance uncertainties (especially in view of the possible differences between C II and C III abundances).

Heger & Langer (2000) have computed models of rotating massive stars (M= 8–20$M_\odot$) that include surface abundance changes caused by rotationally induced mixing. They find that surface ^{14}N-abundances can increase by about a factor of 2 (as observed in two of the Cep OB2 members), in 12–20$M_\odot$ stars that have rotational velocities greater than about 200 km s^{-1} and ages of ∼2–5 Myr. The two Cep OB2 stars with N-abundances enhanced by about +0.3 dex have masses close to 15$M_\odot$, and ages of a few Myr. With projected rotational velocities of 100 and 140 km s^{-1}, respectively, these two stars could easily have true rotational velocities of 200 km s^{-1} or larger. A test of the mixing hypothesis could be facilitated by a comparison of boron abundances in a sample of these stars.

5.5 Conclusions

Both the LTE and non-LTE abundances of C, N, O, Mg, Al, and Si derived here continue to indicate that young O and B stars in this part of the Galaxy have slightly subsolar abundances. The inclusion of C III lines in this analysis does, however, yield carbon abundances that are somewhat closer to solar than those abundances derived from C II lines.

With 9 Cep OB2 members in this sample, plus 8 members with low values of $v \sin i$ studied previously (Paper I), the chemical abundances in this association are now better defined and we have probed the chemical composition of the gas that formed the OB stars of this association with stellar masses roughly between 7–15 $M_{\odot}$ as much possible. Two distinct age subgroups within Cep OB2 can be identified based upon the stellar parameters derived here, with both subgroups having similar elemental abundances. Two N-rich stars are identified in the older subgroup, however, and these two stars are both rapidly rotating ($v \sin i \geq 100$ km s^{-1}) and rather massive (M$\sim$ 15 $M_{\odot}$). Their nitrogen overabundances compare well to those predicted from stellar models by Heger & Langer (2000) that include surface abundance changes brought about by rotationally induced mixing.

Capítulo 6

Abundâncias Químicas de Estrelas OB de Associações OB, Aglomerados Abertos e Regiões H II [1]

Resumo: Abundâncias químicas de carbono, nitrogênio, oxigênio, alumínio, magnésio, silício e enxofre, determinadas a partir de síntese espectral, são apresentadas neste capítulo para uma amostra de estrelas OB distribuídas no disco Galáctico. Os perfis sintéticos foram obtidos a partir de considerações fora do ETL no cálculo da formação das linhas. Os resultados deste estudo podem ser combinados com abundâncias de estrelas OB em associações próximas do Sol apresentadas nos capítulos anteriores, a fim de compor uma base homogênea de dados de abundâncias químicas de estrelas OB que possibilite a análise de gradiente radiais de metalicidade no disco da Galáxia. Tal base de dados homogênea é essencial para a investigação detalhada dos padrões de abundâncias no disco. De modo geral, as distribuições de abundâncias estelares obtidas apresentam dispersões que devem ser analisadas considerando-se as posições relativas das estrelas no disco Galáctico. As abundâncias solares, comumente adotadas como referência, estão próximas do limite superior das distribuições de abundâncias de oxigênio, magnésio, silício e enxofre obtidas para as estrelas OB da amostra; as abundâncias de carbono, nitrogênio e alumínio são menores do que as abundâncias solares.

---

[1] **Daflon, S., Cunha, K. & Butler, K. (2002a) a ser submetido (Paper IV)**

6.1 Introduction

Massive OB stars are excellent indicators of the chemical composition of the interstellar medium: they are young, so their photospheric abundances should represent the original composition of the gas from which they formed. Besides that, they are, in principle, not far from their place of birth. Based on this assumption, OB stars are good candidates in order to trace the distribution of the chemical composition in the Galactic disk. Other young objects like H II regions can also be used to study the variations of the chemical abundances along the Galactic radius. The chemical analyses of H II regions show that the radial gradients of metallicity exist, but their magnitudes are still a matter of debate. The most well-sampled element in H II regions is oxygen and the radial gradients derived for this element varies from $-0.07\,\mathrm{dex\,kpc^{-1}}$ (Shaver *et al.* 1983) to $-0.04\,\mathrm{dex\,kpc^{-1}}$ (Deharveng *et al.* 2000).

In the case of B stars, the first studies of the radial abundance gradients covered a restrict region within 2.5 kpc from the Sun, and found almost null gradients (e.g., Fitzsimmons *et al.* 1992, Kaufer *et al.* 1994). More recent stellar analyses presented steeper gradients (Gummersbach *et al.* 1998, Rolleston *et al.* 2000), compatible with the results obtained from the gas. We note, however, that even the most recent work on the radial gradient of stellar abundance present weak points: they are either based upon small samples of stars (the case of Gummersbach *et al.* 1998, with 16 B stars) or the abundance analysis is based on LTE (the case of Rolleston *et al.* 2000).

The homogeneity of the abundance data is of course relevant to address the variations on the chemical composition of the Galactic disk, once systematic errors in the chemical analysis could in principle create spurious abundance patterns. Rolleston *et al.* (2000), however, claim that an LTE approach is enough in order to define the magnitude of the radial gradients. This may be true (or not) to define the inclination of a linear fit of the chemical abundances as a function of Galactocentric distances, but it is not valid to successfuly represent the distribution of the chemical composition in the Galactic disk: for this, correct absolute abundances are essential.

In previous papers (Daflon, Cunha & Becker 1999, Daflon *et al.* 2001a, Daflon *et al.* 2001b), we presented chemical abundances obtained from the fitting of synthetic non-LTE line profiles for a sample of OB stars members of OB associations close to the Sun, with $d < 2.0$ kpc. The spectral syntheses were done with a non-LTE approach and the derived abundances are therefore based on more realistic calculations. At the same time, the fitting of synthetic profiles instead of equivalent width measurements makes it possible to determine the chemical composition of stars with high projected rotational velocities, which is very common among OB stars. In this study we add to the construction of a homogeneous base of stellar abundance data, derived from the fitting of non-LTE theoretical profiles to high resolution spectra. We present non-LTE abundances of carbon, nitrogen, oxygen, magnesium, aluminum, silicon and sulfur for main-sequence OB stars members of open clusters, OB associations and H II regions of the Galactic disk.

6.2 Observations

The present sample was chosen in order to provide abundance information for an ongoing study of the abundance pattern of the Galactic Disk. For this purpose, we selected stars located in different positions in the Disk, based on preliminary distance determinations from the literature. We attempted to observe whenever possible more than one star per open cluster and OB association; some observed spectra, however, were discarded due to the star being a spectroscopic binary, misclassified as a B star or also for being a very rapidly rotating star for which an abundance analysis could not be done. In the outer part of the disk the lack of information about open clusters and OB associations led us to seek for target stars in distant H II regions.

The observational data consists of high resolution spectra obtained with the ESO 1.52m telescope at La Silla, Chile, coupled to FEROS (Fiber fed Extended Range Optical Spectrograph) and a 2048×4096 CCD detector. The complete coverage is 3600-9200 Å distributed in 39 orders, with resolution $\lambda/\Delta\lambda$=48,000 or 2.2 pixels per $\Delta\lambda$ (Kaufer *et al.* 1999). The data reduction was done online with MIDAS package and consisted of flat fielding, extraction, wavelength calibration, correction of the barycentric velocity and merging of the orders into a 1-D spectrum.

Our previous studies of stellar abundances (Paper I, II and III) are based on high resolution spectra collected at the Mc Donald Observatory, University of Texas, Austin. Two stars of Paper II (HD 344783 and BD+24°3880 of the Vul OB1 association) were also observed with the ESO 1.52m telescope so that a comparison between the stellar spectra could reveal any possible systematic differences between them. This was done by directly comparing the equivalent widths measured in both spectra: the equivalent widths measured in the spectra obtained at ESO and Mc Donald show good agreement and present no systematic differences.

The sample stars have spectral types O9-B2, V=8-12 mag and are mainly on the main-sequence. The exposure times were chosen as to give a minimum signal-to-noise ratio of a hundred at ~4650 Å. In Table 6.1 we list the sample stars and as well as their associated open cluster, OB association or H II region, their spectral type, V magnitudes, dates of observation, exposure time in minutes and S/N ratios at 4650 Å. In Figure 6.1 we present a sample spectrum in the region $\lambda\lambda 4625 - 4670$Å with the typical signal-to-noise of our sample (S/N~120) for the star BD-00°1491, also listed in the literature as Sh2 285-6.

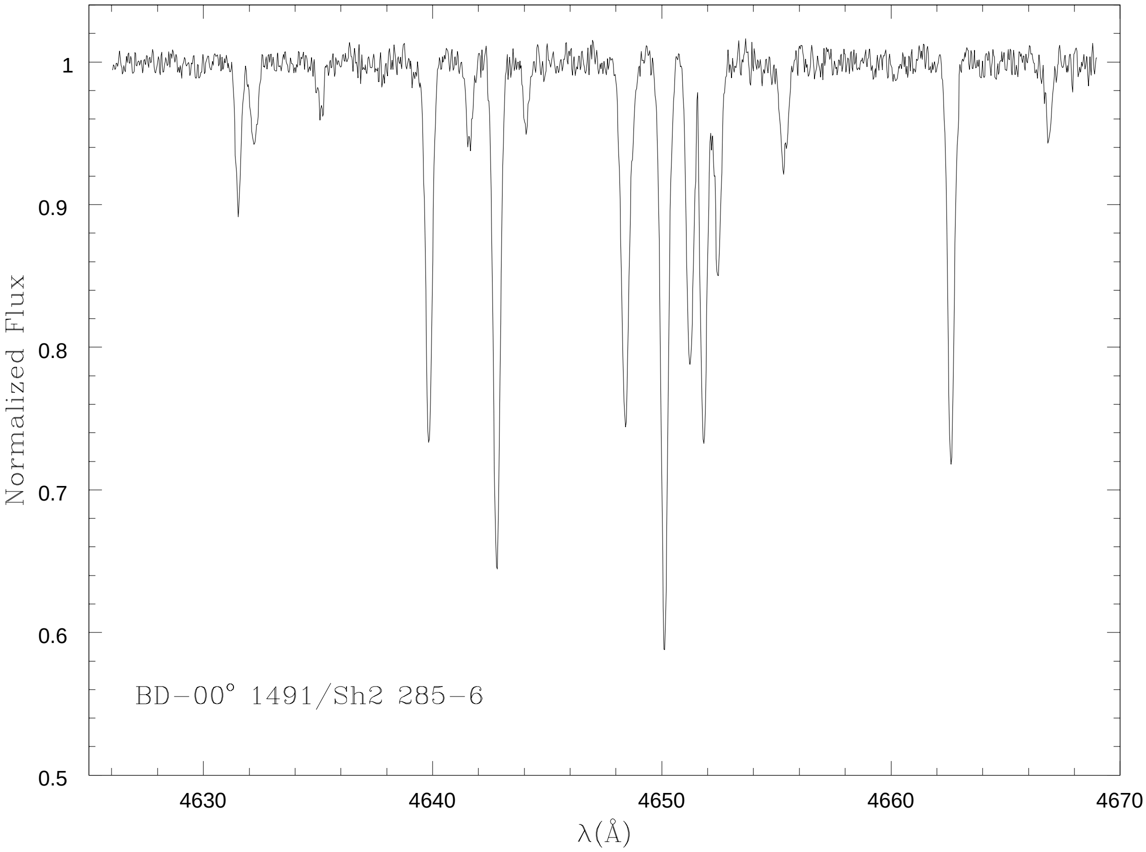

Figure 6.1: A sample spectrum in the region 4625-4670 Å with S/N=120 for the sharp-lined star BD-00°1491=Sh2 285-6.

Table 6.1: Observational Data

Star	Cluster	MK	V	date	t_{exp}	S/N
S2R3N09	NGC 1893	B1.5III	11.7	02/03/2001	105	80
S2R2N43	NGC 1893	B1III	11.5	02/08/2001	120	70
LS 404	NGC 2414	B1V	11.8	11/28/1999	95	90
LS 428	NGC 2414	B0.5V	11.8	11/28/1999	90	100
CPD-59° 4532	NGC 4755	B1V	10.2	02/29/2000	60	140
CPD-59° 4535	NGC 4755	B1V	10.2	04/09/2000	60	130
CPD-59° 4544	NGC 4755	B2V	10.2	04/09/2000	60	100
CPD-59° 4560	NGC 4755	B1.5V	9.6	04/08/2000	60	150
LS 3719	NGC 6204	B1III	9.6	04/11/2000	60	180
CPD-41° 7723	NGC 6231	B1V	9.5	06/13/2000	50	110
CPD-41° 7730	NGC 6231	B1V	9.3	06/13/2000	50	150
HD 326332	NGC 6231	B0.5V	9.7	06/13/2000	60	110
HD 326364	NGC 6231	B0IV	9.6	06/13/2000	60	90
BD-12° 4978	NGC 6604	B1V	10.4	07/23/2000	60	100
BD-12° 5074	NGC 6611	B1V	10.3	06/23/1999	60	130
BD-13° 4921	NGC 6611	B0.5V	9.9	06/23/1999	50	120
BD-13° 4930	NGC 6611	O9.5V	9.4	06/23/1999	40	140
BD-13° 4934	NGC 6611	B1V	9.5	06/23/1999	50	130
HD 308810	IC 2944	B1V	9.6	02/19/2000	60	120
HD 308817	IC 2944	B1.5V	10.7	02/19/2000	60	100
CPD-61° 3579	Stock 16	B2V	10.5	07/22/2000	60	80
LS 4257	Trumpler 27	B0V	11.5	07/23/2000	90	110
LS 4271	Trumpler 27	O9III	10.7	07/23/2000	80	100
HD 166033	Sh2 32	B1V	9.9	06/13/2000	40	90
HD 314031	Sh2 32	B0.5V	9.9	07/23/2000	60	160
Sh2 47-3	Sh2 47	B0V	10.3	04/09/2000	70	140
Sh2 247-1	Sh2 247	O9V	11.1	02/20/2000	90	80
LS 45	Sh2 253	B1.5V	12.6	11/26/1999	120	80
HD 48691	Sh2 284	B0.5IV	7.8	11/25/1999	30	300
BD-00° 1491	Sh2 285	B0V	12.0	11/25/1999	105	120
CPD-48° 8705	Ara OB1	B0V	8.5	06/23/1999	30	170
HD 149065	Ara OB1	B2V	8.4	06/23/1999	30	150
HD 46202	Mon OB2	O9V	8.2	11/28/1999	30	200
HD 172427	Sct OB2	B1IV	9.5	04/11/2000	50	140
HD 172488	Sct OB2	B0.5III	7.6	04/11/2000	25	170

6.3 Analysis

6.3.1 Effective Temperatures and Gravities

Stellar parameters were derived with a photometric calibration plus the fitting of the wings of $H\gamma$, using the same methodology presented and discussed in Daflon, Cunha & Becker (1999). Effective temperatures are determined using a 2-order calibration for the reddening-free parameter Q=(U-B)-0.72(B-V). This photometric calibration is anchored on a temperature scale based on a iterative procedure combining photometric calibration for the Strömgren indices and the fitting of the wings of $H\gamma$. The Q-parameter was first adopted in Paper I as a temperature indicator, instead of this iterative procedure itself, basically due to the lack of Strömgren photometry for the majority of the stars of that sample listed in the literature. As the main object of the present study is to construct a homogeneous database of stellar abundances, we adopt the same calibration to preserve the consistency of our temperature scale. Once we fixed the effective temperature, we fitted LTE synthetic wings of $H\gamma$ (Kurucz, 1979) to the observed profiles to obtain the surface gravity ($\log g$). The photometric calibration provides effective temperatures with an uncertainty of roughly 4%, as discussed in Paper I, considering an error of 0.01 mag in the measurements of the photometric indices. We estimate an error of 0.1 dex in the determination of the surface gravity, primarily imparted by the placement of the continuum. The stellar parameters of the studied targets are distributed within the range between 21000 to 33000 K for effective temperature and 3.6-4.6 for gravity. In Table 6.2 we list the Q-parameters, the adopted effective temperature and gravity.

As a consistency check, we investigated the relative strength of metallic lines as a function of temperature. We compared, for example, the relative intensities of O II lines and C III lines in the region of 4650 Å, N III lines at 4634, 4641 Å and line ratios of He I/He II as these are sensitive to $T_{\rm eff}$ for the hotter stars. For three stars listed in Table 6.2 (marked with “*”) we consider that the effective temperatures derived from the photometric calibration do not agree with their observed spectra; the $T_{\rm eff}$ s derived for these stars are among the highest temperatures in our sample. In the following we discuss each star in turn: *(i)* LS 4271 presents only one measurement of UBV photometry (Moffat *et al.* 1977) which gives Q=-0.859. For this value we derived initially $T_{\rm eff}$=30950 K. However, the intensity of He

Table 6.2: Stellar Parameters

Star	Q	T_{eff}	$\log g$
S2R3N09	-0.794	26830	3.98
S2R2N43	-0.782	26160	3.91
LS 404	-0.723	23270	4.32
LS 428	-0.816	28140	4.56
CPD-59° 4532	-0.730	23550	4.30
CPD-59° 4535	-0.715	22920	4.23
CPD-59° 4544	-0.739	23980	4.08
CPD-59° 4560	-0.724	23300	3.95
LS 3719	-0.742	24120	3.60
CPD-41° 7723	-0.751	24550	4.07
CPD-41° 7730	-0.748	24350	4.15
HD 326332	-0.803	27350	4.00
HD 326364	-0.839	29610	4.15
BD-12° 4978	-0.810	27750	4.25
BD-12° 5074	-0.783	26210	4.37
BD-13° 4921	-0.816	28100	4.10
BD-13° 4930	-0.857	30830	4.40
BD-13° 4934	-0.859	30950	4.48
HD 308810	-0.789	27040	4.32
HD 308817	-0.715	22910	4.28
CPD-61° 3579	-0.811	27840	4.38
LS 4257	-0.837	29460	4.10
LS 4271	-0.859	32190*	3.85
HD 166033	-0.804	27410	4.26
HD 314031	-0.784	26270	4.36
Sh2 47-3	-0.843	29870	4.10
Sh2 247-1	-0.896	32430*	4.26
LS 45	-0.713	22830	4.04
HD 48691	-0.829	28940	4.20
BD-00° 1491	-0.837	29480	3.95
CPD-48° 8705	-0.841	30930*	4.56
HD 149065	-0.666	21090	4.24
HD 46202	-0.870	31720	4.08
HD 172427	-0.786	26360	3.94
HD 172488	-0.789	26530	3.65

II lines at $\lambda\lambda$ 4200, 4542 and 4686 Å suggest a higher temperature for this star. We then corrected the derived temperature by +4% and obtained $T_{\rm eff}$=32190 K, which is the adopted temperature. Massey *et al.* (2001) listed log T=4.553 (T_{eff}=35730 K) based on their MK classification for this star, which is O8.5 III. *(ii)* The same correction was applied for the star CPD-48° 8705. Four different sets of photometric indices are listed in the literature for this star and the possible temperatures derived vary from 26490 to 29740 K, which corresponds to a difference of more than 10%. However, even the highest temperature was not compatible with relative strength of He II and C III lines present in the star's spectra. So, we applied a correction of +4% for its highest temperature and adopted $T_{\rm eff}$=30930 K for this star. No other effective temperature is listed in the literature for CPD-48° 8705. *(iii)* For Sh2 247-1, we initially derived $T_{\rm eff}$=33730 K from the photometry listed in Haug (1970), the only source available. This temperature, however, seems to be very high to account for the observed ratios between He I and He II lines and the intensity of the He II line at 4542Å. In this case, we lowered the effective temperature by 4% and adopted the value of $T_{\rm eff}$= 32430 K for this star. This star was studied by Gummersbach *et al.* (1998), who derived T_{eff}=30800 from Balmer lines combined to the ionization equilibrium of Si II/Si III/Si IV lines.

6.3.2 Non-LTE Abundances

Chemical abundances are derived from the fitting of non-LTE theoretical profiles to the observed spectral lines. The model atmospheres are fully-blanketed, plane-parallel LTE models calculated with ATLAS9 code (Kurucz, 1992) for a constant microturbulence velocity of ξ = 2kms^{-1} and solar composition. Departures from LTE are considered in the line formation calculations; the program DETAIL is used to solve the equations of statistical equilibrium and transfer. These calculations are strongly dependent on the completeness of the adopted model atom and require the description of an appropriate number of levels and transitions to yield accurate level populations. The model atoms used in this analysis are described in Eber & Butler (1988 - C II), Becker & Butler (1989 - N II), Becker & Butler (1988 - O II), Becker & Butler (1990 - Si III), Przybilla *et al.* (2001 - Mg II), Dufton *et al.* (1986 - Al III) and Vrancken *et al.* (1996 - S III). The line profiles are calculated with code SURFACE, assuming Voigt profile functions. Atomic lines in the neighborhood of ±3Å around the lines of interest were considered in order to construct a linelist for each spectral region. For consistency, we use the same linelists of Paper III. In this paper, however, we include some spectral regions containing weak lines (these were not analyzed in the spectra of the high $v \sin i$ B stars of Paper III). The selected transitions and atomic data for the included spectral regions are listed in Table 6.3, with the wavelength, excitation potential and $\log(gf)$ for each element present in the region. The gf-values come mainly from TOPbase and, when not available in this database, from the Kurucz web site (URL cfau5.harvard.edu/).

Table 6.3: Linelists

Wavelength interval	λ(Å)	Species	χ(eV)	$\log(gf)$
4359-4367	4361.53	S III	18.24	-0.75
S III	4364.75	S III	18.32	-0.85
	4366.91	O II	23.01	-0.24
4464-4469	4465.44	O II	30.43	0.34
O II	4466.60	O II	28.94	0.24
	4467.76	S III	18.31	-1.10
	4467.95	O II	30.43	0.22
4510-4515	4510.88	N III	35.67	-0.45
Al III	4512.56	Al III	17.81	0.40
	4514.85	N III	35.70	0.23
4526-4531	4527.86	N III	38.49	-0.24
Al III	4529.19	Al III	17.81	0.66
	4530.41	N II	23.49	0.67
4888-4892	4890.85	O II	26.30	-0.35
O II				
5141-5153	5143.50	C II	20.70	-0.21
C II	5145.17	C II	20.71	0.19
	5151.05	Al III	23.54	0.25
	5151.08	C II	20.71	-0.18
5188-5192	5190.57	O II	26.55	-0.46
O II				

We derived non-LTE abundances, microturbulence velocities and projected rotational velocities following the procedure discussed in Paper III. Some examples of profile fitting are shown in Figure 6.2 for the star BD-00° 1491. The adopted microturbulence is $\xi = 6\mathrm{kms}^{-1}$;

in these examples, the values of the projected rotational velocity are between 9.5 and 12 kms^{-1}. The mean projected rotational velocity for the star is the average of the $v \sin i$ obtained from the fitting of the individual lines of all the element. The microturbulence velocities, projected rotational velocities and mean elemental abundances plus dispersions are presented in Table 6.4. The abundances listed in Table 6.4 represent the mean abundance for all the fitted lines of the same specie and a standard deviation which is the line-to-line scatter of the abundances.

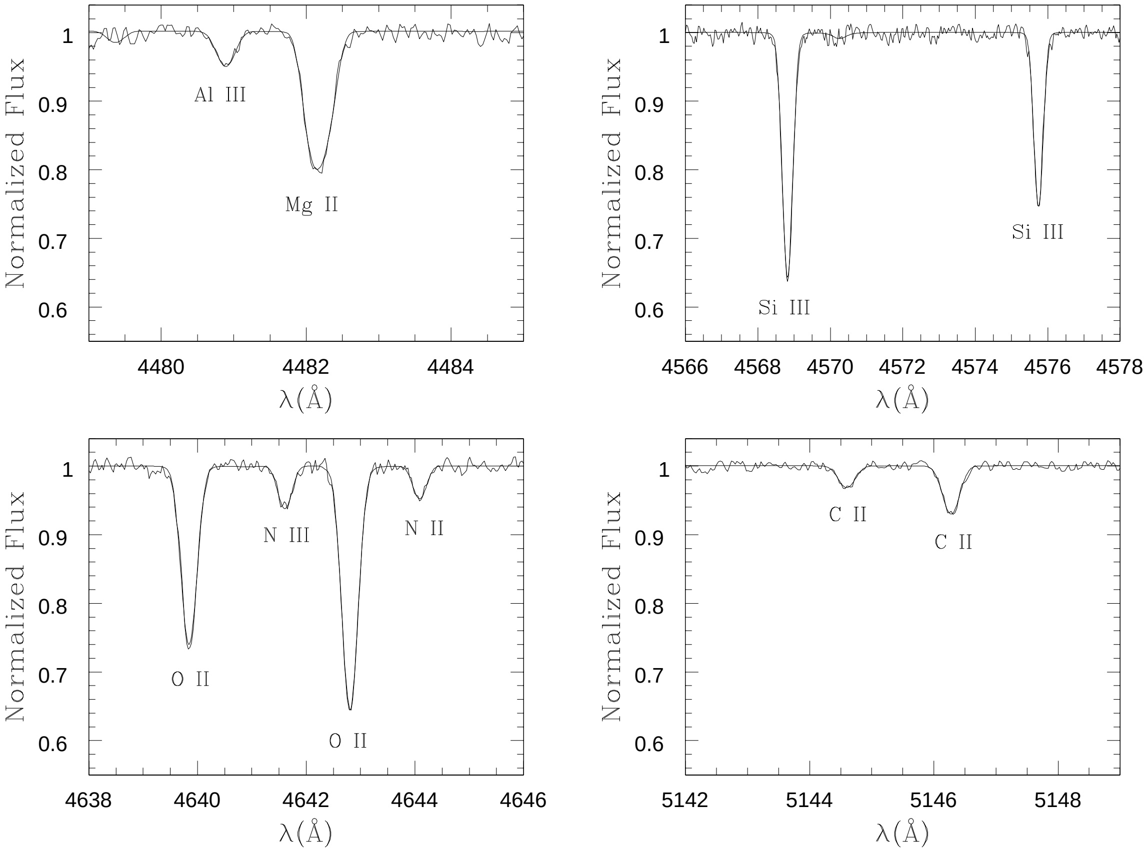

Figure 6.2: Some examples of line synthetic profiles fitted to the observed spectra of the star BD-00°1491 for $\xi = 6$kms^{-1}. The N III line at 4641Å is calculated in LTE; all the other profiles are from non-LTE calculations. The values of $v \sin i$ needed for these fits vary between 9.5 and 12 kms^{-1}.

Table 6.4: Non-LTE Abundances

Star	ξ (km s^{-1})	log ϵ(C)	log ϵ(N)	log ϵ(O)	log ϵ(Mg)	log ϵ(Al)	log ϵ(Si)	log ϵ(S)	$v \sin i$ (km s^{-1})
S2R3N09	7	8.00±0.11	7.31±0.14	8.46±0.12	7.18	5.81±0.08	6.81±0.15	7.06±0.16	11±3
S2R2N43	7	-	7.32±0.12	8.27±0.13	-	-	6.73±0.03	-	54±5
LS 428	5	-	7.21±0.15	8.06±0.07	7.08	-	6.58±0.19	-	32±5
LS 404	8	8.12	7.40±0.12	8.37±0.10	-	6.05	6.87	-	33±3
CPD-59° 4532	6	8.25	7.58±0.08	8.48±0.06	7.13	-	7.01±0.16	7.35	71±2
CPD-59° 4535	4	8.21±0.08	7.53±0.05	8.58±0.13	7.58	6.04	7.00±0.10	7.20	68±4
CPD-59° 4544	4	8.32±0.12	-	8.61±0.09	7.55	6.25	7.11±0.02	7.25	69±5
CPD-59° 4560	9	-	7.74±0.06	8.65±0.12	7.78	-	7.16±0.06	-	192±12
LS 3719	11	8.12	7.72±0.13	8.68±0.11	7.32	6.10	7.57±0.04	-	77±6
CPD-41° 7723	5	8.11±0.07	7.47±0.11	8.50±0.11	-	5.98±0.04	6.91±0.12	7.20±0.20	26±2
CPD-41° 7730	3	8.10±0.11	7.53±0.15	8.53±0.09	7.04	5.77±0.02	6.92±0.14	7.20±0.24	12±1
HD 326332	7	8.20±0.06	7.56±0.08	8.50±0.15	7.43	5.95±0.04	7.12±0.13	7.15±0.25	23±3
HD 326364	10	8.38±0.17	7.93±0.12	8.48±0.13	7.48	6.20±0.17	7.45±0.12	7.23±0.19	19±4
BD-12° 4978	3	-	7.55±0.07	8.53±0.11	7.57	6.10	7.20±0.20	-	61±4
BD-12° 5074	2	-	7.50±0.14	8.45±0.09	7.21	5.83	6.86±0.15	7.11±0.05	19±3
BD-13° 4921	7	8.35	7.57±0.12	8.61±0.17	7.35	-	7.07±0.18	-	86±7
BD-13° 4930	7	8.11	7.62±0.14	8.54±0.17	7.48	6.30±0.07	7.18±0.05	7.29	20±3
BD-13° 4934	6.5	-	7.76±0.06	8.67±0.13	7.52	6.18±0.11	7.42±0.20	7.24	80±6
HD 308810	5	8.28	7.41±0.11	8.45±0.12	7.30	5.81	7.03±0.09	7.42	51±4
HD 308817	5	-	7.51±0.15	8.60±0.13	7.53	6.21±0.09	7.14±0.14	-	57±4
CPD-61° 3579	6.5	8.50	7.77±0.06	8.48±0.10	7.25	6.12	7.08±0.05	7.30	78±6
LS 4257	10	8.45	7.81±0.13	8.58±0.17	7.80	6.30	7.53±0.02	7.47	88±4
LS 4271	8	-	-	8.52±0.20	-	-	7.44±0.03	-	61±10
HD 166033	4	-	7.69±0.02	8.73±0.07	-	-	7.38±0.15	-	73±4
HD 314031	5	8.20	7.71±0.09	8.60±0.14	7.50	6.27	7.14±0.09	7.25	94±3
Sh2 47-3	6.5	8.21±0.01	7.53±0.09	8.52±0.14	7.48	6.32±0.13	7.40±0.08	7.15	16±2
Sh2 247-1	12	-	7.48	8.21±0.15	7.25	-	7.43±0.02	-	23±5
LS 45	7	8.00	7.36±0.09	8.46±0.15	6.99	5.85±0.21	6.96±0.12	-	22±4
HD 48691	8	8.01±0.03	7.44±0.14	8.47±0.09	7.42	5.68	6.87±0.03	7.08±0.04	53±6
BD-00° 1491	6	8.10±0.03	7.45±0.12	8.45±0.13	7.34	6.06±0.24	7.27±0.12	6.95±0.24	12±2
CPD-48° 8705	6	-	7.62±0.11	8.40±0.10	7.28	-	7.06±0.08	7.25	65±5
HD 149065	4	8.29±0.04	7.61±0.05	8.52±0.09	7.52	6.12±0.13	7.17±0.06	7.23	24±1
HD 46202	9	-	7.22±0.05	8.11±0.12	6.87	5.92±0.23	7.14±0.03	6.94	24±3
HD 172427	8	8.26±0.14	7.52±0.12	8.51±0.16	7.70	6.23±0.12	7.75±0.09	7.45	53±5
HD 172488	11	8.35	7.66±0.07	8.58±0.17	7.76	6.43±0.19	7.69±0.12	-	100±7

In this Section we also present Mg, Al, and S abundances for those stars studied in Papers I and II. In the first paper, we derived non-LTE abundances of carbon, nitrogen and oxygen and silicon for 8 stars with low projected rotational velocity belonging to the Cep OB2 association. The sample was later extend to include 15 stars belonging to five other OB associations (Paper II). The observational data consists of high resolution, high signal-to-noise spectra of main sequence B stars belonging to OB associations and are discussed in Papers I and II. The sample stars are listed in Table 6.5, with the corresponding associations. The theoretical profiles of Mg II, Al III and S III were broadened and fitted to the observed profiles. The final non-LTE abundances of magnesium, aluminum and sulfur are listed in columns 3, 4 and 5 of Table 6.5 for each star. The elemental abundances are represented by the average of the individual line abundances and the respective dispersions. In this analysis we discarded star HD 202253 of Cyg OB 7 association because for this star there was only one spectral region suitable for fitting, centered on 4480 Å, but it was close to a region of picket-fence and the normalization of the continuum in this region was very inaccurate. We thus decided not to analyse this star.

The overall picture of the differences between LTE and non-LTE abundances are discussed in Paper I, II and III. The non-LTE corrections (LTE−Non-LTE abundances) of carbon, nitrogen and oxygen are typically smaller than 0.1 dex. Silicon and magnesium present larger corrections that may be of the order of 0.25 dex; aluminum, on the other hand, present non-LTE corrections < 0.08 dex scattered around zero. The sulfur abundances for the stars in our sample were analyzed only considering the LTE approach in Paper II. There, we found $\sim$ solar abundances for sulfur, but a more complete analysis, based on non-LTE abundances, was needed to verify if this result is real or arise from the analysis uncertainties. The derived Non-LTE abundances of sulfur can be compared with these LTE results, and we find non-LTE corrections scattered around zero within ±0.2 dex. Considering the 10 stars in Paper II for which we derived LTE sulfur abundances we obtain $< \log\epsilon(\mathrm{S}) >_{LTE} = 7.29\pm0.26$ and $< \log\epsilon(\mathrm{S}) >_{Non-LTE} = 7.22 \pm 0.10$, that is, the non-LTE sulfur abundances are slightly lowered but is still comparable with the sulfur abundance in the Sun within the uncertainties.

Table 6.5: Mg, Al and S Abundances

Association	Star	$\log\epsilon$(Mg)	$\log\epsilon$(Al)	$\log\epsilon$(S)
Cep OB2	HD 205794	7.33	5.93	7.34
	HD 206183	7.36	6.17±0.06	7.05
	HD 206267	7.21	5.70	7.28
	HD 206327	7.27	5.98±0.05	7.17±0.05
	HD 207538	7.42	6.15±0.29	-
	HD 239724	7.48	6.02	7.16±0.16
	HD 239742	7.81	6.00	7.19
	HD 239743	7.33	6.01±0.03	-
Vul OB1	BD 24° 3880	7.59	6.24±0.19	7.28±0.08
	HD 344783	7.31	6.25	7.13±0.03
Cyg OB3	HD 227460	7.46	6.11±0.17	7.22
	HD 227586	7.21	5.87	7.21
	HD 227757	7.39	6.29±0.23	7.34
Cyg OB7	HD 197512	7.38	5.98±0.07	7.11±0.19
Lac OB1	HD 214167	-	-	7.07
	HD 214680	7.47	6.12±0.25	-
	HD 216916	7.52	6.18±0.16	7.29
	HD 217227	7.52	6.09	7.28
	HD 217811	-	6.01	7.15±0.18
Cep OB3	BD 62° 2125	7.03	5.84±0.02	7.20±0.21
	HD 217657	7.12	5.71±0.11	7.17
	HD 218342	7.44	5.99±0.01	7.06±0.08

6.3.3 Abundance Uncertainties

Abundance analyses are subject to errors in the determination of the stellar parameters and the fitting of the line profiles. The uncertainties in the determination of the temperature and gravity are of 4% and 0.1 dex, respectively (we refer to Paper I for a detailed discussion on this subject); The microturbulence velocity can be determined within an error of $\pm 1.5\mathrm{km\,s^{-1}}$, from the $\log\epsilon$(O) *vs.* ξ plot. Besides these sources of uncertainties, the fitting of line profiles is also subject to errors in the placement of the continuum of the observed spectra and the choice of the projected rotational velocity. We assume an error of 5% due to the continuum and 7% in the choice of $v \sin i$, based on the χ^2-minimization to find a best fit. We considered these uncertainties independent to compute the changes in the elemental abundances for each parameter variation: one parameter was changed at a time, while the others were kept constant, and a new theoretical profile was fitted. This study was proceeded for N II, O II, Mg II, Al III and Si III in Paper III. In general, the total errors for N and Al are smaller than 0.15 dex. Oxygen, magnesium and silicon present larger errors of the order of 0.20 dex, which are mainly dominated by the uncertainties in the effective temperature. Magnesium is especially sensitive to microturbulence in the lower end of our temperature scale, where the selected Mg II line is stronger; the three silicon lines are all intermediate to strong lines in the spectra of the main sequence stars and are also dependent on the choice of microturbulence. In this paper we present the changes imparted on the abundances of C II and S III by the uncertainties. The total errors ($(\sum \delta_i^2)^{1/2}$, where δ_i are the individual errors) are listed in Table 6.6 for two stars of our samples with temperatures close to 20,000 K and 30,000 K. The errors for carbon abundances derived from C II lines are smaller than 0.1 dex for range of temperatures of the studied stars. For S III, the effective temperatures are the main source of uncertainties in the determination of sulfur abundances.

6.4 Discussion of the Results

6.4.1 The Abundance Pattern

The non-LTE abundances of C, N, O and Si, as a function of effective temperature, are shown in Figure 6.3. In the Figure 6.4 we present the non-LTE abundances of Mg, Al and S as a function of $T_{\rm eff}$ for all the stars, including those stars members of OB associations listed in the Table 6.5. In general, the non-LTE elemental distributions show no trend with temperature, which suggest that our abundance analyses are not subject to major systematic uncertainties. In the following we discuss each studied element separately:

Carbon - The mean carbon abundance for the whole sample is 8.21 ± 0.14. In the Figure 6.3 we adopt the carbon abundance suggested by Holweger (2001), which is 8.592 ± 0.108. The difference between our mean abundance and the solar abundance is -0.38 dex. This result

Table 6.6: Abundance Uncertainties

Ion	Correction	HD 149065	BD-13° 4930
C II	$\delta(\mathrm{T_{eff}})$	-0.03	$+0.08$
	$\delta(\log g)$	0.00	-0.01
	$\delta(\xi)$	-0.01	0.00
	$\delta(v \sin i)$	$+0.01$	$+0.01$
	δ(continuum)	$+0.02$	$+0.02$
	$(\sum \delta_i^2)^{1/2}$	$+0.04$	$+0.08$
S III	$\delta(\mathrm{T_{eff}})$	-0.12	-0.09
	$\delta(\log g)$	$+0.03$	0.00
	$\delta(\xi)$	-0.03	-0.01
	$\delta(v \sin i)$	$+0.01$	$+0.01$
	δ(continuum)	$+0.02$	$+0.02$
	$(\sum \delta_i^2)^{1/2}$	$+0.13$	$+0.09$

is consistent with the underabundance of carbon, relative to the Sun, derived in Papers I and II using the same C II lines. In paper III we attempted to derive non-LTE carbon abundances for a sample of high $v \sin i$ B stars using the strong C III lines at 4647-4651 Å. The average carbon abundances for 8 stars was 8.39 ± 0.15 and three stars presented $\log \epsilon(\mathrm{C_{III}}) \geq 8.50$. The discrepancy between C II and C III non-LTE abundances was not removed if the temperature scale was adjusted whithin the uncertainties and it was stressed that this point still deserves some effort to be clarified.

Nitrogen - The solar nitrogen abundance listed by Holweger and Grevesse & Sauval show a very good agreement - 7.931 ± 0.111 and 7.92 ± 0.06, respectively - and are 0.38 dex higher than the mean abundance for this sample, which is 7.55 ± 0.17. Only one star in our sample, HD 326364, presents a solar abundance of nitrogen ($\log \epsilon(\mathrm{N}) = 7.93 \pm 0.12$). No correlation between nitrogen abundances and effective temperatures is observed.

Oxygen - The recent analyses of the oxygen abundance in the Sun bring it down to 8.736 ± 0.078 (Holweger 2001) and even 8.69 ± 0.05 (Allende Prieto, Lambert & Asplund 2001). We consider the average between these two values, $\log \epsilon(\mathrm{O}){=}8.72$, as a reference for the solar oxygen. Although some stars in our sample have oxygen abundances very close or even higher than the Sun, the bulk of the distribution is sub-solar by roughly 0.2 dex. The mean oxygen abundance for the sample stars is 8.49 ± 0.15. Oxygen abundances show a slight dependence with the effective temperature and a linear fit to the abundance points has a slope of -1.4×10^{-5}. This dependence is determined by the stars LS 428, Sh2 247-1 and HD 46202, which present oxygen abundances lower than 8.21 dex. If these stars are removed from the fitting, the slope changes to -1.9×10^{-6} and the oxygen decreases only 0.02 dex as the $T_{\rm eff}$ runs from 20,000 to 30,000 K. The lower abundances presented by these stars are possibly due to their location in outer parts of the Galactic Disk and we thus consider the oxygen abundances are essentially independent of the effective temperature.

Magnesium - The abundances of magnesium presented in the Figure 6.4 include the stars listed in the Tables 6.4 and 6.5. The distribution of $\log\epsilon$(Mg) shows a large spread; the lowest and the highest magnesium abundances are, respectively, 6.87 and 7.81, with ~1 dex of difference between them. Magnesium abundance is derived from the triplet of Mg II at 4481 Å, blended in one single profile. This is a strong profile for the stars with $T_{\rm eff} \leq 25000$, that reaches its maximum intensity at late-B/A stars. Consequently, the magnesium abundances for the stars with lower temperatures are more sensitive to the choice of microturbulence. The line strength decreases considerably for higher $T_{\rm eff}$ and so does the dependence of magnesium abundances on the microturbulence.

The magnesium abundance in the Sun suggested by Holweger (2001) is 7.538 ± 0.060. This value is in the high end of the Mg abundance distribution for B stars in the Figure 6.4. The difference between the magnesium abundance in the Sun and the mean value for B stars is -0.168.

Aluminum - The abundances obtained for the stars listed in Tables 6.4 and 6.5 are presented in the Figure 6.4. The difference between the mean abundance for the B-stars ($<\log\epsilon({\rm Al_B})>= 6.05\pm0.18$), and the solar abundance derived by Grevesse & Sauval (1998) ($\log\epsilon({\rm Al})_\odot=6.47$) is -0.42 dex. The aluminum abundances show a slight correlation with temperature as the abundances are increased by 0.11 dex as the temperatures run from 20,000 to 30,000K. This difference, however, is roughly of the same magnitude of the total errors estimated in the abundance analysis.

Silicon - Silicon presents the largest spread ($<\log\epsilon({\rm Si})>= 7.16 \pm 0.29$) among the elements studied here. The solar value assigned by Holweger (2001) is 7.536 ± 0.049; although

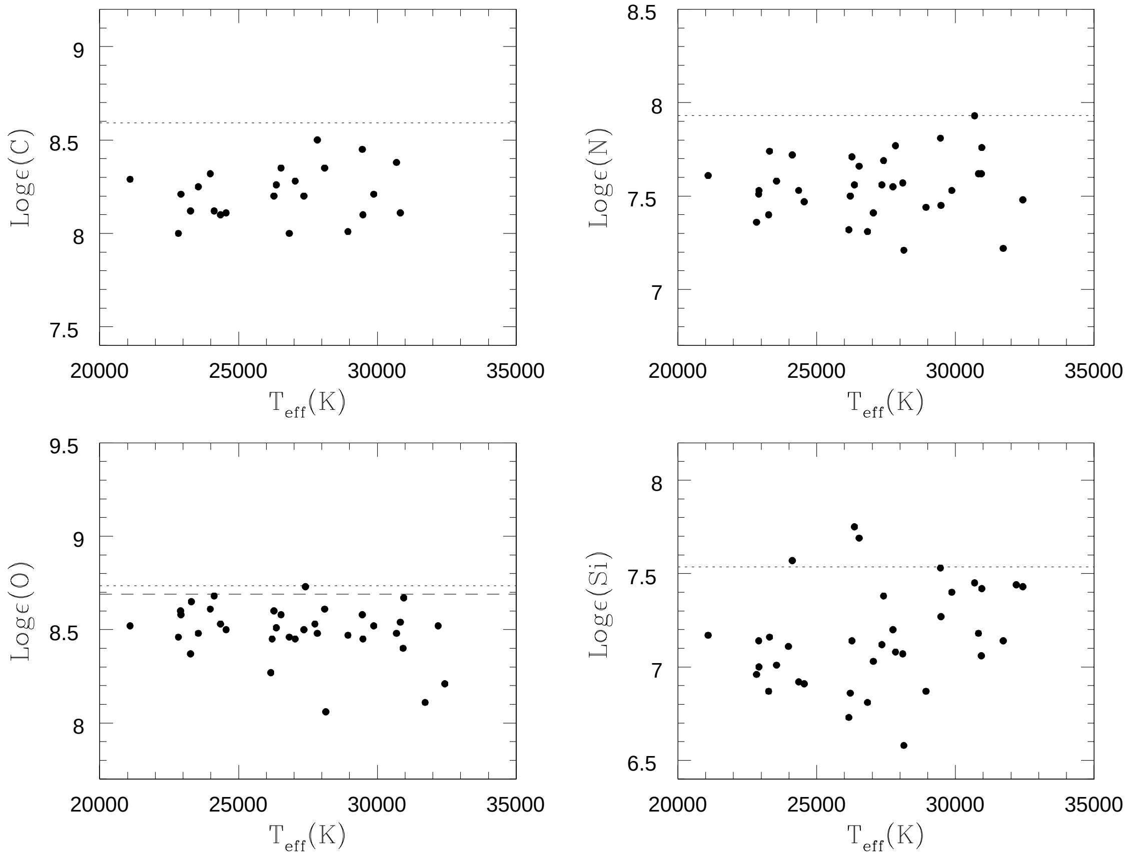

Figure 6.3: Elemental abundances of carbon, nitrogen, oxygen and silicon as a function of T_{eff}, for the stars listed in Table 6.4. Dotted lines represent the solar abundances listed by Holweger (2001): 8.592, 7.931, 8.736 and 7.536 for C, N, O and Si, respectively. The dashed line represents the oxygen abundance (8.69±0.05) derived by Allende Prieto, Lambert & Asplund (2001). Carbon, nitrogen and oxygen show no correlation with temperature; silicon presents a slight dependence on T_{eff}. Carbon and nitrogen abundances are sub-solar, scattered within $\sim$ 0.5 and $\sim$ 0.7 dex, respectively. The oxygen abundance in the Sun represents the upper limit of the distribution of oxygen abundances, with a scatter of $\sim$ 0.7 dex; silicon presents a large dispersion and the bulk of stars present sub-solar abundances, although some stars are scattered around the solar value.

four stars in our sample present silicon abundances higher than 7.50 dex, the mean abundance for the B-stars is subsolar by -0.376 dex. In this analysis, silicon abundances come from the fitting of three lines of the same multiplet, all of them with intermediate intensity. This introduces a dependence of the silicon abundances on the choice of the microturbulence velocity, even in a non-LTE analysis like ours. This may be the source of the correlation between silicon abundances on effective temperature, which shows a slope of $+2.64 \times 10^{-5}$, representing a change of +0.26 dex in the silicon abundance in the temperature range 20,000-30,000K.

Sulfur - Sulfur abundances are based on two weak lines of S III ($\lambda\lambda$ 4361 and 4364 Å) which are on the edge of the wing of Hγ. For this reason, we renormalized both the observed and the theoretical profiles taking the wing of Hγ as the continuum. Sulfur abundances are quite independent of $T_{\rm eff}$ and the mean abundance obtained for this sample is 7.21 ± 0.12; this is 0.12 dex lower than the sulfur abundance in the Sun, 7.33 ± 0.11, reported by Grevesse & Sauval (1998). About 60% of the stars in our sample present sulfur abundance ~solar, considering the uncertainties in our analysis and in the solar value.

6.4.2 Microturbulence Velocity

The distributions of microturbulence velocities derived here are shown in the Figure 6.5 as a function of stellar parameters. In the top panel we plot ξ as a function of effective temperature. The average of the ξ-values for the stars with $T_{\rm eff} \leq 25000$K (11 stars) is $<\xi_{\rm cold}>= 5.9 \pm 2.5$kms^{-1}; on the other hand, the $<\xi_{\rm hot}>$ for the 6 stars with $T_{\rm eff} \geq 30000$K is 8.1 ± 2.2kms^{-1}. Gies & Lambert (1992) also report a similar result for their nonsupergiant stars, with mean microturbulences of 4 and 6 kms^{-1} at $T_{\rm eff} = 17000$K and $T_{\rm eff} = 30000$K, respectively.

High microturbulence velocities are usually associated with the evolutionary stage. For example, Vrancken *et al.* (2000) report $\xi = 12$kms^{-1} (derived from the ionization balance of silicon) for the two supergiants in their sample and $\xi = 9$kms^{-1} for the stars with luminosity class II and III. Their microturbulences derived from the oxygen lines are even higher: 13 kms^{-1} for nonsuperginats and 21 kms^{-1} for supergiants. In the specific case of supergiants, Lamers & Achmad (1994) conclude that the velocity fields resultant of mass loss contribute for an overestimate of the microturbulence velocity in these evolved stars. In our sample, the majority of the targets are main sequence or subgiants stars. The lowest surface gravity is 3.60. Nevertheless, we observe an increasing of the ξ-value as the $\log g$ decreases toward the

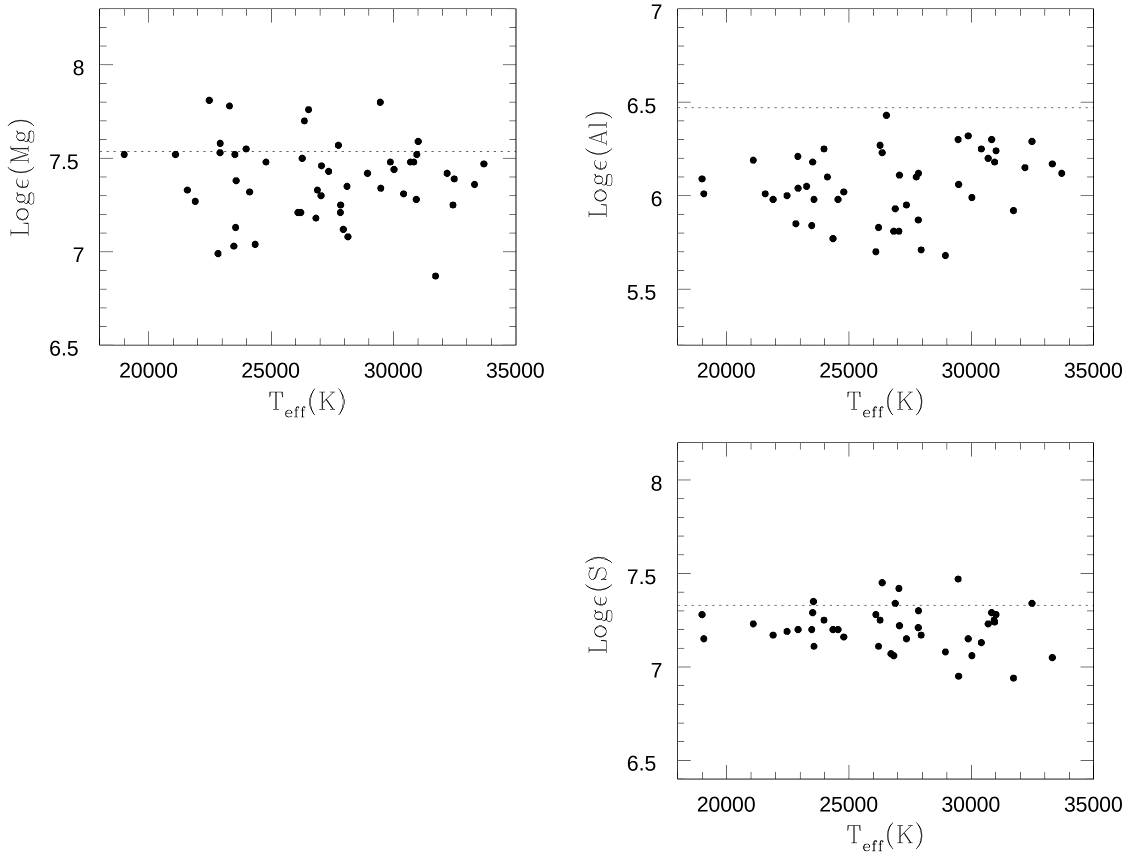

Figure 6.4: Elemental abundances of magnesium, aluminum and sulfur as a function of T_{eff}, for the stars listed in Tables 6.4 and 6.5. The dotted lines represent the solar abundances listed by Holweger (2001 - magnesium: 7.538) and Grevesse & Sauval (1998 - aluminum: 6.47 and sulfur: 7.33). The abundances are independent of the effective temperature. Magnesium shows the largest scatter (~1 dex) and many stars present abundances equal or higher than solar. Aluminum abundances are all sub-solar, except for one star, which presents $\log \epsilon(\mathrm{Al})$ very close to the solar value. Sulfur abundances are less dispersed, with the Sun occupying the upper limit of the distribution.

end of the main sequence. The $< \xi >$ for the stars with $\log g > 4.0$ is $6.1 \pm 2.4 \mathrm{kms}^{-1}$ while $< \xi >= 8.4 \pm 1.8 \mathrm{kms}^{-1}$ for the stars with $\log g \leq 4.0$. Only one star in the "low-gravity" group is also present in the "high-temperature" group (LS 4271). The other stars with $\log g \leq 4.0$ present temperatures varying from 23300 to 29480 K. Therefore, the observed trend of microturbulence with temperature is not purely a reflection of evolutionary effects. In our analysis, however, the microturbulence is introduced as a requirement for the derived abundances be independent of the line strength, with a classical approach. Moreover, the profile fitting is generally better, especially in the wings, for a non-zero microturbulence.

6.4.3 Nebular and Stellar Abundances

For some H II regions associated with target stars in our sample we can find abundances of N, O and S based on analyses of the chemical composition of the gas. These values from the literature are gathered in Table 6.7 and compared with the stellar abundances of the same elements derived here. For the H II regions Sh2 284 and Sh2 285 and the open cluster NGC 6604, which is associated with the H II region Sh2 54, we list the abundances of the individual stars (as we have one star per H II region/cluster, namely HD 46891, BD-00°1491 and BD-12°4978, respectively). For NGC 6611, we list the mean abundance for the 4 stars of our sample belonging to this open cluster. Below, we summarize the main characteristics of each nebular work included in the comparison.

Shaver *et al.* (1983) used radio recombination lines to derive electron temperatures and, subsequently, abundances of N, O, S, Ne and Ar, based on optical spectra of the H II regions NGC 6604, NGC 6611 and SH2 284. Their derived oxygen abundances are accurate within $< 25\%$. Deharveng *et al.* (2000) derived electron temperatures and oxygen abundances from oxygen emission line ratios. NGC 6604 and NGC 6611 were studied by the authors and they quote an uncertainty smaller than 0.08 dex for the abundances that are listed in the table. For comparison, they recalculated the oxygen abundances from line ratios given in the literature; the recomputed abundances of NGC 6604 and Sh2 284 are based on Shaver's line ratios. Fich & Silkey (1991) estimated the abundances of He, N, O, S and Ar in 18 H II regions at the edge of the Galaxy by combining optical spectra and radio recombination lines. The uncertainties in their abundance determinations for Sh2 285 are of the order of 0.10-0.14 dex.

From inspection of Table 6.7, we note that oxygen abundance in the stellar content of NGC 6611 is smaller than in the gas by -0.19 dex, if we consider the abundances of Shaver *et al.* (1983) for M 16. However, if we take into account the oxygen abundance obtained by Deharveng *et al.* (2000) for M 16, the difference $\Delta = \log \epsilon_{\rm star} - \log \epsilon_{\rm gas}$ changes to $+0.04$ dex.

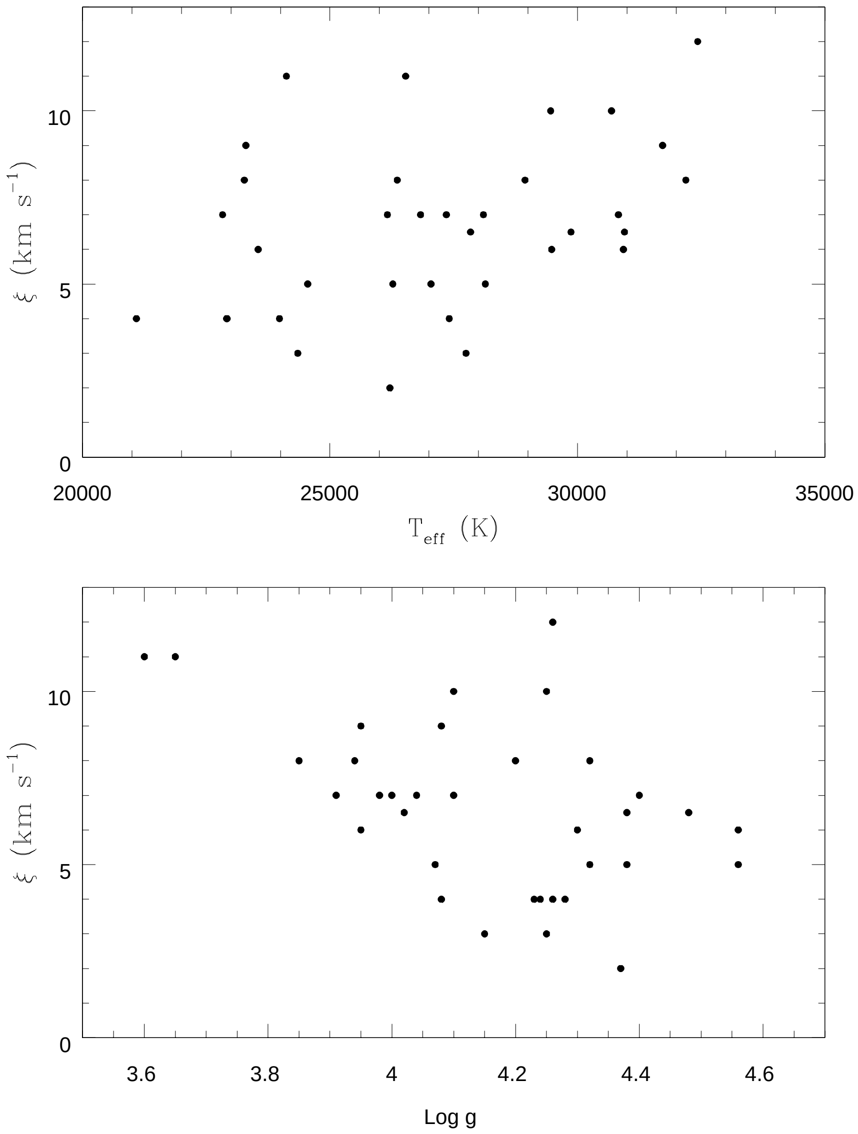

Figure 6.5: Microturbulence velocity as a function of effective temperature (*top panel*) and gravity (*bottom panel*). The mean value of ξ increases for higher temperatures and lower gravities, in the direction of the end of the main sequence.

The nebular abundances of oxygen are supposed to be lower than the stellar abundances as $\sim 20 \pm 5\%$ of the oxygen is expected to be trapped in grains (Meyer *et al.*, 1998) and not accessible in the gaseous abundances. In this sense, Deharveng's oxygen abundance for NGC 6611 is in better agreement with our stellar abundance determination for this H II region. We note that Gummersbach *et al.* (1998) derived non-LTE oxygen abundance of 8.63±0.10 for one star in NGC 6611, which agrees with our determination within the uncertainties. For nitrogen, there is a good agreement between stellar and nebular abundance results, within the uncertainties. The nitrogen abundances derived by the analyses of the stars and the gas show good agreement.

In the case of NGC 6604, the difference between the oxygen abundance of the stars and the gas is Δ=-0.19, considering Shaver's results; Δ=-0.07 and -0.11 if we adopt the two different oxygen abundances obtained by Deharveng *et al.* (2000), using their data or Shaver's data, respectively. For the latter, there is a marginal agreement within the uncertainties. The association between Sh2 54 and NGC 6604, however, is questioned by Caplan *et al.* (2000), who noted that these objects seem spatially disconnected.

The oxygen abundances in the gas of Sh2 284 obtained by Shaver *et al.* (1983) and Deharveng *et al.* (2000) are larger than our stellar abundance ($\log \epsilon(\mathrm{O})=8.47\pm0.09$ for the star HD 48691) by 0.11 and 0.19 dex, respectively. This is consistent with the expected oxygen depletion within the errors. On the other hand, the nitrogen abundance in the stellar photosphere is 0.29 dex higher than in the gas, exceeding the uncertainties. The chemical composition of the gas in H II region Sh2 285 was studied by Fich & Silkey (1991), who find $\log \epsilon(\mathrm{N}) = 7.26^{+0.11}_{-0.10}$ and $\log \epsilon(\mathrm{S}) = 6.33^{+0.14}_{-0.13}$ (they do not list oxygen abundance for Sh2 285). The nitrogen abundance show marginal agreement, considering the uncertainties. The sulfur abundances, however, show a large difference star−gas (Δ=+0.62 dex) that could not be explained by the errors involved in the chemical analyses.

6.5 Summary and Conclusions

We present a homogeneous database of chemical abundances of B stars constructed by means of non-LTE syntheses. The temperature scale and the surface gravity are derived from a photometric calibration for the reddening-free indice Q coupled to the fitting of broadened wings of Hγ. Microturbulences are obtained by requiring that the O II lines yield abundances independent of the line strength. The non-LTE abundances of carbon, nitrogen, oxygen, magnesium, aluminum, silicon and sulfur are derived from the fitting of non-LTE synthetic profiles to the observed spectra. The pattern of the elemental abundances with respect to the distribution in the Galactic Disk will be explored in a future work: in the present we attempt to derive the absolute abundances using a consistent methodology in order to minimize the possible systematic errors arising from the abundance analysis. The main conclusions of this paper are:

1) The mean elemental abundances, relative to the Sun, show differences that vary from -0.10 dex, as for sulfur, to -0.46 dex, as for aluminum. Although some stars present solar abundances, the bulk of the abundance distributions are sub-solar, even considering the newest (and lowest) solar abundances in the literature. The abundance distributions present a considerable scatter star-to-star; the larger spread is observed for magnesium and silicon, which present also the larger abundance uncertainties. This scatter will be further investigated in terms of the relative stellar positions in the Galactic Disk.

2) The microturbulence velocities derived from the non-LTE analysis show a positive correlation with effective temperature. A negative correlation between surface gravity and microturbulence is also found, with the more evolved stars having larger microturbulence. This trend with temperature, however, cannot be totally attributed to evolutionary effects.

3) A comparison between nebular and stellar abundance is possible for some objects in our sample: for two of them (NGC 6611 and Sh2 284), our stellar oxygen abundances are lower than the nebular by roughly the same amount expected by the depletion of oxygen into grains, considering the uncertainites. The abundances obtained here for NGC 6604 are inconsistent with the nebular abundances listed in the literature for Sh2 54; the connection between these two objects, however, is not certain. Nitrogen abundances in the stellar photospheres show large discrepancies relative to the gaseous components and the differences generally exceed the uncertainty in the analysis. The observed discrepancies may be introduced by the systematic differences in the methods adopted in the chemical analysis of the stellar photospheres and nebulae.

Table 6.7: Stellar and Nebular Abundances

	Stellar (This Study)			Nebular			
Object	$\log \epsilon(\mathrm{N})$	$\log \epsilon(\mathrm{O})$	$\log \epsilon(\mathrm{S})$	$\log \epsilon(\mathrm{N})$	$\log \epsilon(\mathrm{O})$	$\log \epsilon(\mathrm{S})$	Source
NGC 6611	7.61	8.57	7.21	7.65	8.76	-	Shaver *et al.* (1983)
(M 16)	±0.11	±0.09	±0.09	-	8.53	-	Deharveng *et al.* (2000)
NGC 6604	7.55	8.53	-	7.75	8.72	-	Shaver *et al.* (1983)
(Sh2 54)	±0.07	±0.11		-	8.64	-	Deharveng *et al.* (2000) (Shaver's data)
				-	8.60	-	Deharveng *et al.* (2000)
Sh2 284	7.44	8.47	7.08	7.15	8.36	-	Shaver *et al.* (1983)
	±0.14	±0.09	±0.04	-	8.28	-	Deharveng *et al.* (2000) (Shaver's data)
Sh2 285	7.45	8.45	6.95	7.26	-	6.33	Fich & Silkey (1991)
	±0.12	±0.13	±0.24	$^{+0.11}_{-0.10}$	-	$^{+0.14}_{-0.13}$	

Capítulo 7

Os Gradientes Radiais de Abundâncias no Disco Galáctico [1]

Resumo: O objetivo principal deste trabalho é a construção de uma base de dados de abundâncias estelares homogênea e consistente, que possibilite a análise da distribuição das abundâncias de estrelas OB ao longo do disco Galáctico. Os capítulos anteriores apresentam a descrição da metodologia aplicada na construção dessa base de dados, além de discussões a respeito dos padrões locais de abundâncias. Este capítulo é dedicado à análise da distribuição de abundâncias no contexto mais geral do disco Galáctico, focalizando especialmente os gradientes radiais de metalicidade. A amostra analisada cobre uma região compreendida entre 4.4 e 12.9 kpc do centro da Galáxia, considerando que o Sol se encontra a 7.6 kpc do centro Galáctico. De maneira geral, os gradientes determinados aqui são menos acentuados do que os resultados obtidos pelos trabalhos mais recentes sobre gradientes radiais de abundâncias estelares: para o oxigênio, que apresenta o resultado mais robusto dentre os elementos analisados, foi obtido um gradiente de $-0.031\,\mathrm{dex\,kpc^{-1}}$. A nossa amostra foi ampliada com a inclusão de 10 estrelas localizadas nas regiões interna ($2.7 < R_g < 3.8$ kpc) e externa ($10.1 < R_g < 15.7$ kpc) do disco, com base em dados espectroscópicos da literatura (as temperaturas efetivas e abundâncias em não-ETL foram calculadas de acordo com as nossas escalas). O gradiente de oxigênio para a amostra estendida é mais inclinado ($-0.043\,\mathrm{dex\,kpc^{-1}}$), sendo que a modificação na magnitude do gradiente foi introduzida principalmente pela inclusão das estrelas mais próximas do centro Galáctico.

---

[1] **Daflon, S. & Cunha, K. (2002b) a ser submetido (Paper V)**

7.1 Introduction

Chemical evolution models of the Galaxy describe the history of its chemical composition. These models basically put together stellar evolution and nucleosynthesis, the stellar initial mass function and the star formation rate with assumed initial conditions, and derive solutions to the differential equations that describe the recycling of the gas. The end products of the models must reproduce and explain certain observational constraints, such as the age-metallicity relation, the metallicity gradients in the Galactic disk and the chemical composition of the Sun. Reliable observational data are thus crucial in constraining the choice of adopted assumptions in the construction of the chemical evolution models.

One very important observational constraint for the chemical evolution models is the distribution of the abundances in the Galactic disk as a function of the distance to the Galactic center: the radial metallicity gradients. Besides the Milky Way, radial gradients are commonly observed in external spiral and elliptical galaxies (Henry & Worthey, 1999). In these cases, individual objects are not resolved and the metallicity is traced by photometric properties. In our Galaxy, such gradients may be determined by the analysis of the chemical composition of ionized gas or stellar photospheres; the exact values of these gradients, however, still remain somewhat uncertain.

Consider oxygen, for example; the radial gradient of oxygen based on the analysis of H II regions derived by Shaver *et al.* (1983) is -0.07 $\mathrm{dex\,kpc^{-1}}$. The same gradient is obtained for oxygen by Maciel & Köppen (1994) based on planetary nebulae abundances. Meanwhile, the analyses of young stars of that time (e.g., Fitzsimmons *et al.* 1990, Kaufer *et al.* 1994) suggested an almost null gradient. Definite conclusions concerning the stellar data, however, are limited by two points in these abundance analyses: *(i)* non-homogeneous abundance data are derived with the assumption of LTE, introducing systematic errors in abundance determination, and, *(ii)* the stellar samples are rather small. Recently, Gummersbach *et al.* (1998) and Rolleston *et al.* (2000) reanalyzed the chemical compositions of B stars in the Galactic disk and obtained gradients of the order of -0.07 $\mathrm{dex\,kpc^{-1}}$ for oxygen. The comprehensive study of Gummersbach *et al.* was based on non-LTE abundances, however, it was restricted to a small sample of 16 B stars. Rolleston *et al.* (2000) extended the stellar sample to 77 B stars of the disk. They adopted LTE line formation, although this approach is not necessarily a good one in early-type stars analyses, since the magnitude of the non-LTE corrections is a function of T_{eff} and $\log g$ and their study was based on a sample of stars with a relatively large interval of T_{eff}'s, from 17500 to 33500 K. Concerning the value of slope itself, an agreement between nebular and stellar abundances gradients was achieved. New difficulties arise, however, when the most recent works on the nebular gradients of oxygen are considered, which tend now to find flatter gradients: Deharveng *et al.* (2000) obtained a gradient of $-0.039\,\mathrm{dex\,kpc^{-1}}$ for oxygen in H II regions; Martins & Viegas (2001) find a gradient of $-0.054\,\mathrm{dex\,kpc^{-1}}$ for planetary nebulae. This inconsistency is observed also for nitrogen. For the other elements, carbon, magnesium, aluminum and silicon, abundances are obtained only in stellar photospheres, whereas so far systematic studies of sulfur abundances were only restricted to the gas (we note that in this study we present for the first time a large database of non-LTE abundances of sulfur in OB stars).

Clearly, the magnitudes of the radial abundance gradients are still poorly established. Concerning the OB stars, an analysis of the radial gradients that is based on a homogeneous and self-consistent abundance database, using non-LTE calculations, is still needed to discuss in detail the abundance patterns in the Galactic disk. In Papers I through IV we have presented and discussed a methodology based on the fitting of synthetic non-LTE profiles to high resolution observed spectra, which was applied to a sample of OB stars in order to construct a homogeneous database of stellar abundances. Here, this set of abundance data is analyzed in terms of radial gradients in the Galactic disk.

7.2 The Observational Data

This study is based on non-LTE abundances obtained in a series of Papers (Paper I – IV) of late-O to early-B type stars members of OB associations, open clusters, and H II regions along the Galactic disk. The observational data used in the abundance analysis consist of high resolution spectra obtained at McDonald Observatory, University of Texas, Austin, USA and the European Southern Observatory, La Silla, Chile (ESO). The spectra from McDonald are of high resolution (R=60,000) and high signal-to-noise ($S/N \geq 150$) obtained with the 2.1 m telescope coupled to the Sandiford echelle spectrograph. Spectra with lower resolution (R∼12,000), centered on H_γ, were also obtained with the 2.7 m telescope. The sample observed at McDonald is basically of OB associations within 2.5 kpc from the Sun.

High resolution (R$\sim$48,000) spectra were also obtained with the 1.52 m telescope at ESO; the sample stars observed in the South are distributed along the Galactic disk, ranging from 4.4 to 12.9 kpc in Galactocentric distance. Together, the samples observed at McDonald and ESO contain 70 OB-star members of 25 OB associations, open clusters, and H II regions (hereafter, these objects will be referred to as "clusters", for simplicity).

7.2.1 The Non-LTE Abundances

Homogeneity of the chemical data is an important part of any analysis of the distribution of the chemical abundances in the Galactic disk. The use of different methodologies (e.g., LTE and non-LTE abundance determinations) may introduce systematic differences in the abundance results and affect the magnitudes of the radial gradients. For this reason, we adopted one unique methodology throughout the analyses of OB stars in Papers I-IV, producing homogeneous scales of effective temperature, gravity, and abundances. The chemical abundances of C, N, O, Mg, Al, Si and S for the individual stars were derived from the fitting of theoretical profiles to the observed spectra; non-LTE effects were considered in the line formation.

One assumption made in the calculation of the gradient was to consider that the cluster abundances are represented by the average of the abundance of its studied stellar members. For all of the studied clusters we analyzed a number of stars that varied from 1 to 5 members, (exception being the Cep OB2 association, for which we analyzed 17 OB stars). The mean elemental abundances adopted for each cluster are listed in Table 7.1, together with the number of stars studied in each cluster. In this table we also list the non-LTE abundances of C, N, O and Si derived by Cunha & Lambert (1994) for the Ori OB1 association; we note that the stellar parameters and abundances derived for Ori OB1 are in the same scale of the rest of our sample and thus may be directly compared.

Table 7.1: Cluster Abundances

Object	$\log\epsilon(C)$[n]	$\log\epsilon(N)$[n]	$\log\epsilon(O)$[n]	$\log\epsilon(Mg)$[n]	$\log\epsilon(Al)$[n]	$\log\epsilon(Si)$[n]	$\log\epsilon(S)$[n]
Sh2 47	8.21[1]	7.53[1]	8.52[1]	7.48[1]	6.32[1]	7.40[1]	7.15[1]
Ser OB1	8.23 ± 0.17[2]	7.61 ± 0.11[4]	8.57 ± 0.09[4]	7.39 ± 0.14[4]	6.10 ± 0.24[3]	7.13 ± 0.23[4]	7.21 ± 0.09[3]
Sh2 32	8.20[1]	7.70 ± 0.01[2]	8.66 ± 0.09[2]	7.50[1]	6.27[1]	7.26 ± 0.17[2]	7.25[1]
NGC 6204	8.12[1]	7.72[1]	8.68[1]	7.32[1]	6.10[1]	7.57[1]	–
Trumpler 27	8.45[1]	7.81[1]	8.55 ± 0.04[2]	7.80[1]	6.30[1]	7.48 ± 0.06[2]	7.47[1]
NGC 6231	8.20 ± 0.13[4]	7.62 ± 0.21[4]	8.50 ± 0.02[4]	7.32 ± 0.24[3]	5.97 ± 0.18[4]	7.10 ± 0.25[4]	7.19 ± 0.03[4]
NGC 6604	–	7.55[1]	8.53[1]	7.57[1]	6.10[1]	7.20[1]	–
Ara OB1	8.29[1]	7.62 ± 0.01[2]	8.46 ± 0.08[2]	7.40 ± 0.17[2]	6.19[1]	7.11 ± 0.08[2]	7.24 ± 0.02[2]
Vul OB1	–	7.77 ± 0.33[2]	8.46 ± 0.25[2]	7.45 ± 0.20[2]	6.25 ± 0.20[2]	7.44 ± 0.08[2]	7.20 ± 0.11[2]
Stock 16	8.50[1]	7.77[1]	8.48[1]	7.25[1]	6.12[1]	7.08[1]	7.30[1]
Sct OB2	8.30 ± 0.06[2]	7.61 ± 0.07[2]	8.54 ± 0.05[2]	7.73 ± 0.04[2]	6.33 ± 0.14[2]	7.72 ± 0.04[2]	7.45[1]
NGC 4755	8.26 ± 0.06[3]	7.62 ± 0.11[3]	8.58 ± 0.07[4]	7.51 ± 0.27[4]	6.14 ± 0.15[2]	7.07 ± 0.08[4]	7.27 ± 0.08[3]
IC 2944	8.20[1]	7.46 ± 0.07[2]	8.52 ± 0.11[2]	7.41 ± 0.16[2]	6.01 ± 0.28[2]	7.08 ± 0.08[2]	7.42[1]
Cyg OB3	8.15 ± 0.23[2]	7.60 ± 0.15[4]	8.58 ± 0.12[5]	7.46 ± 0.24[4]	6.10 ± 0.17[4]	7.38 ± 0.17[5]	7.26 ± 0.07[3]
Cyg OB7	8.05[1]	7.83 ± 0.25[3]	8.69 ± 0.20[3]	7.36 ± 0.02[2]	6.13 ± 0.21[2]	7.15 ± 0.09[3]	7.11[1]
Lac OB1	8.36 ± 0.02[3]	7.68 ± 0.11[5]	8.67 ± 0.16[5]	7.50 ± 0.03[3]	6.10 ± 0.07[4]	7.26 ± 0.20[5]	7.20 ± 0.11[4]
Cep OB2	8.17 ± 0.09[5]	7.57 ± 0.14[17]	8.53 ± 0.14[17]	7.41 ± 0.21[16]	6.01 ± 0.18[16]	7.25 ± 0.30[17]	7.20 ± 0.10[6]
Cep OB3	–	7.56 ± 0.06[2]	8.54 ± 0.13[3]	7.20 ± 0.21[3]	5.85 ± 0.14[3]	7.09 ± 0.18[3]	7.14 ± 0.07[3]
Ori OB1*	8.39 ± 0.11[15]	7.76 ± 0.13[15]	8.72 ± 0.13[18]	–	–	7.13 ± 0.13[18]	–
Mon OB2	–	7.22[1]	8.11[1]	6.87[1]	5.92[1]	7.14[1]	6.94[1]
Sh2 247	–	7.48[1]	8.21[1]	7.25[1]	–	7.43[1]	–
NGC 2414	8.12[1]	7.30 ± 0.13[2]	8.21 ± 0.22[2]	7.08[1]	6.05[1]	6.72[1]	–
Sh2 253/Bo 1	8.00[1]	7.36[1]	8.46[1]	6.99[1]	5.85[1]	6.96[1]	–
NGC 1893	8.00[1]	7.32 ± 0.01[2]	8.36 ± 0.13[2]	7.18[1]	5.81[1]	6.77 ± 0.06[2]	7.06[1]
Sh2 284/Do 25	8.01[1]	7.44[1]	8.47[1]	7.42[1]	5.68[1]	6.87[1]	7.08[1]
Sh2 285	8.10[1]	7.45[1]	8.45[1]	7.34[1]	6.06[1]	7.27[1]	6.95[1]

* non-LTE abundances from Cunha & Lambert (1994)

7.2.2 The Distances

The Galactocentric distances R_g, projected onto the Galactic plane, are calculated from

$$R_g^2 = R_\odot^2 + (d\cos b)^2 - 2R_\odot d \cos l \cos b,$$

where $R_\odot$ is the Galactocentric distance of the Sun, d is the distance between the object and the Sun and l, b are the Galactic longitude and latitude of the object, respectively.

In this study, the distance of the Sun to the Galactic center is taken to be 7.6 kpc. This value was defined by Maciel (1993) based on the space distribution of globular clusters, assuming that the clusters are spherically distributed around the Galactic center. Similar values for the Galactocentric distance of the Sun have been recently derived. Dambis *et al.* (1995) derived the parameters of the Galactic rotation curve from kinematic data of classical Cepheids, obtaining $R_\odot$=7.1±0.5. Glushkova *et al.* (1998) obtained $R_\odot = 7.3\pm0.3$ kpc, using kinematic data for a combined sample including open clusters, red supergiants and Cepheids to derive rotation-curve parameters for the Galaxy. The newest values of $R_\odot$, in general, tend to be smaller than 8 kpc, which is smaller than the values frequently used in the past that were as large as 10 kpc.

The distances to the Sun for the objects in our sample come from the literature. In general, the distances to the open clusters and OB associations are derived from a color-magnitude diagram or from spectral type *vs.* intrinsic color calibrations; the typical error of the distances from the Sun are inferred to be of the order of 10% in these cases. An inspection of different literature values for a given cluster, however, indicates that the discrepancy among the listed values may be higher than the assigned uncertainties in the individual studies. For the nearest objects in our sample, the OB associations Ori OB1, Lac OB1 and Cep OB2, distances based on HIPPARCOS data for member stars (de Zeeuw *et al.* 1999) are available. When more than one distance determination for a given cluster was available in the literature, we adopted a mean value as the cluster distance. In Table 7.2 we list the Galactic coordinates and the different distances to the Sun for the studied clusters. Also listed are the adopted mean distance with the corresponding dispersion and the Galactocentric distance derived. In general, the dispersions are $\sim$ 20%; however, 8 objects, namely NGC 6204, NGC 6604, NGC 4755, Vul OB1, Cep OB2, Sh2 247, NGC 1893 and Sh2 285, present larger dispersions (20% - 50%).

The distances of the H II regions are more critical; these are the most distant objects in our sample, both in the direction of the Galactic center (Sh2 47) and in the anticenter direction (Sh2 247, Sh2 253, Sh2 284 and Sh2 285). Most of these distances are based on the analyses of few stars, or even one star. However, published distances for Sh2 47, Sh2 253 and Sh2 284 show little discrepancy and are consistent within the expected errors. On the other hand, the distances listed for the H II region Sh2 285 are quite discrepant: Lahulla (1987) considered 5 stars and obtained a spectroscopic distance of 6.4 kpc. Moffat *et al.* (1979) derived d=6.9 kpc based on UBV photometry and spectral types of two stars; the same distance was obtained by Turbide & Moffat (1993) from the fitting of theoretical isochrones for eight stars. Rolleston *et al.* (1994) derived a smaller distance of d=4.3 kpc, based on theoretical evolutionary tracks, for two members of Sh2 285. Here, we adopt the mean distance of 5.9 ± 1.4 kpc, which puts Sh2 285 at a distance of 12.9 kpc from the Galactic center. Sh2 247 is at 2.2 kpc from the Sun, according to Lahulla (1987), while Moffat *et al.* (1979) put this H II region at d=3.5 kpc; the adopted distance for Sh2 247 is 2.8 ± 0.9, corresponding to R_g=10.4 kpc. Also critical is the distance of the open cluster NGC 1893, which varies from 3.6 kpc (Cuffey, 1973) to 6.02 kpc (Marco *et al.* , 2001). Here we adopted $< d >= 4.5 \pm 1.0$ kpc for this cluster, from which we derive R_g=12.5 kpc.

In Figure 7.1 we show the positions of the clusters of our sample projected onto a section of the Galactic plane. The inclined lines superposed to the points represent the range of Galactocentric distances defined by the smallest and largest distances for a given cluster. The dotted lines depict concentric circles with Galactocentric distances of 5, 10 and 15 kpc. The dashed line connects the Sun to the Galactic center and represents the direction of $l = 0°, 180°$.

7.3 The Radial Gradients

7.3.1 Our Results

Radial Gradients can be obtained from a linear fit of the form $a + bx$ to the non-LTE abundances as a function of Galactocentric distance; the radial gradients for each element are represented by the coefficient b. The coefficients of the best fits, $a \pm \sigma a$ and $b \pm \sigma b$, and correlation coefficients R are listed in Table 7.3 for each element studied, together with

Table 7.2: Cluster Distances

Cluster	$l(^\circ)$	$b(^\circ)$	$\mathrm{d}_\odot$(kpc)	$<\mathrm{d}_\odot>$(kpc)	R_g(kpc)
Sh2 47	15.3	0.1	$3.7^1, 3.1^2$	3.4±0.4	4.4
Ser OB1	17.0	0.8	$2.19^3, 2.5^4, 2.6^5, 1.68^6$	2.2±0.4	5.5
Sh2 32	7.3	-2.0	$1.8^8, 2.2^9$	2.0±0.3	5.6
NGC 6204	338.3	-1.1	$2.51^3, 2.6^4, 1.32^6, 1.94^7$	2.1±0.6	5.7
Trumpler 27	355.1	-0.7	$2.0^5, 1.65^{11}, 2.1^{32}$	1.9±0.2	5.7
NGC 6231	343.5	1.2	$1.8^4, 1.6^5, 1.77^6, 2.0^{10}$	1.8±0.2	5.9
NGC 6604	18.3	1.7	$0.70^4, 2.1^5, 1.64^{12}$	1.5±0.7	6.2
Ara OB1	336.3	-1.4	$1.38^3, 1.4^6, 1.59^7, 1.1^{13}$	1.4±0.2	6.3
Vul OB1	59.4	-0.1	$2.0^3, 2.54^7, 3.5^{17}$	2.7±0.7	6.6
Stock 16	306.1	0.1	$1.9^5, 2.0^{14}$	1.9±0.1	6.7
Sct OB2	39.0	7.6	$1.0^3, 1.17^{15}$	1.1±0.1	6.8
NGC 4755	303.2	2.5	$2.34^4, 1.03^6, 1.9^{16}$	1.8±0.7	6.8
IC 2944	294.6	-1.4	$2.1^4, 2.0^5, 1.95^6, 2.2^{18}$	2.1±0.1	7.0
Cyg OB3	73.5	2.0	$2.29^3, 1.9^5, 2.31^7$	2.2±0.2	7.3
Cyg OB7	90.0	2.0	0.83^3	0.83	7.6
Lac OB1	96.8	-16.1	$0.6^3, 0.63^7, 0.368^{19}$	0.6±0.1	7.7
Cep OB2	99.2	3.8	$0.83^3, 0.95^5, 0.96^7, 0.615^{19}$	0.8±0.2	7.8
Cep OB3	110.4	2.8	$0.87^3, 0.725^6, 0.84^7$	0.8±0.1	7.9
Ori OB1	205.0	-17.4	$0.5^3, 0.43^4, 0.56^7, 0.438^{19}$	0.5±0.1	8.0
Mon OB2	206.5	-2.1	$1.51^3, 1.62^6, 1.63^7, 1.67^{20}$	1.6±0.1	9.1
Sh2 247	188.9	0.8	$3.5^{23}, 2.2^{24}$	2.8±0.9	10.4
NGC 2414	231.0	2.0	$3.98^{21}, 4.2^{22}$	4.1±0.1	10.7
Sh2 253/Bo 1	192.4	3.2	$4.4^{23}, 4.8^{27}, 4.06^{29}$	4.4±0.4	11.9
NGC 1893	173.6	-1.7	$3.7^6, 3.6^{25}, 4.3^{26}, 4.8^{27}, 6.02^{28}$	4.5±1.0	12.1
Sh2 284/Do 25	211.9	-1.3	$5.2^{23}, 5.6^{30}, 5.5^{33}$	5.4±0.2	12.5
Sh2 285	213.9	-0.6	$6.9^{23,30}, 4.3^{31}, 6.4^{24}$	5.9±1.4	12.9

1: Crampton *et al.* (1978), 2: Lahulla (1985), 3: Humphreys (1978), 4: Alter *et al.* (1970), 5: Feinstein (1994), 6: Becker & Fenkart (1971), 7: Mel'nick & Efremov (1985), 8: Blitz *et al.* (1982), 9: Vogt & Moffat (1975), 10: Crampton *et al.* (1971), 11: van der Hucht *et al.* (1980), 12: Moffat & Vogt (1975a), 13: Kaltcheva & Georgiev (1992), 14: Crampton (1971), 15: Reichen *et al.* (1990), 16: Shobbrook (1984), 17: Sagar & Joshi (1981), 18: Tovmassian *et al.* (1998), 19: de Zeeuw *et al.* (1999), 20: Pérez (1991), 21: Humphreys & McElroy (1984), 22: Fitzgerald & Moffat (1980),23: Moffat *et al.* (1979), 24: Lahulla (1987), 25: Cuffey (1973), 26: Tapia *et al.* (1991), 27: Fitzsimmons (1993), 28: Marco *et al.* (2001), 29: Moffat & Vogt (1975b), 30: Turbide & Moffat (1993), 31: Rolleston (1994), 32: Moffat *et al.* (1977), 33: Lennon *et al.* (1990).

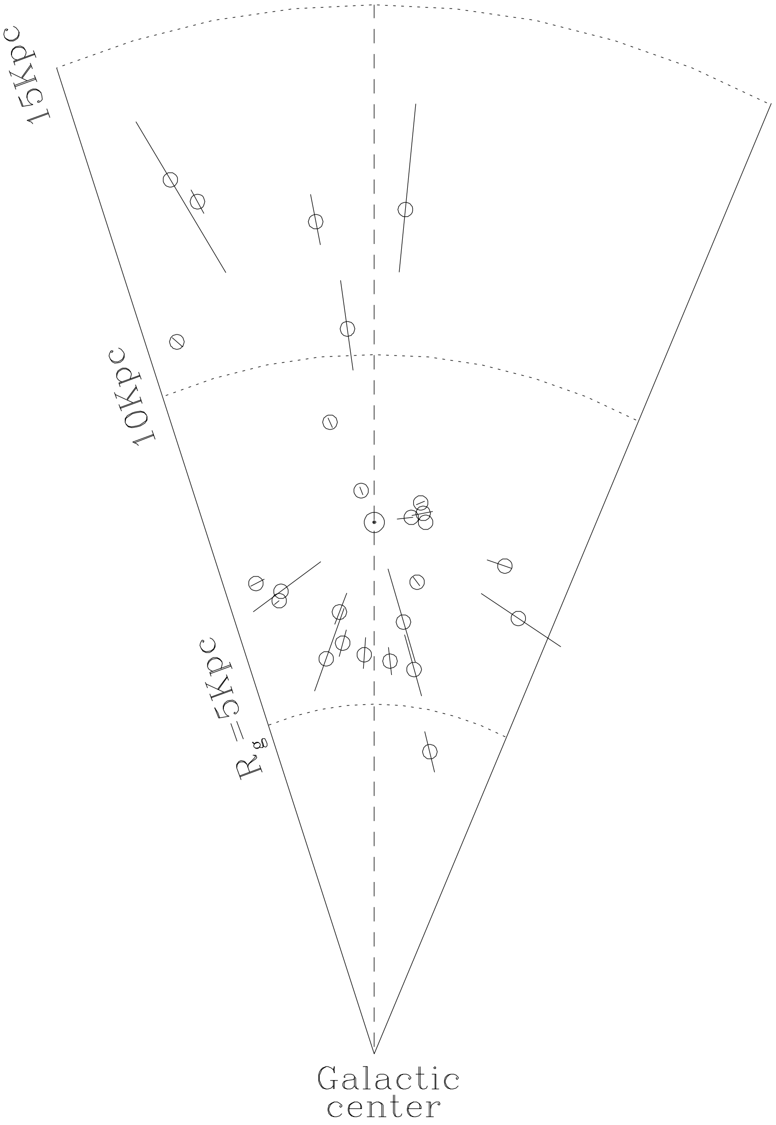

Figure 7.1: The distribution of the observed objects projected onto a section of the Galactic Plane. The Sun is represented at $R_\odot$=7.6 kpc. The dashed line connects the Sun to the Galactic center and represents the direction $l = 0, 180°$; concentric circles at the distances of 5, 10 and 15 kpc of the Galactic center are depicted by dotted lines. The inclined lines superposed to the points show the range of R_g calculated from different distances in the literature.

the number, n, of objects used in each fit. The gradients of the seven elements studied are shown in Figure 7.2: the points represent the mean abundances computed for the clusters (Table 7.1) and the straight lines represent the gradients obtained from linear fits. The radial gradients for all the elements studied could be represented by a single slope of -0.041 ± 0.007. The Sun is shown at a Galactocentric distance of 7.6 kpc. The standard solar abundances adopted here as a reference are C: 8.592 ± 0.108, N: 7.931 ± 0.111, Mg: 7.538 ± 0.060 and Si: 7.536 ± 0.049, from Holweger (2001); Al: 6.47 ± 0.07 and S: 7.33 ± 0.11, from Grevesse & Sauval (1998). The oxygen abundance adopted for the Sun is 8.72 ± 0.03, representing the average between the solar oxygen abundances quoted by Holweger (2001: 8.736 ± 0.078) and Allende Prieto *et al.* (2001: 8.69 ± 0.05). In general, the solar abundances of oxygen, magnesium, silicon and sulfur are at the upper envelope of the stellar abundance distributions obtained for these elements at $R_g = 7.6$ kpc. Magnesium and silicon exhibit large scatters, but we note that these species show the largest abundance uncertainties among the studied elements. The abundance distribution of carbon, nitrogen and aluminum are below the solar values by roughly 0.3 dex. The abundances of carbon and sulfur, derived from weak lines, are not accessible in the stars with high projected rotational velocities and, thus, are not measured in all the objects of our sample.

Table 7.3: Radial Gradients of Elemental Abundances ($a + bx$)

log(X/H)	a	σa	b	σb	n	R
C	8.466	0.085	-0.033	0.010	21	-0.64
N	7.916	0.087	-0.043	0.011	26	-0.68
O	8.745	0.086	-0.031	0.010	26	-0.58
Mg	7.714	0.126	-0.044	0.015	25	-0.55
Al	6.448	0.086	-0.048	0.011	24	-0.72
Si	7.580	0.148	-0.049	0.018	26	-0.60
S	7.488	0.098	-0.037	0.012	20	-0.62

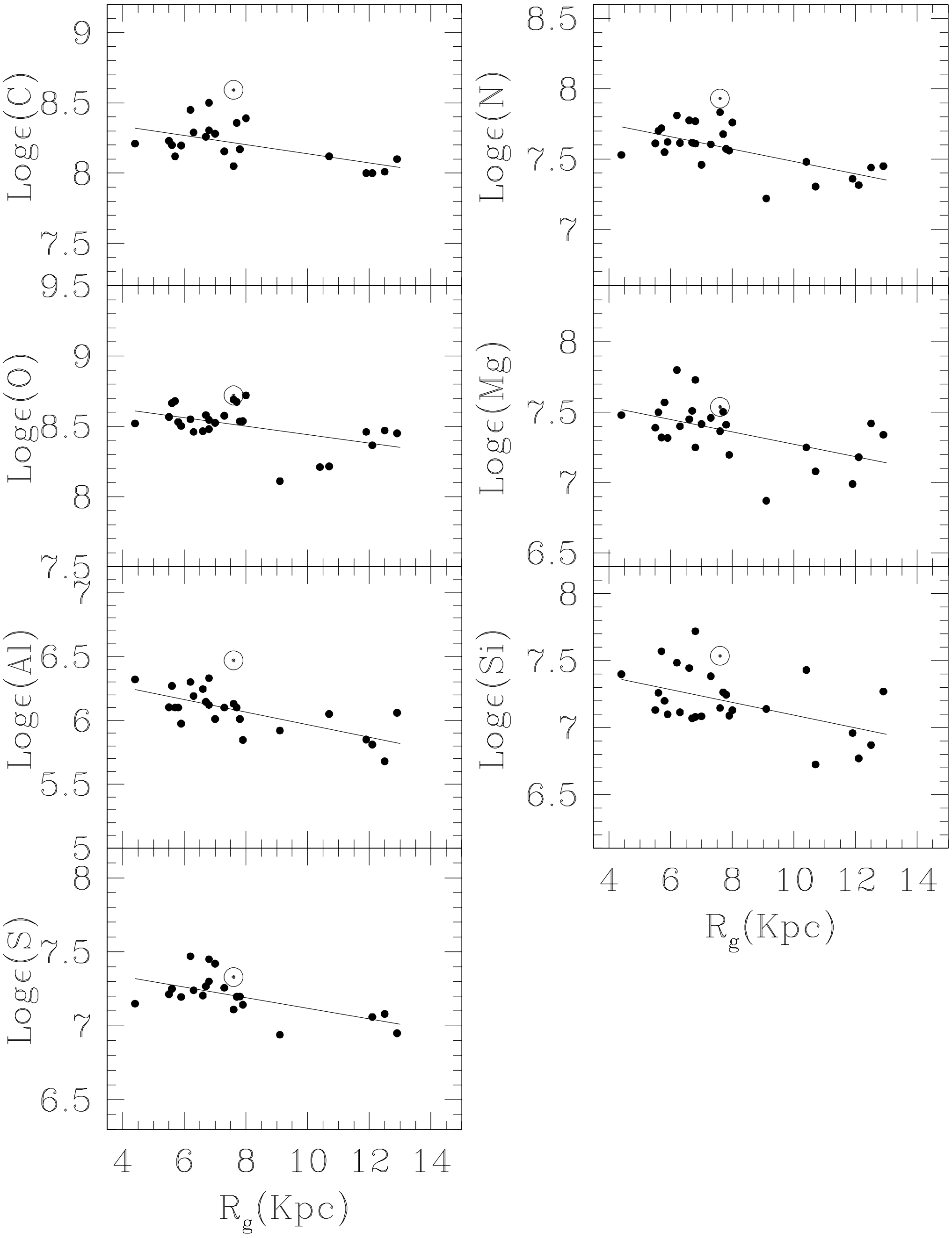

Figure 7.2: The elemental gradients in the Galactic disk derived for C, N, O, Mg, Al, Si and S. The abundances are represented by the mean value for each cluster listed in Table 7.1. The Sun is at $R_{g\odot}$=7.6kpc; solar abundances are from Holweger (2001 - C, N, Mg and Si) and Grevesse & Sauval (1998 - Al and S). The adopted oxygen abundance for the Sun, which is 8.72, is the average between Holweger (2001) and Allende Prieto *et al.* (2001).

7.3.2 Uncertainties

The derived gradients are subject to uncertainties imparted by both the determination of non-LTE abundances and adopted distances for the studied clusters. It is important to address the impact of these errors on the derived magnitude of the abundance gradient. A typical uncertainty in the derived abundances is 0.15 dex and 10% is the adopted error in the distance determinations.

In order to quantify these effects, we take oxygen, for example, and for each parameter (distances and oxygen abundances), separately, we applied random corrections with a maximum value equal to the respective uncertainty. A new gradient was then calculated considering the perturbed distances and abundances. This procedure was repeated 5,000 times and the average of the 5,000 new gradients was taken. A mean gradient of $-0.030 \pm 0.001\,\mathrm{dex\,kpc^{-1}}$ was obtained for the random corrections applied to the distances and $-0.030 \pm 0.005\,\mathrm{dex\,kpc^{-1}}$ in the case of the abundances. If the random corrections are applied simultaneously to the distances and oxygen abundances, the mean perturbed gradient is $-0.030 \pm 0.007\,\mathrm{dex\,kpc^{-1}}$. The distribution of the perturbed gradients are shown in the histograms of the Figure 7.3. The dotted line represents the distribution of the oxygen gradients obtained for the random corrections in the oxygen abundances; the solid line refers to the gradients for the distances corrected by 10% and the dashed line shows the distribution of perturbed gradients obtained when the distances and abundances are corrected at the same time. However, based on the discussion of the distances to the most distant objects, one recognizes that the distance uncertainty is probably being underestimated. If the distance uncertainty is increased to 20%, the average gradient obtained for the perturbed distances is $-0.030 \pm 0.002\,\mathrm{dex\,kpc^{-1}}$; in the case of the gradients obtained when both parameters are corrected, the average gradient is not changed. For both parameters, distances and abundances, random errors produce a normal distribution of perturbed gradients, as expected, but the errors in the abundances impart a larger dispersion around the mean gradient.

NGC 1893, Sh2 247 and Sh2 285 are among the most distant objects in our sample and deserve special attention regarding their distance determinations. Due to their large Galactocentric radii, they are especially important in defining the abundance gradients. The distances listed in the literature for these objects show differences of 35-40% relative to their adopted distances to the Sun. Here we used the mean distances of 4.5 ± 1.0 kpc for NGC 1893,

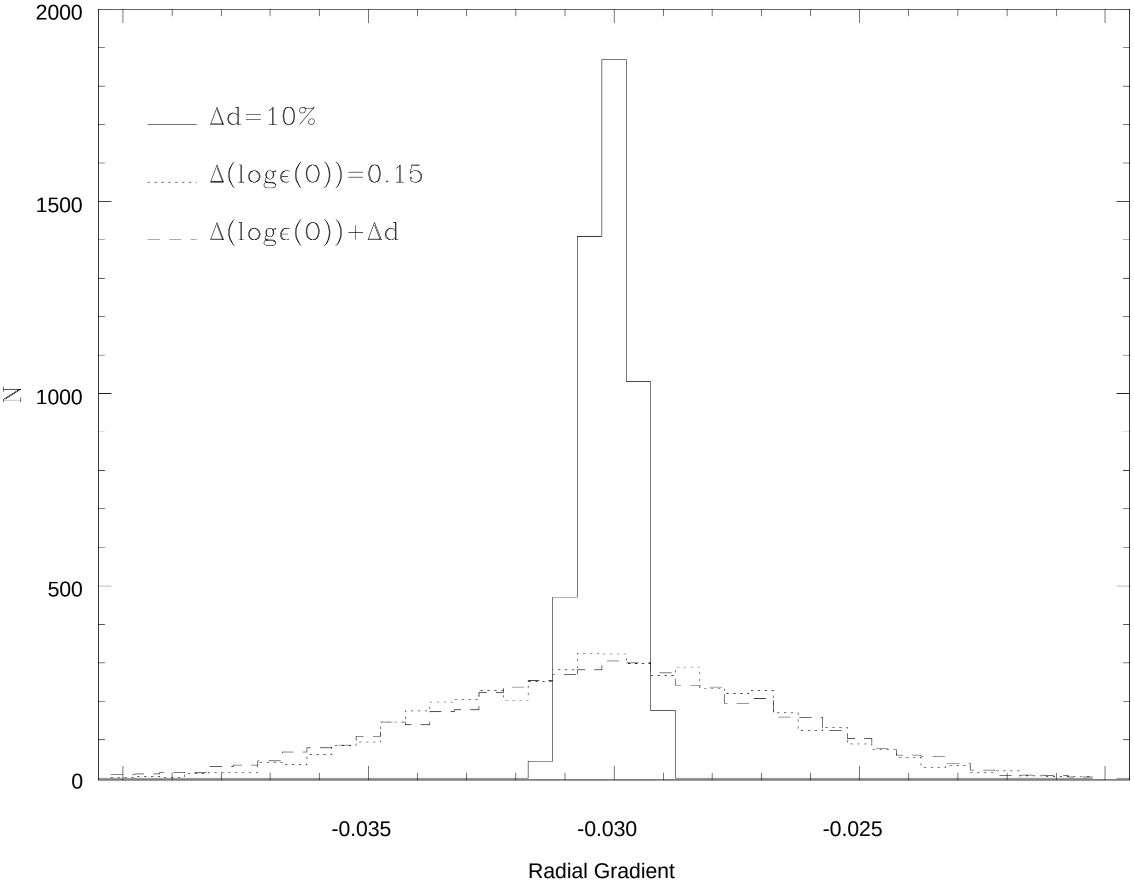

Figure 7.3: The distribution of perturbed radial gradients of oxygen obtained for random corrections applied separately on the distances (±10%, solid line) and oxygen abundances (±0.15 dex, dotted line). The dashed histogram represents the distribution of perturbed gradients when both parameters are corrected simultaneously.

2.8 ± 0.9 kpc for Sh2 247, and 5.9 ± 1.4 kpc for Sh2 285. However, if smaller distances were taken to these objects (3.6 kpc (Cuffey 1973), 2.2 kpc (Lahulla 1987) and 4.3 kpc (Rolleston *et al.* 1994), respectively), the oxygen gradient would be $-0.036 \pm 0.011\,\mathrm{dex\,kpc^{-1}}$. On the other hand, the oxygen gradient would flatten to $-0.028 \pm 0.010\,\mathrm{dex\,kpc^{-1}}$ if we had adopted d=6.02 kpc (Marco *et al.* 2001) for NGC 1893. We note that these values are, however, within the uncertainty in the oxygen gradient in the Table 7.4 (0.010 dex).

The adopted distance of the Sun to the Galactic center ($R_{\odot}$=7.6 kpc - Maciel, 1993) is smaller than the values frequently used, which are 10 and 8.5 kpc; however, the use of larger values of $R_\odot$ translates a maximum difference of 0.03 kpc in the Galactocentric distances of the clusters and will not change significantly the radial gradient.

7.4 Discussion

7.4.1 Comparison With the Literature

In order to enlarge this study as much as possible, we attempted to include a sample of stars located out of our interval of Galactocentric distances and not in our sample, that had been analyzed in previous studies of the Galactic metallicity gradients using stellar abundances. This was only possible for oxygen, as other for the elements only a small number of measured lines in common with our analysis could be found in the literature. The stellar abundances of targets were not directly taken from the literature, but were analyzed as follows: we used the Q-calibration, adopted throughout our abundance study, in order to derive a new effective temperature for the star and adopted its surface gravity from the literature. We then calculated non-LTE profiles of O II lines that reproduced the published equivalent widths. The Galactocentric distances were also recalculated for $R_\odot$ = 7.6kpc, using the mean distances from the literature, when more than one distance determination was available. The adopted distances and derived non-LTE abundances are listed in Table 7.4.

From Gummersbach *et al.* (1998) we reanalyzed Sh2 217-3, the farthest star and with the lowest abundance in their sample. Our non-LTE oxygen abundance for this star is $\log\epsilon(O) = 7.95 \pm 0.11$, while Gummersbach *et al.* derived 7.89 ± 0.10. With this star added to our sample we obtained a gradient of oxygen of $-0.041 \pm 0.011\,\mathrm{dex\,kpc^{-1}}$, which agrees marginally with our original result, within the uncertainties. We also reanalyzed the stars in the outer part of the disk studied by Rolleston *et al.* (2000). We selected the most distant stars in the Rolleston *et al.* that we had not observed: RLWT 13, RLWT 41, Sh2 208-6, Sh2 289-2, Sh2 289-4 and Sh2 283-2. The equivalent widths for these stars are from Smartt *et al.* (1996b), the same source of spectroscopic data adopted by Rolleston *et al.* The new oxygen abundance gradient obtained, with the addition of these six stars, is $-0.032{\pm}0.009\,\mathrm{dex\,kpc^{-1}}$, in excellent agreement with our standard value. This suggest that, even though our sample does not cover the very outer parts of the disk, the magnitude of the radial gradient is not

Table 7.4: Derived Abundances and Adopted Distances.

Cluster	$l(^\circ)$	$b(^\circ)$	$\mathrm{d}_\odot$(kpc)	$<\mathrm{d}_\odot>$(kpc)	R_g(kpc)	$\log\epsilon(O)$
LS 5130	21.1	−5.6	6.9^1	6.9	2.7	8.68±0.20
LS 4419	351.8	−5.9	5.2^1	5.2	2.6	8.78±0.19
LS 4784	1.7	−6.1	3.8^1	3.8	3.8	9.06±0.36
RLWT 41	184.0	0.5	$3.2^4, 1.9^5$	2.5	10.1	8.0±0.06
Sh2 217	159.2	3.3	$5.2^2, 4.29^3$	4.7	12.1	7.95±0.11
RLWT 13	186.0	0.5	$7.1^4, 4.6^5$	5.8	13.4	8.47±0.14
Sh2 208	151.0	2.0	$7.6^2, 9.4^3, 3.4^5, 10.0^6$	7.6	14.7	8.37±0.23
Sh2 289	219.0	−4.6	$7.9^2, 7.8^5, 8.51^7$	8.1	14.7	8.22±0.06
Sh2 283	210.0	−2.4	$9.1^2, 9.7^5, 7.31^7$	8.7	15.7	8.18±0.10

1: Smartt *et al.* (2001), 2: Moffat *et al.* (1979), 3: Caplan *et al.* (2000), 4: Philip *et al.* (1990), 5: Smartt *et al.* (1996c), 6: Lahulla (1985), 7: Turbide & Moffat (1993)

determined by only the outermost stars.

Following the idea of incorporating as much as possible of literature data to this study, we included three stars of Smartt *et al.* (2001), located in the inner part of the Galactic disk. (For the coolest star, LS 5127, we obtained a T_Q 16% higher than that quoted by the authors; this, together with only 4 O II lines in common with our line lists, could introduce a large uncertainty in the analysis and we elect not to include this star). These stars, reanalyzed by adopting our temperature scale and non-LTE line formation, were combined with our sample, yielding a new gradient of $-0.041 \pm 0.010\,\mathrm{dex\,kpc^{-1}}$ for the oxygen. Despite the change in the slope (of approximately the error of the fit), we note that the stars towards the Galactic center produce a larger effect on the oxygen gradient than the outermost stars. In Figure 7.4 we show the cluster abundances as a function of Galactocentric distance for our sample (filled circles), with the addition of our derived abundances for the stars discussed above: stars from Rolleston *et al.* (2000 – originally analyzed by Smartt *et al.* , 1996b,c) and Smartt *et al.* (2001) are represented by open triangles and open squares, respectively. The star Sh2 217-3 from Gummersbach *et al.* (1998) is represented by the open pentagon. The gradient obtained from this combined sample is $-0.043 \pm 0.008\,\mathrm{dex\,kpc^{-1}}$.

A comparison of the radial distribution of elemental abundances obtained in this study

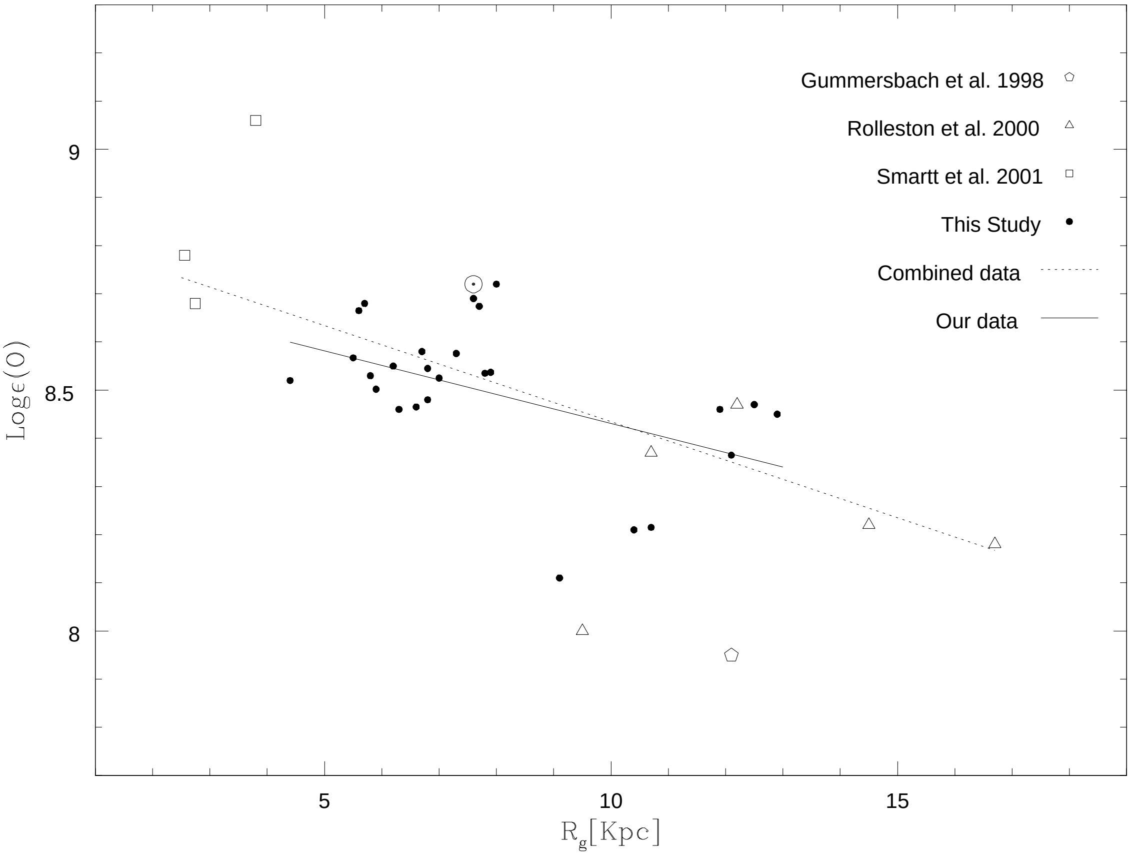

Figure 7.4: Radial gradients of oxygen obtained with the combined sample. The filled circles represent our original sample. The open symbols represent the non-LTE abundances derived from the published equivalent widths: squares are for the stars close to Galactic center of Smartt *et al.* (2001), triangles are the outermost stars of Rolleston *et al.* (2000) and the pentagon is for the star Sh2 217-3 of Gummersbach *et al.* (1998). Our oxygen gradient of $-0.031 \pm 0.010\,\mathrm{dex\,kpc}^{-1}$ is represented by the dotted line and the straight line depicts a gradient of $-0.043 \pm 0.008\,\mathrm{dex\,kpc}^{-1}$.

with previous results from the literature is needed. First, we will focus on the comparison of the oxygen gradient, which tend to show the tightest results within the studied elements. Gummersbach *et al.* (1998) analyzed 16 B stars in the disk within $5.6 < R_g < 13.5$ ($R_\odot$=8.5 kpc). Ten stars with R_g >8 kpc are from Kaufer *et al.* (1994, who originally found an almost null gradient for nitrogen and oxygen, by combining their own LTE abundances with abundances published in the literature), with the addition of six stars lying in the inner disk (R_g <8 kpc). Non-LTE abundances were derived and their resulting gradients are: $-0.036 \pm 0.014\,\mathrm{dex\,kpc^{-1}}$ for carbon, $-0.078 \pm 0.023\,\mathrm{dex\,kpc^{-1}}$ for nitrogen, $-0.067 \pm 0.024\,\mathrm{dex\,kpc^{-1}}$ for oxygen, $-0.082 \pm 0.026\,\mathrm{dex\,kpc^{-1}}$ for magnesium, $-0.045 \pm 0.023\,\mathrm{dex\,kpc^{-1}}$ for aluminum and $-0.107 \pm 0.028\,\mathrm{dex\,kpc^{-1}}$ for silicon. The oxygen gradient obtained by Gummersbach *et al.* (1998) is strongly dependent on the star Sh2 217-3, which lies ~13 kpc from the Galactic center. If this star is discarded and the gradient of oxygen recalculated for the 15 remaining stars, a shallower gradient of $-0.035 \pm 0.024\,\mathrm{dex\,kpc^{-1}}$ is derived. Such a dependence on one star is due to the small size of their sample (16 stars in total, representing 11 positions in the disk). Note that the addition of this star, with re-scaled temperatures, non-LTE abundance and distance, to our sample (as shown in the previous section) produces a smaller effect on the gradient value than that produced in the Gummersbach's sample.

Five stars of their sample belong to the Ori OB1 association while the rest of the sample (excluding Sh2 217-3) consists of 10 stars in the region $5.6 < R_g < 12.0$ kpc and represents the bulk of their data, with 9 positions in the disk. A direct comparison of the abundance distribution obtained for the stars in Orion and in the disk may be done in terms of the difference between the largest and the smallest oxygen abundance in each sub-sample $\Delta(O)$. According to Gummersbach's results, the Orion stars have $\Delta(O)$=0.63, while for the stars in the rest of the disk the difference is 0.59 dex. In other words, the local abundance pattern in the Orion association shows a scatter that is of the same order as that of the radial abundance distribution. The abundance spread in the subgroups of the Ori OB1 association was studied by Cunha & Lambert (1994). They found large dispersions for the oxygen and silicon abundances that could not be explained by the analysis uncertainties. Moreover, the abundances are correlated with the ages and relative positions within the association, suggesting that a process of self-enrichment by nucleossynthesis products of supernovae type II explosions might have happen in Orion. This pattern of self-enrichment was not observed in the smaller OB association of Cep OB2 (Daflon, Cunha & Becker 1999, Daflon *et al.* 2001b) - which showed a homogeneous chemical composition.

Concerning the other elements studied by Gummersbach *et al.*, their gradients of carbon and aluminum are similar to our derived gradients; nitrogen and magnesium are also dependent on the star Sh2 217-3, but the changes in the magnitude of the gradient are smaller than that observed for the oxygen. The silicon gradient of Gummersbach *et al.* (1998) is very steep and is basically defined by the silicon rich star Hogg 22-5 ($\log \epsilon(Si) = 8.20 \pm 0.10$), besides the star Sh2 217-3. Disregarding these two stars would result in a silicon gradient of $-0.068\,\mathrm{dex\,kpc^{-1}}$.

Abundance data for OB stars of the Galactic disk within R_g=6.1 to 13.2 kpc have also been derived independently by the irish group in the period 1983-1994, using different scales of effective temperatures (spectroscopic and photometric) and abundance (in LTE and non-LTE). The abundance data were later extended to larger Galactocentric radii by Smartt *et al.* (1996a, b, c). This stellar sample, combined with the former, was studied by Smartt & Rolleston (1997), who then derived a radial gradient of $-0.07 \pm 0.01\,\mathrm{dex\,kpc^{-1}}$ for oxygen. The latter, however, was based on non-LTE abundances obtained from tabulated theoretical equivalent widths of O II lines published by Becker & Butler (1988), which were based on inadequately line-blancketed LTE model atmospheres of Gold (1984). Even if the magnitude of the oxygen gradient were not affected by the choice of model atmospheres (which is not necessarily true due to the fact that the sample stars bracket a wide range in stellar parameters), the absolute abundances are almost certainly affected.

More recently, Rolleston *et al.* (2000) compiled the observational data (stellar parameters, distances and equivalent widths) from these previous studies and re-computed the stellar abundances using an LTE approach. They obtained an oxygen gradient of $-0.067 \pm 0.008\,\mathrm{dex\,kpc^{-1}}$ for 73 stars, representing 22 positions in the Galactic disk. Given the differences in the techniques adopted in the original studies, they analyzed how sources uncertainty (e.g. T_{eff}−scale, microturbulence, line sets and distances) would affect the radial gradients. As a general conclusion, they found that no single parameter would change significantly the magnitude of the gradient. They also derived non-LTE abundances of O II and Mg II in order to test the validity of the LTE approach for B stars. The non-LTE abundances were obtained from a grid of predicted non-LTE equivalent widths calculated with the programs DETAIL/SURFACE, based on non-LTE model atmospheres of Hubeny (1988). The model atoms of oxygen and magnesium are from Becker & Butler (1988) and Mihalas (1972), respectively. Their results suggest that the adoption of the non-LTE abundances did not change the estimates of the radial gradients of oxygen and magnesium, although they recognized that the absolute abundances may be in error.

The inner part of the disk was particularly well studied by Smartt *et al.* (2001). They analyzed 4 B stars within 2.5-5 kpc of the Galactic center and found LTE oxygen abundances ∼solar (considering the value of 8.72 adopted here) for two of them, while the other two stars show overabundance of oxygen relative to the Sun of the order of 0.3 dex. This result is inconsistent with the abundances expected from a simple extrapolation towards smaller Galactocentric distances of the oxygen gradient obtained by Rolleston *et al.* (2000), this means 9.2-9.3 dex. In their analysis, however, the stars show enhanced LTE abundances of C, N, Mg, Al, Si and S, in agreement with the continuation of the gradients of Rolleston *et al.* (2000) towards smaller Galactocentric distances.

The Galactic Chemical Evolution Models

Hou *et al.* (2000) and Alibés *et al.* (2001) presented radial gradients expected from their models of Galactic Chemical Evolution. Both studies assume the infall of external material and the same multi-slope power-law IMF. The basic differences between the two studies is that Alibés *et al.* (2001) considered two different compositions for the infalling matter: primordial and enriched. Hou *et al.*, on the other hand, deliberately neglected the yields from intermediate mass stars in order to check if the observations could be reproduced, using only the yields of massive stars (from Woosley & Weaver, 1995 and Maeder, 1992).

The elemental radial gradients predicted by the models of Hou *et al.* are steeper than our observed gradients, for both types of stellar yields: the oxygen gradients are $\sim -0.06\,\mathrm{dex\,kpc^{-1}}$, while nitrogen and aluminum show steeper gradients of about -0.09 dex kpc^{-1}. The radial gradients of Alibés *et al.* (2001), calculated for enriched infalling matter, are slightly flatter than those predicted assuming primodial infalling material: the oxygen gradients are -0.047 and $-0.053\,\mathrm{dex\,kpc^{-1}}$, respectively. They are somewhat steeper than the observed oxygen gradient obtained from our original sample, but agree very well with gradients derived from the extended sample. The gradients calculated for other elements are also steeper than ours and agree only marginally considering the uncertainties.

Chiappini *et al.* (2001) considered four different scenarios in their models of Galactic chemical evolution, by basically changing the halo evolution. One of their models (model B) gives the flattest slopes, with the oxygen gradient being in agreement with the gradient derived by Deharveng *et al.* (2000). On the other hand, a steeper gradient, consistent with a gradient of $-0.07\,\mathrm{dex\,kpc^{-1}}$, may be obtained with their models A and C. The differences between the three models are the adopted halo mass density profiles and the density thresholds in the halo phase and suggests that the differences in the history of the halo evolution affects mainly the outer gradients ($R_g > 10$ kpc) whereas the inner gradients are unchanged.

In Figure 7.5 we show our non-LTE cluster abundances compared to the theoretical radial gradients predicted by Hou *et al.* (2000 – thick solid line), Alibés *et al.* (2001 – thin solid and dotted lines) and Chiappini *et al.* (2001 – thin dashed lines). Concerning the chemical composition of the Sun, the abundances of O (we note that we consider a lower oxygen abundance in the Sun), Mg, Al, Si and S are well fitted by the radial gradient of Hou *et al.*, whereas the predicted solar abundances of C and N are underestimated, possibly due to the lack of the yields from intermediate mass stars. Alibés *et al.* (2001) reproduced the solar abundances for six elements while the predicted nitrogen abundance is higher than the observed value. In the case of the Chiappini *et al.* (2001), all their four models fit the solar abundances of N, S and O (for the latter, we recall that they considered the higher value of Grevesse & Sauval, 1998). Considering the abundances of the OB stars, the predicted gradients of C, N, O, Al and Si are, in general, above the observed abundances, (except for the C and N gradients of Hou *et al.*, 2000, as discussed above). Magnesium gradient is well fitted by the model of Hou *et al.*, while Alibés *et al.* predict somewhat higher abundances for this element. The distribution of sulfur abundances derived from our sample is better reproduced by the models of Chiappini *et al.* (2001), whereas the choice of a best model gradient is only possible when considering stars located at the edge of the Galactic disk.

7.4.2 Abundance Ratios

Besides the elemental abundance profiles within the Galactic disk, the radial gradients of the abundance ratios are also important as different pairs of elements can have different origins. For example, magnesium, silicon and sulfur are expected to follow the behavior of oxygen, as they are all primary elements that are expected to be produced in supernovae type II (Hou *et al.*, 2000 and Alibés *et al.*, 2001). For each cluster of our sample, we derive the abundance ratios relative to the oxygen, normalized to the corresponding abundance ratio in the Sun ($[X/O] = \log(X/O)/(X/O)_\odot$). The gradients of [X/O] in the Galactic disk are listed in Table 7.5. The distribution of the abundance ratios as a function of the

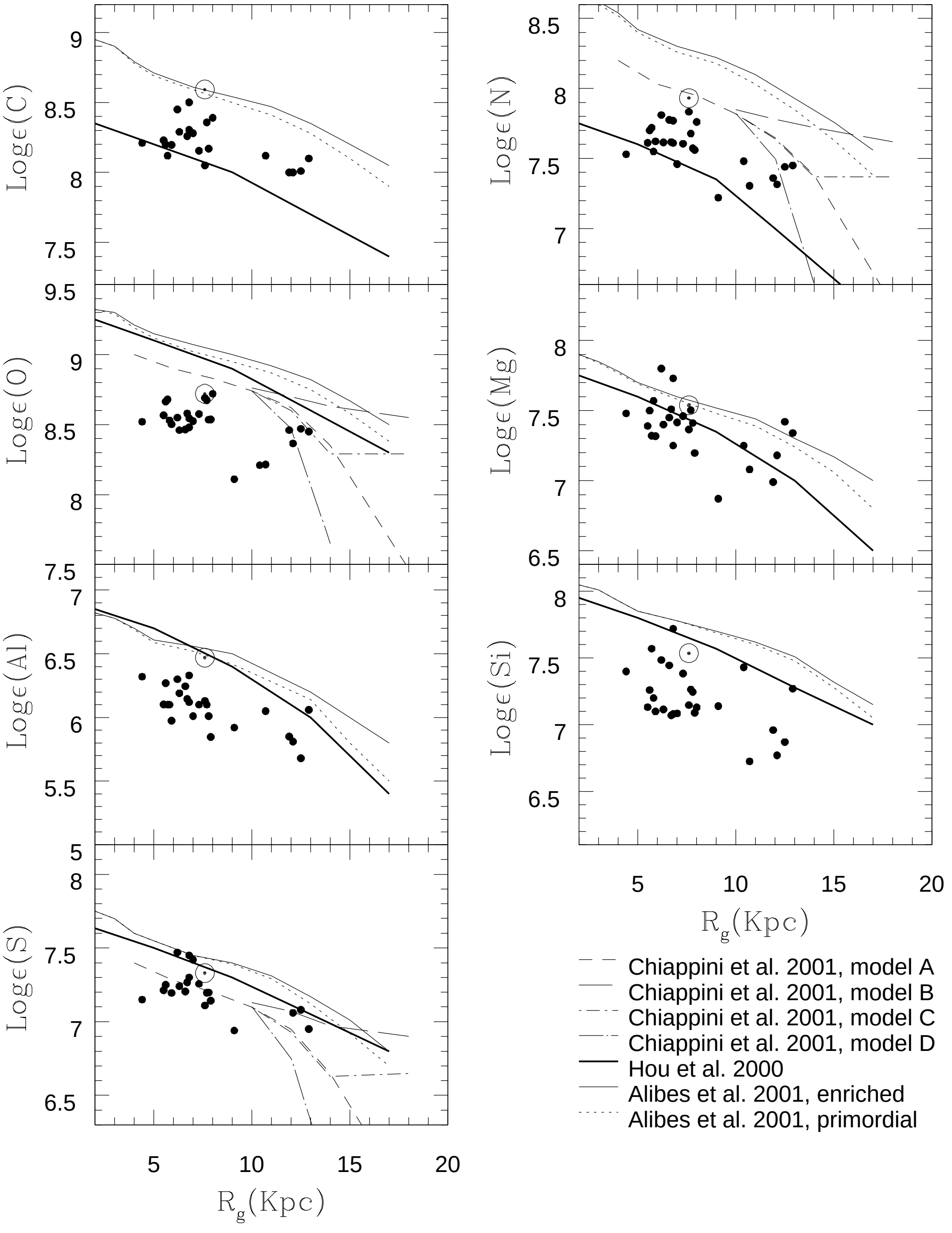

Figure 7.5: Clusters abundances compared to the predicted radial gradients of Hou *et al.* (thick solid line), Alibés *et al.* (2001 - thin solid and dotted lines) and Chiappini *et al.* (2001 - thin dashed lines).

Galactocentric disk is displayed in the panels of Figure 7.6. None of the six elements show any significant dependence of [X/O] on R_g and the radial gradients are all flatter than $\sim -0.02\,\mathrm{dex\,kpc^{-1}}$. The ratios of magnesium, silicon and sulfur relative to oxygen are $\sim$ solar, while C/O, N/O and Al/O are slightly below the Solar value. The similar behavior of oxygen, magnesium, silicon and sulfur throughout the disk is expected, since they are all returned to the interstellar medium through supernovae II explosions as mentioned above. The production of nitrogen and aluminum quite probably depends on the metallicity of the interstellar medium (Hou *et al.*, 2000 and Alibés *et al.*, 2001); in this sense, N/O and Al/O are expected to decrease with Galactocentric radius. From our data, Al/O does show a small gradient with R_g ($\sim -0.02\,\mathrm{dex\,kpc^{-1}}$) but N/O may be considered as constant ($-0.012\,\mathrm{dex\,kpc^{-1}}$) across the disk. Carbon, like oxygen, is a primary element; however, the main producers of carbon are not yet clearly defined. If the main source of carbon is massive stars, one would expect the carbon gradient to be steeper than oxygen, resulting in the decrease of C/O with R_g (Hou *et al.*, 2000). In general, all of the abundance ratios obtained for our sample are approximately constant across the disk; the average slope for all the elements studied here is $-0.014 \pm 0.005\,\mathrm{dex\,kpc^{-1}}$.

Table 7.5: Radial Gradients of Abundance Ratios ($a + bx$)

[X/O]	a	σa	b	σb
C	-0.133	0.123	-0.008	0.015
N	-0.040	0.077	-0.012	0.010
Mg	0.158	0.125	-0.013	0.017
Al	-0.017	0.126	-0.021	0.017
Si	0.019	0.180	-0.018	0.022
S	0.200	0.119	-0.015	0.014

Rolleston *et al.* (2000) find a gradient of $-0.04 \pm 0.02\,\mathrm{dex\,kpc^{-1}}$ for N/O; this gradient is increased to $-0.06 \pm 0.02\,\mathrm{dex\,kpc^{-1}}$ if the four stars of Smartt *et al.* (2001) are included. Our radial gradient of N/O, on the contrary, almost vanishes. Alibés *et al.* (2001) expect radial gradients of C/O, Mg/O, Al/O, Si/O and S/O ≤ -0.01 (estimated from their figures 4, 6 and 7) from their chemical evolution model. Their expected gradient of N/O is $-0.02\,\mathrm{dex\,kpc^{-1}}$,

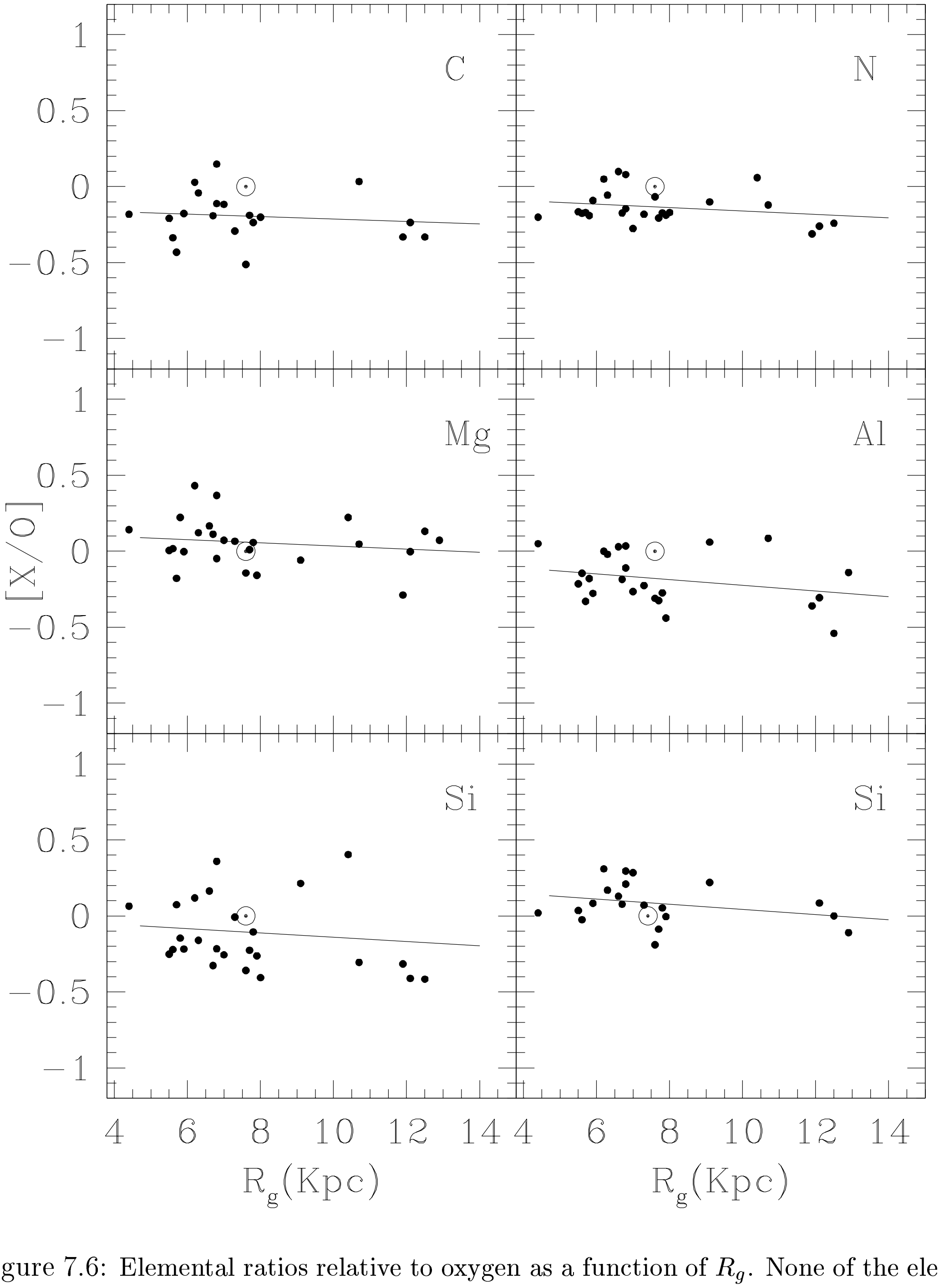

Figure 7.6: Elemental ratios relative to oxygen as a function of R_g. None of the elements show clear trends with the Galactocentric distance across the Galactic disk.

which agrees within the uncertainties with our observations. The Galactic evolution models of Hou *et al.* (2000) predict small (flatter than $-0.02\,\mathrm{dex\,kpc^{-1}}$, estimated from their figure 9) trends of the abundance ratios with Galactocentric distance for C, Mg, Al, Si and S relative to oxygen; for N/O, they find a steeper gradient, which we estimate from their figure 9 to be $\leq -0.04\,\mathrm{dex\,kpc^{-1}}$.

7.4.3 The Galactic Spiral Arms

The clusters sampled in this study are distributed in three spiral arms of the Galaxy: 11 clusters belong to the inner arm of Sagittarius-Carina, 9 clusters lie on the Local arm and the outer arm of Perseus contains 5 clusters. The mean oxygen abundances of the clusters in each arm are 8.55 ± 0.07, 8.48 ± 0.20 and 8.39 ± 0.11, respectively. The larger scatter observed for the Local arm is due mainly to the inclusion of Mon OB2 and NGC 2414, which are assigned by Becker & Fenckart (1971) as members of the Local arm. These objects, however, have a mean oxygen abundance of 8.16 ± 0.07, a much lower oxygen abundance than that obtained for the rest of the clusters in this arm (8.57 ± 0.08); it is even lower than the mean abundance of the Perseus arm. Smartt *et al.* (1996b) examined chemical compositions towards the Galactic anticenter and obtained a strong depletion of oxygen for the field star RLWT 41, that could not be accounted for by the analysis uncertainties. Based on its relative position in the Galactic Plane, they suggest that RLWT 41 was possibly formed in the inter-arm gap between the Local and Perseus arms. Would this also be possible for the OB associations Mon OB2 and NGC 2414? Unfortunately, in our study both associations are poorly sampled and any further conclusions would need to be anchored by a more detailed analysis of the chemical compositions of these objects.

7.5 Conclusions

We have studied the distribution of the chemical abundances of OB main-sequence stars in the Galactic Plane. A uniform methodology was adopted throughout the stellar sample, producing a homogeneous database of non-LTE chemical abundances of carbon, nitrogen, oxygen, magnesium, aluminum, silicon and sulfur. A total of 70 stars were analyzed, with those stars being members of 25 open clusters, OB associations or H II regions in the Galactic plane. With the addition of the non-LTE abundances derived by Cunha & Lambert (1994) for the Orion association, our sample represents 26 positions in the disk between 4.4 and 12.9 kpc from the Galactic center. The main conclusions of this work are:

1. The radial gradients derived are flatter than the most recent results presented in the literature. The average slope is $-0.041 \pm 0.007\,\mathrm{dex\,kpc^{-1}}$; the flattest gradient is obtained for oxygen $-0.031 \pm 0.010\,\mathrm{dex\,kpc^{-1}}$ and the steepest is that of silicon $-0.049 \pm 0.018\,\mathrm{dex\,kpc^{-1}}$. Concerning the other studies on radial gradients of stellar abundances, the oxygen gradient obtained by Gummersbach *et al.* (1998) is strongly dependent on the abundance of the outermost star in their sample; if this star is discarded, the oxygen gradient derived for the rest of their sample is consistent with the gradient derived here. Their gradients of carbon and aluminum agree very well with our values; on the other hand, the silicon gradient of Gummersbach *et al.* is much steeper than ours. Rolleston *et al.* (2000) also discussed the radial gradients of abundances using a LTE approach to derive the stellar abundances. They obtained steeper gradients, varying from $-0.05\,\mathrm{dex\,kpc^{-1}}$, for aluminum to $-0.09\,\mathrm{dex\,kpc^{-1}}$, for nitrogen.

2. We extended our stellar sample to include regions with $2.7 < R_g < 3.8$ kpc and $10.1 < R_g < 15.7$ kpc by including the published equivalent widths of 10 stars to derive the non-LTE abundance of oxygen. With this extended sample we obtain a radial oxygen gradient equal to $-0.043 \pm 0.008\,\mathrm{dex\,kpc^{-1}}$. The change in the magnitude of this gradient is basically due to the addition of the 3 stars located in the inner regions; such a variation in the slope could not be produced if we included only the outermost stars in our sample.

3. The abundance ratios are approximately independent of the Galactocentric distance. The slopes are $\leq -0.02\,\mathrm{dex\,kpc^{-1}}$ for C, N, Mg, Al, Si, and S relative to the oxygen abundance. The gradients of abundance ratios predicted by the Galactic chemical evolution models of Hou *et al.* (2000) and Alibés *et al.* (2001) are in agreement with the present observational results.

Capítulo 8

Conclusões Gerais

Neste trabalho foram analisadas as abundâncias químicas de 70 estrelas B da seqüência principal distribuídas ao longo do plano Galáctico. Essas estrelas são membros de 25 associações OB, aglomerados abertos e regiões H II que estão localizados a distâncias de 4.4 a 12.9 kpc do centro Galáctico, considerando $R_{\odot}$=7.6 kpc. A análise da composição química dessas estrelas foi realizada seguindo uma metodologia única para todas as estrelas da amostra, definida de modo a garantir a homogeneidade e auto-consistência dos resultados obtidos, desde a escala de temperaturas até as abundâncias estelares. As temperaturas efetivas e gravidades superficiais estão em uma escala baseada em calibrações fotométricas associadas ao ajuste de perfis sintéticos da linha Hγ. Os modelos atmosféricos adotados foram calculados em ETL com o programa ATLAS9. Dentre os modelos atmosféricos disponíveis atualmente, os modelos em ETL combinados com uma função de distribuição de opacidades que inclui milhões de linhas atômicas representam melhor as atmosferas das estrelas B do que os modelos atmosféricos fora do ETL com uma função de distribuição de opacidades menos completa. Um ponto relevante da metodologia adotada foi a opção pela determinação das abundâncias estelares via síntese de perfis, calculados sem a aproximação ETL na teoria de formação das linhas. Os perfis teóricos fora do ETL foram calculados utilizando-se os programas DETAIL, que calcula as populações do níveis, e SURFACE, que calcula os perfis sintéticos para essas populações. A síntese de perfis espectrais foi uma ferramenta indispensável na análise empreendida: os altos valores de $v \sin i$ típicos das estrelas B dificultam ou mesmo impossibilitam a medida de larguras equivalentes, reduzindo significativamente o número de estrelas para as quais é possível se determinar abundâncias químicas. A utilização da síntese possibilitou a ampliação da amostra analisada, incluindo estrelas com altas velocidades rotacionais projetadas, que normalmente seriam descartadas.

O resultado principal desse trabalho é um conjunto de abundâncias de carbono, nitrogênio, oxigênio, magnésio, alumínio, silício e enxofre que permite a análise da distribuição da composição química tanto localmente, como no caso da associação de Cep OB2, quanto no contexto mais amplo do disco Galáctico. Em linhas gerais, as conlusões deste trabalho são:

1. A associação de Cep OB2 foi analisada detalhadamente, com base em uma amostra de 17 estrelas, o que representa aproxidamente 30% das estrelas com tipos espectrais entre O9 e B3 formadas na associação. As abundâncias não-ETL médias de C, N, O e Si de Cep OB2 sugerem que essa associação é 0.2-0.3 dex sub-abundante nesses elementos em relação ao Sol. As estrelas de Cep OB2 podem ser divididas em dois sub-grupos de idades distintas, mas as abundâncias estelares não apresentam variações significativas em função da idade ou posição relativa. De modo geral, as dispersões das abundâncias são compatíveis com os erros esperados na análise, indicando que Cep OB2 é quimicamente homogênea.

2. A análise de aglomerados abertos e associações numa região mais próxima do Sol (até $\sim$2 kpc) mostrou que, em geral, as abundâncias solares representam o limite superior da distribuição de abundâncias de oxigênio, magnésio, silício e enxofre, considerando as dispersões de cada distribuição. As abundâncias de carbono, nitrogênio e alumínio são sub-solares em 0.2-0.3 dex.

3. A razão de abundâncias N/O das estrelas com altas velocidades rotacionais projetadas foram analisadas em função do valor de $v \sin i$ obtido. Duas estrelas com altas abundâncias de nitrogênio foram especialmente destacadas: elas se encontram em estágios evolutivos mais avançados ao mesmo tempo que possuem $v \sin i > 100 \mathrm{km\,s^{-1}}$. Estes resultados concordam com as previsões de Heger & Langer (2000) de que a rotação pode induzir modificações nas abundâncias superficiais de estrelas massivas.

4. A distribuição das abundâncias químicas em função da distância ao centro da Galáxia é caracterizada por gradientes da ordem de -0.03 a $-0.05\,\mathrm{dex\,kpc^{-1}}$. Os erros obti-

dos dos ajustes lineares são da ordem de 0.01, exceto para silício e magnésio, que apresentam um espalhamento um pouco maior. Os gradientes obtidos são: $-0.033 \pm 0.010\,\mathrm{dex\,kpc^{-1}}$ para o carbono, $-0.043 \pm 0.011\,\mathrm{dex\,kpc^{-1}}$ para o nitrogênio, $-0.031 \pm 0.010\,\mathrm{dex\,kpc^{-1}}$ para o oxigênio, $-0.044 \pm 0.015\,\mathrm{dex\,kpc^{-1}}$ para o magnésio, $-0.048 \pm 0.011\,\mathrm{dex\,kpc^{-1}}$ para o alumínio, $-0.049 \pm 0.018\,\mathrm{dex\,kpc^{-1}}$ para o silício e $-0.037 \pm 0.012\,\mathrm{dex\,kpc^{-1}}$ para o enxofre.

5. Os gradientes obtidos neste estudo são, em geral, menos inclinados do que aqueles obtidos em dois trabalhos mais recentes sobre gradientes radiais de abundâncias estelares: Gummersbach *et al.* (1998) e Rolleston *et al.* (2000). O primeiro desses trabalhos apresentou abundâncias não-ETL para uma pequena amostra de estrelas do disco. O gradiente de oxigênio obtido é fortemente dependente do objeto de maior distância Galactocêntrica, a estrela Sh2 217-3. Se essa estrela for descartada da amostra inicial, o novo gradiente obtido para o restante da amostra é igual a $-0.035\,\mathrm{dex\,kpc^{-1}}$ (em contraste com o gradiente original: $-0.067\,\mathrm{dex\,kpc^{-1}}$). Os gradientes de carbono e alumínio obtidos por Gummersbach *et al.* são consistentes com os nossos valores. O gradiente de silício, por outro lado, mostra grande discrepância: a nossa distribuição aponta um gradiente igual a $-0.049 \pm 0.018\,\mathrm{dex\,kpc^{-1}}$ enquanto que eles obtiveram $-0.107 \pm 0.028\,\mathrm{dex\,kpc^{-1}}$. O estudo realizado por Rolleston *et al.* (2000) é baseado em uma coletânea de dados espectroscópicos (parâmetros estelares e medidas de larguras equivalentes) e utiliza a aproximação ETL no cálculo das abundâncias químicas. Os gradientes obtidos são da ordem de $-0.07\,\mathrm{dex\,kpc^{-1}}$ e foram avaliados considerando-se as diferenças sistemáticas das análises originais (de onde foram obtidos os parâmetros atmosféricos e larguras equivalentes). Em linhas gerais, conclui-se que essas diferenças sistemáticas não introduzem maiores incertezas na determinação dos gradientes. A amostra de Rolleston *et al.* foi estendida na direção do centro da Galáxia por Smartt *et al.* (2001), que observaram um achatamento do gradiente de oxigênio para $R_g < 5$ kpc. Este padrão, segundo Smartt *et al.*, não é seguido por outros elementos α como silício e magnésio e nem pelo nitrogênio: esses elementos mantêm um gradiente constante na direção do centro Galáctico.

6. O impacto dos erros nas distâncias ao Sol e na determinação das abundâncias não-

ETL sobre o valor do gradiente de oxigênio foi testado aplicando-se uma distribuição de erros aleatórios com valores máximos iguais a 10% e 0.15 dex sobre as distâncias e abundâncias, respectivamente. 5000 novos gradientes foram calculados. Estes gradientes apresentam-se normalmente distribuídos em torno do valor original, com dispersões iguais a 0.001, no caso das correções aplicadas às distâncias, e 0.005, no caso das abundâncias. Este resultado sugere que as incertezas nas abundâncias têm um peso maior na determinação dos gradientes radiais do que os erros nas distâncias.

7. As associações OB de Mon OB2 e NGC 2414 apresentam abundâncias bastante baixas em relação à distribuição total de abundâncias. As suas posições relativas no disco introduzem um parâmetro particularmente interessante, que parece sugerir uma relação entre as baixas abundâncias observadas e a localização destes objetos entre os braços espirais Local e Perseus. As duas associações, entretanto, não estão bem representadas na amostra e seria necessária uma análise mais detalhada das suas composições químicas antes de se tirar conclusões a respeito da sua história evolutiva. De qualquer forma, este resultado mostra a importância de se analisar padrões locais de abundâncias como, por exemplo, nas regiões entre os braços Galácticos.

8. A nossa amostra original foi estendida nas regiões $2.7 < R_g < 3.8$ kpc e $10.1 < R_g < 15.7$ kpc, considerando-se estrelas OB analisadas por Gummersbach *et al.* (1998), Rolleston *et al.* (2000). e Smartt *et al.* (2001). No total, 10 estrelas, representando 9 posições diferentes no disco Galáctico, foram adicionadas à nossa amostra. As temperaturas efetivas foram recalculadas na nossa escala em função do índice livre de avermelhamento Q. As gravidades superficiais foram obtidas das fontes citadas. Abundâncias em não-ETL de oxigênio foram obtidas a partir de perfis sintéticos que reproduzissem as medidas de larguras equivalentes publicadas. Com essa amostra estendida, obtivemos um gradiente radial de oxigênio igual a $-0.043 \pm 0.008\,\mathrm{dex\,kpc^{-1}}$. Essa modificação na magnitude do gradiente, entretanto, não seria observada se apenas as estrelas da região mais externa do disco fossem incluídas: neste caso, o gradiente obtido praticamente não se modifica. A variação na inclinação foi determinada, de fato, pela inclusão das estrelas mais próximas do centro Galáctico.

Bibliografia

[1] Afflerbach, A., Churchwell, E. & Werner, M. W. 1997, ApJ 478, 190

[2] Alibés, A., Labay, J. & Canal, R. 2001, A&A, in press (astro-ph/0107016)

[3] Allen, C. 1973, 'Astrophysical Quantities' (London: Athlone Press)

[4] Allende Prieto, C., Lambert, D. L., & Asplund, M. 2001, ApJ 556, L63

[5] Aller, L. H., & Jugaku, J. 1958, ApJ 127 125

[6] Alter, G., Balazs, B., & Ruprecht, J. 1970, in 'Catalogue of Star Clusters and Associations' (Hungary: Akademiai Kiada Budapest)

[7] Andrievsky, S. M., Kovtyukh, V. V., Luck, R. E., Lépine, J. R. D., Bersier, D., Maciel, W. J., Barbuy, B., Klochkova, V. G., Panchuk, V. E. & Karpischek, R. U. 2002a, A&A 381, 32

[8] Andrievsky, S. M., Bersier, D., Kovtyukh, V. V., Luck, R. E., Maciel, W. J., Lépine, J. R. D. & Beletsky, Yu. V. 2002b, A&A 384, 140

[9] Balona, L. A. 1984, MNRAS 211, 973

[10] Battinelli, P. & Capuzzo-Dolcetta, R. 1991, MNRAS 249, 76

[11] Becker, S. R. & Butler, K. 1988a, A&A 201, 232

[12] Becker, S. R. & Butler, K. 1988b, A&AS 74, 211

[13] Becker, S. R. & Butler, K. 1988c, A&AS 76, 331

[14] Becker, S. R. & Butler, K. 1989, A&A 209, 244

[15] Becker, S. R. & Butler, K. 1990, A&AS 84, 95

[16] Becker, W. & Fenckart, R. 1971, A&AS 4, 241

[17] Blaauw, A. 1964, ARA&A 2, 213

[18] Blaauw, A. 1991, in 'The Physics of Star Formation and Early Stellar Evolution', ed. C. J. Lada & N. D. Kylafis (Kluwer: Dordrecht), p. 125

[19] Blitz, L. Fich, M. & Stark, A. A. 1982, ApJS 49, 183

[20] Bochkarev, N. G. & Sitnik, T. G. 1985, Ap&SS 108, 237

[21] Burgess, A. & Seaton, M. F. 1960, MNRAS 120, 121

[22] Butler, K. 1984, Ph.D. Thesis, University of London

[23] Butler, K. 1994, http://ccp7.dur.ac.uk/Docs/detail.ps

[24] Cameron, L. M. 1985, A&A 147, 47

[25] Caplan, J., Deharveng, L., Peña, M., Costero, R & Blondel, C. 2000, MNRAS 311, 317

[26] Caputo, F., Marconi, M, Musella, I. & Pont, F. 2001, A&A 372, 544

[27] Cardelli, J. A., Clayton, G. C. & Mathis, J. S 1989, ApJ 345, 245

[28] Chiappini, C., Matteucci, F. & Romano, D. 2001, ApJ 554, 1044

[29] Conti, P. S. 1973, ApJ 179, 181

[30] Crampton, D. L. 1971, AJ 76, 260

[31] Crampton, D. L., Georgelin, Y. M. & Georgelin, Y. P. 1978, A&A 66, 1

[32] Crawford, D. L., Barnes, J. V., Hill, G. & Perry, C. L. 1971, AJ 76, 1048

[33] Cuffey, J. 1973, AJ 78, 747

[34] Cunha, K. & Lambert, D. L. 1992, ApJ 399, 586

[35] Cunha, K. & Lambert, D. L. 1994, ApJ 426, 170

[36] Cunha, K., Smith, V. V. & Lambert, D. L. 1998, ApJ 493, 195

[37] Cunto, W. & Mendonza, C. 1992, Rev. Mex. Astron. Astrof. 23, 107

[38] Daflon, S. 1997, Dissertação de Mestrado/ON

[39] Daflon, S., Cunha, K. & Becker, S. 1999, ApJ 522, 950 (Paper I)

[40] Daflon, S., Cunha, K., Becker, S. & Smith, V. V. 2001a, ApJ 552, 309 (Paper II)

[41] Daflon, S., Cunha, K., Butler, K. & Smith, V. V. 2001b, ApJ 563, 325 (Paper III)

[42] Dambis, A. K.. Mel'nik, A. M. & Rastorguev, A. S. 1995, Astron. Letters 21, 291

[43] Davis, J. & Shobbrook, R. R. 1977, MNRAS 178, 651

[44] Deharveng, L., Peña, M., Caplan, J. & Costero, R. 2000, MNRAS 311, 329

[45] Deutschman, W. A., Davis, R. J. & Schild, R.E. 1976, ApJS 30, 97

[46] de Zeeuw, P. T. & Brand, J. 1985, in 'Birth and Evolution of Massive Stars and Stellar Groups', eds. Boland, W. & van Woerden, H. (D. reidel Publishing Company), p. 95

[47] de Zeeuw, P. T., Hoogerwerf, R., de Bruijne, J. H. J., Brown, A. G. A., & Blaauw, A. 1999, AJ 117, 354

[48] Dufton, P. L., Brown, P. J. F., Lennon, D. J. & Lynas-Gray, A. E. 1986, MNRAS 222, 713

[49] Dufton, P. L., Brown, P. J. F., Fitzsimmons, A. & Lennon, D. J. 1990, A&A 232, 431

[50] Ebbets, D. 1979, ApJ 227, 510

[51] Eber, F. 1987, Diplomarbeit Ludiwig-Maximiwilans Universität, Munich

[52] Eber, F. & Butler, K. 1988, A&A 202, 153

[53] Feinstein, A. 1994, Rev. Mex. Astron. y Astrof. 29, 141

[54] Fich, M. & Silkey, M. 1991, ApJ 366,107

[55] Fitzgerald, M. P. & Moffat, A. F. J. 1980, MNRAS 193, 761

[56] Fitzsimmons, A. 1993, A&AS 99, 15

[57] Fitzsimmons, A., Brown, P. J. F., Dufton, P. L. & Lennon, D. J. 1990, A&A 232, 437

[58] Fitzsimmons, A., Dufton, P. L. & Rolleston, W. R. J. 1992, MNRAS 259, 489

[59] Flower, P. J. 1977, A&A 54, 31

[60] Friel, E. D. 1995, ARA&A 33, 381

[61] Garmany, C. D & Stencel, R. E. 1992, A&AS 94, 211

[62] Garrison, R.F. & Kormendy, J. 1976, PASP 88, 865

[63] Gehren, T., Nissen, P. E., Kudritzki, R. P. & Butler, K. 1985, in 'Proceedings of the ESO Workshop on 'Production and Distribution of C, N, O Elements", p. 171, Garching

[64] Gies, D. R., & Lambert, D. L. 1992, ApJ 387, 673

[65] Glushkova, E. V., Dambis, A. K, Mel'nik, A. M. & Rastorguev, A. S. 1998, A&A 329, 514

[66] Golay, M. 1958, Publ. Obs. Geneve Ser. A 57, 373

[67] Gold, M. 1984, Diplomarbeit, Ludwig Maximilian Universität

[68] Grevesse, N., Noels, A. & Sauval, A. J. 1996, in 'Cosmic abundances', ed. S. S. Holt & G. Sonneborn (San Francisco: ASP), p. 117

[69] Grevesse, N. & Sauval, A. J. 1998, Space Sci. Rev. 85, 161

[70] Gulati, R. K., Malagnini, M. L. & Morossi, C. 1989, A&AS 80, 73

[71] Gummersbach, C. A., Kaufer, A., Schäfer, D. R., Szeifert, T. & Wolf, B. 1998, A&A 338, 881

[72] Harris III D.L. 1955, ApJ 121, 554

[73] Hauck, B. & Mermilliod, M. 1980, A&AS 40, 1

[74] Hauck, B. & Mermilliod, M. 1998, A&AS 129, 431

[75] Haug U. 1970, A&AS 1, 35

[76] Heger, A. & Langer, N. 2000, ApJ 544, 1016

[77] Henry, R. J. 1970, ApJ 161, 1153

[78] Henry, R. B. C. & Worthey, G. 1999, PASP 111, 919

[79] Herrero, A., Kudritzki, R. P., Gabler, R., Vílchez, J. M. & Gabler, A. 1992, A&A 261, 209

[80] Holweger, H. 2001, in Solar and Galactic Composition, ed. R. F. Wimmer-Schweingruber (American Institute of physics), p. 23

[81] Hou, J. L., Prantzos, N. & Boissier, S. 2000, A&A 362, 936

[82] Howarth, I. D. & Prinja, R. K. 1989, ApJS 69, 527

[83] Hubeny, I. 1988, Computer Physics Comm. 52, 103

[84] Hubeny, I. 1992, in 'The Astrophysics of Early-type Stars', eds. U. Heber & C. S. Jeffery (Berlin: Springer-Verlag), p. 377

[85] Humphreys, R. M. 1978, ApJ 38, 309

[86] Humphreys, R. M. & McElroy, D.B. 1984, in 'Catalogue of Stars in Stellar Associations and Young Clusters', Univ. of Minnesota

[87] Janes, K. A. 1979, ApJSS 39, 135

[88] Johnson, H. L. 1958, Lowell Obs. Bull. 4, 37

[89] Kaltcheva, N. T. & Georgiev, L. N. 1992, MNRAS 259, 166

[90] Kaufer, A., Szeifert, Th., Krenzin, R., Baschek, B & Wolf, B. 1994, A&A 289, 740

[91] Kaufer, A., Stahl, O., Tubbesing, S, Nørregaard, P., Avila, G., François, P., Pasquini, L. & Pizzella, A. 1999, The ESO messenger 95, 8

[92] Kilian, J., Montenbruck, O., & Nissen, P.E. 1991, A&AS 88, 101

[93] Kilian-Montenbruck, J., Gehren, T & Nissen, P. E. 1994, A&A 291, 757

[94] Kurucz, R. L. 1979, ApJS 40, 1

[95] Kurucz, R.L., 1991, in 'Stellar Atmospheres: Beyond Classical Models', Crivellari L. et al. (eds), NATO ASI Ser. C-152, p 441

[96] Kurucz, R. L. 1992, ATLAS9 Stellar Atmosphere Programs and 2 km/s Grid CD-Rom 13, Smithsonian Astrophysical Observatory, Cambridge.

[97] Lahulla, J. F. 1985, A&AS 61, 537

[98] Lahulla, J. F. 1987, AJ 94, 1062

[99] Lamers, H. J. G. L. M. & Achamad, L. 1994, A&A 291, 856

[100] Lennon, D. J., Dufton, P. L. , Fitzsimmons, A., Gehren, T. & Nissen, P. E. 1990, A&A 240, 349

[101] Lester, J. B., Gray, R. O., & Kurucz, R. L. 1986, ApJS 61, 509

[102] Maciel, W. J. 1993, Ap&SS 206, 285

[103] Maciel, W. J. & Chiappini, C. 1994, Ap. & SS 219, 231

[104] Maciel, W. J. & Köppen, J. 1994, A&A 282, 436

[105] Maciel, W. J. & Quireza, C. 1999, A&A 345, 629

[106] Maeder, A. 1992, A&A 264, 150

[107] Marco, A., Bernabeu, G. & Negueruela, I. 2001, AJ 121, 2075

[108] Martin, P. & Roy, J. 1994, ApJ 424, 599

[109] Martins, L. P. & Viegas, S. M. M. 2000, A&A 361, 1121

[110] Massey, P., DeGioia-Eastwood, K. & Waterhouse, E. 2001, AJ 121, 1050

[111] Mathis, J. S. 1995, Rev. Mex. Astron. Astrof. (Conference Series) 3, 207

[112] McCarthy, J. K., Sandiford, B.A., Boyd, D. & Booth, J. 1993, PASP 105, 881

[113] McCuskey, S. W. 1970, in 'The Spiral Structure of Our Galaxy', ed. W. Becker & G. Contopoulos (Reidel: Dordrecht), p. 191

[114] McEachran, R. P. & Cohen, M. 1983, J. Phys. B 16, 3125

[115] Mel'nik A.M. & Efremov Yu.N. 1995, PAZh 21, 13

[116] Meyer, D. M., Jura, M & Cardelli, J. A. 1998, ApJ 493, 222

[117] Mihalas, D. 1972, ApJ 177, 115

[118] Mihalas, D. 1978, 'Stellar Atmospheres' (San Francisco: W. H. Freeman and Co.)

[119] Moffat, A. F. J. & Vogt, N. 1975a, A&AS 20, 155

[120] Moffat, A. F. J. & Vogt, N. 1975b, A&AS 20, 85

[121] Moffat, A. F. J., Fitzgerald, M. P. & Jackson, P. D. 1977, ApJ 215, 106

[122] Moffat, A. F. J., Fitzgerald, M. P. & Jackson, P. D. 1979, A&AS 38, 197

[123] Morossi, C. & Crivellari, L. 1980, A&AS 60,365

[124] Morrison, N. D. 1975, ApJ 200, 113

[125] Olive, K. A. & Schramm, D. N. 1982, ApJ 257, 276

[126] Pérez, M. R. 1991, Rev. Mex. Astron. y Astrof. 22, 99

[127] Philip, A. G. D., Chomey, F. R. & Dubois, P. 1990, PASP 102, 654

[128] Przybilla, N., Butler, K., Becker, S. R. & Kudritzki, R.P. 2001, A&A 369, 1009

[129] Reeves, H. 1972, A&A 19, 215

[130] Reeves, H. 1978, in 'Protostars and Planets', ed. T. Gehrels (Tucson: Univ. Arizona Press), p. 399

[131] Reichen, M., Lanz, T., Golay, M. & Huguenin, D. 1990, Ap&SS 163, 275

[132] Rolleston, W. R. J., Brown, P. J. F., Dufton, P. L. & Fitzsimmons, A. 1993, A&A 270, 107

[133] Rolleston, W. R. J., Dufton, P. L. & Fitzsimmons, A. 1994, A&A 284, 72

[134] Rolleston, W. R. J., Smartt, S. J., Dufton, P. L. & Ryans, R. S. I. 2000, A&A 363, 537

[135] Sagar, R. & Joshi, U. C. 1981, Ap&SS 75, 465

[136] Schaller, G., Schaerer, D., Meynet, g., & Maeder, A. 1992, A&AS 96, 269

[137] Scharmer, G. B. 1981, ApJ 249, 720

[138] Seaton, M. J. 1962, in 'Atomic and Molecular Processes', ed. D. R. Bates (New York: Academic Press), cap. 11.

[139] Seaton, M. J., Zeippen, C. J., Tully, J. A., Pradham, A. K., Mendonza, C., Hibbert, A. & Berrington, K. A. 1992, Rev. Mex. Astron. Astrof. 23, 19

[140] Shaver, P.A., McGee, R.X., Newton, M.P., Danks, A.C. & Pottasch, S.R. 1983, MNRAS 204, 53

[141] Shobbrook, R. R. 1984, MNRAS 206, 273

[142] Simonson III, S. C. 1968, ApJ 154, 923

[143] Simonson III, S. C. & van Someren Greve, H. W. 1976, A&A 49, 343

[144] Smartt, S. J., Dufton, P. L. & Rolleston, W. R. J. 1996a, A&A 305, 164

[145] Smartt, S. J., Dufton, P. L. & Rolleston, W. R. J. 1996b, A&AS 116,483

[146] Smartt, S. J., Dufton, P. L. & Rolleston, W. R. J. 1996c, A&A 310, 123

[147] Smartt, S. J. & Rolleston, W. R. J. 1997, ApJ 481, L47

[148] Smartt, S. J. 2001, in 'The Chemical Evolution of the Milky Way: Stars versus Clusters', ed. F. Giovannelli & F. Matteucci (Kluwer: Dordrecht), vol. 255

[149] Smartt, S. J., Venn, K. A., Dufton, P. L., Lennon, D. J., Rolleston, W. R. J. & Keenan, F. P. 2001, A&A 367, 86

[150] Sofia, U. J., & Meyer, D. M. 2001, ApJ 554, L221

[151] Tapia, M., Costero, R., Echevarría, J. & Roth, M. 1991, MNRAS 253, 649

[152] Tovmassian, H. M., Epremian, R. A., Kovhannesian, R. Kh., Cruz-Gonzalez, G., Navarro, S. G. & Karapetian, A. A. 1998, AJ 115, 1083

[153] Turbide, L. & Moffat, A. F. J. 1993, AJ 105, 1831

[154] van der Hucht, K. A., The, P. S. & Bakker, R. 1980, PASP 92, 837

[155] van Regemorter, H. 1962, ApJ 136, 906

[156] Vila-Costas, M. B. & Edmunds, M. G. 1992, MNRAS 259, 121

[157] Vílchez, J. M. & Esteban, C. 1996, MNRAS 280, 720

[158] Vogt, N. & Moffat, A. F. J. 1975, A&A 39, 477

[159] Vrancken, M, Butler, K & Becker, S. R. 1996, A&AS 311, 661

[160] Vrancken, M., Lennon, D. J., Dufton, P. L. & Lambert, D. L. 2000, A&A 358, 639

[161] Wade, R. A., Rucinski, S. M. 1985, A&ASS 60, 471

[162] Werner, K. & Husfeld, D. 1985, A&A 148, 417

[163] Werner, K. 1988, A&A 204, 159

[164] Westin, T. N. G. 1985, A&AS 60, 99

[165] Wolff, S. C., Edwards, S. & Preston, G. W. 1982, ApJ 252, 322

[166] Woosley, S. E. & Weaver, T. A. 1995, ApJS 101, 181

[167] Zelwanowa, E & Schoeneich, W. 1971, Astron. Nachr. 293, 155